COMENIUS UNIVERSITY IN BRATISLAVA
FACULTY OF MATHEMATICS, PHYSICS AND INFORMATICS

Gamma-ray and conversion-electron spectroscopy at CERN-ISOLDE facility

ACADEMIC DISSERTATION
FOR THE DEGREE OF
DOCTOR OF PHILOSOPHY

2019

Ing. Matúš SEDLÁK

COMENIUS UNIVERSITY IN BRATISLAVA
FACULTY OF MATHEMATICS, PHYSICS AND INFORMATICS

Gamma-ray and conversion-electron spectroscopy at CERN-ISOLDE facility

ACADEMIC DISSERTATION
FOR THE DEGREE OF
DOCTOR OF PHILOSOPHY

Subject:	Nuclear and subnuclear physics
Branch of study:	4.1.5. Nuclear and subnuclear physics
Institute:	Institute of Physics, Slovak Academy of Sciences
Department:	Department of Nuclear Physics
Supervisor:	Mgr. Martin VENHART, PhD.

Bratislava 2019

Ing. Matúš SEDLÁK

Comenius University in Bratislava
Faculty of Mathematics, Physics and Informatics

THESIS ASSIGNMENT

Name and Surname:	Ing. Matúš Sedlák
Study programme:	Nuclear and Subnuclear Physics (Single degree study, Ph.D. III. deg., full time form)
Field of Study:	Nuclear And Subnuclear Physics
Type of Thesis:	Dissertation thesis
Language of Thesis:	English
Secondary language:	Slovak

Title: Gamma-ray and conversion-electron spectroscopy at CERN-ISOLDE facility

Annotation: Excited states of odd-mass isotopes can provide a valuable information about the deformation of neclei (axial or triaxial) and shape coexistence. Neutron deficient odd-mass isotopes of gold, 181,183Au, were studied by the TATRA spectrometer during IS521 experiment at ISOLDE. Their excited states were populated by the beta+/EC decay of 181;183Hg precursors. IS521 experiment will continue with simultaneous detection of gamma rays and conversion electrons, which will lead to conversion coefficients determination for nuclear transitions. The Broad Energy Germanium (BEGe) detector as the gamma-ray detector was employed in this type of the experiment for the first time and it will be used for the next run also. This detector has a great resolution and peak shapes of almost ideal Gaussian. This makes the level scheme construction significantly easier. The windowless lithium-drifted silicon (Si(Li)) detector, cooled with liquid nitrogen, will be used for the detection of conversion electrons. Objectives of the thesis will be the level schemes construction of 181,183Au isotopes, electric monopole transition identification and comparison of results with overall excited states systematics of odd-mass isotopes of gold.

Tutor:	Mgr. Martin Venhart, PhD.
Department:	FMFI.KJFB - Department of Nuclear Physics and Biophysics
Head of department:	prof. RNDr. Stanislav Tokár, DrSc.
Assigned:	18.08.2015
Approved:	18.08.2015 RNDr. Štefan Olejník, DrSc. Guarantor of Study Programme

.....
Student

.....
Tutor

Univerzita Komenského v Bratislave
Fakulta matematiky, fyziky a informatiky

75188393

ZADANIE ZÁVEREČNEJ PRÁCE

Meno a priezvisko študenta: Ing. Matúš Sedlák
Študijný program: jadrová a subjadrová fyzika (Jednoodborové štúdium, doktorandské III. st., denná forma)
Študijný odbor: jadrová a subjadrová fyzika
Typ záverečnej práce: dizertačná
Jazyk záverečnej práce: anglický
Sekundárny jazyk: slovenský

Názov: Gamma-ray and conversion-electron spectroscopy at CERN-ISOLDE facility
Spektroskopia gamma žiarenia a konverzných elektrónov na zariadení CERN-ISOLDE

Anotácia: Vzbudené stavy nepárnych izotopov nesú informáciu o deformácii atómových jadier (axiálnej ako aj triaxiálnej), ako aj tvarovej koexistencii. V experimente IS521 na zariadení ISOLDE boli pomocou spektrometra TATRA študované nepárne izotopy zlata, 181,183Au. Ich vzbudené stavy boli populované pomocou beta+/EC premeny materských izotopov 181;183Hg. V plánovanom pokračovaní experimentu budú gama žiarenie a konverzné elektróny detegované simultánne, čo umožní stanovenie koeficientov vnútornej konverzie pre jadrové prechody. Na detekciu gama žiarenia bol po prvý krát v tomto type experimentu využitý germániový detektor typu BEGe a bude použitý aj v jeho pokračovaní. Ten dosahuje vynikajúce energetické rozlíšenie a takmer ideálne gaussovský tvar píku. To umožňuje výrazne zjednodušenú konštrukciu rozpadovej schémy. Na detekciu konverzných elektrónov bude použitý bezoknový Si(Li) detektor, chladený tekutým dusíkom. Cieľmi práce bude skonštruovať rozpadové schémy izotopov 181,183Au, identifikovať prípadné elektrické monopólové prechody a výsledky porovnať s celkovou systematikou vzbudených hladín nepárnych izotopov zlata.

Školiteľ: Mgr. Martin Venhart, PhD.
Katedra: FMFI.KJFB - Katedra jadrovej fyziky a biofyziky
Vedúci katedry: prof. RNDr. Stanislav Tokár, DrSc.

Dátum zadania: 18.08.2015

Dátum schválenia: 18.08.2015 RNDr. Štefan Olejník, DrSc.
garant študijného programu

.....
študent

.....
školiteľ

Declaration of Authorship

I, Ing. Matúš SEDLÁK, declare that this thesis titled, "Gamma-ray and conversion-electron spectroscopy at CERN-ISOLDE facility" and the work presented in it are my own. I confirm that:

- This work was done wholly or mainly while in candidature for a research degree at this University.
- Where I have consulted the published work of others, this is always clearly attributed.
- Where I have quoted from the work of others, the source is always given. With the exception of such quotations, this thesis is entirely my own work.
- I have acknowledged all main sources of help.

Signed:

Date:

Univerzita Komenského v Bratislave
Fakulta Matematiky, Fyziky a Informatiky

Abstrakt

Philosophiae Doctor

Spektroskopia gamma žiarenia a konverzných elektrónov na zariadení CERN-ISOLDE

Ing. Matúš SEDLÁK

Témou práce je systematické štúdium tvarovej koexistencie nepárnych izotopov zlata v oblasti s neutrónovým číslom N = 104. Experimentálna časť tejto práce sa opiera o realizáciu experimentu IS521 na zariadení ISOLDE. Excitované stavy izotopov ^{181,183}Au boli populované β^+/EC premenou ^{181,183}Hg prekurzorov, ktoré boli dodané zariadením ISOLDE. Jadrová štruktúra izotopov ^{181,183}Au bola študovaná pomocou simultánnej spektroskopie konverzných elektrónov a γ kvánt. TATRA spektrometer, ktorý obsahuje unikátny páskový transportný systém založený na amorfnej kovovej páske, bol vyvinutý a úspešne použitý. Nový Broad Energy Germanium (BEGe) detektor bol použitý v experimente v oblasti základného výskumu jadrovej štruktúry po prvýkrát. Tento detektor má výborné rozlíšenie, spojité pozadie a takmer ideálne tvarované píky podobné Gaussovému rozdeleniu, čo umožňuje lepšie rozoznanie píkov v multipletoch a určenie energie píkov s presnosťou na $30\,\mathrm{eV}$. Vďaka tejto presnosti mohol byť použitý kombinačný princíp, ktorý navrhli Rydberg a Ritz, na zostavovanie rozpadových schém. Pri štúdiu nuklidov s nepárnym hmotnostným číslom často čelíme spektrám, ktoré sa vyznačujú veľkou hustotou píkov. Preto bola použitá inovatívna metóda na separáciu pôvodnej premeny od dcérskych premien v spektrách. Rozpadová schéma nuklidu ^{183}Au bola značne doplnená a opravená oproti tej v predošlej štúdii a rozpadová schéma pre nuklid ^{181}Au bola skonštruovaná po prvýkrát. Boli doplnené systematiky niektorých stavov a mierna zmena tvaru bola identifikovaná pomocou ich porovnania s PTRM výpočtami. Hlavným výsledkom práce je pozorovanie parabolického trendu v systematike vnorených (intruder) stavov s minimom presne medzi dvoma neutrónovými uzavretými vrstvami, N = 104, čo zodpovedá izotopu ^{183}Au.

Comenius University in Bratislava
Faculty of Mathematics, Physics and Informatics

Abstract

Philosophiae Doctor

Gamma-ray and conversion-electron spectroscopy at CERN-ISOLDE facility

by Ing. Matúš SEDLÁK

The topic of this thesis is the systematic study of the shape coexistence in odd-mass Au isotopes in the vicinity of N = 104 mid-shell point. Experimental part of the thesis was performed at ISOLDE facility, within the scope of the IS521 experiment. Excited states of ^{181,183}Au isotopes were populated by β^+/EC decay of ^{181,183}Hg precursors produced by ISOLDE. Nuclear structure of ^{181,183}Au isotopes was investigated by means of simultaneous spectroscopy of conversion electrons and γ rays. A unique tape transportation system TATRA, based on rapidly quenched metallic tape, was designed and successfully commissioned. For the first time in the fundamental nuclear structure experiment, novel Broad Energy Germanium (BEGe) detector was used. Its supreme energy resolution, together with almost ideally Gaussian peak shape allowed peak recognitions in many multiplets and the determination of peak energies with $30\,\mathrm{eV}$ precision. It was so precise, that Rydberg-Ritz combination principle was used for level scheme constructions. An enormous complexity of measured spectra emerges in the case of odd-mass nuclei study. Therefore, innovative method was developed. Results of the study are significantly improved level scheme of the ^{183}Au in comparison with previous work and the level scheme of the ^{181}Au was constructed for the first time. Systematics of particular states of odd-Au isotopes were extended and slight change in shape based on PTRM calculations was observed. The key result is observation of a parabolic trend in the systematics of intruder states with its minimum in neutron midshell point N = 104 (^{183}Au).

Preface and Acknowledgement

This thesis is aimed on γ-ray and conversion-electron spectroscopy of neutron-deficient ^{181,183}Au isotopes. Its purpose is the systematic study of the shape coexistence in odd-mass Au isotopes in the vicinity of N = 104 mid-shell point. Previously, only limited information about nuclear structure of these Au isotopes were available and mostly in-beam studies were performed. However, these studies could provide mostly information about yrast states. The critical step in understanding the systematic behaviour of intruder configurations was the discovery of the isomer in ^{179}Au. These data revealed the parabolic trend of excitation energy of intruder states in odd-mass Au isotopes.

In order to investigate this trend further, dedicated experiment for β-decay study was proposed by my supervisor Martin Venhart in 2011. However, nothing was sure at that time and no appropriate experimental device was available. I have become a member of the team in 2012, during my bachelor degree studies. Since than, we have developed a unique device capable of capture the radioactive beam, transport the sample to the detection point and simultaneously measure γ rays and conversion electrons in high vacuum conditions. This device was named TATRA and I was responsible for technical drawings and design of the tape transportation system. When the Si(Li) detector arrived, its preamplifier was incompatible to our digital data acquisition system. Therefore, I have developed the converter circuit for it and conversion electrons were measured with it later. Three experiments has been carried out with the TATRA spectrometer and I was part of realisation team of all of them. Later on, I was analysing data from IS521 experiment (partially ^{183}Hg and the whole ^{181}Hg data). I have acquired a lot of knowledge about various topics from mechanical engineering, through data analysing to nuclear structure features. This thesis is just a cherry on the top of all our efforts.

My greatest Thank You goes to my supervisor Martin Venhart for his really wide support, valuable advices, many corrections, a lot of fruitful discussions, his great memory of hundreds of articles and for the opportunity to work on IS521 project. This journey would not have been possible without him.

I would also like to thank Vladislav Matoušek for that many years of help, support, advices and a lot of discussions. I am grateful to Matúš Balogh for help with ROOT, HDTV, C++, experimental work and for many news from all kind of fields.

Finally, I am grateful to my wife, family and friends for continuous support.

Contents

List of Figures

List of Tables

List of Abbreviations

AC	**A**lternating **C**urrent
ADC	**A**nalog to **D**igital **C**onverter
AEGIS	**A**ntihydrogen **E**xperiment: **G**ravity, **I**nterferometry, **S**pectroscopy
ALICE	**A** **L**arge **I**on **C**ollider **E**xperiment
AMS	**A**lpha **M**agnetic **S**pectrometer
ASACUSA	**A**tomic **S**pectroscopy **A**nd **C**ollisions **U**sing **S**low **A**ntiprotons experiment
ASPIC	**A**pparatus for **S**urface **P**hysics and **I**nterfaces at **C**ERN
ASPIC	The **A**pparatus for **S**urface **P**hysics and **I**nterfaces at **C**ern
ATLAS	**A** **T**oroidal **L**HC **A**pparatu**S**
ATRAP	**A**ntihydrogen **TRAP**
AWAKE	Proton Driven Plasm**A** **WAKE**field Acceleration Experiment
BASE	**B**aryon **A**ntibaryon **S**ymmetry **E**xperiment
BEGe	**B**road **E**nergy **Ge**rmanium
CAST	**C**ERN **A**xion **S**olar **T**elescope
CERN	**C**onseil **E**uropéen pour la **R**echerche **N**ucléaire
CE	**C**onvesion **E**lectrons
CF	**C**on**F**lat^{TM} type of the vacuum flange
CLOUD	**C**osmics **L**eaving **OU**tdoor **D**roplets experiment
CMS	**C**ompact **M**uon **S**olenoid
COMPASS	**CO**mmon **M**uon and **P**roton **A**pparatus for **S**tructure and **S**pectroscopy
COLLAPS	**COL**linear **LA**ser **SP**ectroscopy
CRIS	**C**ollinear **R**esonance **I**onization **S**pectroscopy
DC	**D**irect **C**urrent
DGF	**D**igital **G**amma **F**inder
DIRAC	**DI**meson **R**elativistic **A**tom **C**omplex
EC	**E**lectron **C**apture
FET	**F**ield **E**ffect **T**ransistor
FWHM	**F**ull **W**idth at **H**alf **M**aximum
GSI	**G**esellschaft für **S**chwer**i**onenforschung mbH
HPGe	**H**igh **P**urity **Ge**rmanium
I/O	**I**nput or **O**utput
IC	**I**nternal **C**onversion
IDS	**I**SOLDE **D**ecay **S**tation
ISOLDE	**I**sotope **S**eparator **O**n-**L**ine **DE**vice
ISO	**I**nternational **O**rganization for **S**tandardization
ISS	**I**SOLDE **S**olenoidal **S**pectrometer
LHC	**L**arge **H**adron **C**ollider
LHCb	**L**arge **H**adron **C**ollider **b**eauty experiment
LHCf	**L**arge **H**adron **C**ollider **f**orward experiment

LN_2	**L**iquid **N**itrogen
MOEDAL	**MO**nopole and **E**xotics **D**etector **A**t the **L**HC
MOS	**M**etal-**O**xide **S**emiconductor
OFCu	**O**xygen **F**ree **C**opper
OSQAR	**O**ptical **S**earch for **Q**ED Vacuum Bifringence, **A**xions and Photon **R**egeneration experiment
PCB	**P**rinted **C**ircuit **B**oard
PTFE	**P**oly**t**etra**f**luoro**e**thylene
PXI	**P**CI e**X**tensions for **I**nstrumentation
RAID	**R**edundant **A**rray of **I**ndependent **D**isks
RIB	**R**adioactive **I**on **B**eam
SAS	**S**lovac **A**cademy of **S**ciences
SHIP	**S**eparator for **H**eavy **I**on reaction **P**roducts
SMA	**S**ub**M**iniature version **A** connector
SSL	**S**uper **S**i(**L**i)
TATRA	**TA**pe **TRA**nsportation system
TMP	**T**urbo**M**olecular **P**ump
TOTEM	**TOT**al cross section, **E**lastic scattering and diffraction dissociation **M**easurement at the LHC
TRP	**T**ransistor **R**eset type **P**reamplifier
UHV	**U**ltra **H**igh **V**acuum
nTOF	**n**eutron **T**ime-**O**f-**F**light facility

Introduction

The atomic nucleus, discovered by Ernest Rutherford in 1911 by interpretation of the famous gold-foil experiment [1] performed by Hans Geiger and Ernest Marsden, represents one of the fundamental building blocks of the matter in the Universe. It takes place between atoms and the hadrons in a chain of basic constituents, which stretches from quarks to galaxies. In common with many of its neighbours in the chain, the basic problem of nuclear structure physics is a quantum many-body one. Therefore, nuclear physics continues to be one of the most fascinating fields in a fundamental science. Nucleus generally consists of a large finite number of nucleons (neutrons and protons) interacting via a strong short-range force. The precise form of this effective interaction is still not known. In a sense, its determination is one of the fundamental goals of nuclear physics. The route, towards this goal, involves systematic predictions and domains testing of its applicability of the current models by probing excited states of nuclei in a great detail.

Besides the scientific importance of nuclear physics there is also an enormous societal impact. Nowadays, the area of nuclear physics applications is very broad, including power generation via nuclear fission and, in the future, also the fusion, nuclear waste management, imaging, and tumour therapy in nuclear medicine, security applications, material science, etc. With dramatic development of new technologies within past decade will more and more new applications appear with a short periodicity.

Important feature related to the nuclear structure is the shape coexistence, i.e., observation of differently shaped excited states (eigenstates) in particular atomic nucleus. The shape coexistence is known as a feature of nuclei over 50 years with three extensive reviews published [2–4].

This thesis deals with the systematic study of the shape coexistence in odd-Au isotopes in the vicinity of $N = 104$ mid-shell point. Odd-mass isotopes in general herald the unique systems for nuclear structure studies, where the odd particle (proton or neutron) acts as a probe of the even-even core and yields information on independent particle states, of deformation (both axial and triaxial shapes), on pairing (from the blocking effect), on rotational collectivity, and on identification of intruder states almost free of mixing. The coupling of independent particle states with core excitations lead to high level density at low energies in odd-mass nuclei.

Moreover, unlike in even-even nuclei, the decay schemes involve multiple paths to the ground states and multipolarities of transitions are dominated by $M1$ and mixed $M1 + E2$. This is reflected in an enormous complexity of measured spectra, both for γ rays and conversion electrons. Therefore, an excellent energy resolution is critical parameter. To achieve acceptable conditions, innovative methods needed to be developed to study odd-mass nuclei.

Experimental part of the thesis was performed at ISOLDE facility, within the scope of the IS521 experiment [5]. Excited states of ^{181,183}Au isotopes were populated by β^+/EC decay of ^{181,183}Hg precursors produced by ISOLDE. Nuclear structure of ^{181,183}Au isotopes was investigated by means of simultaneous spectroscopy of conversion electrons and γ rays. A unique tape transportation system TATRA, based on rapidly quenched metallic tape, was designed and successfully commissioned. For the first time in the fundamental nuclear structure experiment, novel Broad Energy Germanium (BEGe) detector was used. Its supreme energy resolution, together with almost ideally Gaussian peak shape allowed peak recognitions in many multiplets and the determination of peak energies with $30\,\mathrm{eV}$ precision. It was so precise, that Rydberg-Ritz combination principle [6] was used for level scheme constructions.

Decay scheme of ^{183}Hg was significantly improved [7] in comparison with previous work [8]. Decay scheme of ^{181}Hg was constructed for the first time.

Chapter 1

Nuclear structure

This chapter is based on the knowledge acquired during my studies and literature [9–17].

1.1 Spherical shell model

The nuclear shell model and complementary nuclear pairing models are ones of the most thoroughly developed and the best understood models of the nucleus. The shell model has its origin in the evidence for energy shells in nuclei similar to those in atoms. This leads to an independent-particle description of nucleus. The main motivation for independent-particle approximation is occurrence of energy gaps at the proton and neutron numbers 2, 8, 20, 28, 50, 82 and 126 (so-far observed for neutrons only) and these are known as magic numbers. These magic numbers are related to fully occupied shells (closed shells). Evidence for closed shells comes, e.g., from observation of energy gaps in two-neutron (two-proton) separation energies, see Fig 1.10 in [9].

The shell model is build on a single particle potential and two-body residual interactions between independent particles. The model breaks down, when residual interactions produce correlations and some or all nucleons appear in collective behaviour. However, the shell model is still valid if some of the nucleons can be described as independent particles so they are not involved in the collective mode. The nuclear Hamiltonian can be expressed as a sum of an independent-particle Hamiltonians and residual interaction $\hat{V}$, i.e.,

$$\hat{H} = \sum_{n=1}^{A} \left[\frac{\hat{p}_n^2}{2M} + U(r_n) \right] + \hat{V}, \tag{1.1}$$

where $\hat{\boldsymbol{p}}_n = -i\hbar\nabla_n$ is the momentum of the n'th nucleon, M is mass of a nucleon, $\boldsymbol{r}_i$ is its position vector and U is a potential for a central single-particle field.

Very important is the choice of the single-particle potential, because unlike the potential for electrons in atoms, there is no well-defined centre in atomic nucleus. The

nuclear single-particle potential is an averaging of the interaction between nucleons, and therefore it is mean single-particle field, which leads to flexibility in the choice of the single-particle potential. There are two simple and analytically solvable single-particle potentials where magic numbers occur: The infinite square well potential (equation 1.2) and the harmonic oscillator (equation 1.3). They are both unrealistic because they are infinitely deep and predict wrong magic numbers. The most realistic single-particle potential is the Woods-Saxon potential. It is based on the mean single-particle field, which follows the density distribution of the nucleons in a nucleus determined experimentally. But the equation 1.1 with the Woods-Saxon potential can't be solved analytically, so there is lack of transparency and it is no easy to use. The equation for infinite square well potential is

$$U(r) = \begin{cases} -V_0 & if\ r < R \\ \infty & if\ r \geq R, \end{cases} \tag{1.2}$$

and the equation for the harmonic oscillator potential is

$$U(r) = \begin{cases} -V_0[1 - \frac{r^2}{R^2}] & if\ r < R \\ 0 & if\ r \geq R, \end{cases} \tag{1.3}$$

and the equation for the Woods-Saxon potential is

$$U(r) = -V_0 \left\{ 1 + exp\left(\frac{r - R}{a} \right) \right\}^{-1}, \tag{1.4}$$

where V_0 is potential well depth, a is length of the surface thickness, r is distance from the centre and R is the radius of the nucleus.

It is impossible to obtain correct magic numbers only by appropriate mean-field potential choice. It is necessary to consider the spin-orbit interaction for each nucleon. For the discovery of strong spin-orbit interaction occurring for each nucleon, which was a key step to establishing a single-particle description of nucleons in the nucleus, the Nobel Prize was given to Maria Goeppert Mayer [18] and J. H. D. Jensen [19] in 1963. The spin-orbit interaction originates from the strong force and the choice of its form is phenomenological like the single-particle potential. The spin-orbit interaction is described by the theory of spin and angular momentum and for a given nucleon can be expressed in the form

$$\hat{H}_{SO} = \xi \vec{\boldsymbol{l}}.\vec{\boldsymbol{s}}, \tag{1.5}$$

where ξ is an empirical parameter (usually negative), $\vec{\boldsymbol{l}}$ is the orbital angular momentum and $\vec{\boldsymbol{s}}$ is the intrinsic spin of the nucleon. When this spin-orbit operator is included in calculations we can obtain the correct magic numbers. The example of

such calculation is shown in Fig. 1.1.

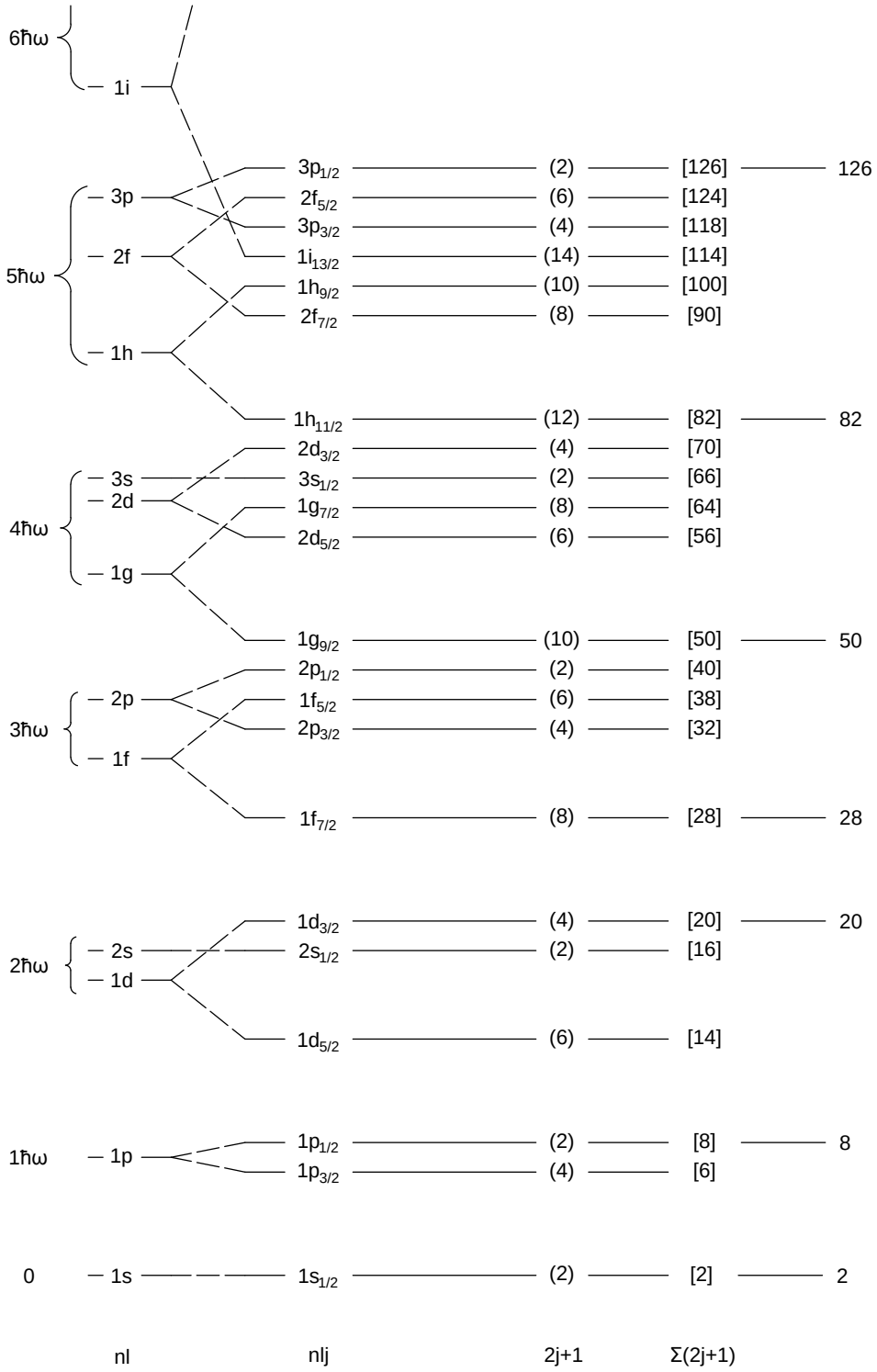

FIGURE 1.1: Energy level sequence for a single particle moving in a bottom flattened spherical harmonic oscillator potential and spin-orbit coupling terms. Levels are labelled by quantum numbers (radial - n, orbital angular momentum - l, and total spin j). Level occupancies are in brackets and rightmost numbers are magic numbers. Figure is adapted from [9].

We can assume that nuclei with number of nucleons for closed shell plus or minus one nucleon manifest single-particle behaviour. For testing this assumption there are nuclei with doubly-closed shells, i.e. ${}^{4}_{2}\mathrm{He}_{2}$, ${}^{16}_{8}\mathrm{O}_{8}$, ${}^{40}_{20}\mathrm{Ca}_{20}$, ${}^{48}_{20}\mathrm{Ca}_{28}$, ${}^{56}_{28}\mathrm{Ni}_{28}$, ${}^{132}_{50}\mathrm{Sn}_{82}$ and ${}^{208}_{82}\mathrm{Pb}_{126}$, and odd-mass nuclei adjacent to them. Low-lying states of odd-mass nuclei adjacent to ^{40}Ca are shown in Fig. 1.2 and this can be compared with calculated configuration in Fig. 1.1.

The shell model fails even with single-particle and/or single-hole excitation when the excited nucleon became a pair with nucleon in the next shell, which will lower the energy of the state via pairing correlations. These states with lower energy that shell model predicts are intruder states. For example the state $1f_{7/2}$ in ^{39}Ca and ^{39}K, which are shown in Fig. 1.2 is intruder state according to the shell model calculation in Fig. 1.1. Intruder states are responsible for shape coexistence and are discussed in greater detail in Section 1.7.

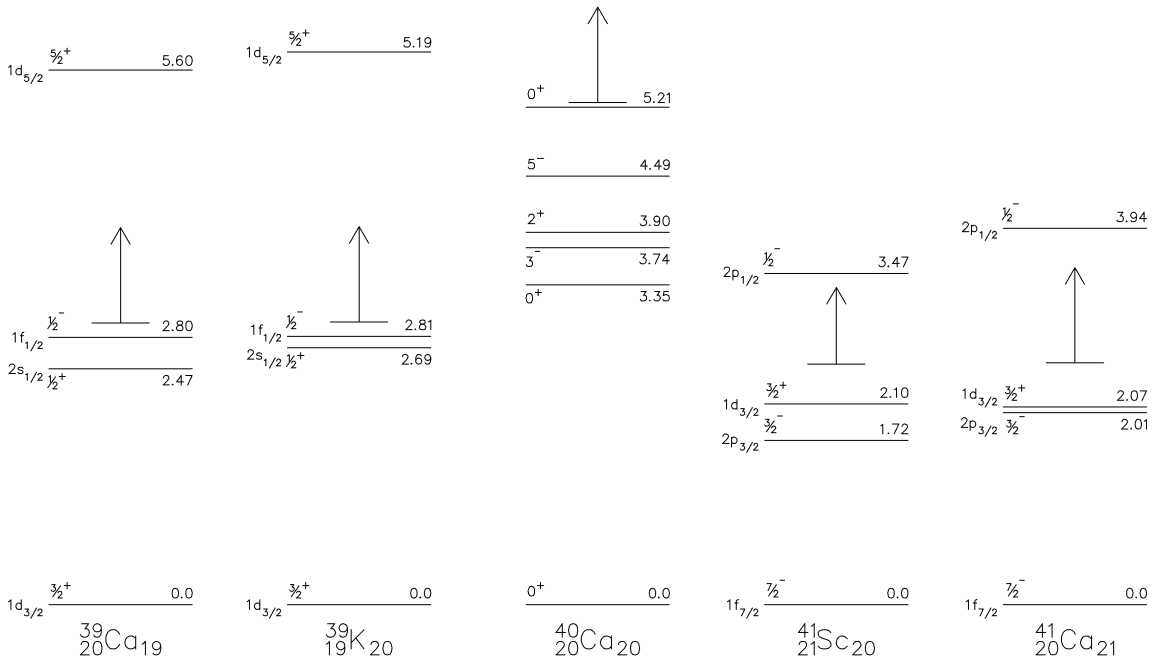

FIGURE 1.2: Single-particle and single-hole states of isotopes adjacent to ^{40}Ca. Figure is adapted from [9].

1.2 Deformed nuclei

1.2.1 Nilsson model

S. G. Nilsson introduced a deformed version of single-particle shell model in 1955, see [20] and references therein. It replaces the spherical harmonic oscillator potential with spheroidal potential. The Nilsson model is an extreme form of a unified model and describes the nucleus in terms of all its individual nucleons, bound in a permanently deformed potential, for example in the form

$$V = \frac{m(\omega_\perp^2(x^2+y^2)+\omega_z^2 z^2)}{2} - \kappa\hbar\omega_0[2\vec{ls}+\mu l^2], \tag{1.6}$$

where $\omega_\perp = \omega_0^2(1+\frac{2}{3}\epsilon), \omega_z = \omega_0^2(1+\frac{4}{3}\epsilon), \omega_0$ is the spherical oscillator frequency and parameters κ and μ adjust strength of ls and l^2 terms. The parameter ϵ is the Nilsson deformation parameter, which positive value indicate a prolate spheroid and when it is negative the nucleus is oblate. The Hamiltonian for Nilsson model is analytically solvable in the limit of $\epsilon \to 0$ or in the limit of $\epsilon \to \infty$ only. Without deformation, Nilsson single-particle energies are defined as in the spherical shell model with N, l and j as quantum numbers. In the asymptotic limit of large deformation, mixing of eigenstates of Hamiltonian is small, single-particle energies are defined by four quantum numbers: N, n_z, Λ (the eigenvalue of l_z) and Ω (the eigenvalue of j_z). Energy levels are usually labelled with quantum numbers as $\Omega[Nn_z\Lambda]$.

- Ω - the projection of the total angular momentum on the symmetry axis.
- N - the total oscillator shell quantum number.
- n_z - the number of oscillator quanta in the z direction.
- Λ - the projection of angular momentum along the symmetry axis.

Graphical representation of Nilsson asymptotic quantum numbers is shown in Fig. 1.3.

Nilsson diagrams are plots of single-particle energy levels as a function of deformation parameter, see example in the Fig. 1.4.

1.2.2 Deformation parametrisation

Aage Bohr introduced a hydrodynamic collective model [22] in 1952. It's concept was based on an earlier liquid drop model, which turns out to be overly restricted and imprecise. However, the principle of combining independent-particle and collective degrees of freedom in a single model developed in many ways to the more general

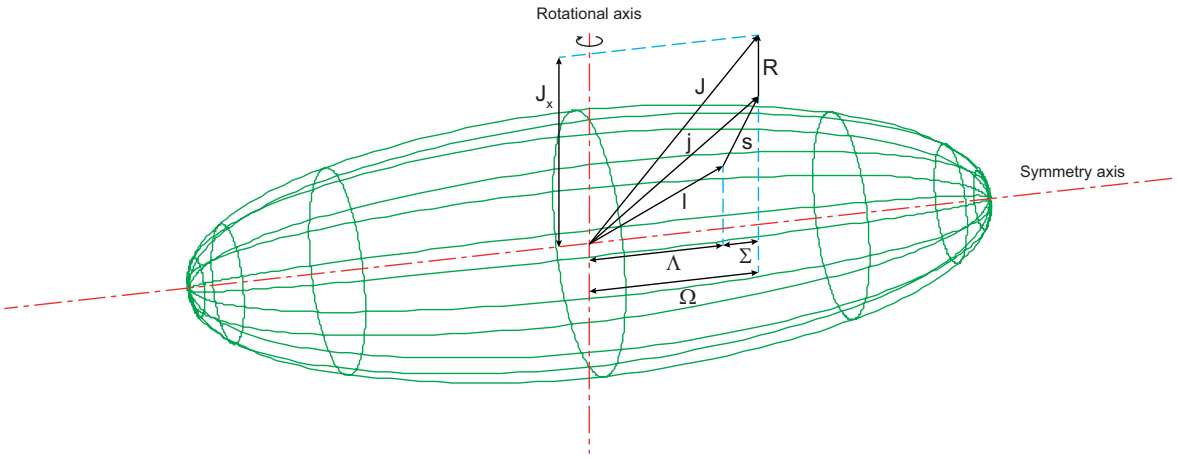

FIGURE 1.3: Schematic of a single-particle coupling to core and the Nilsson asymptotic quantum numbers.

form. The Bohr model was formulated in the terms of surface deformation parameters $\alpha_{\lambda\mu}$ in radial surface function

$$R(\theta,\phi) = R_0(1 + \sum_{\lambda=0}^{\infty}\sum_{\mu=-\lambda}^{\lambda} \alpha_{\lambda\mu}Y_{\lambda\mu}(\theta,\phi)), \tag{1.7}$$

where R_0 is radius of the sphere and $Y_{\lambda\mu}$ are functions of spherical harmonics.

When only quadrupole deformation is considered ($\lambda = 2$), the system of five parameters $\alpha_{\lambda\mu}$ reduces to only two independent parameters (α_{20}, α_{22}) because of

$$\begin{aligned} \alpha_{22} &= \alpha_{2-2}, \\ \alpha_{21} &= \alpha_{2-1} = 0. \end{aligned} \tag{1.8}$$

In order to construct model with angular momentum properties, the quadrupole moments were defined on a spherical-tensor basis. The spherical-tensor quadrupole moments define point in the five dimensional Euclidean space. However, polar coordinates (β,γ) parametrisation can be used to simplify the notation:

$$\begin{aligned} \alpha_{20} &= \beta cos\gamma, \\ \alpha_{22} &= \frac{1}{\sqrt{2}}\beta sin\gamma, \end{aligned} \tag{1.9}$$

where β is radial coordinate and γ is angular coordinate in spherical polar coordinate system. It turns out from transformation, that β is restricted to be positive and $\gamma \to \gamma - \frac{2k\pi}{3}$, where k is an integer (see [9] for more details). Spherical polar coordinate plane is shown in Fig. 1.5, where each $\frac{\pi}{3}$ segment is the transformation of the first one, and thus γ can be restricted to interval $< 0, \frac{\pi}{3} >$. When $\gamma = 0$ the shape is axially symmetric prolate, when $0 < \gamma < \frac{\pi}{3}$ it is the region of triaxial shapes and when $\gamma = \frac{\pi}{3}$

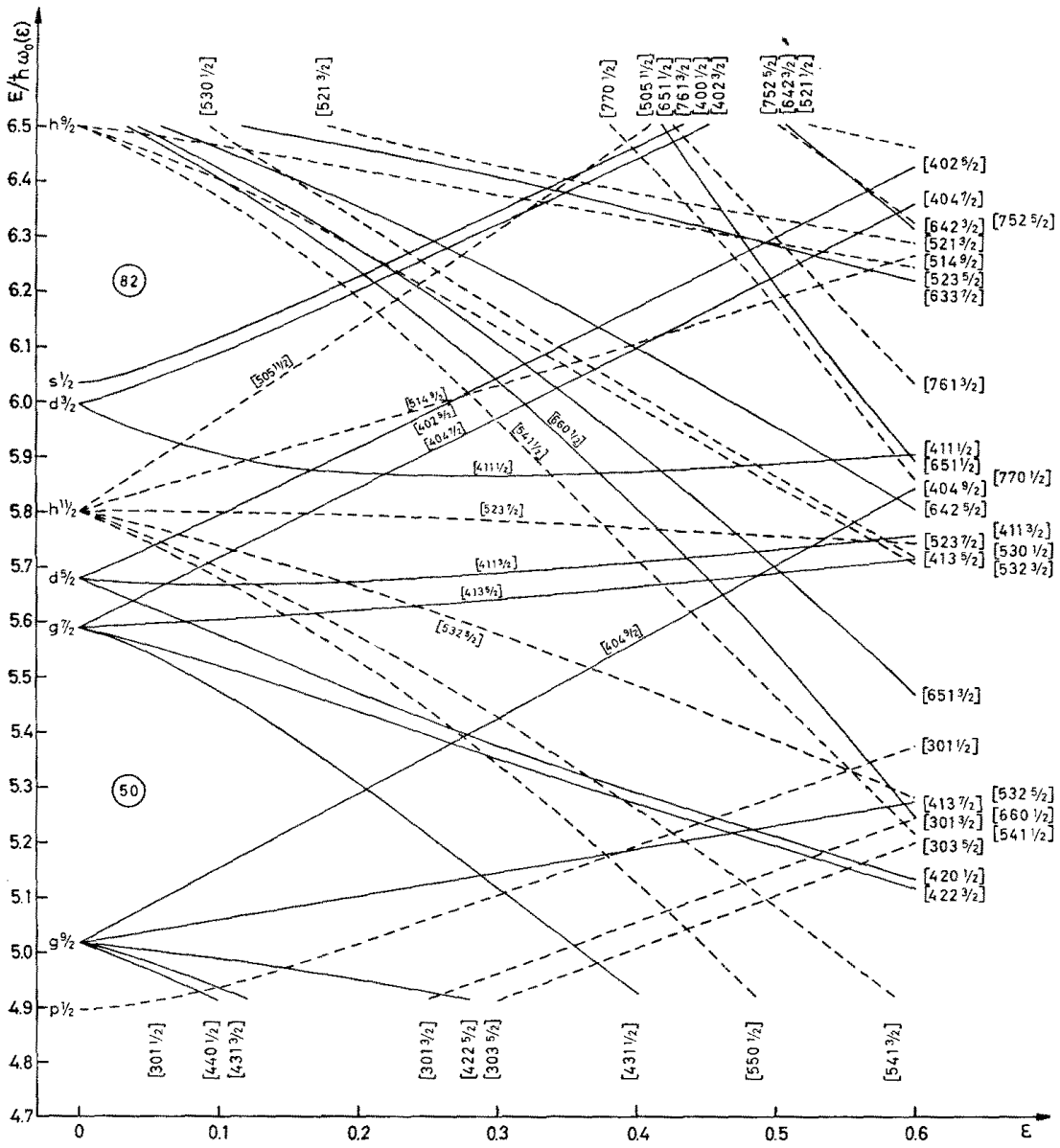

FIGURE 1.4: Nilsson diagram for protons in nuclei with 50≤Z≤82. Energies are in units of $\hbar\omega_0$. Energy levels are labelled by their spherical shell model quantum numbers (l,j) for $\epsilon = 0$ or by Nilsson asymptotic quantum numbers ($\Omega[Nn_z\Lambda]$) for $\epsilon > 0$. The diagram is adapted from [21].

the shape is axially symmetric oblate.

1.3 Particle-Core Coupling Model

In-odd mass isotopes, the unique-parity configurations usually create isolated groups of excited states, since they members predominantly decays within the family. Therefore, they can be easily isolated in otherwise complicated spectra. Due to

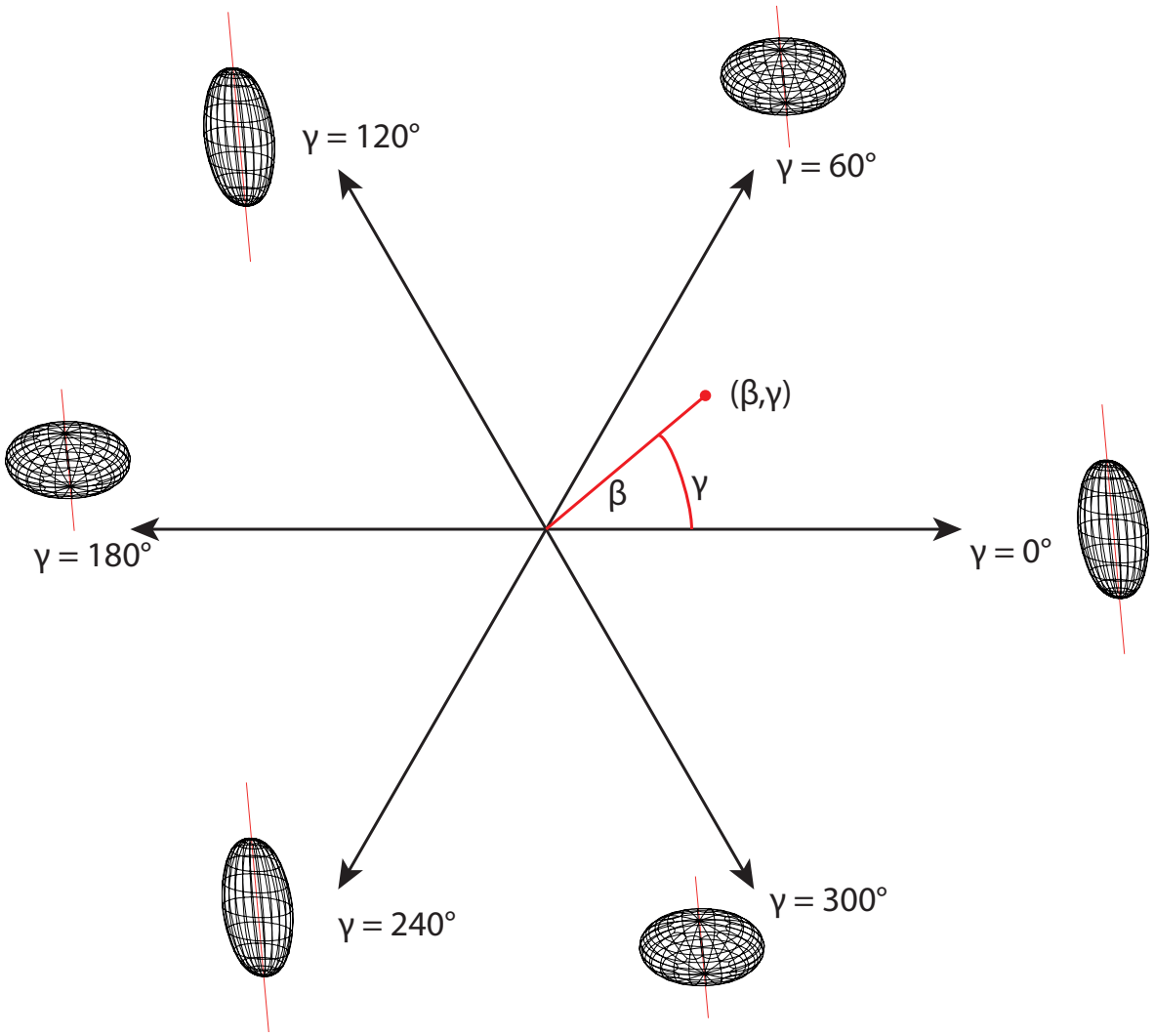

FIGURE 1.5: Spherical polar coordinates (β, γ) plane divided into six equivalent parts with prolate and oblate shapes visualisation.

almost pure configuration of the odd particle (or hole), the information on the shape (including triaxiality) and collective motion of the core can be extracted [23–25].

In a simple theoretical model an odd nucleon in a single j-shell couples to a (triaxially) deformed core.

Three extremes of this model are evident, see Fig. 1.6:

- **(A) Spherically symmetric nuclei.** Very weak coupling of the odd particle, leads to presence of spin multiplets located around excited states of the core. This situation occurs in odd-mass neighbours of magic nuclei. For example, the ^{206}Pb isotope has 2^+ excited state at $803\,\mathrm{keV}$, and in ^{207}Bi ($^{206}\mathrm{Pb}\otimes\pi^{+1}1h_{9/2}$) the $5/2^- \div 13/2^-$-quintuplet located between 670 and $1148\,\mathrm{keV}$ was observed. More details on these nuclei is, e.g., in [26].

- **(B) Axially symmetric oblate nuclei ($\gamma = 60^o$).** Bands based on the Nilsson states with $\Delta I = 1$ sequences are observed. The angular momentum $\vec{j}$ of the

odd particle has a sharp projection Ω on the symmetry axis. Rotation of the core $\vec{R}$ proceeds about the axis, which is perpendicular to the symmetry axis (and $\vec{j}$). This gives a rise to bands with $\Delta I = 1$ spin sequences.

- **(C) Axially symmetric prolate nuclei ($\gamma = 0^o$)**. The decoupled rotational bands with $\Delta I = 2$ sequences are observed. Missing unfavoured signature partners are shifted to higher energies. The structure of these bands is interpreted in terms of strong Coriolis interaction, which aligns the $\vec{j}$ with the rotation axis, i.e., $\vec{j}$ is parallel with $\vec{R}$ [27]. This give a rise to bands with $\Delta I = 1$ spin sequences. If the deformation is large ($\beta \gg 0.2$), the band becomes $\Omega = 1/2$ Nilsson configuration with Coriolis decoupling factor $a = j + 1/2$.

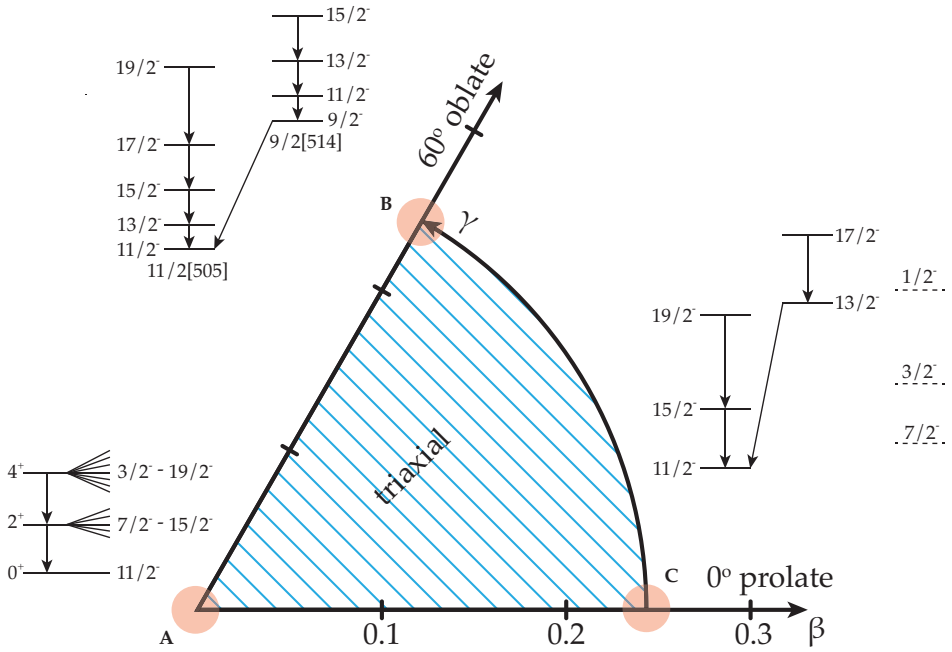

FIGURE 1.6: Triaxial deformation in (β, γ) coordinates system with three extreme situation, when axial symmetry is reached and examples of excited states schemes. (A) is spherical symmetric shape, (B) is axially symmetric oblate shape and (C) is axially symetric prolate shape. Figure is adapted from [28].

Thus, the type of excited states order is determined by the relative direction of $\vec{j}$ and $\vec{R}$: $\Delta I = 1$ bands for perpendicular and $\Delta I = 2$ bands for parallel. While in axially symmetric nuclei $\vec{R}$ can be only perpendicular to the symmetry axis, triaxial nuclei can rotate about all intrinsic axes. Therefore, their spectrum is composed by a superposition of the $\Delta I = 1$ and $\Delta I = 2$ bands.

Hamiltonian describing coupling of the odd particle to the triaxial core can be written as:

$$\widehat{H} = \widehat{H}_{rot} \begin{pmatrix} 1 & \\ & 1 \end{pmatrix} + (\epsilon_j - \lambda_F) \begin{pmatrix} 1 & \\ & -1 \end{pmatrix} + V_{int} \begin{pmatrix} 1 & \\ & -1 \end{pmatrix} + \Delta \begin{pmatrix} & 1 \\ 1 & \end{pmatrix}. \tag{1.10}$$

The triaxial-rotor Hamiltonian $\widehat{H}_{rot}$ can be expressed as:

$$\widehat{H}_{rot} = \sum_{i=1}^{3} \frac{(I_i - j_i)^2}{2\,\mathscr{J}_i}, \tag{1.11}$$

where tree-moments of inertia $\mathscr{J}_i$ are given as:

$$\mathscr{J}_i = \mathscr{J}_0 \frac{4}{3} \sin^2(\gamma - \frac{2}{3}\pi i) \quad i = 1, 2, 3, \tag{1.12}$$

and $\mathscr{J}_0$ can be empirically determined to be:

$$\mathscr{J}_0 = \frac{\hbar^2 \beta^2 A^{7/3}}{408\,\mathrm{MeV}}. \tag{1.13}$$

The interaction between triaxial core and unpaired nucleon can expressed as:

$$V_{int} = \sqrt{\frac{4\pi}{5}} k\beta \Big(\cos\gamma Y_{20} + \frac{\sin\gamma}{\sqrt{2}} \big(Y_{22} + Y_{2-2} \big) \Big), \tag{1.14}$$

where k is the interaction strength and can be determined empirically:

$$k = \frac{206\,\mathrm{MeV}}{A^{1/3}}. \tag{1.15}$$

The Pauli matrices in 1.10 refer to particle and hole substates. Particle and hole states are mixed by the pairing term, where Δ is the pair gap parameter. It can be determined from odd-even mass differences. The model has in total three free parameters: β, γ and λ_F (Fermi energy). The procedure of diagonalisation of the Hamiltonian 1.10 together with further details on the model are given in [29]. The Hamiltonian 1.10 obeys particle-hole symmetry: particle coupled with the core with parameters $(\beta, \gamma, \lambda_F)$ has the same energy spectrum as a hole coupled to a core with parameters $(\beta, 60^o - \gamma, -\lambda_F)$.

Example of the spectrum of an $1h_{11/2}$ particle as a function of the γ parameter is given in Fig. 1.7. It is evident that the spectrum changes gradually from a decoupled at $\gamma = 0^o$ (see case **C** in above text) to a strongly-coupled structure at 60^o (case **B**) when passing through the triaxial plane. Different regions of γ deformation have typical signature. This allows to deduce the γ parameter from measured spectra of

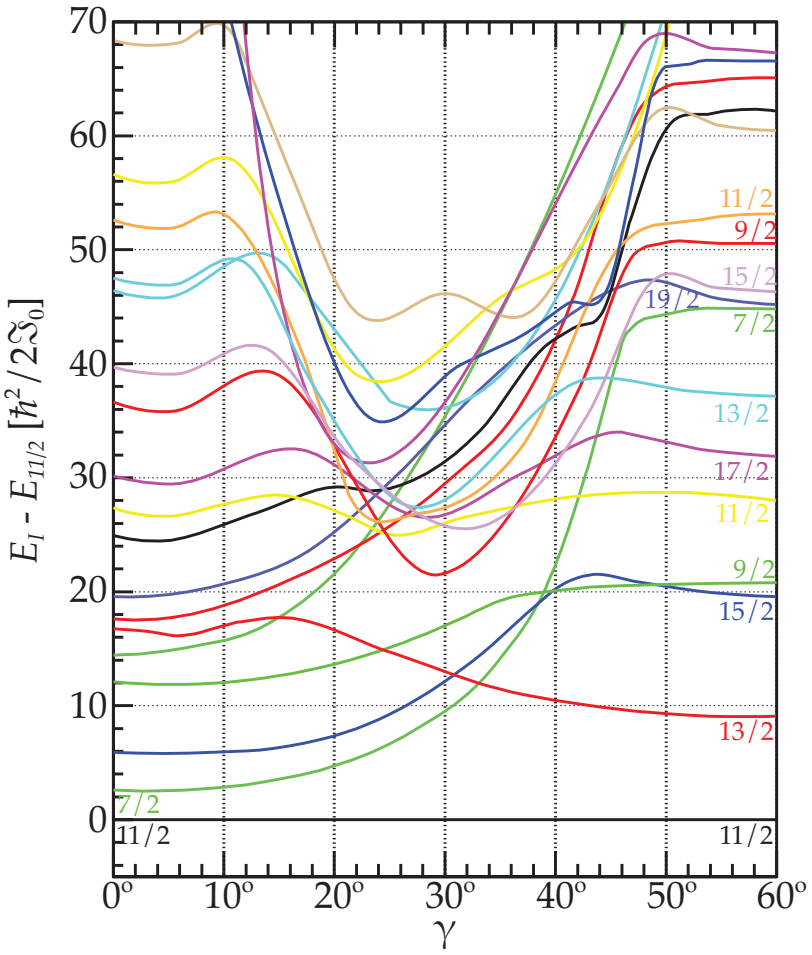

FIGURE 1.7: The odd-A spectrum as a function of the γ parameter for $\beta A^{2/3} = 5$, $\lambda_F = \epsilon_1$, and $j = 11/2$. Only the states with $E_I - E_{11/2} < 45\,\hbar^2/2\,\mathcal{I}_0$. Figure is adapted from [28].

odd-mass isotopes.

Example of this approach is in Fig. 1.8, which gives comparison of experimental data with calculation for states associated with $1h_{9/2}$ proton-particle and $1h_{11/2}$ proton-hole configurations in various Tl, Au, and Ir isotopes. It indicates smooth transition from prolate, through triaxial to oblate shape going from Ir to Au and Tl isotopes.

1.4 Nuclear transitions

1.4.1 Emission of γ rays

Quanta of electromagnetic radiation are called γ rays, when they are emitted by atomic nuclei due to transitions between their discrete excited states. Therefore, the energy of the γ ray E_γ due to the conservation law of energy and momentum, is

$$E_\gamma = E_i - E_f - E_R, \tag{1.16}$$

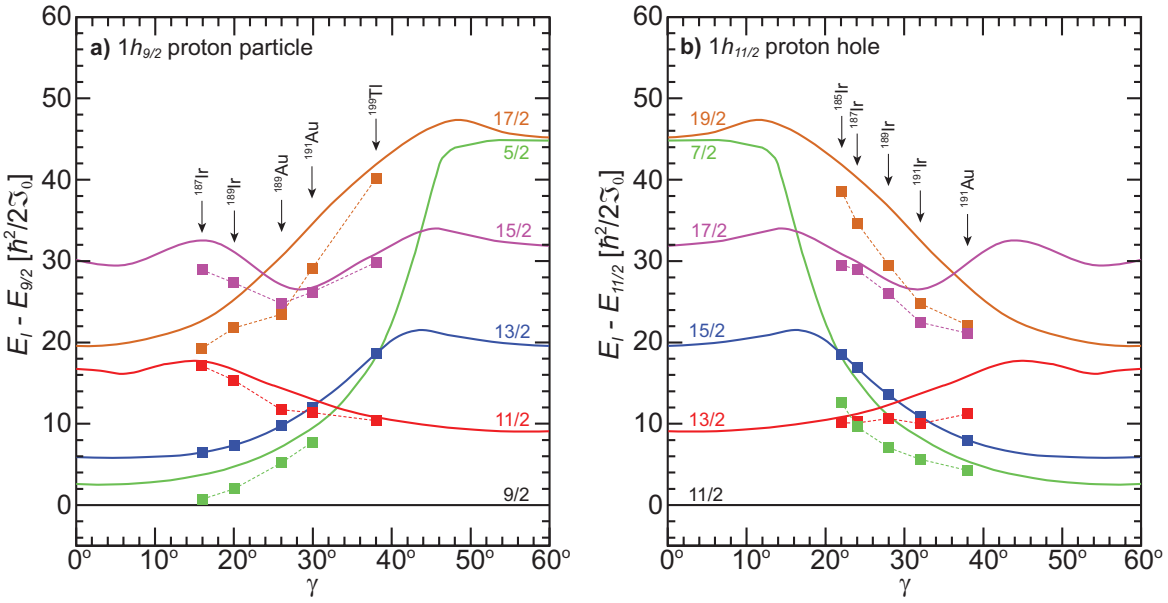

FIGURE 1.8: Comparison of experimental data with calculation for states associated with $1h_{9/2}$ proton-particle and $1h_{11/2}$ proton-hole configurations in various Tl, Au, and Ir isotopes. State $13/2$ in (a) and $15/2$ in (b) were used for normalisation. Data are adapted from [28] and *Evaluated Nuclear Data Files*.

where E_i and E_f are excitation energies of initial and final levels and E_R is the recoil energy of the nucleus, which is often neglected (correction in order of 10^{-5} fraction of E_γ).

For any γ-ray emission, the angular momentum $\boldsymbol{L}$ is

$$\boldsymbol{J}_i = \boldsymbol{J}_f + \boldsymbol{L} \tag{1.17}$$

where i and f refer to initial and final states. The relationship of the scalar magnitudes of J and L is

$$|J_f - L| \leq J_i \leq J_f + L, \tag{1.18}$$

γ-ray must carry at least one unit of angular momentum (spin of photon is 1) and in general γ-ray transition can involve more L values.

It is useful to consider transition rates by properties of electromagnetic multipole radiation, where we can define 2^L as multipole order (L = 1 for dipole, L = 2 for quadrupole, etc.) and use E for electric and M for magnetic radiation. The parity of the radiation field is

$$\pi(EL) = (-1)^L \tag{1.19}$$

for electric and

$$\pi(ML) = (-1)^{L+1} \tag{1.20}$$

for magnetic multipoles. From these 1.18-1.20 selection rules for electromagnetic transitions can be formulated, see Tab. 1.1.

ΔJ	0	1	2	3	4
$\pi_i\pi_f = -1$	$E1$ $(M2)$	$E1$ $(M2)$	$M2$ $E3$	$E3$ $(M4)$	$M4$ $E5$
$\pi_i\pi_f = 1$	$M1$ $E2$	$M1$ $E2$	$E2$ $(M3)$	$M3$ $E4$	$E4$ $(M5)$

TABLE 1.1: Table of allowed multipolarities for some ΔJ. The E0 transition is not included because it is non-radiative transition. Transition in brackets are allowed but less probable.

The probability of the transition is governed by matrix element of the multipole operator

$$m_{fi}(\sigma L) = \int \psi_f^* m(\sigma L)\psi_i dv, \tag{1.21}$$

where σ can be E or M, ψ_f and ψ_i are wave functions of initial and final nuclear state. This probability of transition is associated with decay constant λ, which we cannot evaluate without knowledge of initial and final wave functions. However, we can use Weisskopf estimates [14, 30] for pure single-particle electric transitions

$$\lambda(EL) \cong \frac{8\pi(L+1)}{L[(2L+1)!!]^2}\frac{e^2}{4\pi\epsilon_0\hbar c}\left(\frac{E}{\hbar c}\right)^{2L+1}\left(\frac{3}{L+3}\right)^2 cR^{2L} \tag{1.22}$$

and magnetic transitions

$$\lambda(ML) \cong \frac{8\pi(L+1)}{L[(2L+1)!!]^2}\left(\mu_p - \frac{1}{L+1}\right)^2\left(\frac{\hbar}{m_p c}\right)^2\left(\frac{e^2}{4\pi\epsilon_0\hbar c}\right)\left(\frac{E}{\hbar c}\right)^{2L+1}\left(\frac{3}{L+2}\right)^2 cR^{2L-2}, \tag{1.23}$$

where $R = R_0 A^{\frac{1}{3}}$, $R_0 \cong 2.25 \times 10^{-15}\,\mathrm{m}$, λ is in s^{-1} and $(\mu_p - \frac{1}{L+1})^2 \approx 10$. These calculations provide reasonable relative comparisons of transition rates where we can assume that the nucleus is spherical and there is a pure single-particle excitation. We can see from equations 1.22 and 1.23 that the lower multipolarities are dominant and for given multipole order electric radiation is more probable than magnetic radiation but we need consider parity change also, equation 1.19.

Deformed nuclei have many nucleons in collective motion and half-lives of these states differ from Weisskopf estimation significantly. For example $E2$ transitions are faster that they are comparable with $M1$ transitions and mixtures of $M1 + E2$ are very common in these cases. $E1$ transitions are typically much slower [31]. There is

sometimes difficult to compute theoretical γ-ray intensities and must be measured instead.

Multipolarity	Decay constant of transition	
	Electric	Magnetic
1	$1.0 \times 10^{14} A^{2/3} E^3$	$5.6 \times 10^{13} E^3$
2	$7.3 \times 10^{7} A^{4/3} E^5$	$3.5 \times 10^{7} A^{2/3} E^5$
3	$34 A^2 E^7$	$16 A^{4/3} E^7$
4	$1.1 \times 10^{-5} A^{8/3} E^9$	$4.5 \times 10^{-6} A^2 E^9$

TABLE 1.2: Table of decay constant calculations for some electromagnetic transitions based on the Weisskopf estimation [14, 30], where E is energy in MeV, A is mass number and decay constants are in s^{-1}.

1.4.2 Internal conversion

Higher order process, which competes with gamma ray emission, is that of internal conversion. Excited nuclear states can deexcite without emission of γ-ray. Deexcitation energy is transferred to one of the atomic electrons and this electron is ejected from an atom. Energy of emitted conversion electron is given as

$$E_{ce} = E_i - E_f - B - E_R, \tag{1.24}$$

where i and f stands for initial and final state, B is binding energy of the electron and E_R is recoil energy.

The ratio of the number of emitted conversion electrons, N_e, to the number of emitted γ-rays, N_γ, is internal-conversion coefficient α and is given as

$$\alpha = \frac{N_e}{N_\gamma}. \tag{1.25}$$

The conversion electron can be emitted not only from K shell but also from L, M, etc. and their subshells. Therefore, there are also partial internal-conversion coefficients defined ($\alpha_K, \alpha_{L1}, \alpha_{L2}$, etc.), which depend on the transition energy and the multipolarity. This values can be computed with very high precision by the BrIcc code developed at Australian National University [32], see Tab. 1.3 for some examples. Not only measurements of α but also ratios of shell or subshell internal-conversion coefficients (e.g., α_K/α_L or α_{L12}/α_{L3}, etc.) can be used to determine the multipolarity even without knowledge of the γ-ray intensity.

Internal-conversion coefficients have some features like:

1. They increase as Z^3, where Z is proton number
2. They decrease rapidly with transition energy E, approximately $E^{-2.5}$
3. They increase as the multipole order increases
4. They decrease approximately as $1/n^3$ for higher atomic shells $n > 1$

$E_\gamma[keV]$	$E_{Kce}[keV]$	$E1$	$M1$	$E2$	$M2$	$E3$	$M3$
160.11	79.39	0.126	1.90	0.823	11.10	9.93	56.07
284.4	203.68	0.0305	0.384	0.120	1.519	0.655	5.244
317.88	237.06	0.0235	0.283	0.0864	1.05	0.415	3.41
730.93	650.21	0.00398	0.0315	0.0109	0.0827	0.0282	0.179

TABLE 1.3: Table of total internal-conversion coefficients of ^{183}Au calculated with BrIcc [32] for some of its γ-ray energies and transitions.

1.5 Atomic relaxation processes

During a decay process, the ionisation radiation or electrons from atomic shell are emitted, which leads to ionisation or excitation of some atoms. Excited or ionised atoms have different configuration of the orbital electrons, which may lead to occurrence a vacancy in one of the lower shells. This vacancy is filled rapidly from higher shells and one or more fluorescent (characteristic) X-rays may be emitted. X-rays are electromagnetic radiation like γ-rays but originates in atomic shell and the energy of these X-rays is given by the energy difference between the initial and final states of electrons in the atom. For example if the vacancy is created in the K shell, than the K X-ray is emitted when the vacancy is filled. If the electron, which filled the K-shell vacancy, comes from the L shell than the K_α photon is emitted and its energy is equal to the difference in binding energies between the K and the L shell. When the electron came from the M shell, the K_β photon is emitted, etc. After the K vacancy is filled, the vacancy in higher shell is created and is filled rapidly also and L- and/or M-, ... series of fluorescent (characteristic) X-rays are emitted. These X-rays are called characteristic because they are unique for each element and they are often used in the elemental analysis of unknown samples. Examples of electron binding energies of some elements are shown in Tab. 1.4.

There are two additional modes of atomic deexcitation, the Auger effect and the Coster-Kronig transitions. The Auger effect is alternative process to the X-ray

emission and it is roughly analogue of the internal conversion but in the atom rather than in the nucleus. In this case the excitation energy of the atom is transferred to the electron in the higher shell. This Auger electron is ejected from the atom with energy equal to the difference between the atomic excitation energy and the binding energy of the shell from which was the electron ejected. The Auger process adds hole in higher shell, which can be filled by another Auger process, leading to more holes. The probability that filling a vacancy in the shell results in the emission of an X-ray and not an Auger electron is called fluorescence yield.

There is complication with determining fluorescence yields for the subshells because of Coster-Kronig transitions. These transitions can occur in some elements when an electron in one the subshell can move to a lower subshell, in the same major shell without X-ray emission. This effect occur only within major shell so the total fluorescence yields for the whole shell are not affected.

Element	Electron binding energy in eV						
	K	L1	L2	L3	M1	M2	M3
$_{77}$Ir	76111	13419	12824	11215	3174	2909	2551
$_{78}$Pt	78395	13880	13273	11564	3296	3027	2645
$_{79}$Au	80725	14353	13734	11919	3425	3148	2743
$_{80}$Hg	83102	14839	14209	12284	3562	3279	2847
$_{81}$Tl	85530	15347	14698	12658	3704	3416	2957
$_{82}$Pb	88005	15861	15200	13035	3851	3554	3066

TABLE 1.4: Table of electron binding energies [33] in K,L and M shell of some elements in eV.

1.6 Two-state mixing

It is very rare that the wave function for each state consists of only a single term. In more realistic calculations, nuclear states are complex mixtures of many components which leads to diagonalisation of a large Hamiltonian matrix and certain quantum numbers are then only an approximation. This process is well described in [16]. To solve this complex situation decomposition of the Hamiltonian into part H_0, whose eigenfunctions are the basis states, and part H_1, which mixes the basis states can be the way.

$$H\psi = H_0\psi + H_1\psi = E\psi \tag{1.26}$$

To solve this equation, we can expand ψ to basic states ϕ_i, which are eigenfunctions of H_0 with eigenvalues E_i. In this case, the Hamiltonian equation becomes

$$\begin{bmatrix} E_1 & V_12 & V_13 & \dots & V_1n \\ V_21 & E_2 & V_23 & \dots & \\ . & & & & . \\ . & & & & . \\ . & & & & . \\ V_n1 & & & & E_n \end{bmatrix} \begin{bmatrix} \\ \phi \\ \\ \end{bmatrix} = \begin{bmatrix} \\ E \\ \\ \end{bmatrix} \begin{bmatrix} \\ \phi \\ \\ \end{bmatrix}, \tag{1.27}$$

where ϕ and E are column vectors and V_{in} are partial interactions. The solution is obtained by diagonalising the Hamiltonian, which is simple operation, but in the result, it is almost impossible to keep sight of the basic physics. On the other hand, this full diagonalisation can be simulated by sequences of a few two-state mixing calculations that are trivial.

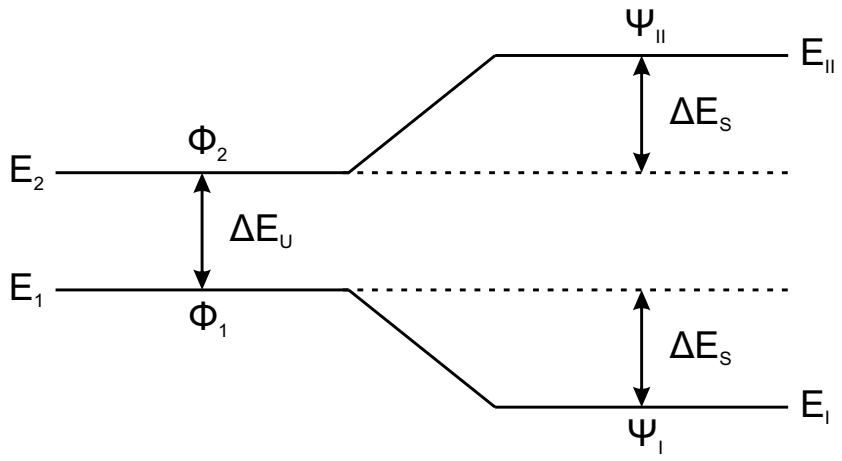

FIGURE 1.9: The illustration of two-state mixing. Initial levels with energies E_1 and E_2 and wave functions ϕ_1 and ϕ_2 are on the left and final shifted levels with wave functions ψ_I and ψ_{II} and final energies E_I and E_{II} are on the right. This illustration is based on [16] (page 19)

The example of situation where two-state mixing takes place is illustrated in Fig. 1.9. Lets take two states with initial energies E_1 and E_2 and wave functions ϕ_1 and ϕ_2. When non-diagonal interaction V is present, then the Hamiltonian matrix is

$$\begin{bmatrix} E_1 & V \\ V & E_2 \end{bmatrix} \tag{1.28}$$

By diagonalising matrix above, we can obtain final wave functions ψ_I and ψ_{II} and final energies E_I and E_{II}. To simplify results, a single universal mixing expression

can be defined as ratio, R,

$$R = \frac{\Delta E_u}{V}, \tag{1.29}$$

of the unperturbed energy difference to the strength of the matrix element. Then the resulting perturbed energies are

$$\begin{aligned} E_{I,II} &= \frac{1}{2}(E_1 + E_2) \pm \frac{1}{2}\sqrt{(E_2 - E_1)^2 + 4V^2} \\ &= \frac{1}{2}(E_1 + E_2) \pm \frac{\Delta E_u}{2}\sqrt{1 + \frac{4V^2}{\Delta E_u^2}} \\ &= \frac{1}{2}(E_1 + E_2) \pm \frac{\Delta E_u}{2}\sqrt{1 + \frac{4}{R^2}}. \end{aligned} \tag{1.30}$$

The energy shift of the perturbed energy from the unperturbed energy is then

$$E_S = \frac{\Delta E_u}{2}\Big[\sqrt{1 + \frac{4}{R^2}} - 1\Big]. \tag{1.31}$$

The mixed wave functions are

$$\begin{aligned} \psi_I &= \alpha\phi_1 + \beta\phi_2, \\ \psi_{II} &= -\beta\phi_1 + \alpha\phi_2, \end{aligned} \tag{1.32}$$

where α and β are amplitudes. The normalisation of amplitudes can be expressed in form of

$$\alpha^2 + \beta^2 = 1, \tag{1.33}$$

and smaller amplitude β is given by

$$\beta = \frac{1}{[1 + (\frac{R}{2} + \sqrt{1 + \frac{R^2}{4}})^2]^{\frac{1}{2}}}. \tag{1.34}$$

The amplitudes of the final wave functions are functions only of R, the ratio of the initial unperturbed energy splitting to the mixing matrix element and equations 1.30 and 1.31 are universal expressions independent of the nature of interaction. The same ratio R always give the same final wave functions, energies and energy shifts compared with initial energy splitting.

1.7 Shape coexistence in atomic nuclei

Beginning of the shape coexistence concept can be tracked back to 1956, when it was used for description of first excited state of doubly-magic nucleus ^{16}O [34]. Since then, the shape coexistence has been observed in many other regions of the

Table of Isotopes, see Fig. 1.10. It was believed that the shape coexistence is a special feature of nuclei located in those regions. However, in most recent shape coexistence review [2] a concept was proposed: shape coexistence is a standard property of any atomic nucleus and therefore without understanding of details of the phenomenon, critical questions of the nuclear structure cannot be addressed. Before more general picture can be settled, more high-quality data is needed.

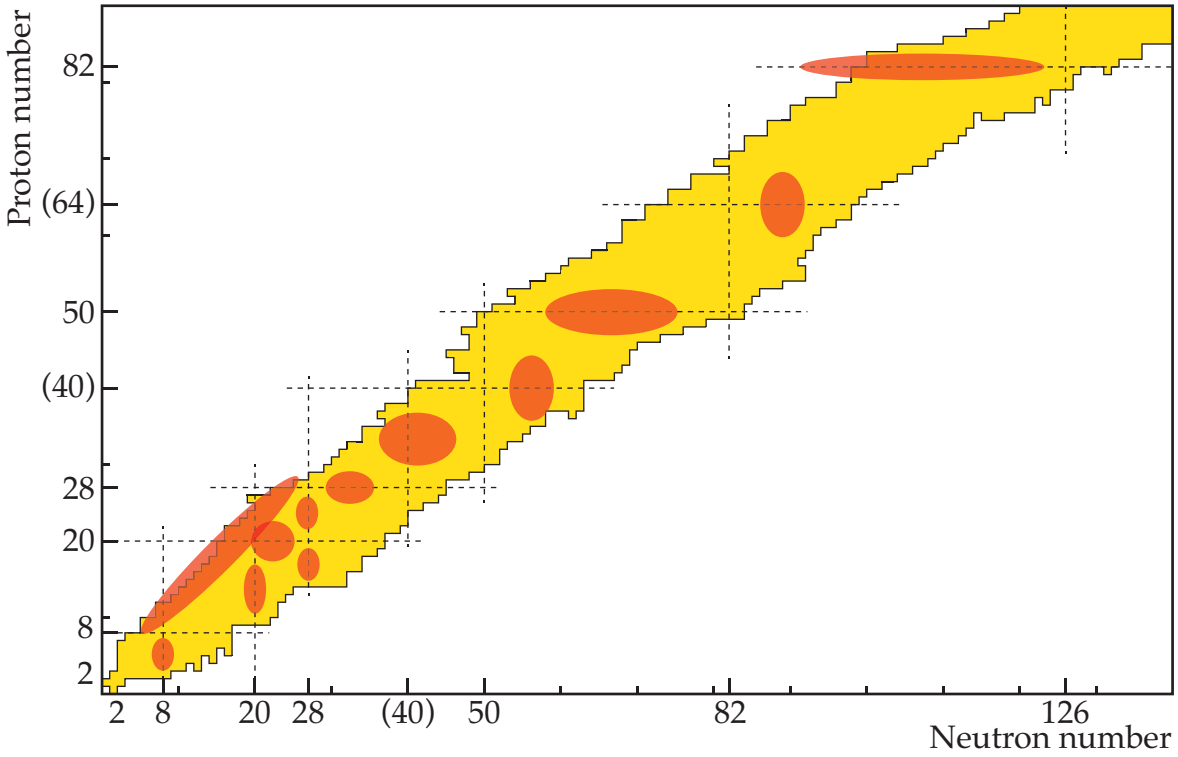

FIGURE 1.10: Regions of the Table of Isotopes, where the shape coexistence has been established. Figure was adapted from [2].

1.7.1 Concept of intruder configurations: ^{16}O

The ground state of doubly-magic isotope ^{16}O can be regarded as $0p$-$0h$ state, i.e., all orbitals below N = 8 and Z = 8 closed shells are occupied, see Fig. 1.11. Naturally, the first-excited state is expected to have negative parity, due to excitation of single particle across the closed shell from $1p_{1/2}$ into $1d_{5/2}$ orbital, i.e. to form the $1p$-$1h$ state. Instead, the 0^+ state was identified at $6049.4\,\mathrm{keV}$ to be the first excited state.

This suggests 4 particle-4 hole ($4p$-$4h$) nature of the state, i.e., four particles (two protons and two neutrons) occupy orbital above the N = 8 and Z = 8 closed shells, see Fig. 1.11. This multi-nucleon excitation across closed shells leaves two orbitals below shells empty. This enhances pairing proton-neutron correlations that massively reduce the excitation energy of 0^+ state. Other 0^+ states are observed

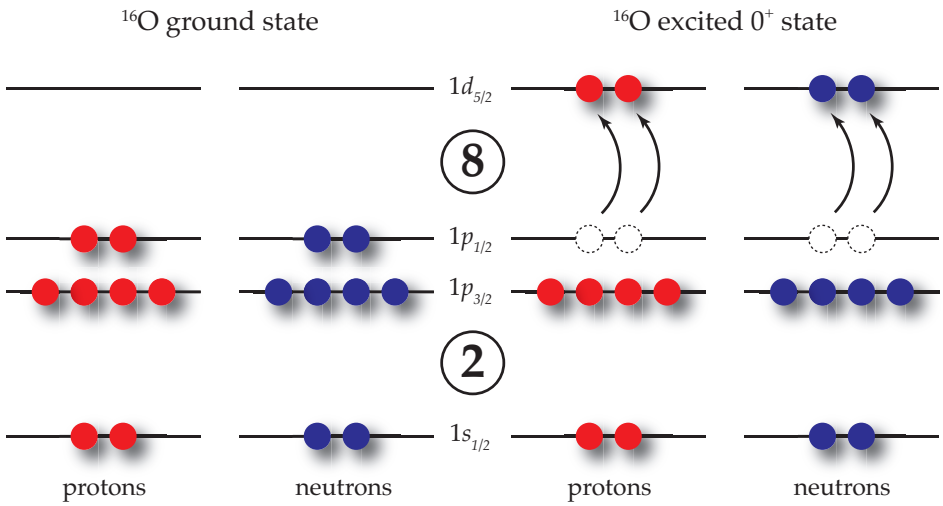

FIGURE 1.11: Nucleonic configuration of the ground state and first excited 0^+ state of doubly-magic nucleus ^{16}O.

11.260 and 12.049 MeV, which are excellent candidates for the $2p$-$2h$ configuration, i.e., excitation of pair of protons or neutrons across the shell. These states do not gain any correlation energy, since all the orbitals for protons or neutrons are occupied up to closed shell. Therefore, the $4p$-$4h$ would be naturally observed to have excitation energy around 24 MeV. This is corroborated also by excitation energy of excited 3^- state, which is at 6129.89 keV. This state is 1p-1h configuration, also suggesting approximately 24 MeV for $4p$-$4h$ states. However, the large reduced $E3$ transition strength $B(E3) = 13.5(7)$ W.u. suggests the admixture of collective configurations in the 3^- state.

States like 0^+ are often called *intruders* because they intrude across closed shells and are observed with very low excitation energies, that cannot be explained by the spherical shell model. The correlation energies that dictate their excitation energies, and result from changing of shell occupancies are indeed massive [35]: e.g., 18 MeV for 0^+ state in the ^{16}O nucleus.

Rotational band based on the 0^+ state was observed in ^{16}O, see Fig. 1.12. The 2^+, 4^+, and 6^+ rotational states are also strongly populated by the ^{12}C(^{7}Li,t)^{16}O α-particle transfer reaction, which indicates the similar configuration. Fig. 1.12 gives the reduced transition probabilities of $E2$ transitions, $B(E2)$, given in Weisskopf units. Enhanced collectivity reflected by large $B(E2)$ values is indication of the deformation of the excited 0^+ state.

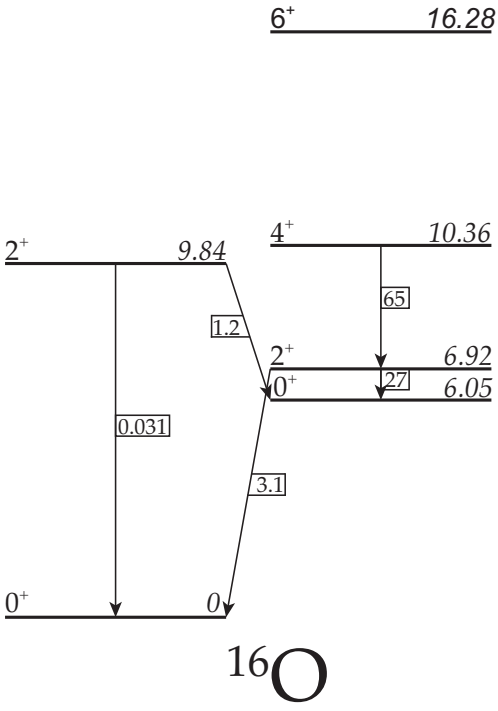

FIGURE 1.12: Part of excited states of ^{16}O isotope. Electric quadrupole transitions, important for understanding of the nature of the states are given together with their $B(E2)$ values in Weisskopf units. Data are adapted from *Evaluated Nuclear Data Files*.

1.7.2 Shape coexistence of neutron-deficient Hg isotopes

Neutron-deficient Hg isotopes exhibit very vivid manifestation of shape coexistence. First evidence came totally unexpectedly from optical hyperfine structure studies of the Hg isotopes, which revealed an enormous isotope shift between ^{185,187}Hg nuclei [36]. Recently, these measurements have been extended to $_{177}$Hg [37], see summaries given in Fig. 1.13.

Observed extreme staggering was soon explained by in-beam γ-ray spectroscopy [39, 40] and decay spectroscopy of even-Hg isotopes [41, 42], that revealed rotational bands build upon excited 0^+ states. The systematics of excited states of even-Hg isotopes is given in Fig. 1.14.

Since relevant isotopes lie far from the beta stability, extreme sensitive experimental techniques had to be developed to characterize ground and excited states. This involves in-beam spectroscopy with tagging technique [43, 44], measurements of lifetimes of excited states [45], decay spectroscopy [38, 46], in-source laser spectroscopy [37], and Coulomb excitation of radioactive-ion beams [47].

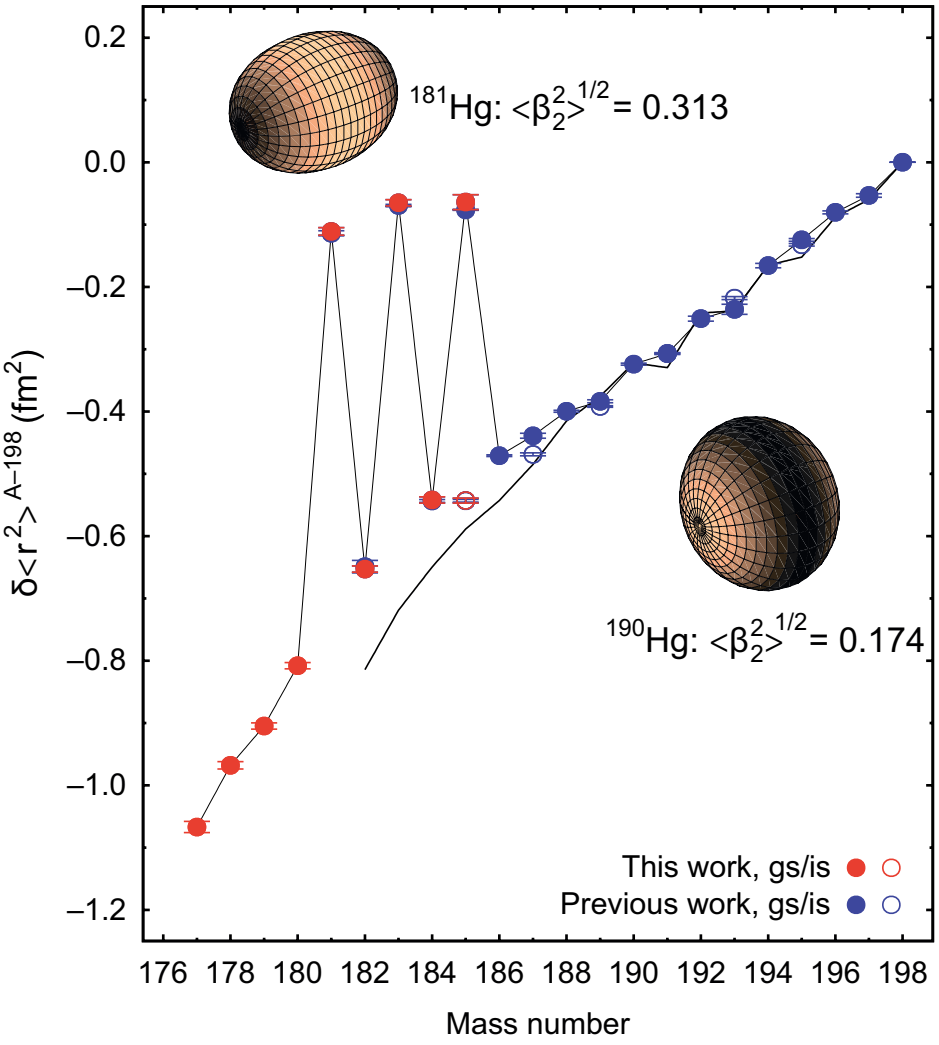

FIGURE 1.13: Results of the in-source resonance ionization spectroscopy study of radiogenic mercury isotopes from [37]. Measured isotope shifts are used to calculate the changes in mean-square charge radii $\delta\langle r^2\rangle$ with respect to A = 198 along the isotopic chain. The results appear as filled red circles (ground states) or open red circles (isomeric states). $^{177\text{-}180}$Hg are new measurements, whereas $^{181\text{-}185}$Hg were re-measured and the data points overlap with those of the literature values (blue circles). The error bars correspond to the standard deviation of measurements. The additional continuous black line illustrates the previously measured quasi-spherical trend of the lead nuclei. Figure is adapted from [37].

1.7.3 Triple shape coexistence in lead isotopes

The shape of ground states of neutron-deficient even-even Pb isotopes was probed by measurement of optical isotope shift, which provides mean square charge radii $\delta\langle r^2\rangle$ [48]. The experiment was performed at ISOLDE facility and employed in-source laser spectroscopy. Only tiny deviations from spherical shape, that are explained by small admixtures of intruder configurations, were observed.

Study of α decay of ^{190}Po isotope, performed at velocity separator SHIP at GSI

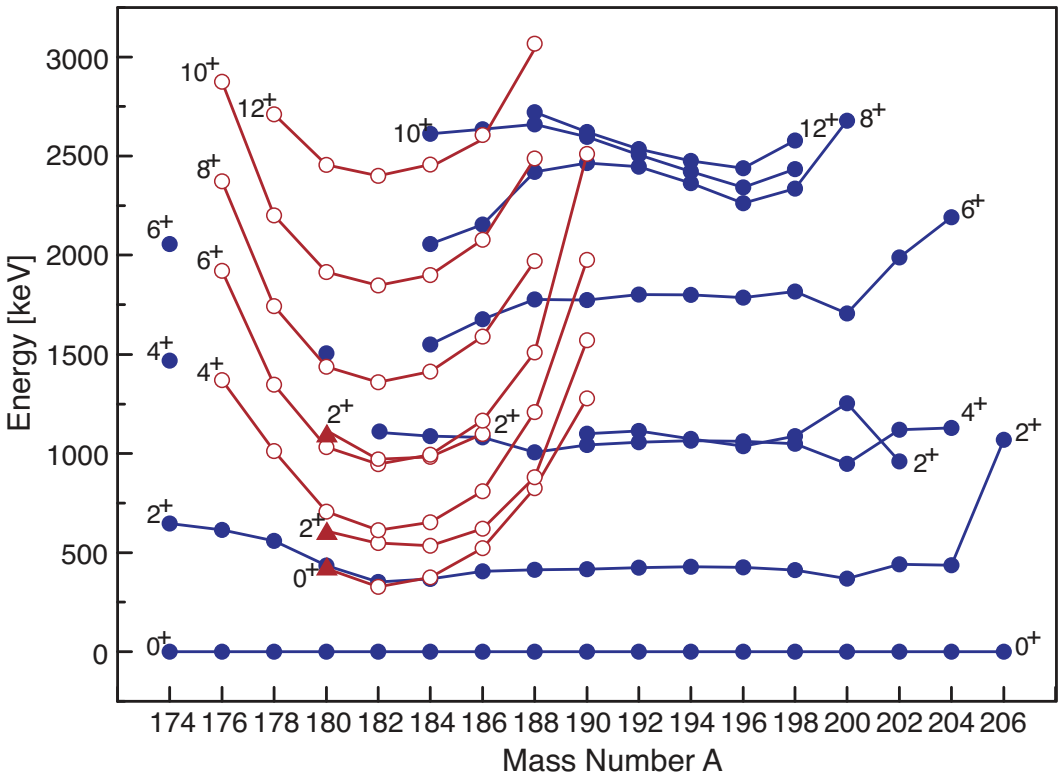

FIGURE 1.14: The systematics of excited states of even-Hg isotopes. Figure is adapted [38].

Darmstadt, revealed two excited 0^+ states in the ^{186}Pb daughter [49]. The excitation energies of these states are 532, and $650\,\mathrm{keV}$, respectively. They are interpreted within the framework of calculations of energies of different configurations as a function of their deformation, using the Woods-Saxon potential. These calculations, see Fig. 1.15, suggest an oblate and prolate minima at about $1\,\mathrm{MeV}$ excitation. Therefore, the excited 0^+ states in ^{186}Pb are interpreted as differently shaped configuration. Since the ground state corresponds to the spherical spherical minimum, see Fig. 1.15, ^{186}Pb isotope is an example of low-energy, near-degenerate triple shape coexistence.

There is no experimental evidence for different shape of three 0^+ states in ^{186}Pb. Two rotational bands were observed [50], that are very likely based on excited 0^+ states. This would suggest their deformation. However, 2^+ states of both rotational bands de-excites to the ground state, and do not feed the band head. This is caused by massive energy factor of E_γ^5, which favourites decay into the ground state. Despite several attempts, transitions feeding excited 0^+ states were not identified. Therefore, 0^+ states in ^{186}Pb are ambiguous, although the work [49] is widely used as a reference for triple shape coexistence (often also as a reference for the shape coexistence in vicinity of $Z = 82$ in general).

In neighbouring even-even lead isotope, ^{188}Pb, three isomeric states were identified [51, 52]. The $K^\pi = 8^-$, $1.2\,\mu\mathrm{s}$ isomer with $9/2^-[624]\otimes 7/2^-[514]$ two-quasineutron

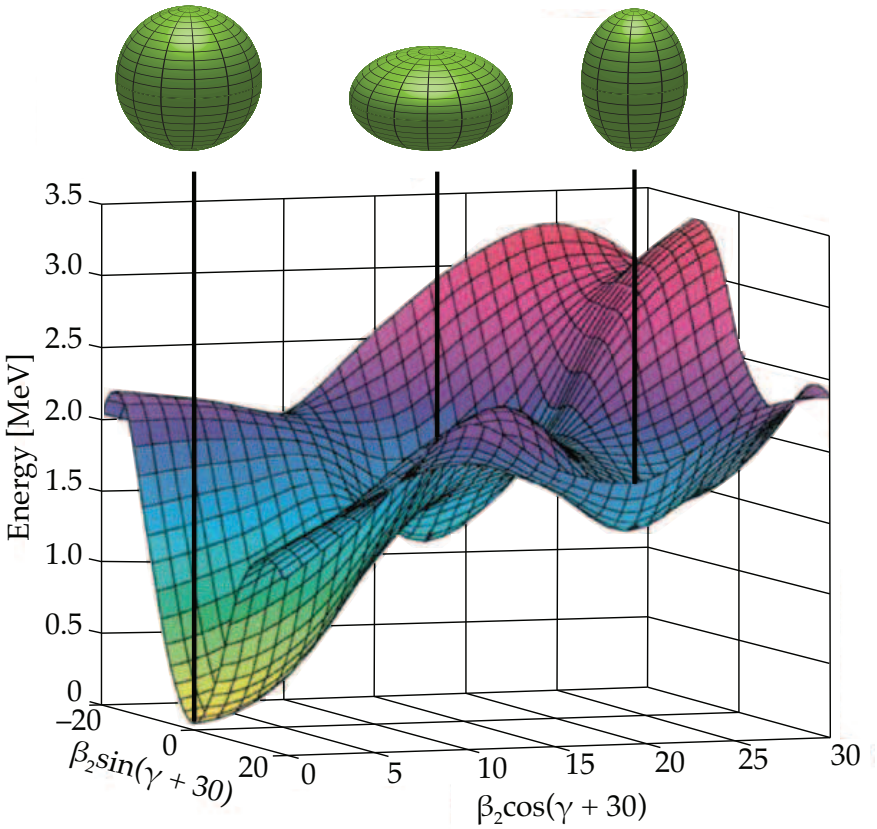

FIGURE 1.15: Visualisation of calculated potential energy as a function of the ^{186}Pb nucleus deformation. Three local minima are indicated, which corresponds to prolate and oblate shapes in the region close to 1 MeV excitation and spherical ground state. Figure is adapted from [49].

configuration is K isomer [53] with prolate deformation. Another K isomer, the $K^\pi = 11^-$, 38 ns state has $9/2^-[505]\otimes 13/2^+[606]$ two-quasiproton configuration with oblate deformation. The nucleonic-configurations assignments are based on decay properties, band structures on the top of these isomers, and by g factor measurements [54]. The 12^+, 38 ns state is a spherical seniority isomer.

Therefore, the ^{188}Pb isotope provides evidence for a triple-shape coexistence. Note, that there are also ambiguous 0^+ states at low excitation energy in ^{188}Pb, that are (probably) analogues of those observed in ^{186}Pb. However their deformed character has not been proven yet.

1.8 Electric Monopole Transitions

Electric monopole transitions ($E0$) are important tool for studies of nuclear structure, specifically for understanding of the shape coexistence [55]. These transitions are allowed to connect only the states with the same spin-parity and cannot proceed

via γ-ray emission (spin of the photon is $1\hbar$). Therefore higher-order processes like interal conversion, internal pair creation, or two photon emission take a place.

The transition rate of $E0$ transition is given as:

$$\frac{1}{\tau(E0)} = \rho^2_{fi}(\Omega_K + \Omega_{L1} + \Omega_{L2} + ... + \Omega_{IP}), \tag{1.35}$$

where Ω values are electronic factors (not dependent on the nuclear structure) for various processes described above, e is elemental charge, and R is the radius of the nucleus in fm units. Electronic factors for internal conversion on K, L_1, and L_2 atomic subshells can be calculated using the BrIcc code [32]. In general, the K/L_1 subshell ratio is $\sim$10 and K/L_2 subshell ratio is $\sim$1000 for $E0$ transitions.

The ρ^2_{fi} value in the equation 1.35 can be expressed using the general electric monopole operator $\hat{T}$ as

$$\rho^2_{fi} = |\frac{\langle f|\hat{T}(E0)|i\rangle}{eR^2}|^2. \tag{1.36}$$

In the simple two-state mixing model, the eigenstates of initial and final state $|i\rangle$ and $|f\rangle$ can be expressed as:

$$\begin{aligned} |i\rangle &= \alpha\,|0\rangle + \beta\,|1\rangle\,, \\ |f\rangle &= \alpha\,|1\rangle - \beta\,|0\rangle\,, \\ \alpha^2 &+ \beta^2 = 1, \end{aligned} \tag{1.37}$$

where $|0\rangle$, $|1\rangle$ are eigenstates of the system, unperturbed by the mixing, and α and β are mixing ampltudes.

Using expression 1.36 for the ρ_{fi} it can be derived:

$$\rho^2_{fi}(E0) = \frac{1}{eR^2}\left[ab\Big(\,\langle 0|\hat{T}(E0)|0\rangle - \langle 1|\hat{T}(E0)|1\rangle\,\Big) + (a^2 - b^2)\,\langle 1|\hat{T}(E0)|0\rangle\,\right]. \tag{1.38}$$

The wave functions are localised mainly at different points in deformation space, therefore:

$$\langle 1|\hat{T}(E0)|0\rangle \simeq 0. \tag{1.39}$$

In the weak mixing approximation, i.e., $ab \simeq 0$, only very retarded $E0$ transition can be observed, since $\rho^2_{fi} \simeq 0$. The most notable example of this is $E0$ deexication of the fission isomeric state in ^{238}U, see Fig. 1.16, which is the most retarded $E0$ transition observed anywhere.

In the strong-mixing limit, there is still $\langle 1|\hat{T}(E0)|0\rangle \simeq 0$, but

$$a \simeq b \simeq \frac{1}{\sqrt{2}}. \tag{1.40}$$

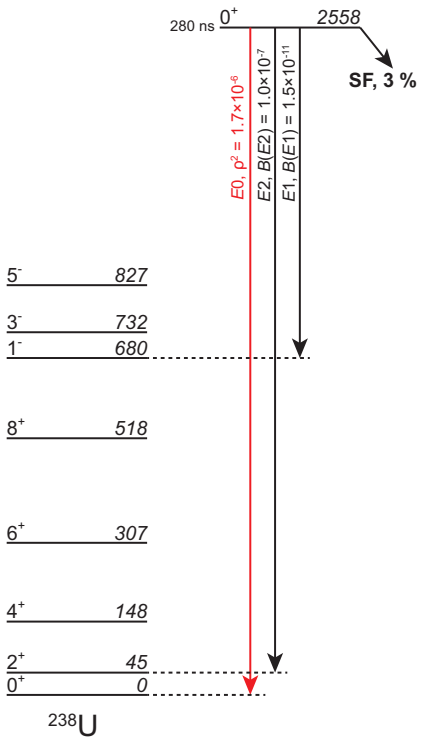

FIGURE 1.16: Electric monopole deexcitation of the fission isomer in ^{238}U. It is slowest known E0 transition. Figure is based on Fig. 3 from [55].

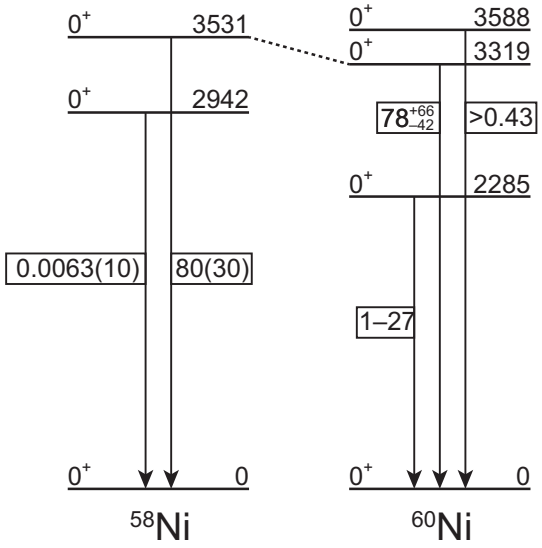

FIGURE 1.17: Electric monopole transition strengths $\rho^2_{fi}(E0) \times 10^3$ in ^{58,60}Ni isotopes. The values are taken from [56].

Therefore, the equation 1.38 can be approximated as

$$\rho^2_{fi}(E0) = \frac{1}{2eR^2}\Big[\,\langle 0|\hat{T}(E0)|0\rangle - \langle 1|\hat{T}(E0)|1\rangle\,\Big]. \tag{1.41}$$

This leads to expression

$$\rho^2_{fi}(E0) = \Big(\frac{3}{64\pi}\Big)^2 Z^2 \Big(\beta_1^2 - \beta_2^2\Big)^2, \tag{1.42}$$

where $\beta_{1,2}$ are quadrupole deformation parameters of initial and final states. Therefore, the strong electric monopole transition is indication of mixing of states and difference in quadrupole deformation parameter (which can be attributed to the mean squared charge radii of nuclei). Thus, observation of electric monopole transition is model-independent signature of shape coexistence.

System that demonstrates above principles are stable Ni isotopes Fig. 1.17 gives lowest 0^+ excited states in ^{58,60,62}Ni isotopes together with electric monopole transitions. Transitions with large $\rho^2_{fi}(E0) \times 10^3 \simeq 80$ are of particular interest. The parent states in both ^{58,60}Ni isotopes, i.e., 3531 and $3319\,\mathrm{keV}$, were observed to be strongly populated in (^{3}He,n) two-proton transfer reactions [57]. This indicates that these are deformed proton-intruder states with $2p$-$2h$ nature. Also, there is a strong mixing between these intruder states and ground states.

Initial 0^+ states with low $\rho^2_{fi}(E0)$ values are interpreted as 0^+ pair excitations within the neutron valence shell. Such states are expected to have the same charge radius as the ground states (and thus the quadrupole deformation parameter). Interestingly, the ^{58}Ni is the isotope with largest known difference of $\rho^2_{fi}(E0)$ between two transitions.

Chapter 2

Nuclear Structure of Au isotopes

In past four decades, the nuclear structure of odd-mass Au isotopes was a subject of intensive experimental investigation. This included α- and β-decay studies, in-beam γ-ray and conversion electrons studies, atomic beam measurements, collinear-laser spectroscopy, resonance ionization mass spectroscopy, isomeric transitions studies, single-proton and deep inelastic transfer reaction studies. Following Chapter summarises the status of understanding of the nuclear structure of odd-mass isotopes.

2.1 Motivation for the study of ^{181,183}Hg $\rightarrow$ ^{181,183}Au decay

Experiments at the UNISOR [58][1] and the ISOCELE[2] facilities [59, 60] revealed interesting, nearly constant excitation energies for many excited states in odd-mass Au isotopes. This constancy appeared to be disrupted in most neutron-deficient isotopes accessible at time [59, 60]. This is due to appearance of intruder configurations at low excitation energies. Complex situation of four coexisting structures was revealed in ^{185,187}Au [61]. Very detailed study of ^{187}Hg $\rightarrow$ ^{187}Au decay [62, 63], which included measurement of 367 internal-conversion coefficients and observation of nine E0 transitions, was performed. A study of ^{185}Hg $\rightarrow$ ^{185}Au was also performed [64], but due to limitations of radioactive-ion beam intensity and low gamma-ray detection efficiency caused that understanding of the detailed structure was lacking. Decay studies of ^{181,183}Hg [8] were performed, but the constructed level schemes are clearly incomplete (^{181}Hg only table with few γ rays was given without level scheme).

Many in-beam γ-ray experiments were performed, but they provided mostly information on yrast configurations. A critical step in understanding the systematic behaviour of intruder configurations was the discovery of the isomer in ^{179}Au [65], see Section 2.6. These data revealed the parabolic trend of excitation energy of intruder

[1] at Oak Ridge National Laboratory, Oak Ridge, Tennessee, U.S.A.
[2] at Institut de Physique Nucléaire, Orsay, France

states in odd-mass Au isotopes with minimum in a vicinity of the N=104 mid-shell point.

Therefore, to elucidate the nuclear structure of odd-mass Au isotopes dedicated experimental programme was initiated by the Department of Nuclear Physics, Institute of Physics, Slovak Academy of Sciences. This included new, high statistics in-beam studies of ^{177,179,187}Au performed at the University of Jyväskylä and iThemba LABS. Complementary to this decays of ^{181,183}Hg isotopes were studied at ISOLDE.

2.2 Measurements of ground state properties of Au isotopes

First attempts to perform direct measurements of spin of the ground state of neutron-deficient Au isotopes can be tracked back to beginning of 60's. The atomic-beam magnetic resonance (ABMR) technique was used to measure spins of $^{191\text{-}196}$Au isotopes [66]. The activities were produced by bombardment of the massive iridium target with the $48-\mathrm{MeV}$ α beam delivered by the 60-inch cyclotron at the Berkley campus of the University of California. The target was then placed into the oven of the ABMR apparatus. To measure activities that passed the device, the small crystal scintillation counters were used: they detected characteristic Pt X rays from electron capture and internal conversion processes. Spin of $3/2$ was determined for ^{191,193,195}Au isotopes.

In 70's, the ABMR device, which was active at Uppsala [67], was reconstructed at the ISOLDE facility at CERN with the goal to perform measurements using atomic-beam magnetic resonance technique with radioactive nuclei. The first experiment performed at ISOLDE aimed on the measurement of spin of $^{186,187,188,189,189\mathrm{m}}$Au isotopes [68]. Since, there was no source of radioactive isotopes of Au available at ISOLDE that time, samples of $^{186\text{-}189}$Au were obtained as decay products of corresponding Hg precursors (produced by bombarding of the molten lead target with $600-\mathrm{MeV}$ proton beam delivered by the CERN synchro-cyclotron). The experiment unambiguously assigned the spin of the ground state of ^{187,189}Au to be $1/2$, which differs from the heavier isotopes. The spin of $11/2$ was determined for $^{189\mathrm{m}}$Au.

The research program at ISOLDE continued with the measurement of the spin of $5/2$ for the ^{185}Au [69] using the ABMR technique. This is interpreted as $5/2^-$ state of $1\mathrm{h}_{9/2}$ proton-intruder configuration.

Recently, in-source laser spectroscopy of ^{177,179}Au isotopes [70] has been performed at ISOLDE. Experiment involved laser-ion source RILIS, which was used for laser-wavelengths across the hyperfine structure of atomic resonance ionization process [71], see Fig. 2.1. The yield of ^{177,179}Au isotopes was measured as a function of the

laser frequency, employing the MR-ToF device [70] and Leuven-Windmill detection system [48, 72].

Spin 1/2 has been unambiguously established for ground states of ^{177,179}Au isotopes. Magnetic moments $\mu = 1.15(5)$ for ^{177}Au and $\mu = 1.01(5)$ for ^{179}Au have been measured. These values suggest a mixed $3s_{1/2} \oplus 2d_{3/2}$ configuration for ground states of these isotopes.

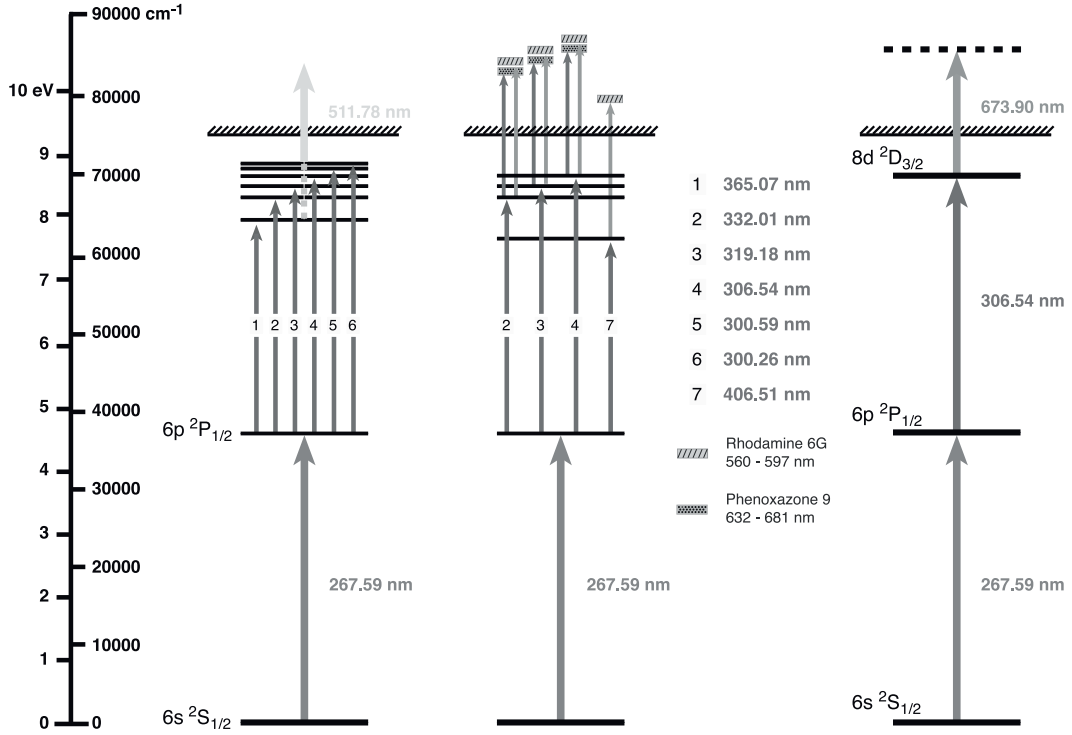

FIGURE 2.1: Optimal ionisation scheme for Au. Figure is adapted from [71].

2.3 β^+/EC decay studies of mass separated samples of odd-Hg isotopes

First studies that employed radioactive-ion beams to study decays of odd-Hg isotopes were performed at the University Isotope Separator (UNISOR) and ISOCELE facilities.

2.3.1 Decay studies at the UNISOR facility

The UNISOR mass separator [73] was operated in an on-line mode using a modified Nielsen oscillating-electron ion source [74]. Radioactive species were produced by fusion evaporation reactions induced by beam delivered by the Oak Ridge isochronous cyclotron. Over the years of operation, many different reaction

products were successfully separated, including neutron-deficient isotopes of Tl, Hg, and Au.

To perform the decay studies of mass-separated samples, compact tape transportation system [75] based on commercial 8-track cartridges was developed. The sample was first collected by a deposition of the low-energy radioactive-ion beam onto the tape. After collection, radioactive sample was transported to the measurement station, where γ rays were detected with lithium-drifted germanium detectors. Conversion electrons were detected with the windowless lithium-drifted silicon detector placed inside of the vacuum chamber and operated at liquid nitrogen temperature. The data acquisition system allowed to acquire the data in a coincidence mode, i.e., γ-γ and γ-electron matrices were produced and analysed. After the measurement period, fresh sample of the radioisotope was deposited and whole process was repeated periodically.

First experiments studied β^+/EC decays of ^{189,191,193,195}Hg isotopes, populating excited states in ^{189,191,193,195}Au daughters [76]. Studies revealed excited states associated with $1h_{11/2}$, $2d_{3/2}$, and $3s_{1/2}$ proton-hole configurations. Proton holes couple to even-even Hg cores, which structures are reflected also in odd-Au isotopes. In addition to them, states associated with $1h_{9/2}$, $2f_{7/2}$, and $1i_{13/2}$ proton-particle configurations were also observed. These structures intrude across the Z = 82 closed shell, since their energies are dictated not only with the single particle energies but also by massive correlations resulting from changing of the shell occupancies. Proton particles couple to even-even Pt cores, resulting in distinct groups of states.

Studies of ^{187}Au [77, 78] and ^{185}Au [61, 64] followed and clearly demonstrated the level of complexity of the nuclear structure that had to be elucidated. The pioneering experiment, which revealed excited states of the ^{187}Au isotope, is one of the most notable decay study of odd-mass isotope ever performed. The ^{187}Hg^m ions were produced via the ^{176}Hf(^{16}O,5n)^{187}Au^m reaction. The energy of ^{16}O^{6+} ions was $125\,\mathrm{MeV}$. The ^{187}Hg^g ions were produced by the decay of ^{187}Tl^{g,m}, which was produced via the ^{176}Hf(^{19}F, 8n)^{187}Tl^{g,m} reaction. The energy of ^{19}F^{8+} ions was $170\,\mathrm{MeV}$. This technique allowed the states populated by the decay of the high- ($13/2^+$) and low-spin ($1/2^+$) state to be analysed separately. This helped to deduce the spin-parity for excited states of ^{187}Au. Conversion electrons and γ rays were detected in both coincidence and singles mode.

Level of complexity is reflected in the density of excited states and thus in the density of transitions observed in acquired spectra. Fig. 2.2 gives part of the spectrum of γ-ray and conversion electron singles observed in the ^{187}Hg$\rightarrow$^{187}Au decay study. Note that peaks indicated in the spectrum were identified by the γ-γ coincidence analysis. Since many unresolved multiplets were present in the spectrum of ^{187}Hg, see example in Fig. 2.3 sophisticated analysis techniques as, e.g., running coincidence

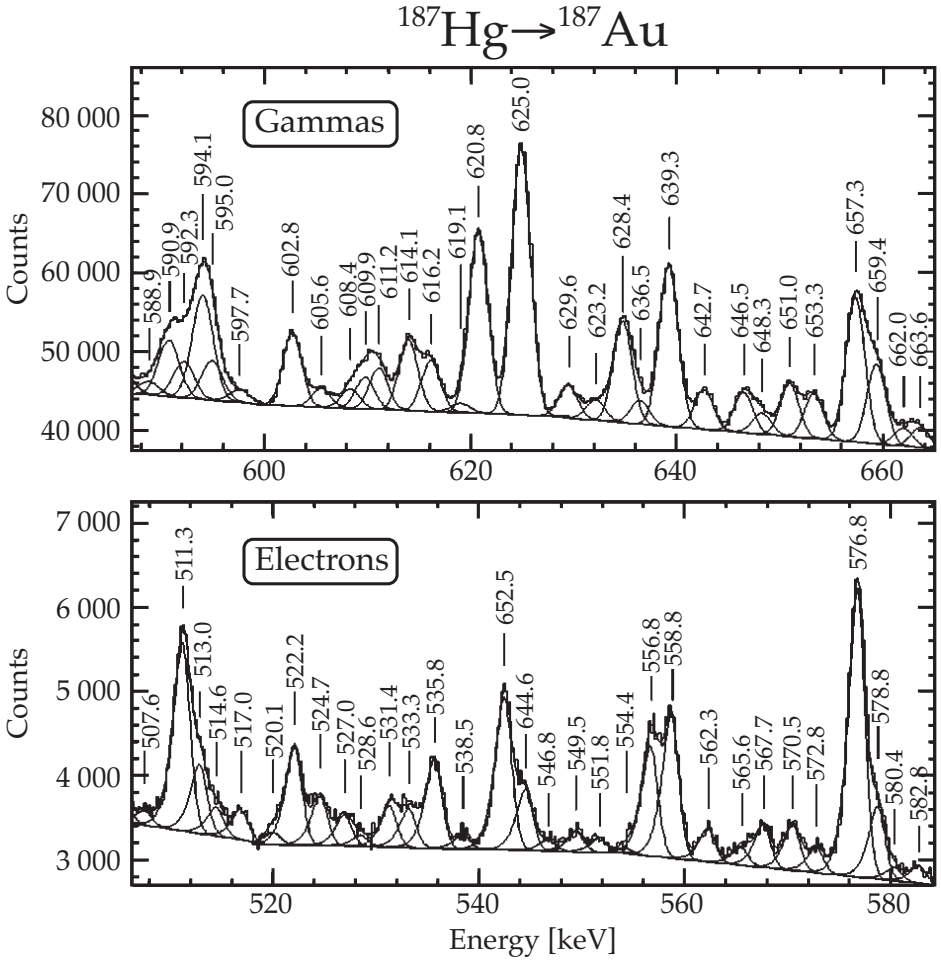

FIGURE 2.2: Spectrum of γ-ray and conversion electron singles, observed in the ^{187}Hg$\rightarrow^{187}$Au decay study. Spectrum is adapted from [77].

gates had to be used. In total, approximately 1700 coincidence spectra were produced and analysed. The key in establishment of internal conversion coefficients was ability to produce background-subtracted γ-gated electron spectra, since presence of unresolved multiplets in the spectra didn't allow to determine them directly from singles spectra. Above efforts were very time consuming allowed to assign more than 99 % of observed γ ray intensity. In total, 367 internal conversion coefficients were determined.

Fig. 2.4 gives the systematics of negative-parity excited states due to rotationally-aligned coupling of the unpaired $1h_{11/2}$ proton to the corresponding even-even Hg core. Evident are spin multiplets due to coupling of non-zero spin core states with odd particle. E.g., the $3/2^-$ member is due coupling of $1h_{11/2}$ proton with 4^+ core excitation. This state can be fed by the β^+/EC decay of $1/2^+$ state in odd-Hg isotope, subsequently feeding the $11/2^-$ via $7/2^-$ state. This effect causes unique population

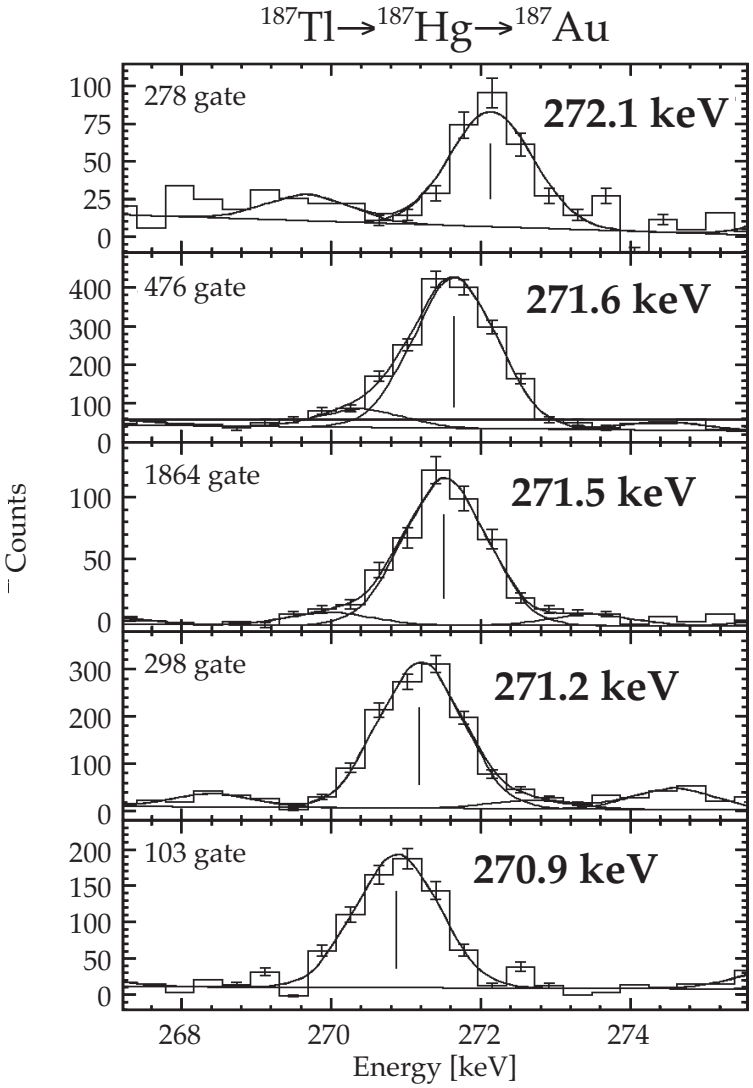

FIGURE 2.3: Five different background-subtracted coincidence spectra, showing five different components of the 271 keV quintuplet. Spectrum is adapted from [77].

of high-spin states by low-spin decays.

Fig. 2.5 gives a systematics of positive parity states in $^{189\text{-}195}$Au isotopes. Markedly stable excitation energies of states, with both positive and negative parity, see Fig. 2.4 and 2.5, suggest that very little is changing in the structure of underlying configurations over 10 mass units.

The level ordering is explained in the terms of particle-plus-triaxial rotor model. Fig. 2.7 gives spectrum of excited states associated with $1h_{11/2}$ proton-hole, and $1h_{9/2}$ proton-particle configurations in ^{189}Au. If the excitation energies of the states (relative to $11/2^-$ band head) of the $1h_{11/2}$ are multiplied by a constant factor of 0.7088, both system show nearly identical energy spacings. As it is explained in Chapter 1, there is a symmetry between particle and hole states in the particle-plus-triaxial rotor

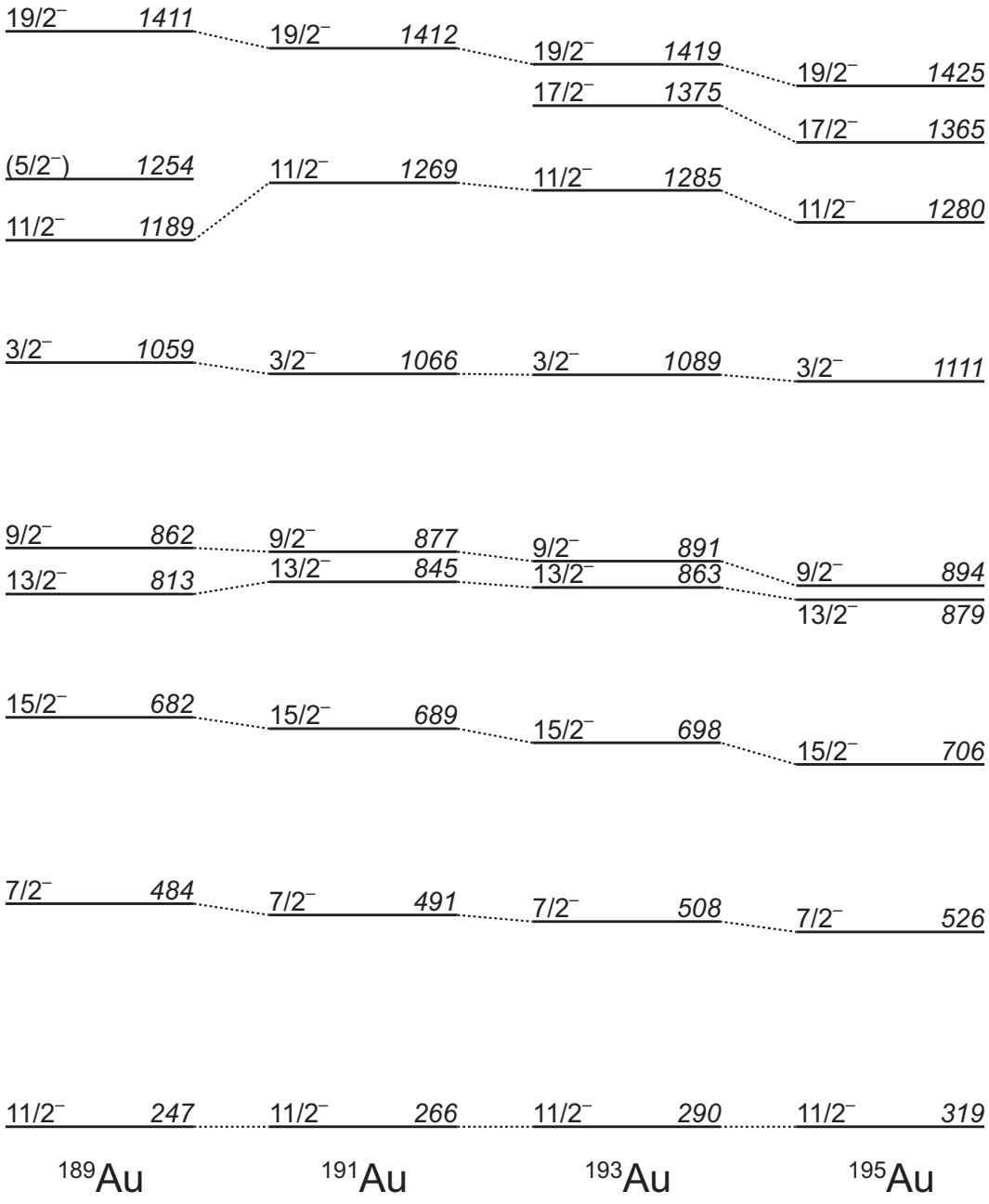

FIGURE 2.4: Systematics of negative-parity states of the $1h_{11/2}$ configuration in odd-Au isotopes. The data are taken from [76].

model. Moreover, the excitation energies of the states strongly depend on $1/\beta^2$ factor. Therefore, approximately:

$$\beta^2_{h_{9/2}} E_I(\gamma, 1h_{9/2}) = \beta^2_{1h_{11/2}} E_I(60^\circ - \gamma, h_{9/2}). \tag{2.1}$$

Based on this, the close similarity of constantly scaled $1h_{9/2}$ and $1h_{11/2}$ systems suggests that $\gamma_{1h_{9/2}} = 60^\circ - \gamma_{1h_{11/2}}$. The energy spacing of the $1h_{11/2}$ system suggests that $\gamma_{1h_{11/2}} = 37(2)^\circ$ and thus $\gamma_{1h_{9/2}} = 23(2)^\circ$ for ^{189}Au. These values are close to those

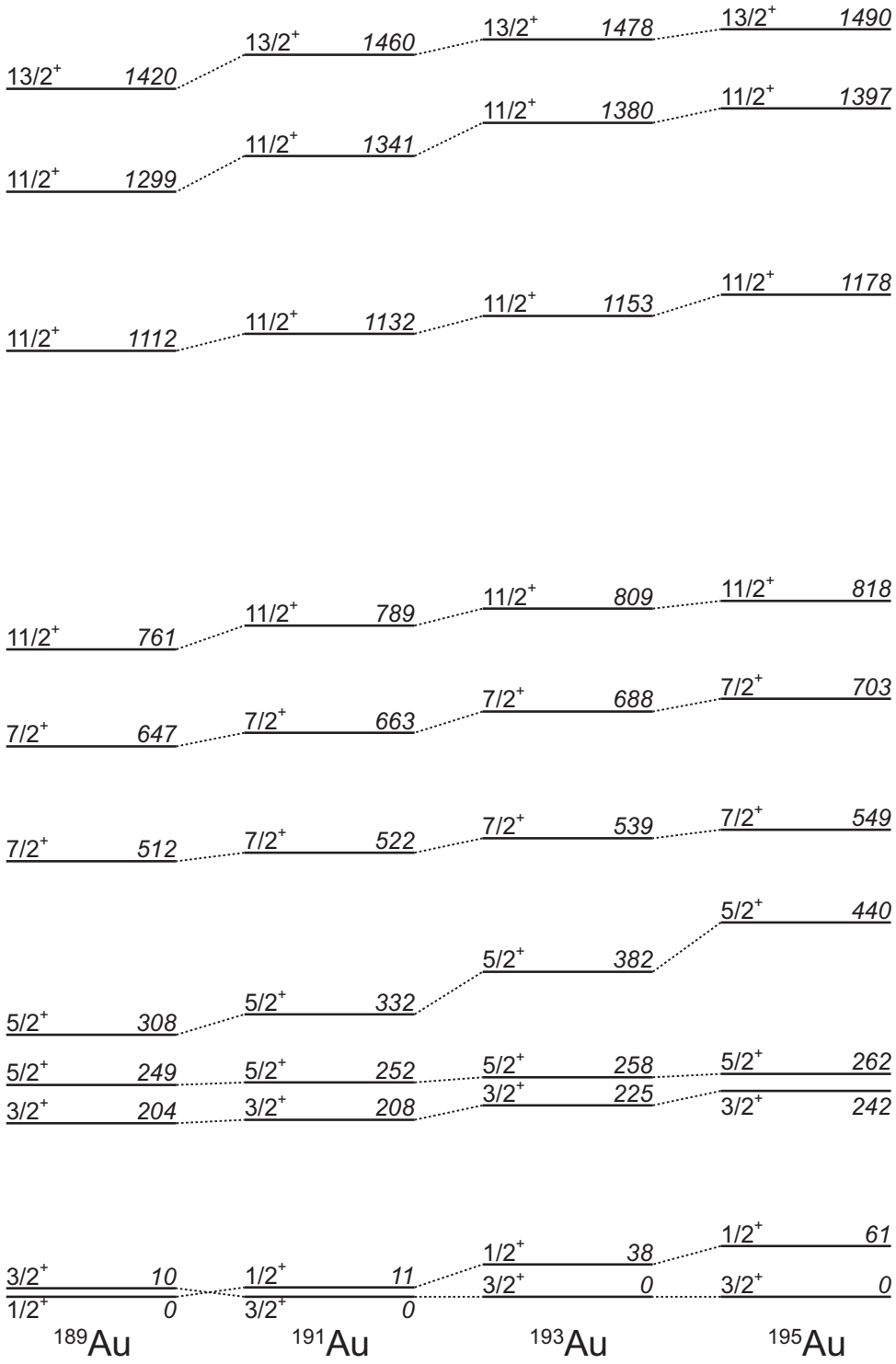

FIGURE 2.5: Systematics of positive-parity states of the $2d_{3/2}$, and $3s_{1/2}$ configuration in odd-Au isotopes. The data are taken from [76].

deduced from the first and second 2^+ energies for ^{188}Pt ($\gamma = 24(2)^\circ$), and for ^{190}Hg ($\gamma = 38(2)^\circ$). Moreover, the scaling factor of 0.71, see Fig. 2.7 is close to the ratio of first excited 2^+ states in both cores, $E(^{188}\text{Pt}, 2^+)/E(^{190}\text{Hg}, 2^+) = 0.636$.

Therefore, the $1h_{9/2}$, and $1h_{11/2}$ structures in ^{189}Au are based on differently shaped

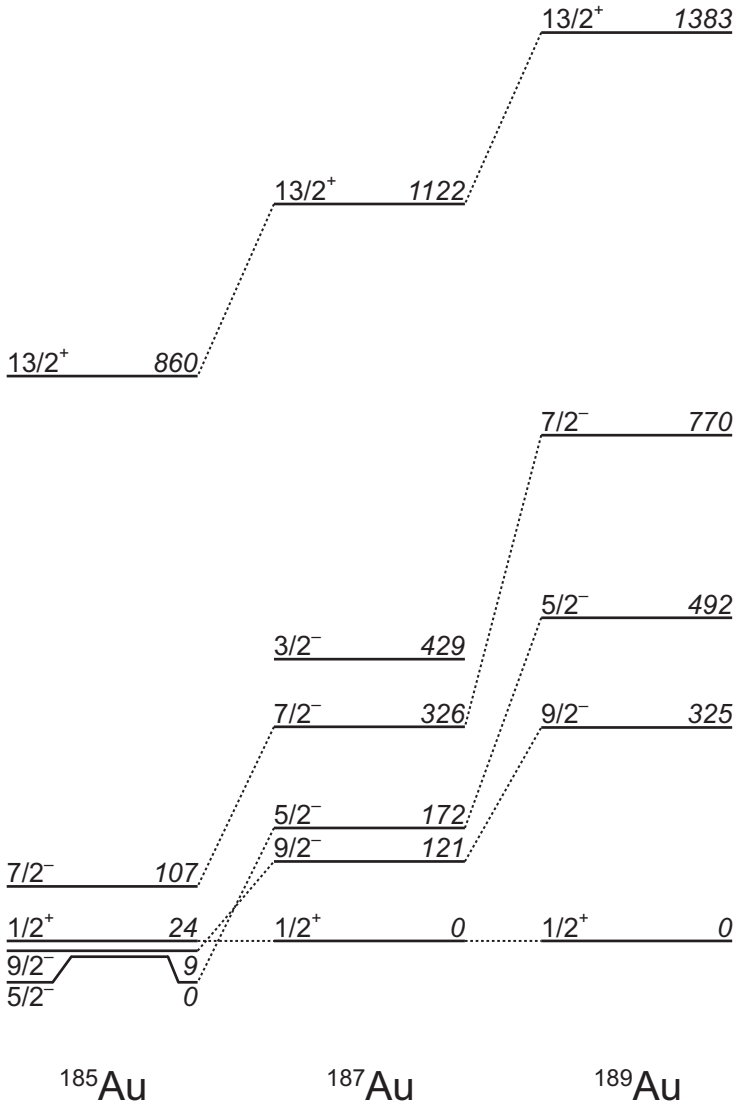

FIGURE 2.6: Systematics of $3/2^-$, $5/2^-$, $7/2^-$, and $9/2^-$ of the $1h_{9/2}$ and $2f_{7/2}$ proton-intruder configurations, and $13/2^+$ of the $1i_{13/2}$ proton-intruder configuration, given relatively to the $1/2^+$ state of the $3s_{1/2}\oplus 2d_{3/2}$ proton-hole configuration. The data are taken from [77].

cores (asymmetric prolate and asymmetric oblate), which are essentially ^{188}Pt and ^{190}Hg. This interpretation is corroborated by observation of retarded $M1$ transitions, see Fig. 2.8, which connect $9/2^-$ and $11/2^-$ bandheads of $1h_{9/2}$, and $1h_{11/2}$ systems.

Fig. 2.9 gives the decay pattern of the $7/2^-$ member of the $1h_{11/2}$ configuration in ^{183,185,187}Au isotopes. The dominant deexcitation is the $E2$ decay into the $11/2^-$ band head. However, $E1$ decays feeding two $5/2^+$ states of the $3s_{1/2}\oplus 2d_{3/2}$ configuration were identified (indicated with red colour in Fig. 2.9). Contrary, the $M1(+E2)$ transitions feeding the $9/2^-$ (indicated with blue colour in Fig. 2.9), $7/2^-$, or $5/2^-$ (not indicated in the Figure) states of the $1h_{9/2}$ proton-particle configuration was not observed. This indicates similar structure of both configurations ($1h_{11/2}$ and

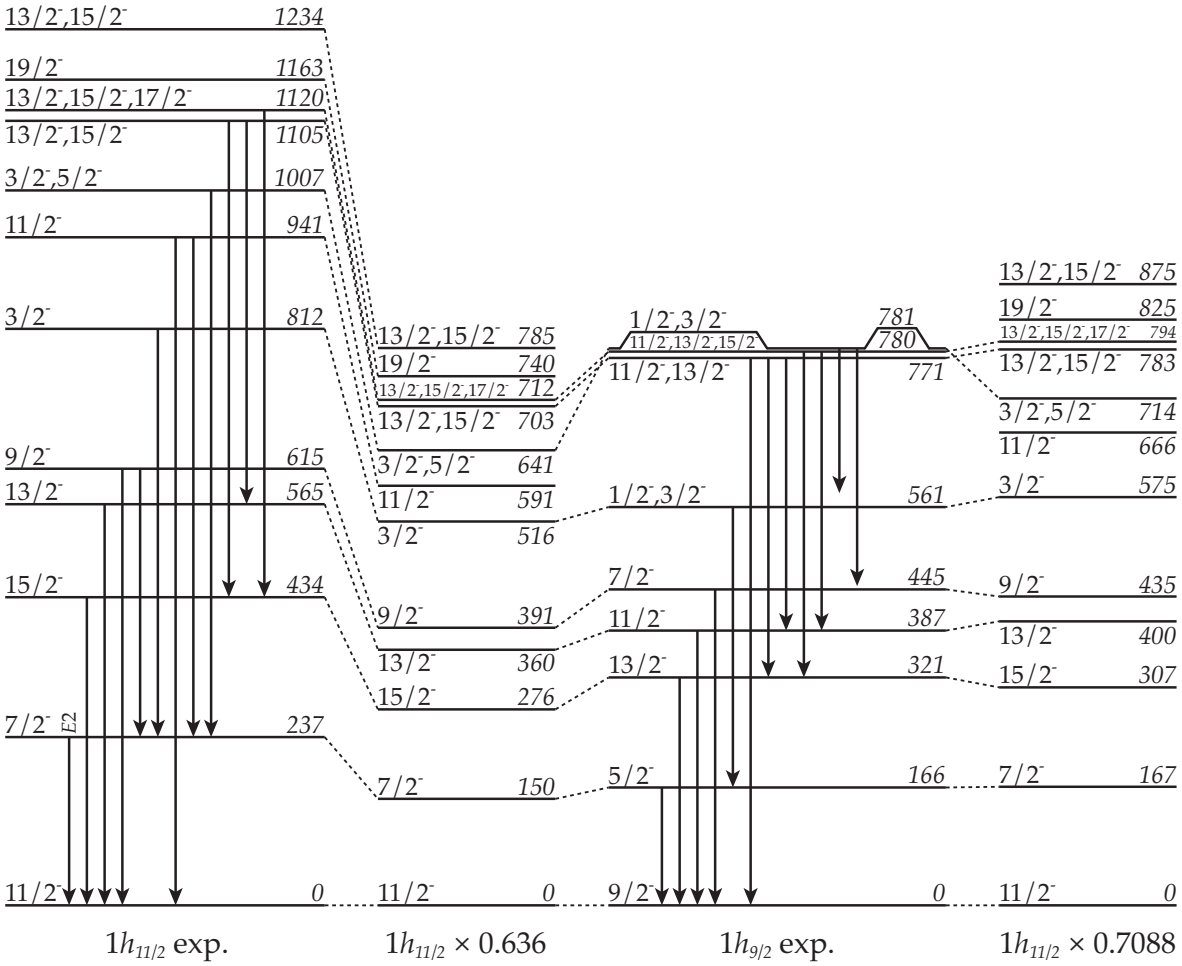

FIGURE 2.7: States associated with $1h_{9/2}$ proton-intruder, and $1h_{11/2}$ proton-hole configurations in ^{189}Au isotope. The energy scale compression factors 0.636 and 0.7088 for the $1h_{9/2}$ band are determined either from the ratio of excitation energies of 2_1^+ states in ^{190}Hg and ^{188}Pt, see the test for details, or by an *ad hoc* ratio that gives closest agreement between both bands. Based on Fig. 1 in [79].

$3s_{1/2}\oplus 2d_{3/2}$), i.e., proton hole coupled to the corresponding even-even Hg core, and corroborates different character of the $1h_{9/2}$ configuration.

Fig. 2.10 gives the decay pattern of the $13/2^+$ state of the $1i_{13/2}$ configuration in ^{185,187,189}Au isotopes. The $13/2^+$ state decays exclusively via $E1$ transitions feeding the $11/2^-$, $13/2^-$, and $15/2^-$ members of the $1h_{9/2}$ proton-particle configuration. No decays into positive-parity states of the $3s_{1/2}\oplus 2d_{3/2}$ proton-hole configuration were observed (available $9/2^+$, $11/2^+$, and $13/2^+$ states are indicated with blue colour in Fig. 2.10).

In both even-even cores, i.e., in ^{188}Hg and ^{186}Pt, excited 0^+ configurations with associated rotational bands occur at low excitation energy [41]. Therefore, at least four types of excitations are expected in ^{187}Au:

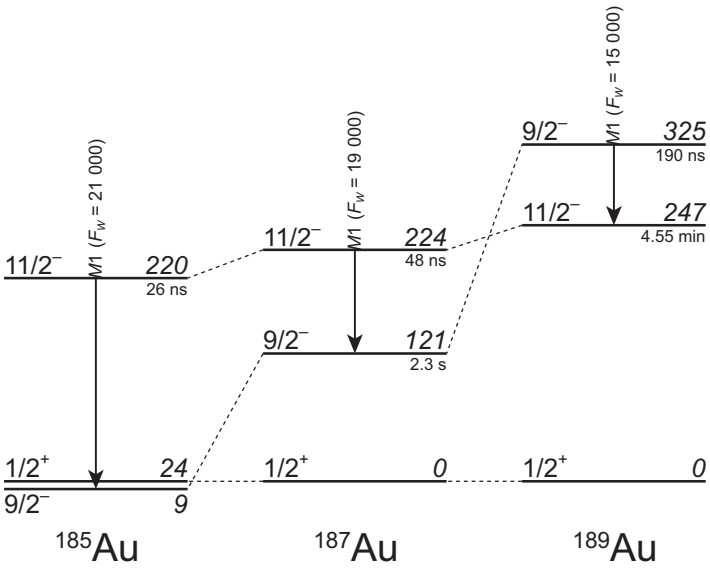

FIGURE 2.8: Systematics of isomeric $M1$ transitions in ^{185,187,189}Au isotopes. The data are taken from [61] and references therein.

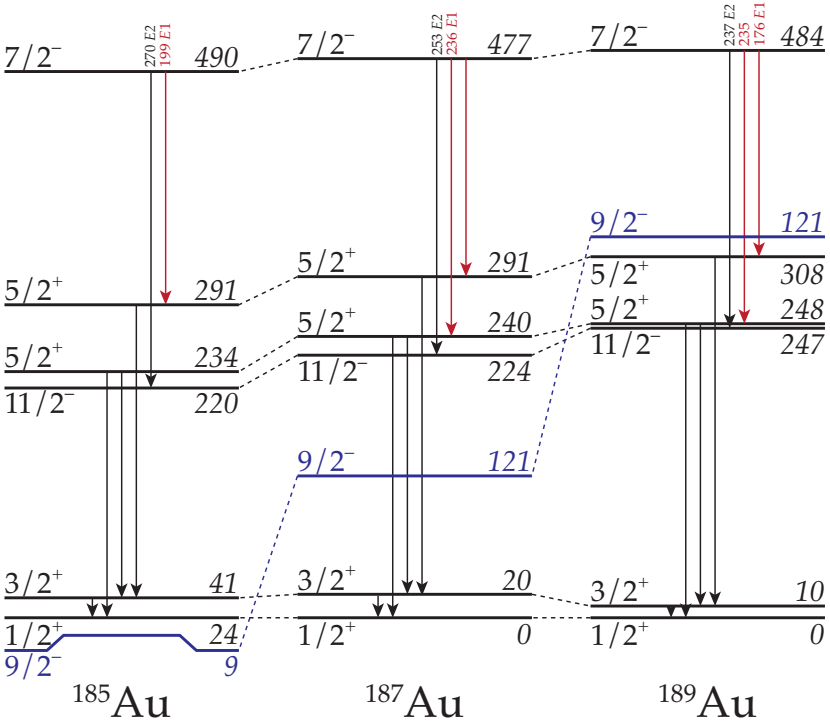

FIGURE 2.9: Decay paths of $7/2^-$ states of the $1h_{11/2}$ proton-hole configurations in ^{185,187,189}Au isotopes. $E1$ transitions are indicated with red arrows. The $9/2^-$ states of the $1h_{9/2}$ configurations, that are not fed from the $7/2^-$ states, are indicated with blue colour. The data were taken from [77].

- proton particle (intruder) coupled to 0^+ ground state in ^{186}Pt

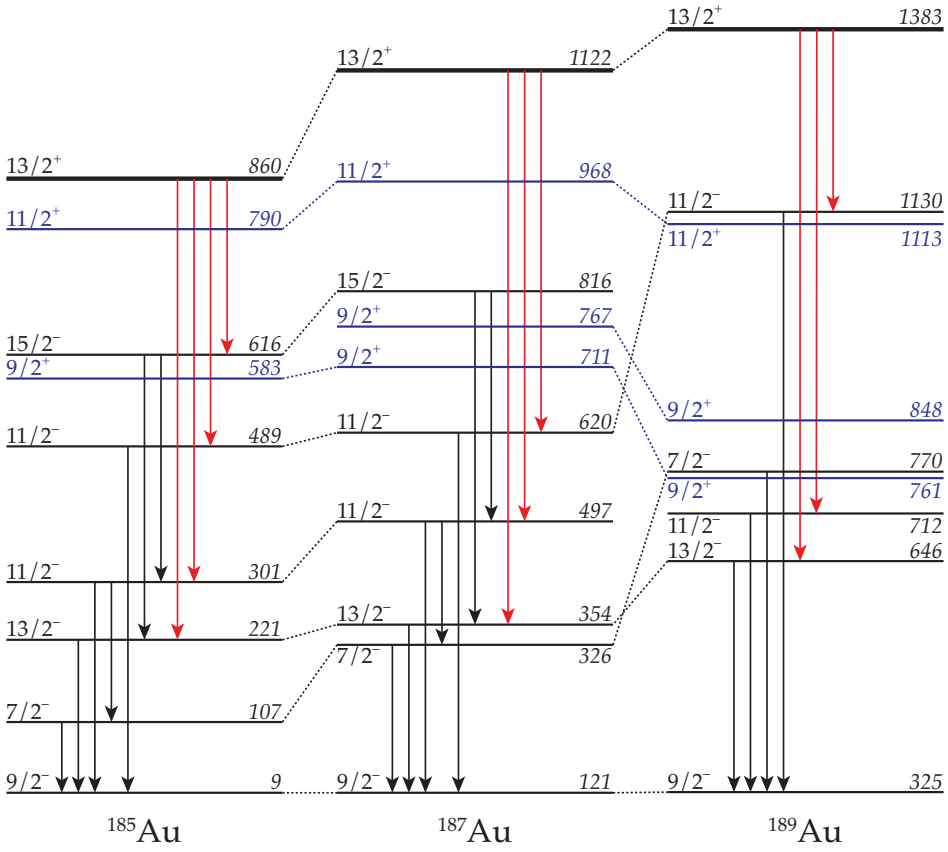

FIGURE 2.10: Decay paths of $13/2^+$ states of the $1i_{13/2}$ proton-intruder configurations in ^{185,187,189}Au isotopes. $E1$ transitions are indicated with red arrows. Positive-parity states of the $2d_{3/2} \oplus 3s_{1/2}$, that are not fed from the $13/2+$ states, are indicated with blue colour. The data were taken from [77].

- proton particle (intruder) coupled to 0^+ excited state (intruder state) in ^{186}Pt
- proton hole coupled to 0^+ ground state in ^{188}Hg
- proton hole coupled to 0^+ excited state (intruder state) in ^{188}Hg

Indeed, such states were identified in ^{185,187}Au isotopes together with corresponding $E0$ transitions, see Fig. 2.11 and 2.12. Between the states with non-zero spin, which is always the case of odd-mass nucleus, the $E0$ transition is competing with $M1$+$E2$ multipolarity. Therefore, the signature of the $E0$ component of the transition is large internal conversion coefficient ($\alpha_K > \alpha_K(M1)$, measured as ratio between intensities of conversion electrons and γ rays. Table 2.1 lists transitions with $\alpha_K > \alpha_K(M1)$ in ^{185,187}Au isotopes. They are interpreted as electric monopole transitions between coexisting states rather than anomaly in the internal conversion process proposed in [82], see the detailed discussion in Section 2.3.2.

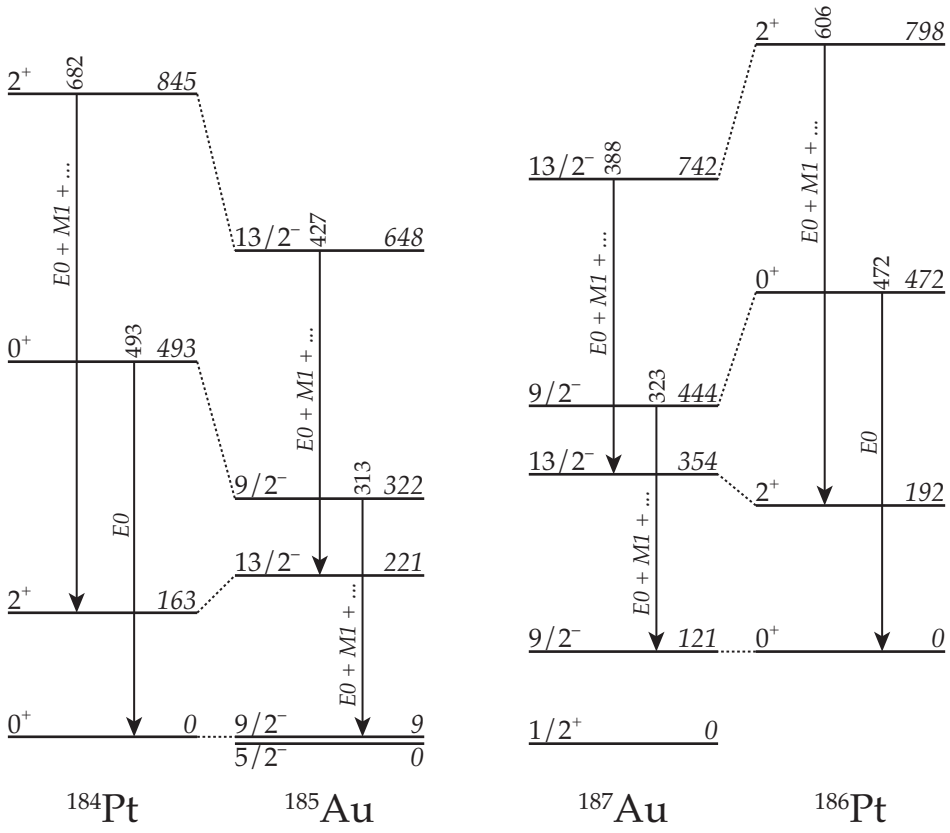

FIGURE 2.11: States of the $1h_{9/2}$ proton-intruder configuration in ^{185,187}Au, compared with 0^+, and 2^+ states in even-even ^{184,186}Pt cores. Corresponding couplings are indicated with dashed lines. Indicated transitions are those, where the $E0$ component was identified, see the text for details. The data for ^{185,187}Au were taken from [64], for ^{184}Pt from [80], and for ^{186}Pt from [81].

Interesting structure in ^{187}Au are two nearly-identical, coexisting bands associated with the $1h_{9/2}$ proton-intruder configuration, see Fig. 2.13. Only favoured signature partners are connected with electric monopole transitions, which is not understood so-far.

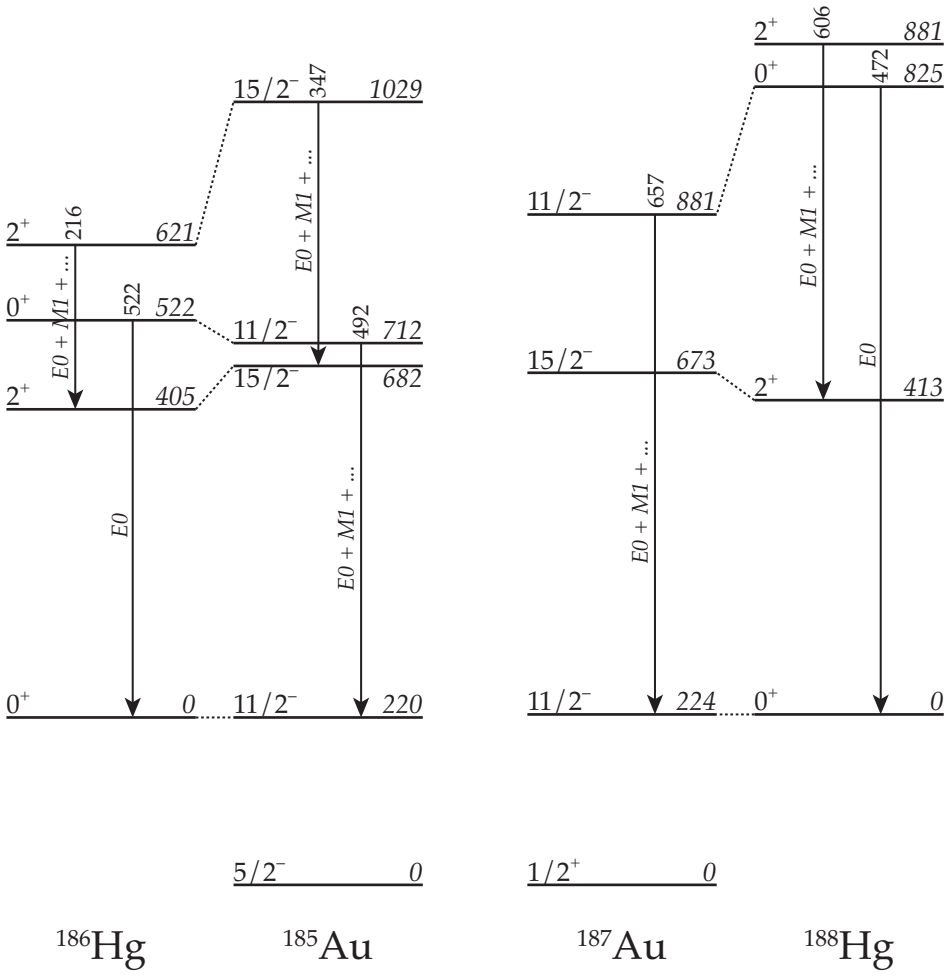

FIGURE 2.12: States of the $1h_{11/2}$ proton-hole configuration in ^{185,187}Au, compared with 0^+, and 2^+ states in even-even ^{186,188}Hg cores. Corresponding couplings are indicated with dashed lines. Indicated transitions are those, where the $E0$ component was identified, see the text for details. The data for ^{185,187}Au were taken from [64], for ^{186}Hg from [83], and for ^{188}Hg from [84].

	E_γ [keV]	J^π	$E_i \rightarrow E_f$ [keV]	α_K(exp.)	$\alpha_K(M1)$	$\alpha_K(E2)$
^{185}Au	313.2	$9/2^-$	$322 \rightarrow 9$	$0.58^{+0.35}_{-0.15}$	0.243	0.056
	426.7	$13/2^-$	$648 \rightarrow 221$	$0.33^{+0.03}_{-0.09}$	0.106	0.027
	491.9	$11/2^-$	$712 \rightarrow 220$	$0.21^{+0.01}_{-0.06}$	0.086	0.022
^{187}Au	270.9	$1/2^-$	$546 \rightarrow 275$	0.59 ± 0.07	0.361	0.080
	284.5	$5/2^-$	$456 \rightarrow 172$	0.52 ± 0.06	0.316	0.071
	322.9	$9/2^-$	$444 \rightarrow 121$	0.62 ± 0.07	0.224	0.052
	388.2	$13/2^-$	$742 \rightarrow 354$	0.64 ± 0.09	0.136	0.033
	437.9	$13/2^-$	$1187 \rightarrow 749$	0.22 ± 0.07	0.099	0.025
	478.1	$17/2^-$	$1167 \rightarrow 689$	0.24 ± 0.10	0.079	0.021
	657.3	$11/2^-$	$881 \rightarrow 224$	0.069 ± 0.02	0.034	0.011

TABLE 2.1: List of transitions with enhanced internal conversion coefficient, i.e., $\alpha_K > \alpha_K(M1)$, interpreted as electric monopoles, see the text for details. The data for ^{187}Au were taken from [77], and for ^{185}Au from [64].

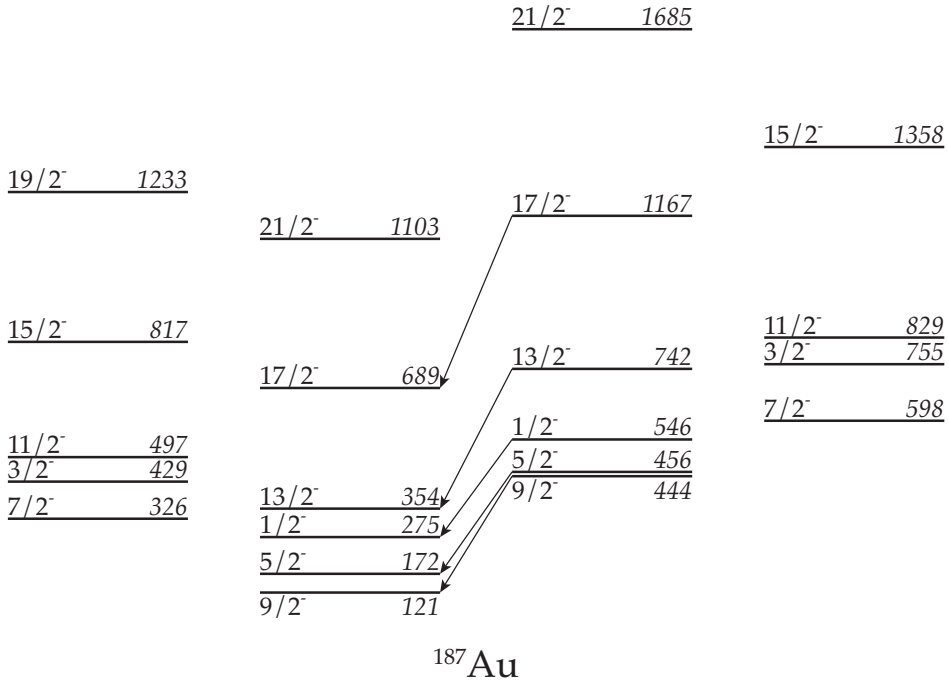

FIGURE 2.13: Part of nuclear structure of ^{187}Au. Note two nearly-identical, coexisting bands associated with the $1h_{9/2}$ proton-intruder configuration. The data for were taken from [77].

2.3.2 Studies of β^+/EC decay of ^{181,183,185}Hg isotopes at ISOCELE facility

Parallel to the UNISOR studies, program dedicated to study of the nuclear structure of odd-Au isotopes was pursued at the ISOCELE facility. For the study of excited states of ^{185}Au [82], the ^{185}Hg samples were produced by bombarding of the molten gold target with the $200-\mathrm{MeV}$ protons from Orsay synchrocyclotron. Hg atoms were evaporated from the target, ionised by the ion source of the ISOCELE and subsequently mass separated with magnetic field and deposited onto the aluminium covered Mylar tape. The tape then moved the sample into the measurement station.

Low-energy γ rays and X rays were detected with a planar hyper-pure germanium detector, high-energy γ rays (up to $2\,\mathrm{MeV}$) were detected with coaxial germanium detectors (both lithium-drifted and hyper-pure). Conversion-electrons with energies below $500\,\mathrm{keV}$ were detected with semicircular magnetic spectrograph operated at magnetic inductions $B = 4.2\times10^{-3}$, 5×10^{-3}, and 1.3×10^{-2} T. Events were recorded on a photographic plate, which was analysed with microdensitometer. Examples of conversion electrons singles spectra are given in Fig. 2.14 and 2.15. Conversion electrons above $500\,\mathrm{keV}$ were detected with cooled lithium drifted silicon detector.

Experimental procedures used at the ISOCELE facility have several serious disadvantages. First, samples were mixture of both low- and high-spin isomer. Therefore, the different feeding from both decays could not be analysed separately and part of the information that is essential for spin assignment is missing. The cardinal mistake that the Orsay group made was the absence of analysis of γ-gated electron spectra. Used magnetic spectrograph does not allow to produce coincidence information and only singles spectrum can be produced. The spectrograph has excellent energy resolution, however even this is not sufficient in the case of odd-Au isotopes near the N = 104 mid-shell point. Unresolved doublets are still present and they significantly influence the deduced internal conversion coefficients.

This led to serious misinterpretation of the data, as it was clearly shown by analysis of γ-gated electron spectra performed by the group working at the UNISOR facility, see the detailed discussion in [61]. The key 36 - $253\,\mathrm{keV}$ coincidence could not be established at magnetic spectrometer. The $36-\mathrm{keV}$ transition, which appeared to have $M1/E2$ multipolarity, is strongly converted ($\alpha = 26$) and therefore is not observed in γ-ray spectra. This coincidence was critical to establish an $36-\mathrm{keV}$ excited state with negative parity in ^{185}Au. Contrary to this [82], assigned the $36-\mathrm{keV}$ state to be of positive parity. A single mistake in one transition appeared to be sufficient to construction of wrong level scheme.

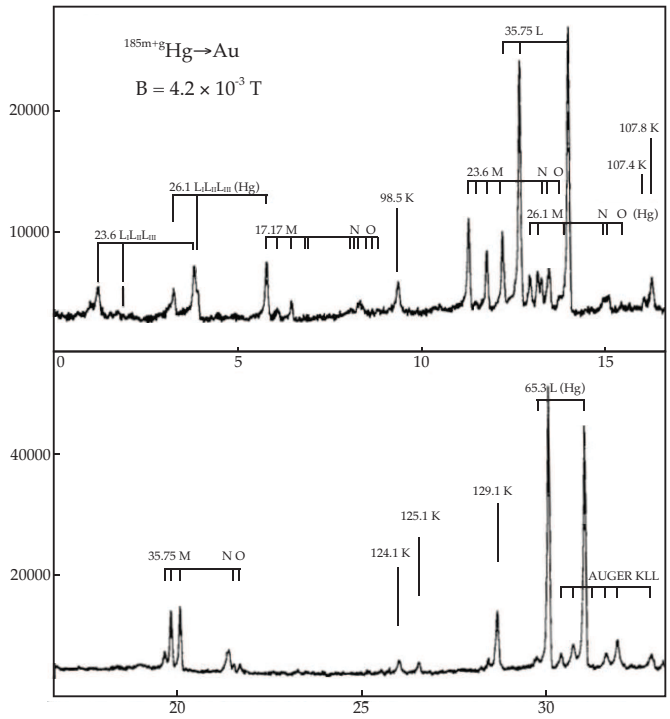

FIGURE 2.14: Low-energy part of the singles spectrum of conversion electrons from ^{185}Hg decay detected with semicircular magnetic spectrograph at the ISOCELE facility. The figure was adapted from [82].

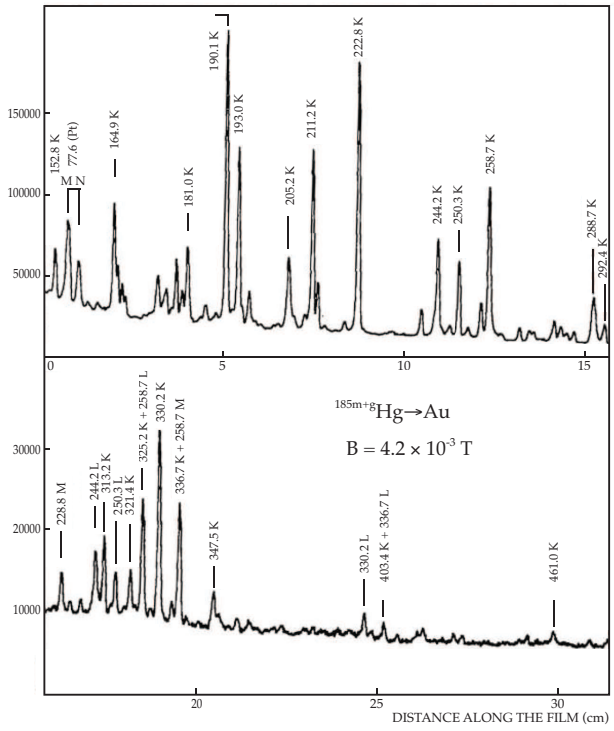

FIGURE 2.15: High-energy part of the singles spectrum of conversion electrons from ^{185}Hg decay detected with semicircular magnetic spectrograph at the ISOCELE facility. The figure was adapted from [82].

2.4 The α-decay studies of ^{181,183,185}Au isotopes

The α decay of $^{181\text{-}186}$Au isotopes was studied at the UNISOR facility [85]. Isotopes with mass numbers $184-186$ were produced by bombarding of Ta foils with a $153-\mathrm{MeV}$ ^{12}C beam. Activities with masses $181-183$ were produced by a $165-\mathrm{MeV}$ ^{19}F beam, which impinged the Yb target (produced by diffusion of Yb into carbon felt). Similar measurement device as was regularly used for β^+/EC studies, see Section 2.3.1, was employed to elucidate the α-decay schemes of above Au isotopes. Cooled lithium drifted silicon detector was used to detect α particles and conversion. Lithium drifted germanium detector, placed outside the vacuum chamber, was employed to observe γ rays. The data acquisition system allowed to measure α-γ coincidences.

Fig. 2.16 gives spectra of α particle singles of isotopes with masses 181 and 183. In coincidence with these events, γ rays were measured [85].

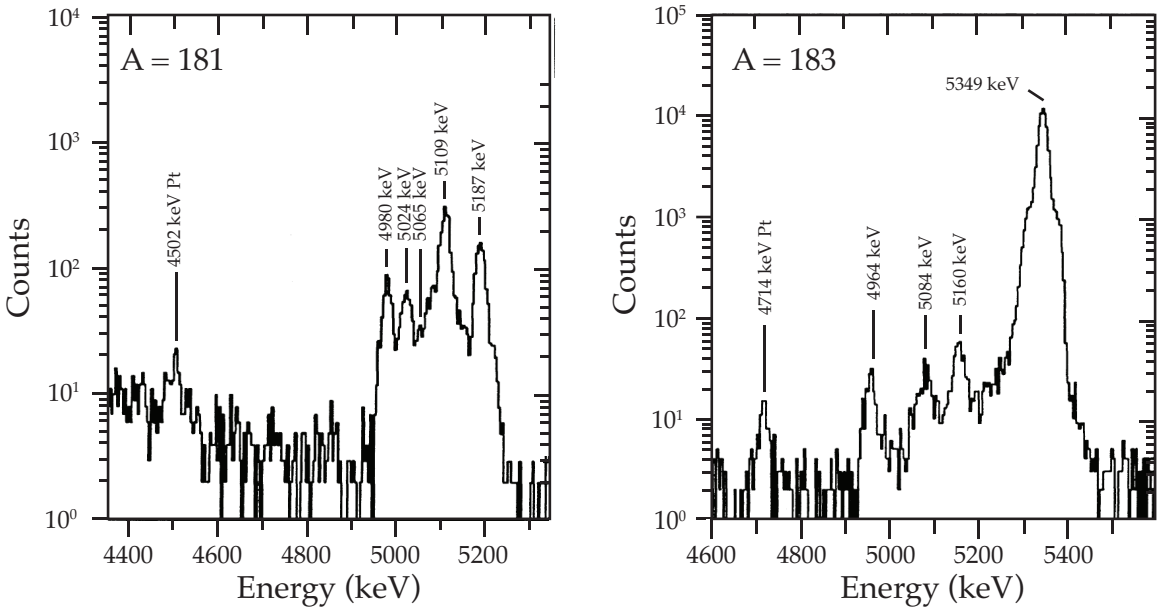

FIGURE 2.16: Parts of α spectra of A = 181 and A = 183 isotopes. Peaks labeled with Pt are assigned to decay of ^{181,183}Pt isotopes, while those labeled with the energy only are assigned to ^{181,183}Au. Figures are adapted from [85].

Using the α-γ analyses, the decay schemes of all studied isotopes were constructed. Fig. 2.17 gives decay schemes of ^{181,183,185}Au, which are relevant for the discussion presented here. The ground state of ^{183,185}Au is known to be the $5/2^-$ state of the $1h_{9/2}$ proton-intruder configuration, see the discussion above. The dominant, unhindered α decays feed ground states of daughter isotopes ^{179,181}Ir suggesting the same configuration. There is significant difference in the α decay pattern between ^{181}Au, and ^{183,185}Au: unhindered decay feeds the excited state in ^{181}Au instead of the

ground state as it is in heavier isotopes. The internal conversion coefficient on the L shell, $\alpha_L = 0.43(15)$, was established for the $148\,\mathrm{keV}$ transition [86], which depopulates state in ^{177}Ir fed by strongest α decay. This establishes either $M1$ or $E2$ mutlipolarity (or mixture of both), since theoretical calculation by BrIcc code gives: $\alpha_L(E1) = 0.02$, $\alpha_L(M1) = 0.27$, and $\alpha_L(E2) = 0.12$. The α decay feeding the ground state is slightly hindered. This suggests a different ground state configuration in ^{181}Au. A candidate is the $3/2^-$ state of the $2f_{7/2}$ intruder configuration.

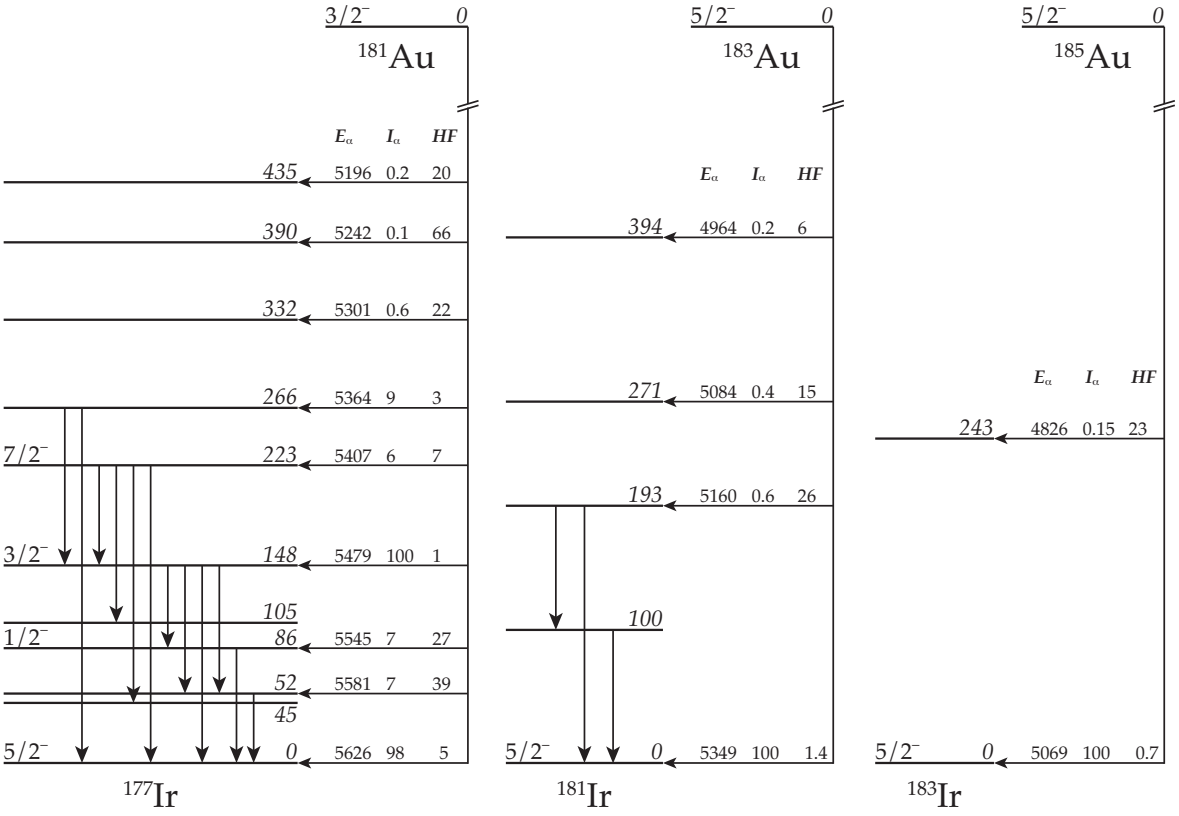

FIGURE 2.17: Level schemes of α decay of ^{181,183,185}Au. The data for were taken from [85].

2.5 Studies of α decay of odd-mass Tl isotopes

Studies of α decay of odd-mass Tl isotopes bring important, although limited, information on the excited states of odd-Au isotopes.

The α decay of the ^{181}Tl isotope was performed at velocity filter SHIP at GSI Darmstadt [87]. The ^{181}Tl nuclei were produced via the ^{144}Sm(^{40}Ca, $p2n$)^{181}Tl. Prior to this experiment, the excitation energy of the $9/2^-$ isomer in ^{181}Tl, $T_{1/2} = 1.40\,\mathrm{ms}$ [87], was not known. The experiment used the time structure of the beam the UNILAC accelerator at GSI, which was composed from 5 ms beam period and 15 ms pause

to identify the deexcitation of the $9/2^-$ isomeric state. Fig. 2.18 (a) gives spectra of γ-ray singles detected in a beam on (red) and pause (black) periods. The $258.0-$ and $577.9-\mathrm{keV}$ transitions are observed in beam on period only. The half-life of 1.40 ms was deduced for the decays that proceeds via them, which corresponds to the decay of $^{181}\mathrm{Tl}^m$ (deduced from its α decay. Both transitions were found to be in a coincidence and their $M1$ ($258.0\,\mathrm{keV}$) and $E3$ ($577.9\,\mathrm{keV}$) multipolarities were established.

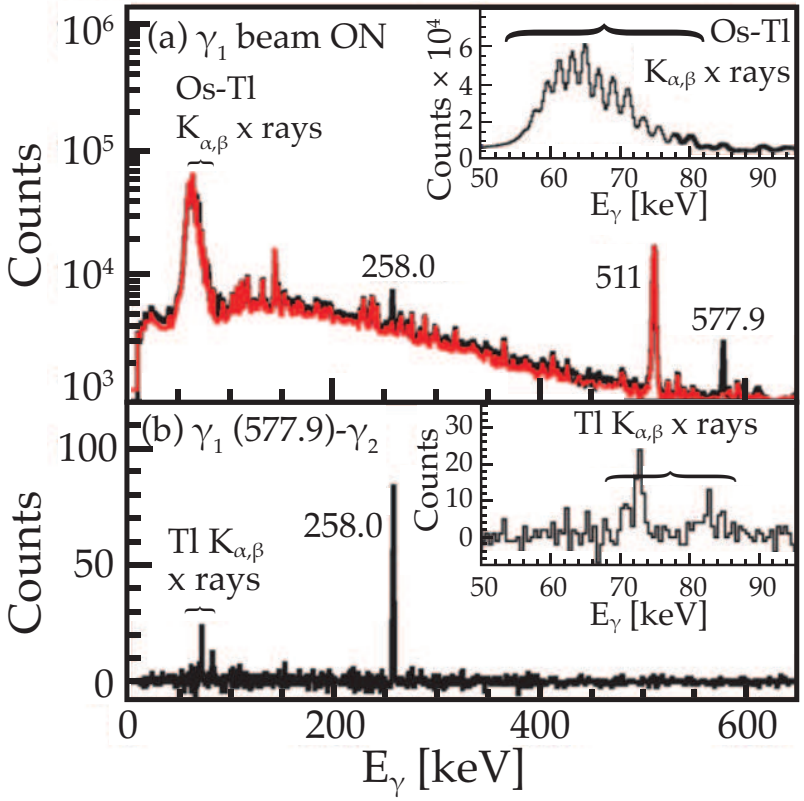

FIGURE 2.18: Spectra of γ-ray singles from α decay of ^{181}Tl detected in a beam on (red) and pause (black) periods on at the UNILAC accelerator at GSI. Figure adapted from [87].

This established the excitation energy of the $9/2^-$ isomer in ^{181}Tl isotope to be $835.9\,\mathrm{keV}$. Its dominant, unhindered α decay ($E_\alpha = 6578(7)\,\mathrm{keV}$) was found to be in coincidence with the $241.7\,\mathrm{keV}$ transition. From characteristic K x rays observed in prompt coincidence with $6578\,\mathrm{keV}$ α particles, the $M1$ multipolarity was established for the $241.7\,\mathrm{keV}$ transition in ^{177}Au. Unhindered character of the α decay suggests the $9/2^-$ spin-parity for the initial state of the $241.7\,\mathrm{keV}$ transition. Therefore, this transition is interpreted as deexcitation of the $9/2^-$ intruder configuration, feeding the $11/2^-$, α-decaying isomer in ^{177}Au, see level scheme in Fig. 2.19. Using, the ground-state α-decay energy, the excitation energy of $189(16)\,\mathrm{keV}$ was determined

for the $11/2^-$ isomer in ^{177}Au. The large experimental uncertainty arises from low precision of measurement of energies of α particles.

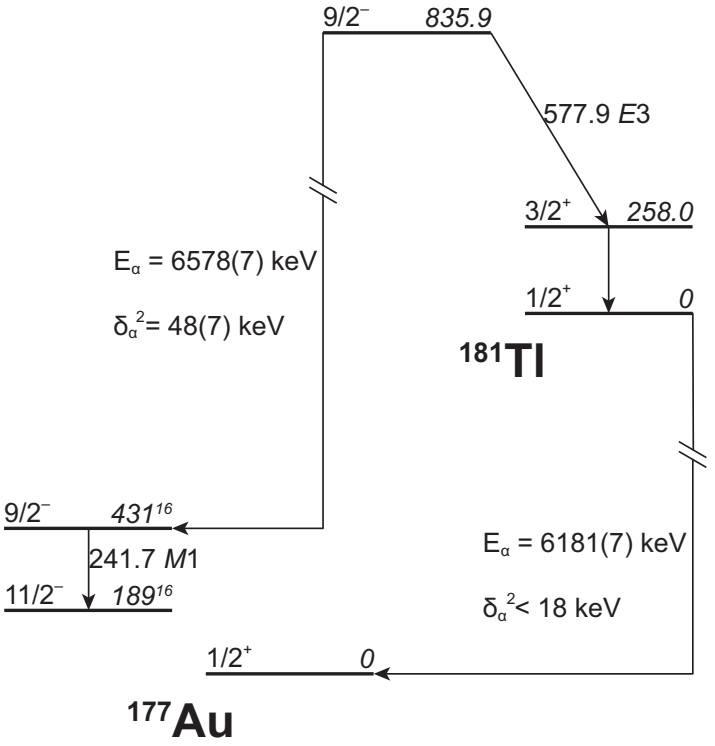

FIGURE 2.19: Level scheme of ^{181}Tl. The data for were taken from [87].

The ground states of all odd-Tl isotopes are assigned as $1/2^+$ due to pure $3s_{1/2}$ configuration. Low reduced α decay width, $\delta_\alpha^2 < 18\,\mathrm{keV}$, for ground-state α decay of ^{181}Tl suggests a different configuration of the ^{177}Au daughter. Indeed, calculations based on extended Hecht-Satchler particle-asymmetric rotor model [88], predict a mixed character of $1/2^+$ in odd-Au isotopes with dominant $2d_{3/2}$ component of the wave function of the odd proton [89]. This causes hindrance of the ground-state α decay of ^{181}Tl.

Contrary to this, unhindered α decays of $1/2^+$ ground states of ^{177,179}Tl isotopes with reduced α decay widths [90], $\delta_\alpha^2 = 41(7)\,\mathrm{keV}$ [91], and $\delta_\alpha^2 = 50(3)\,\mathrm{keV}$ [92], were observed. This suggests a major structure change of ground states of lightest known Au isotopes, which are probably pure $3s_{1/2}$ configurations. Spectroscopic factor of observed proton decay of the ground state of ^{171}Au is consistent with the $3s_{1/2}$ configuration [91].

2.6 Discovery of 326 ns isomeric state in ^{179}Au

An important step in elucidating the nuclear structure of odd-Au isotopes was a discovery of the $326\,\mathrm{ns}$ isomer in ^{179}Au [93]. Experiments were performed at the

Accelerator Laboratory of the University of Jyvaskyla, Finland and employed the RITU gas-filled separator [94] coupled with the GREAT focal-plane spectrometer [95] and at the ISOLDE facility. New isomeric state was identified by a combination of isomer spectroscopy, alpha decay spectroscopy and mass measurements.

The isomer has been found to be strongly populated by alpha decay of $9/2^-$ intruder state in ^{183}Tl isotope, see level scheme given in Fig. 2.20. This suggests intruder nature of the isomeric state in ^{179}Au. The spin-parity of the isomer has been assigned as $3/2^-$, i.e., the same structure as in ^{181}Au isotope, see section 2.4.

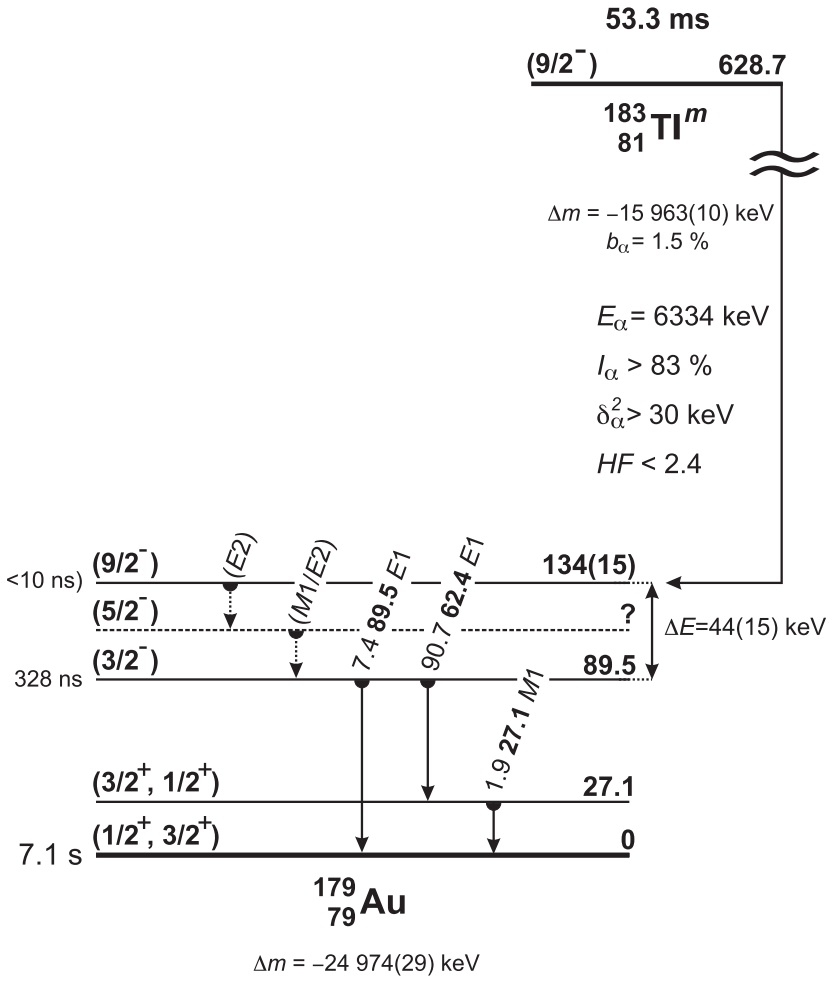

FIGURE 2.20: Level scheme of ^{179}Au isomer populated by ^{183}Tl α decay. Figure adapted from [93].

The $E1$ multipolarity was established for transitions depopulating the isomer, $1/2^+$ and $3/2^+$ assignment of the ground and the first excited state of ^{179}Au. This is corroborated by recent in-source laser spectroscopy experiment performed at ISOLDE, which unambiguously established spin-parity of the ground state to be $1/2^+$ [96].

The discovery of this isomer led to a formation of new research group at Department of Nuclear Physics, Slovak Academy of Sciences in Bratislava. This group took

new spectroscopic initiative that produced (among others) results presented in this thesis.

2.7 Observation of strongly-coupled band in ^{177}Au isotope

Strongly-coupled band has been observed in proton-unbound ^{177}Au isotope [97]. The experiment has been performed in the Accelerator laboratory of the University of Jyväskylä. Excited states of ^{177}Au nuclei were populated using the ^{92}Mo(^{88}Sr, p2n)^{177}Au nuclear reaction. Gamma rays emitted at the target position were detected with JurogamII germanium array. Products of reactions were separated from primary beam with RITU gas-filled separator and detected with the GREAT focal-plane spectrometer. Standard recoil-decay tagging technique [98, 99] was used to identify gamma rays of interest.

Fig. 2.21 gives partial level scheme of ^{177}Au isotope identified in [97], together with corresponding transitions in ^{187}Au isotope. The first $11/2^-$ state is interpreted as coupling of the $1h_{11/2}$ proton hole with 0^+ ground state of corresponding even-even Hg core. Ground states of both ^{178}Hg and ^{188}Hg are known to be weakly deformed configurations [37]. Second $11/2^-$ state is due to coupling of the same $1h_{11/2}$ proton hole with 0^+ state known in Hg isotopes [38, 46].

It was believed that excited 0^+ intruder states across even-Hg isotopic chain are the same configurations. Notable difference between decay pattern and rotational-band build on the second $11/2^-$ state suggest that significant change in the structure

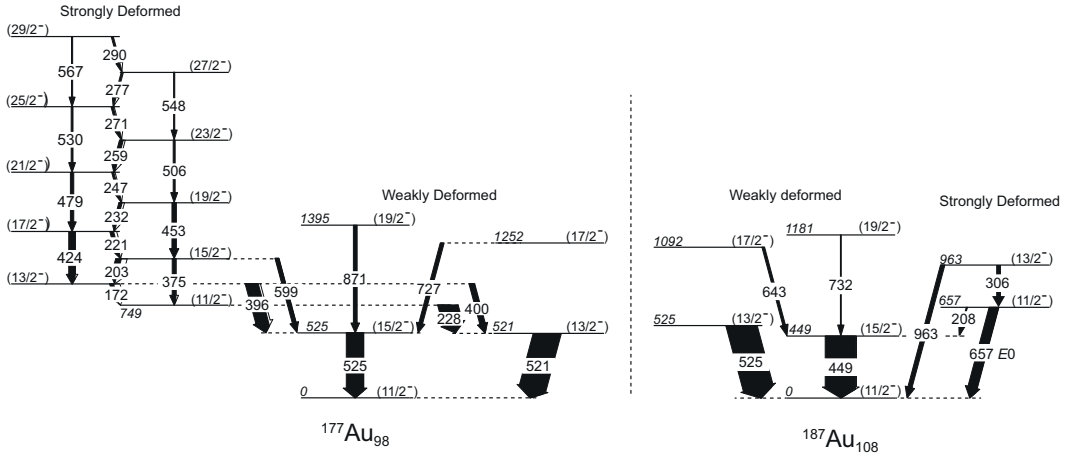

FIGURE 2.21: Partial level scheme of ^{177}Au. Figure adapted from [97].

occurs between ^{186}Hg and ^{178}Hg isotopes.

Chapter 3

Experiment IS521

The CERN-based experiment IS521 (spokesperson: Martin Venhart) has been proposed to study excitation states in neutron deficient odd-Au by simultaneous detection of X-rays, γ rays and conversion electrons [5]. The excited states of odd-Au isotopes were populated by the β^+/EC decay of corresponding Hg isotopes. This study leads to better understanding of nuclear structure and low-energy shape coexistence in the neutron mid-shell region in odd-Au isotopes. The first part of the IS521 experiment was carried out in August 2014 and the second one in August 2016.

3.1 CERN

CERN, located near Geneva on the border between France and Switzerland, is the European Organization for Nuclear Research. The acronym CERN has its origin in 1951, when European Council for Nuclear Research (in French: Conseil Européen pour la Recherche Nucléaire) was established at a meeting of UNESCO in Paris. The convention establishing the organization was signed by 12 states and the European Organization for Nuclear Research officially came into being on 29 September 1954. The provisional CERN Council was dissolved, but the acronym remained. Nowadays, this organization is run by 23 member states, has 3440 employees and approximately 12 500 users (31 December 2017 according to website of CERN) and a total contribution from all countries involved of 1148.2 millions CHF (at 13 March 2018 according to website of CERN). Physicists and engineers at CERN use the world's largest and the most complex scientific instruments to study the fundamental laws of nature, e.g., the elementary particles and nuclear structure. This organization plays role also in the technology development in many fields from material sciences to computing. The main CERN technology inventions are, e.g, World Wide Web (WWW), grid computing, new particle accelerators and detectors, which are nowadays used not only in fundamental research, but also in industry or medicine.

CERN is a city-like complex with two main sites (Meyrin in Switzerland and Prévessin in France) based on a system of accelerators from which is the LHC (Large

Hadron Collider) the newest and the largest one. The LHC is the world's largest and most powerful particle accelerator and consists of a $27-\mathrm{km}$ ring of superconducting magnets with a number of accelerating structures. The beams inside the LHC are made to collide at four locations. While the dominant activity of CERN is the LHC colliding beam programme, there are many experiments and facilities e.g. AEGIS, ALICE, ALPHA, AMS, ASACUSA, ATLAS, ATRAP, AWAKE, BASE, CAST, CLOUD, CMS, COMPASS, DIRAC, *ISOLDE*, LHCb, LHCf, MOEDAL, NA61/SHINE, NA62, NA63, nTOF, OSQAR, TOTEM, UA9. Slovak Republic is a member state of ATLAS, ALICE, NA62 and ISOLDE. Sketch of main accelerators beamlines and some experiments is given in Fig. 3.1.

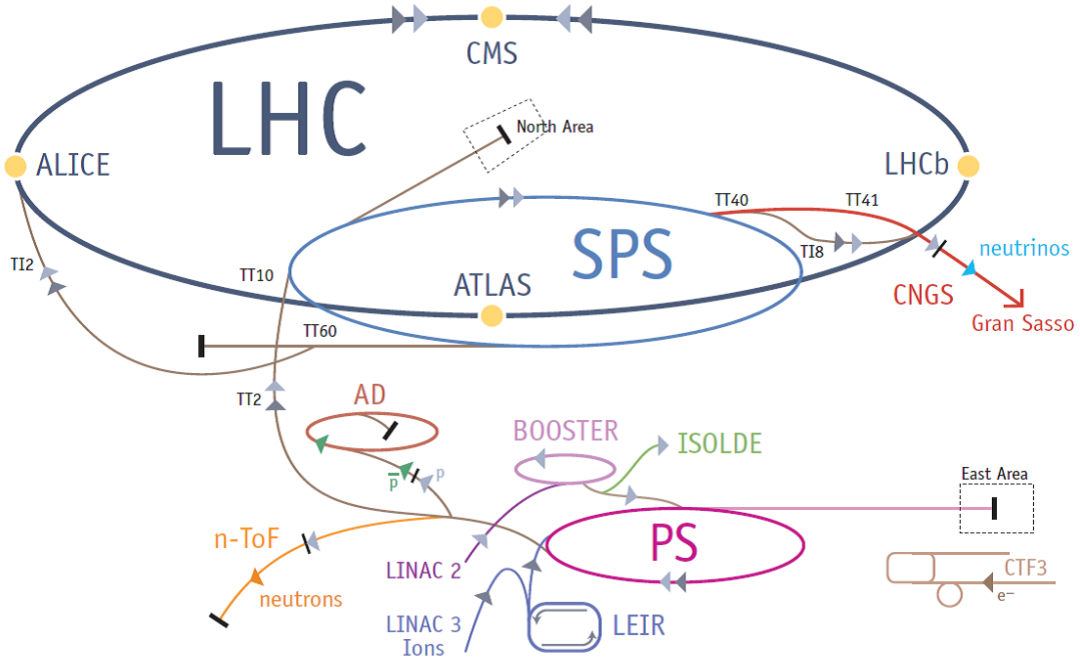

FIGURE 3.1: CERN accelerator infrastructure. Figure adapted from website of CERN

The main route for the acceleration of protons starts in an ion source, which contains a bottle of hydrogen gas and an electric field is used to strip this neutral atoms of their electrons to get protons, see website of CERN. The first accelerator in this proton accelerating chain is Linac 2, which accelerates protons up to the energy of $50\,\mathrm{MeV}$. The beam is then injected into the Proton Synchrotron Booster (PSB), which accelerates the protons to $1.4\,\mathrm{GeV}$ and bunches the beam. Pulsed beam is divided after each accelerator to many facilities or an another accelerator and at this point more than a half of protons go to ISOLDE, see Fig. 3.2. Rest of the protons are further accelerated by the Proton Synchrotron (PS) to the energy of $25\,\mathrm{GeV}$, followed by the Super Proton Synchrotron (SPS) where they are accelerated to $450\,\mathrm{GeV}$. Finally, the protons are injected into two beamlines of the LHC where

they reach their maximum energy of $6.5\,\mathrm{TeV}$ and they are brought into collision at four places, where experimental stations with unique detectors are active.

In years 2019-2021, during the second long shutdown of CERN, the whole injector complex for the LHC is going to be upgraded. Present Linac 2 will be replaced with a brand new Linac 4 with the output beam energy of $160\,\mathrm{MeV}$ instead of $50\,\mathrm{MeV}$. At the PSB, the beam will be accelerated to $2\,\mathrm{GeV}$ instead of $1.4\,\mathrm{GeV}$ and many components and cabling will be replaced in case of other accelerators. The plan is to return to physics experiments in 2021.

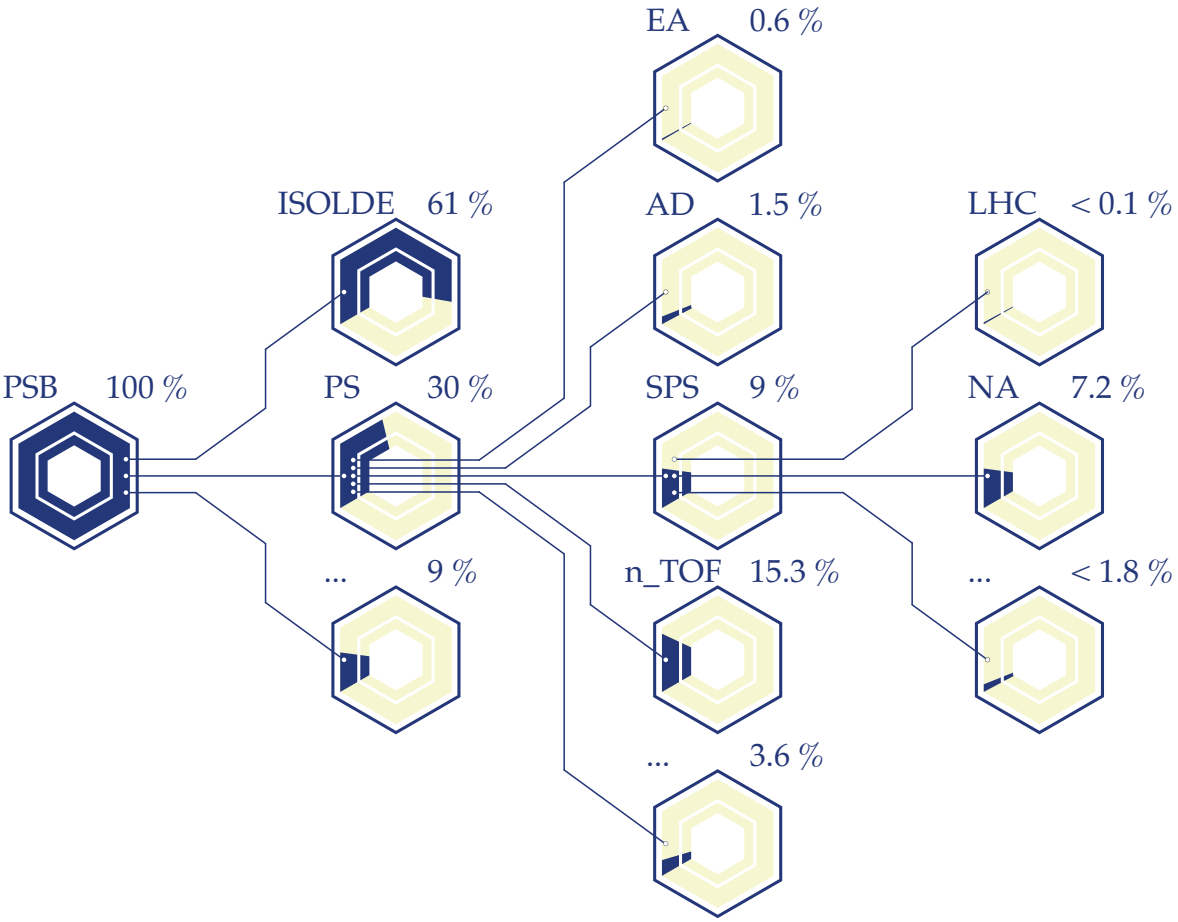

FIGURE 3.2: Graphical interpretation of a distribution of proton beam to facilities or accelerators within CERN. PSB stands for Proton Synchrotron Booster, PS for Proton Synchrotron, EA for Eastern Area fixed target experiments, AD for Antiproton decelerator, n_TOF for Neutron time-of-flight facility, NA for North Area fixed target experiments, and symbol ... for other uses. Figure adapted from website of CERN.

3.1.1 ISOLDE facility

ISOLDE [100] is experimental infrastructure within the CERN complex where the radioactive-ion beam (RIB) is produced and used for various physics experiments. It is active at CERN since 1966. The RIBs are produced with isotope separation on-line

(ISOL) technique, which uses protons from CERN's accelerator complex to produce exotic nuclei of most of the elements. These radioactive nuclei are used for basic research in many areas of science: nuclear physics, nuclear astrophysics, atomic physics, condensed matter physics, radiobiology, and elementary particle physics. The ISOLDE is operated by the consortium of countries. Member states are Belgium, CERN, Denmark, Finland, France, Germany, Greece, Italy, Norway, Poland, Romania, Slovakia, South Africa, Spain, Sweden and the United Kingdom. Slovakia became a member state in 2016 by decision of Minister of Education, Science, Research and Sport of Slovak Republic Mr. Juraj Draxler, as a result of successful IS521 experiment performed by team from Institute of Physics, Slovak Academy of Sciences.

The ISOLDE facility produces radioactive nuclei in reactions induced with protons at the energy of $1.4\,\mathrm{GeV}$ in a variety of special targets. Several different types of reactions can take a place like spallation, fragmentation or fission, making a broad range of elements and isotopes available. Targets are heated, therefore produced radioactive species diffuse out faster before they decay. Scientists and engineers here have worked for decades to develop the best materials and designs for the targets. To produce a beam of a chosen exotic nucleus requires not only the right choice of target material, but also methods to extract the nuclei as ions and to separate them electromagnetically from other species. ISOLDE has pioneered a very selective ionization technique that uses several wavelengths of laser light simultaneously to pick out specific elements. ISOLDE has two electromagnetic separators (for general purpose and high resolution), two target positions and can deliver more than 700 different beams of isotopes from 70 chemical elements.

There are several beamlines for fixed or travelling experimental setups at ISOLDE experimental hall. Fixed experimental setups have permanent position in the experimental hall. Each of them has its own beamline during ISOLDE operation and has the local group responsible for its operation and development. Currently installed fixed experimental setups are ASPIC, COLLAPS, CRIS, IDS, ISOLTRAP, Lucrecia, Miniball and Nicole. Travelling experimental setups are setups, which come to ISOLDE for shorter periods and they are usually systems used for detection of specific decay modes of the studied nuclei. Layout of the ISOLDE experimental hall with experimental setups is shown in Fig. 3.3.

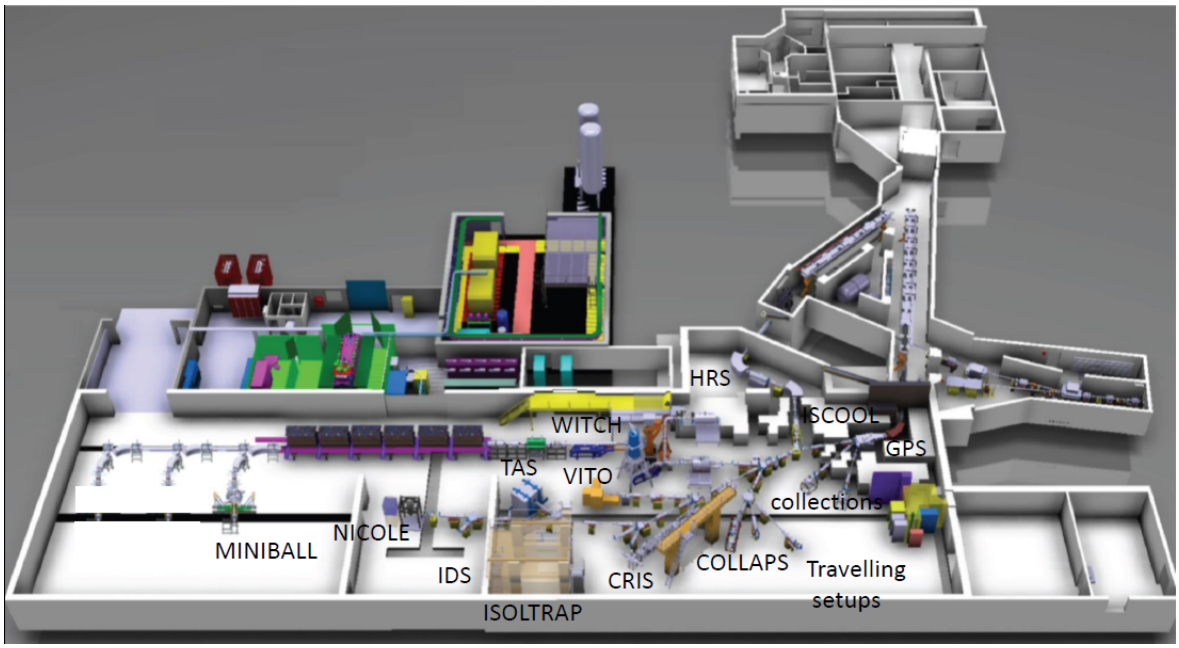

FIGURE 3.3: Layout of the ISOLDE facility with experimental setups. Figure adapted from [100].

The HIE ISOLDE is the next generation post-accelerator aiming at increasing the performance of ISOLDE towards higher energy, higher intensity and improved beam quality. It is operational since 2015. However, it was not used in IS521 experiment.

3.2 Experimental details

A molten lead was used as the ISOLDE target, which was irradiated with the pulsed proton beam delivered by the PSB. A plasma ion source was used for ionisation of isotopes, residuals of nuclear reactions inside the target. These isotopes were extracted with the extracting voltage of $30\,\mathrm{kV}$ and then mass separated using the General Purpose Separator adjusted for required mass number. Elements in the region from Hf to Pt were not extracted from the target, because they are refractory metals. Production and extraction of Pb, Tl and Au was very low, therefore practically pure beam of Hg ions was delivered to the LA1 beamline for travelling experimental setups, where the TATRA spectrometer was installed. A radioactive sample was created by deposition of the Hg beam on the metallic tape of the TATRA's tape transportation system. The sample with sufficient collected activity was transported to the measurement position while the beam gate was closed. This is periodically repeated according to the half-life of the measured isotope. Two separate runs were performed with different detectors coupled to the TATRA system.

3.3 TATRA spectrometer

TATRA [101] is compact spectrometer, which was developed and constructed at the Institute of Physics, Slovak Academy of Sciences in Bratislava, Slovakia. The name, TATRA, is an abbreviation of the TApe TRAnsportation system and also evokes the origin of the system (TATRA Mountains are the highest mountain range in Slovakia).

The spectrometer is composed of a vacuum chamber with the tape transportation system inside, detector of electrons coupled with it and several γ detectors outside, which can be of any type. Its primary purpose are nuclear structure studies, thanks to its capability of measuring γ rays and conversion electrons simultaneously.

TATRA spectrometer has been under development since 2011 and the first use of it was during the first run of the experiment IS521 at the ISOLDE facility in 2014 (see Chapter 3). In that time we were unable to properly measure low-energy γ rays and X-rays, because the measurement point was positioned inside the tube from stainless steel with 2 mm wall thickness. Another problem was non-functioning silicon detector with wrong type of the preamplifier, and therefore no electron data were obtained. Later, the detector was repaired under warranty by the manufacturer and TATRA spectrometer was modified for the better low-energy photons transmission. The measurement point has been moved closer to the main vacuum chamber and it was positioned to the centre of aluminium cube with four $50\,\mu\mathrm{m}$ thin titanium foil windows. Modified TATRA spectrometer was successfully used during the second run of the experiment IS521 in 2016 at the ISOLDE facility. X-rays, γ rays and conversion electrons were measured with the spectrometer. In 2017 TATRA spectrometer was used during the IS571 experiment at ISOLDE, which was led by Leuven group and it was dedicated to study the ^{80}Ga isotope by laser and decay spectroscopy at once. The CRIS experimental setup [102] was used for the laser spectroscopy and TATRA spectrometer was coupled with it for the decay spectroscopy. TATRA is the only tape system, so-far available at ISOLDE, which can cooperate with the device under ultra high vacuum (UHV) conditions without differential pumping system as required for the laser resonance spectroscopy. Further details of TATRA spectrometer and the data acquisition system are given in following subsections.

3.3.1 Tape transportation system

The tape transportation system is the main component of TATRA spectrometer and its aim is collection and transportation of radioactive samples from the collection point to the measurement point (see Fig. 3.4). Samples of radioactive isotopes are produced by a deposition of a radioactive ion beam onto the metallic tape. The

sample is transported into the measurement point right after the ion collection by a swift tape move. Since the sample is radioactive, the activity of studied isotope is continuously decreasing, while activities of daughter isotopes are increasing. When significant fraction of the sample decayed, a new one has to be delivered to the measurement point and the whole procedure is repeated periodically. Collection (ion deposition), transportation and measurement times depend on the half-life of the studied isotope and the yield of radioactive ion beam.

For the tape movement, the system contains only one stepper motor positioned outside the vacuum chamber. A torque from the stepper motor is delivered to the tape through a vacuum rotary feedthrough. The tape is accumulated within a single reel where it is put into outer circumference while the tape is pulled out from the inner circumference. Both ends of the tape are welded together, which creates an endless loop of the tape. This principle comes from Realistic - Radio Shack's 8-track tapes used in the past for the audio recording. Similar system was already used at the UNISOR facility in the past [103] with the original carbon coated plastic tape. In TATRA system, this tape has been replaced by the tape from amorphous metallic alloy (metallic glass). The metallic tape was prepared by rapid quenching (with $10^6\,\mathrm{K\,s^{-1}}$ temperature gradient) of a molten $Fe_{30}Ni_{46}Cr_2Mo_2Si_5B_{15}$ alloy on the surface of a highly polished and smooth copper wheel using a planar flow casting technique [104]. Tape was produced by the Department of Metal Physics at Institute of Physics, Slovak Academy of Sciences. The stepper motor is controlled via industrial PC and all other parts are made of materials suitable for high-vacuum environment like, e.g., stainless steel, PTFE, OFCu, Viton. The tape is insulated from the rest of the system for monitoring of a system failure (e.g. loosen or broken tape). If the contact of the tape with the system is detected as short circuit, the data acquisition system is automatically stopped.

The tape length can be from $3\,\mathrm{m}$ to $80\,\mathrm{m}$, while the accuracy in the tape move is better than $0.5\,\mathrm{mm}$. The stepper motor has $200\,\mathrm{main\ steps/rev}$ with an option of a microstepping ($3200\,\mathrm{steps/rev}$ in our case). The distance between the place of deposition and the measurement point is approximately $67\,\mathrm{cm}$. The sample can be moved by this distance in less than $0.7\,\mathrm{s}$. Principal drawing of the tape transportation system is shown in Fig. 3.4 and its real photography of the system at LA1 beamline is shown in Fig. 3.5.

3.3.2 Vacuum system

To achieve high-vacuum conditions is one of priorities of TATRA spectrometer. It is required for the best detection of electrons emitted by the radioactive sample, silicon detector operation and its resolution. One vacuum chamber, one ceramic

break, two conical reducers, the measurement cube, one cross, one stainless steel bellow and the Si(Li) detector make the whole volume that has to be pumped down.

The vacuum chamber is designed for the high vacuum operation with pressure in order of 10^{-8} mbar. It is 150 mm high cylindrical chamber from the stainless steel with the main ISO-F DN320 flange on its top and nine additional CF flanges for the incident beam, outgoing tape and equipment. The chamber is pumped down

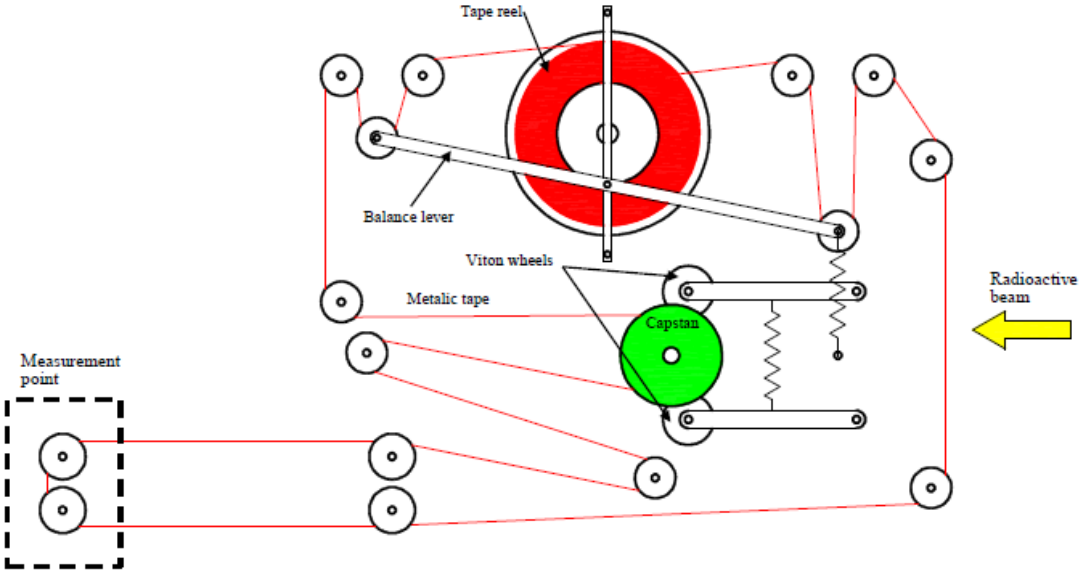

FIGURE 3.4: Operational principle of the tape transportation system. The metallic tape is drawn red, capstan of the stepper motor is green and the incident RIB is yellow arrow.

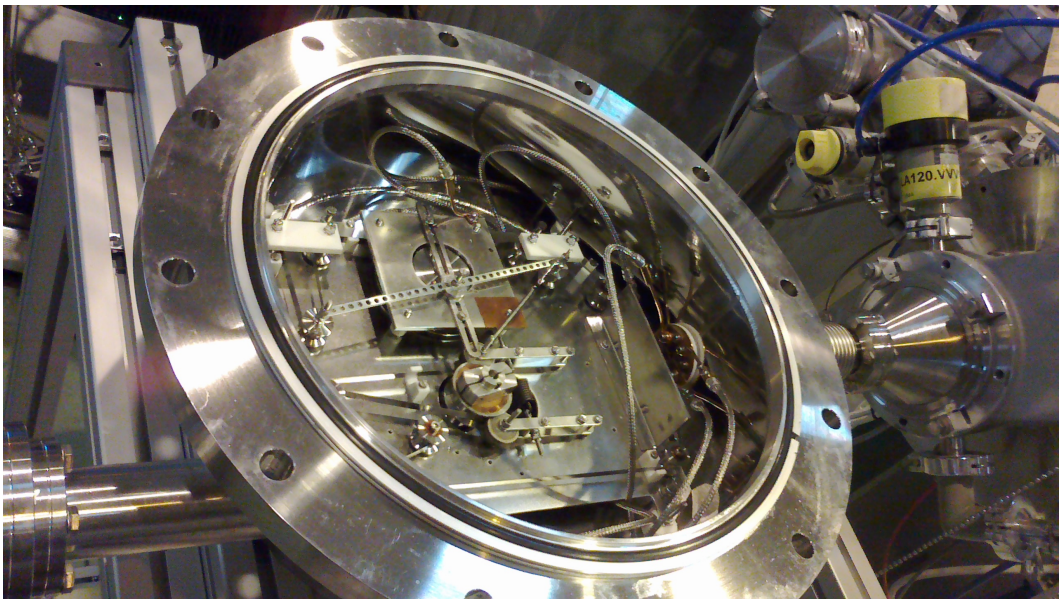

FIGURE 3.5: Photography of opened TATRA chamber with the tape system inside. The chamber is connected to the LA1 beamline in the experimental hall of ISOLDE.

by the Pfeiffer HiPace 300 turbomolecular pump (TMP) with the pumping speed of up to $260\,\mathrm{l\,s^{-1}}$ for N_2 and the Edwards nXDS6i oil-free scroll pump as a backing pump for TMPs. Other flanges are for the vacuum gauge, a venting valve, the rotary feedthrough for the stepper motor and electrical feedthroughs.

The measurement cube is made from special aluminium alloy adapted to use CF flanges [105]. It has six flanges, while one is used for connection to main vacuum chamber, one is for the Si(Li) detector connection and four are blended with $50\,\mu\mathrm{m}$ thick titanium foil serving as windows for the better γ-ray or X-ray transmission. The Si(Li) detector is connected to the measurement cube via a cross, where the vacuum gauge and additional Pfeiffer HiPace 80 TMP (pumping speed of up to $67\,\mathrm{l\,s^{-1}}$ for N_2) are connected. Technical drawings of the vacuum chamber with dimensions are shown in Fig. 3.6.

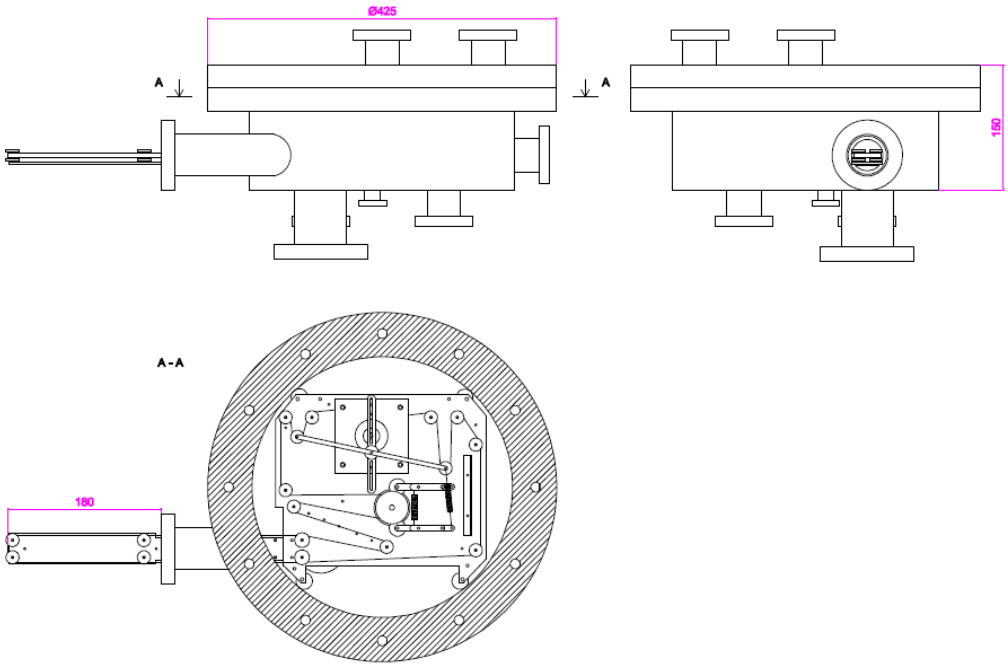

FIGURE 3.6: Technical drawings of the vacuum chamber of the TATRA system.

3.4 Detectors

Presently the TATRA spectrometer has capability to place four detectors around the measurement point of any type and one detector can be placed in the front of the sample inside the vacuum chamber. In the case of IS521 experiment, Ge detectors were used for γ-ray detection and one Si(Li) detector located inside the vacuum chamber was used for the measurement of electrons. Real photo of this system

from the second run of IS521 experiment is given in Fig. 3.7. Details about IS521 experiment and used detectors are in Tables 3.1 and Tab. 3.2.

FIGURE 3.7: Photo of TATRA spectrometer at ISOLDE LA1 beamline with all detectors mounted.

3.4.1 Detection of γ rays

As γ-ray detectors p-type Ortec GEM 70P4-95, n-type GMX 70P4-95 coaxial hyper-pure germanium (HPGe) detectors and Canberra Broad Energy Germanium (BEGe) detectors were used in IS521 experiment. This combination of the detectors is optimized for the best energy resolution for a wide energy range (from X-rays to several MeV γ rays).

HPGe detectors with relative efficiency of more than $70\,\%$ (given relatively to $3 \times 3\,\mathrm{inches}$ NaI(Tl) scintillator) were used for detection of γ rays. They were cooled

IS521 experiment - run 2014	
Dates	23-27 August
Isotopes measured	^{181}Hg, ^{183}Hg
Number of samples	3499, 1801
Conversion electron detector	-
γ-ray detectors	HPGe p-type Ortec GEM 70P4-95 HPGe p-type ISOLDE spare detector BEGe BE2020
γ-ray detection range	$40\,\mathrm{keV}$ to $980\,\mathrm{keV}$ for BEGe $40\,\mathrm{keV}$ to $2500\,\mathrm{keV}$ for HPGe

TABLE 3.1: Details of the first run IS521 experiment.

IS521 experiment - run 2016	
Dates	24-27 August
Isotopes measured	^{183}Hg
Number of samples	700
Conversion electron detector	Super Si(Li) 5 mm thick, 80 mm2
γ-ray detectors	HPGe p-type Ortec GEM 70P4-95 HPGe n-type Ortec GMX 70P4-95 HPGe n-type ISOLDE spare detector BEGe BE6530
γ-ray detection range	$0\,\mathrm{keV}$ to $950\,\mathrm{keV}$ for BEGe $0\,\mathrm{keV}$ to $2400\,\mathrm{keV}$ for HPGe

TABLE 3.2: Details of the second run IS521 experiment.

with an electric X-COOLER III system, which does not need the LN_2. FWHM guaranteed by manufacturer is $1.9\,\mathrm{keV}$ at the $1332\,\mathrm{keV}$ line of the ^{60}Co isotope for GEM and $2.3\,\mathrm{keV}$ for GMX.

BEGe detectors [106] can be used to detect γ rays in the energy range of $3\,\mathrm{keV}$ - $3\,\mathrm{MeV}$. They are commercially available and offer excellent energy resolution, nearly ideal Gaussian peak shape and low noise performance due to their unique electrode structure. BEGe detectors are used in a wide variety of commercial applications, including environmental sample counting, dosimetry and characterisation of nuclear waste, as well as in academic research(e.g. GERDA [107] project or IS521 experiment). Experiment IS521 is the first one (to my knowledge), which used BEGe detector in β-decay study. While these detectors can be used in wide energy range they are optimized for lower energy γ rays (less than $1\,\mathrm{MeV}$) and X-rays with the FWHM in the range from $0.65\,\mathrm{keV}$ to $0.75\,\mathrm{keV}$ at the energy of $122\,\mathrm{keV}$. During IS521 experiment, two different BEGe detectors were used. BE2020 is the smallest, while BE6530 is the largest BEGe detector available on the market and comparisons of their performance are given in Figures 3.8 – 3.10, where the same part of the ^{183}Hg decay γ-ray singles spectrum is shown.

Fig. 3.8 gives a comparison of performance of the BE6530 detector, which is the most efficient BEGe detector with standard coaxial p-type HPGe detector. It is evident that the resolution (FWHM) of the BEGe detector of $0.856\,\mathrm{keV}$ is much better than $1.172\,\mathrm{keV}$ in HPGe case. Compared with conventional LEPS detectors, excellent energy resolution feature is extended to higher energies.

Fig. 3.9 gives a comparison of performance of BE6530 and BE2020 detectors. Although the comparison is not correct, since more statistics was collected with BE2020, as a smaller detector has slightly better energy resolution (FWHM = $0.765\,\mathrm{keV}$). However, its efficiency is approximately factor of 5 lower than that for the largest detector.

The data analysis strongly benefits from employment of special amplifiers connected between detector preamplifier and DAQ. As it is documented in Fig. 3.10, which gives spectrum detected with the same BE6530 detector with different gains, the energy resolution (FWHM = $0.914\,\mathrm{keV}$) is improved with high gain (FWHM = $0.856\,\mathrm{keV}$). In addition to that, peak is divided into more channels of the spectrum, which allows more precise fitting. Therefore it is recommended to use the high gain.

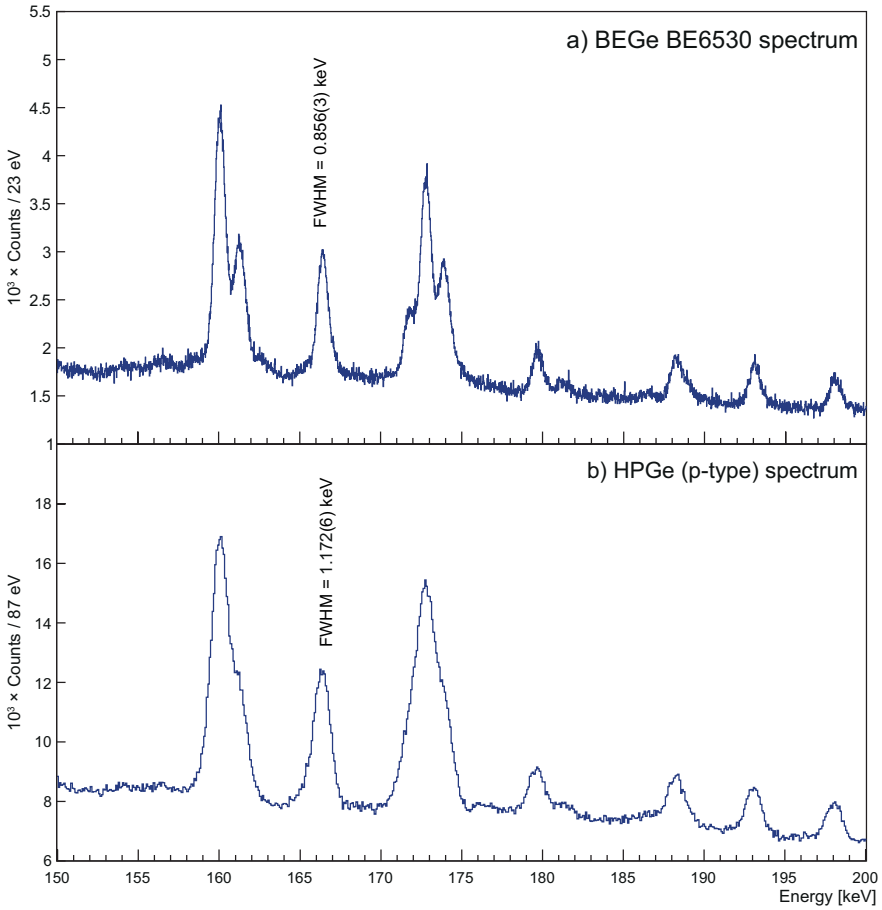

FIGURE 3.8: Part of the single γ-ray spectrum of the ^{183}Hg decay measured during the second run of IS521 experiment by BEGe detector with FWHM = $0.856\,\mathrm{keV}$ (a) and HPGe detector with FWHM = $1.172\,\mathrm{keV}$ (b).

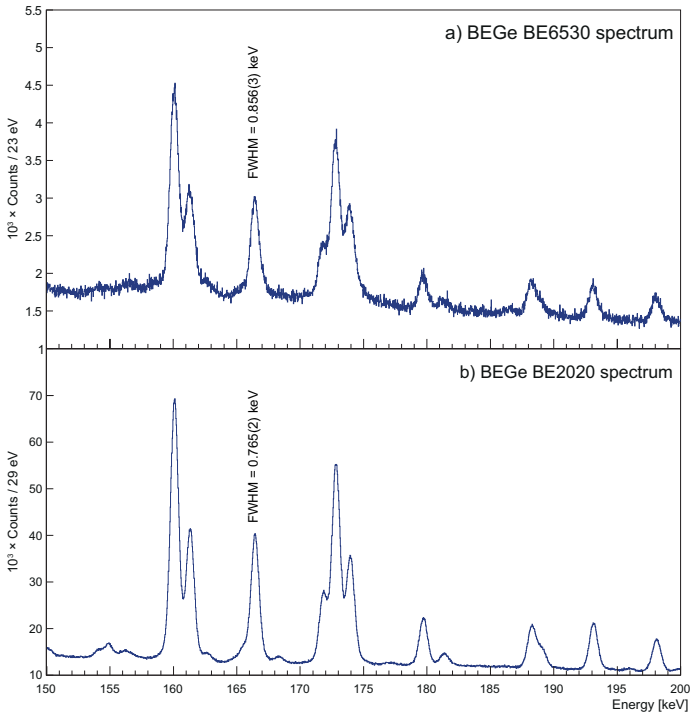

FIGURE 3.9: Part of the single γ-ray spectrum of the ^{183}Hg decay measured by BEGe BE6530 detector with FWHM = $0.856\,\mathrm{keV}$ in the second run (a) and BEGe BE2020 detector with FWHM = $0.765\,\mathrm{keV}$ in the first run of the IS521 experiment (b).

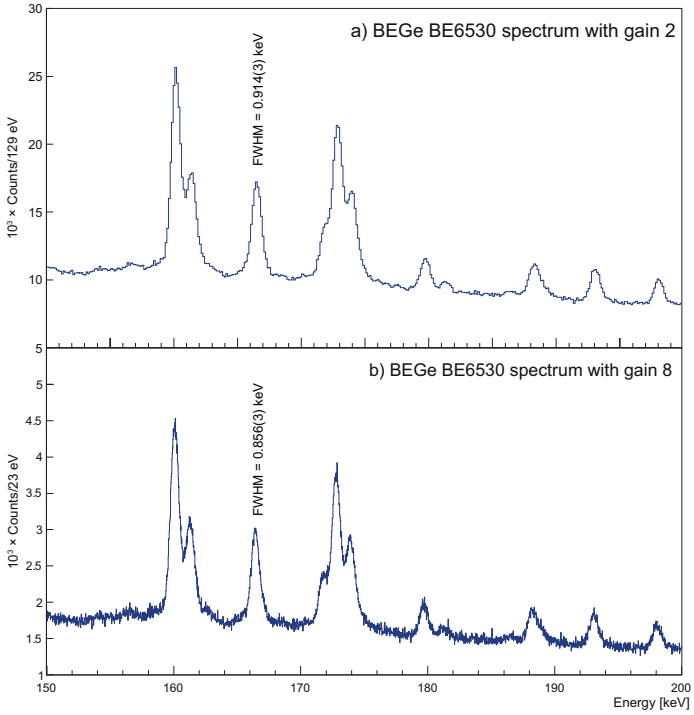

FIGURE 3.10: Part of the single γ-ray spectrum of the ^{183}Hg decay measured during the second run of IS521 experiment by BEGe detector with gain 2 and FWHM = $0.914\,\mathrm{keV}$ (a) in contrary to gain 8 with FWHM = $0.856\,\mathrm{keV}$ (b).

3.4.2 Detection of electrons

As the beta detector the windowless Canberra SSL80155 (Super Si(Li) type) detector, with a thickness of $5\,\mathrm{mm}$ and surface area of $80\,\mathrm{mm}^2$, is used. It is operated at liquid nitrogen temperature to obtain the best energy resolution of electrons. This detector has transistor-reset type of preamplifier (TRP) and many features, e.g., a movable cryostat, which gave us an opportunity to change the distance between the sample and the detector's crystal, and a gate valve, for a case of chamber venting or an option to heat the detector's crystal (deicing). Conversion electrons were detected with FWHM of $1.5\,\mathrm{keV}$ with this detector.

3.5 Electronics

All above mentioned parts of TATRA spectrometer are connected together and can cooperate due to various electronic devices. The stepper motor of the tape transportation system is controlled and powered by its drive, which is operated by PC via NI SCB-100 Board with a hundred I/O connections. The Kollmorgen stepper motor driver's parameters are set up with its software and during measurements it is operated by custom made software for data acquisition. Signals from detectors are modified by custom electronics. In the whole experiment is than only single industrial PC, which controls needed devices, stores the data and communicates with accelerator.

3.5.1 Custom electronics

IS521 experiment would not be successful without used custom electronics like custom signal converter for Si(Li) detector and GO-box. The GO-box is an array of linear amplifiers with the gain of 2, 4 or 8. Each channel has an option of the offset correction and SMA connectors for the input and the output. This amplifier array is constructed like stand-alone unit packeted in the box with its own power supply and it has been designed at the University of Liverpool. GO-box is connected between preamp and DAQ system.

Another piece of custom electronics used in TATRA system is the TRP to RC feedback (RCFB) signal converter. There is need of signal converting because the XIA Pixie-16 DGF accepts only unipolar signal with exponential decay to the baseline and amplitude up to $2.2\,\mathrm{V}$, which is common for the γ-ray detector's preamplifier with RCFB, see red line in Fig. 3.12. Our Si(Li) detector has the integrated TRP and cannot be replaced. This preamplifier has on its output capacitor, which is not grounded via resistor until it is not fully charged so when the charge is created in the detector's

crystal this is stored by this capacitor and we can see DC step on the output voltage, see blue line in Fig. 3.12. When the capacitor is fully charged the transistor logic is set up, the capacitor is discharged while the inhibit signal is produced by the preamplifier and the whole process is repeated. The final signal looks like stairs with rapid fall down while the capacitor is discharged. For that reason I have developed an electric circuit capable of the transform the stairs like signal to signal with the exponential decay to the baseline. The principal electric circuit scheme is shown in Fig. 3.11.

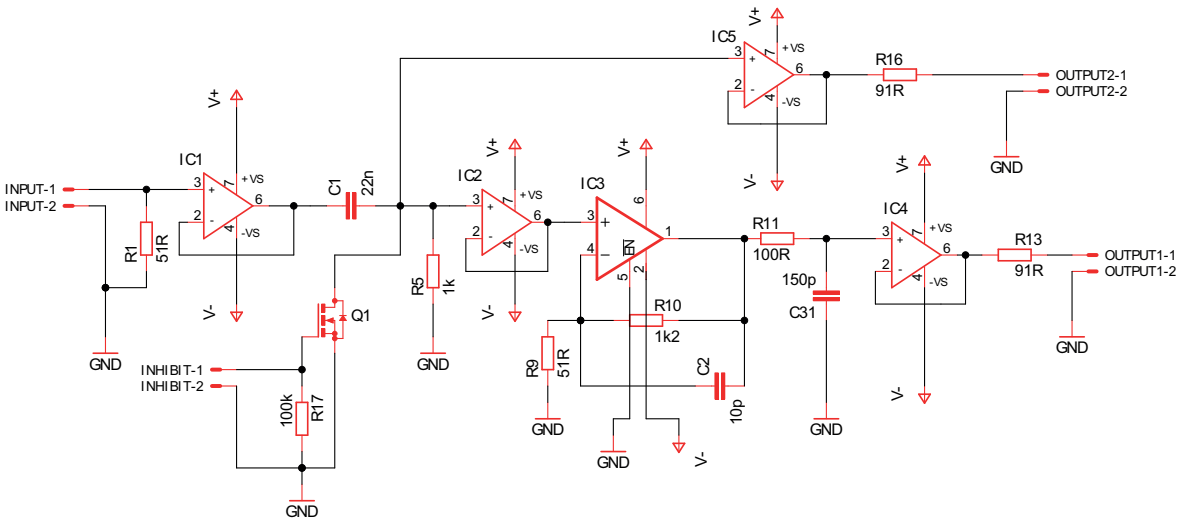

FIGURE 3.11: Principal scheme of the electric circuit developed to convert signal from transistor-reset type preamplifier to RC-feedback-like signal.

The basic concept of this converter is to derive the signal on its input while the capacitor C1 ($22\,\mathrm{nF}$) is charged and continuously discharged via the resistor R5 ($1\,\mathrm{k\Omega}$). The time decay constant is then

$$\tau = RC \cong R_5 C_1 = 22\,\mu\mathrm{s}. \tag{3.1}$$

Problem is with the TRP reset mode when the signal level drops suddenly from more then $3\,\mathrm{V}$ to less then $-1\,\mathrm{V}$ so derivative of this signal is negative with amplitude more than $4\,\mathrm{V}$ what is forbidden for Pixie-16. In this case, the fast transistor (MOS FET) Q1 with protecting diode takes place, which connects the capacitor C1 to the ground, when the inhibit signal appears ($+5\,\mathrm{V}$) and no signal is on the output of the converter. The converter circuit has two energy signal outputs: first amplified and second without amplification. Operational amplifiers IC1, IC2, IC4 and IC5 works in voltage follower mode, just reproduce signal on the input, for impedance matching and circuit separation. The AD811 from the Analog Devices Inc. are used, which are fast ($2500\,\mathrm{V\,\mu s^{-1}}$ slew rate), low noise ($1.9\,\mathrm{nV}/\sqrt{\mathrm{Hz}}$), low distortion,

broad bandwidth ($140\,\mathrm{MHz}$) operational amplifiers and are also used as line drivers. The Linear Technology LT6230-10 operational amplifier labelled as IC3 is used to amplification of the signal for one output. Its properties are broad gain bandwidth ($1450\,\mathrm{MHz}$), low noise ($1.1\,\mathrm{nV}/\sqrt{\mathrm{Hz}}$) and low offset. It was set to integral mode to reduce noise amplification by RC in its negative feedback and with tunable signal gain from approximately 23.5 to 43. The converter circuit is designed as two sided printed circuit board (PCB) and has some additional parts and features, which can not be seen in Fig. 3.11 like power supplies, power line filters, inhibit and veto signal generation. The simulation of the circuit response on the input signal is shown in Fig. 3.12. The converter circuit PCB was placed inside the blank NIM module and it uses the power supply of the NIM crate. Inputs and outputs are BNC connectors located on the front panel of the NIM module together with the potentiometer for gain control, see Fig. 3.14 and Fig. 3.15.

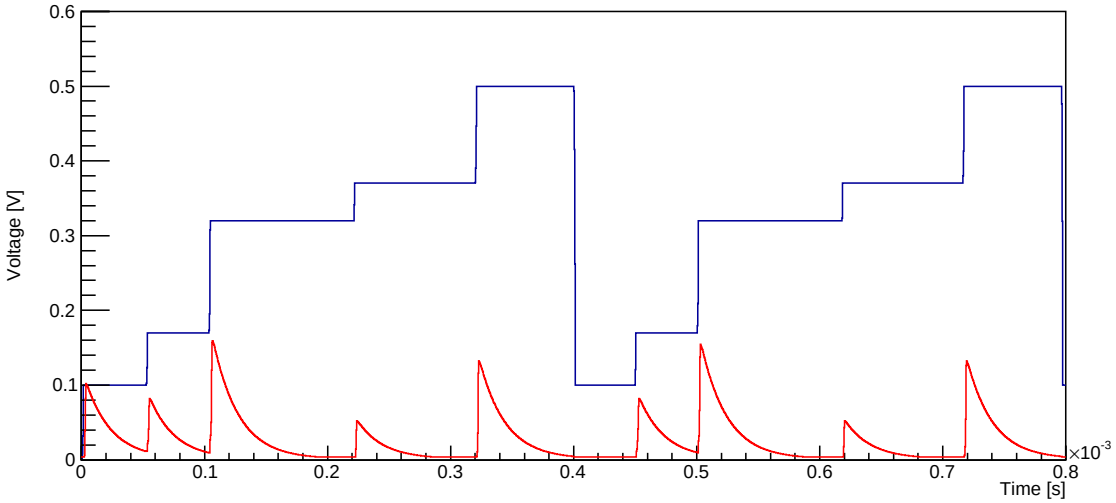

FIGURE 3.12: A simulation of the custom signal converter circuit response (red line) to a stairs like input signal (blue line).

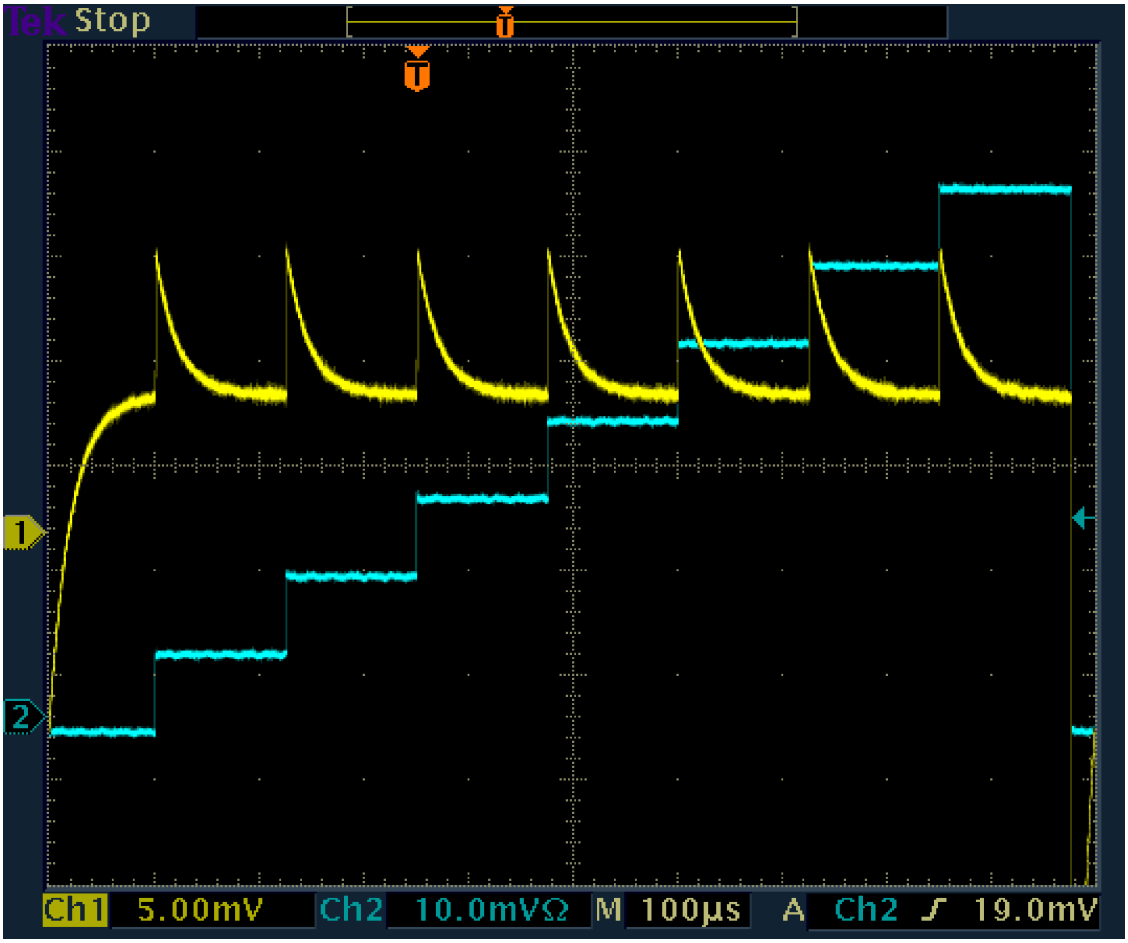

FIGURE 3.13: A screen-shot from an oscilloscope. The output signal of the custom signal converter circuit is provided to channel1 (yellow line) and a stairs like signal from signal generator used as input signal to the converter is also present as channel2 (blue line).

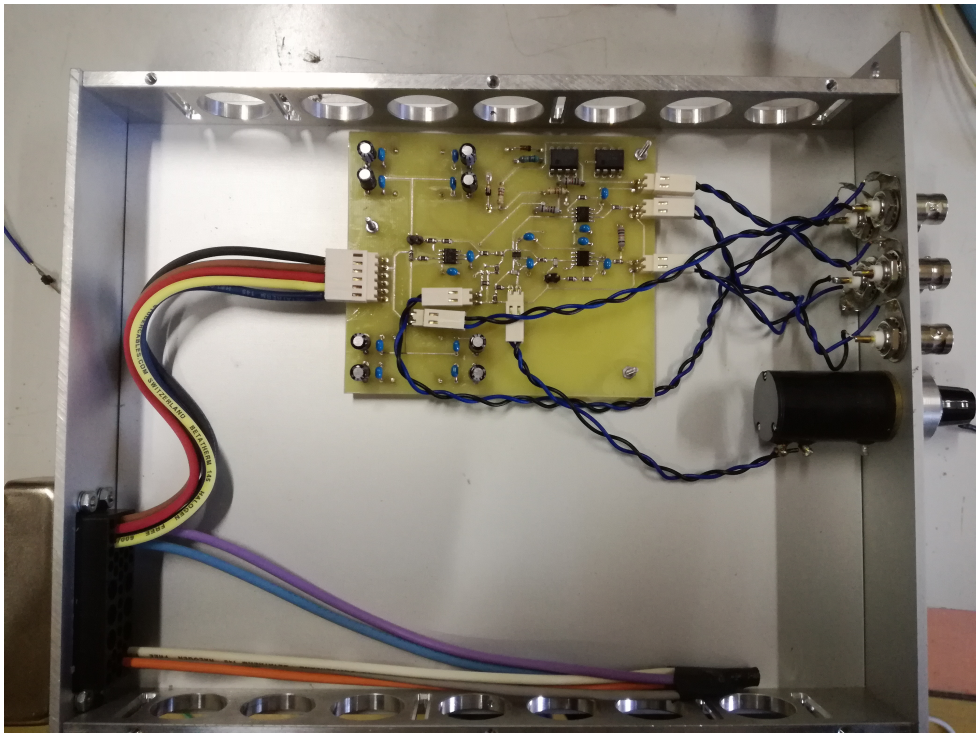

FIGURE 3.14: Real photo of the custom signal converter printed circuit board connected inside the NIM module.

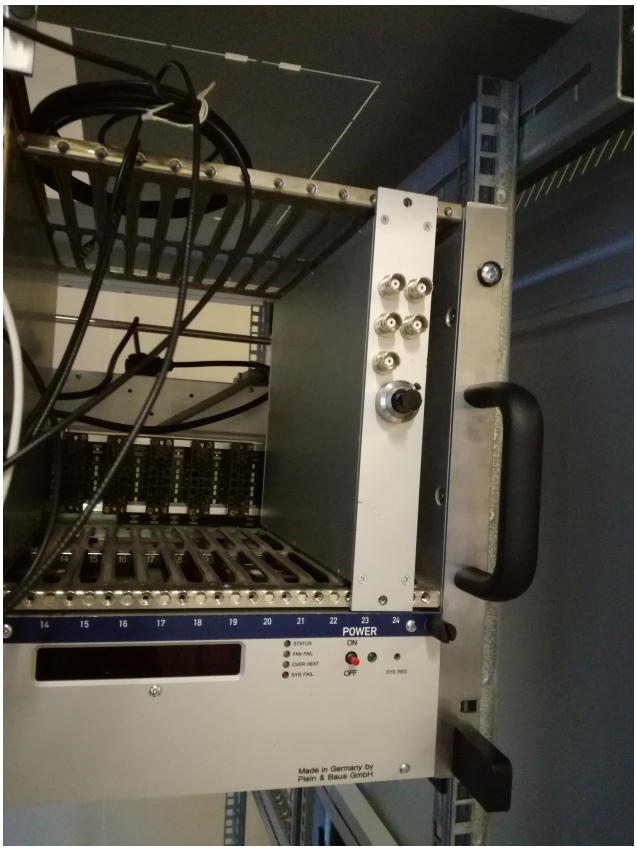

FIGURE 3.15: Photo of the custom signal converter as the NIM module in NIM crate.

3.6 Data acquisition system and data sorting

The data acquisition system (DAQ) is fully-digital, based on the PXI standard and its main component is a Pixie-16 DGF [108] module, which is responsible for digitizing signals from the detectors. The Pixie-16 contains 12-bit ADC with sampling frequency of 250 mega samples per second (MSPS) and a digital oscilloscope Tektronix 544 TDS with resolution of 10 mega samples per second. It stores data in a form of events with time stamps via the computer to a RAID disk array.

The DAQ was operated in a list mode during the experiment IS521. It means that every detection of radiation by any of the detectors was considered as an valid event and after its digitalisation it was stored to binary file with specific structure. Every stored event contains obligatory information (header) about for example the time of arrival, the raw energy, the module channel number (where the detector is connected) or information about being part of pile-up and there can be stored also some optional information like traces, QDC sums, baselines, etc. The basic data structure (header of an event) is shown in the Tab. 3.3. Traces of signals were not recorded due to insufficient transmission of the PXI bus and high event rate. This trigger-less mode of the data acquisition offers the most options for the future off-line analysis using time gates and variety of conditions due to 4 ns precision of time stamps, which is appropriate according to employed detectors.

No.	Data length in bits and meaning					
#0	1	14	5	4	4	4
	Finish code	Event length	Header length	Crate ID	Slot ID	Channel
#1	32					
	Event time low					
#2	1	1	14		16	
	CFD forced	CFD trigg.	CFD fractional time		Event time high	
#4	1		15		16	
	Trace out of range		Trace length		Event raw energy	

TABLE 3.3: Data structure of each event acquired by Pixie-16 modules during the list mode collection. Table was adopted from website of XIA LLC.

Data from each particular sample was stored in a separate binary file. For real analysis, the CERN ROOT framework package [109] was used and this binary files were sorted and converted to TTree objects. TTree objects contains events in a form of entries while each entry has assigned the detector, the raw energy (in ADC channels) and the time stamp (in 4 ns time ticks) of the event as variables. These TTrees can be merged into TChain object of the ROOT package, so the whole experiment can be analysed within one object and all the data can be accessed from one place to work with it.

Chapter 4

Data analysis

The construction of the level scheme is based on coincidence relationships and the Rydberg-Ritz combination principle [6], which can be used due to very good resolution and peak shapes of the BEGe detector (an energy of γ lines can be determined with high precision). All previous steps were essential for construction of the level scheme in our analysis [110]. The procedure was

1. the determination of γ ray energies as precisely as possible using the γ-ray singles spectrum detected with the BEGe detector,
2. the separation of γ rays due to the decay of interest from its daughter decays and/or room background and
3. the analysis of γ-γ coincidence relationships.

In the case that several combinations of γ rays led to the same level, the excitation energies of these levels were determined using the weighted average.

4.1 Energy calibration

Energy calibration is standard procedure at least for HPGe detectors. However, performance of BEGe detectors was essential for IS521 experiment, and therefore the most precise calibration was required. Only BEGe detectors are mentioned in this Section so-far.

Every event has the raw energy, the integer number, within the range of from 0 to 32 768 based on the Pixie-16 module's ADC determination of the input pulse high. For this purpose well known calibration sources of radiation are required. When data from calibration source are taken, peaks with known energy can be fitted with Gaussian distribution (if the number of counts in the peak is high enough) to obtain the channel of their centroid. The calibration curve can be obtained from fitting the dependence between centroid channels of peaks and their energies. A quadratic fit of calibration data was used. The calibration curve of the BEGe detector from the IS521 experiment is shown in the Fig. 4.1.

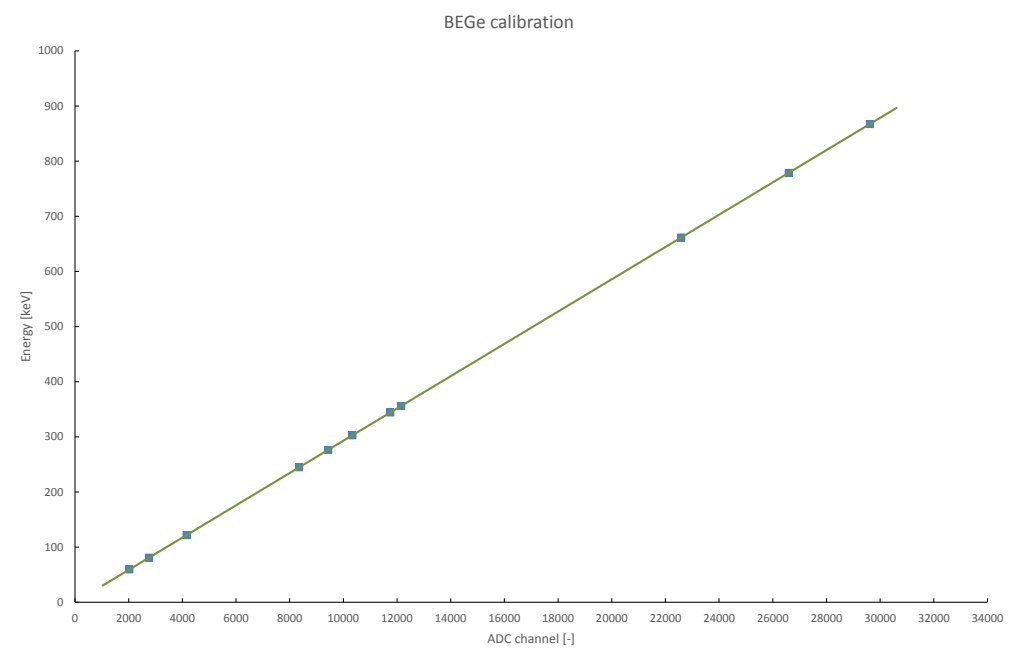

FIGURE 4.1: Chart of the relationship between energy of emitted particles and according ADC channels with polynomial trend-line (green) of equation 4.1. Used γ-ray energies (blue) are in Tab. 4.1.

The equation 4.1 is quadratic function, which was used for the calibration of this BEGe detector.

$$\begin{aligned} E &= AX^2 + BX + C \\ A &= 2.593 \times 10^{-10} \pm 1.963 \times 10^{-11} keV \\ B &= 2.928 \times 10^{-2} \pm 4.816 \times 10^{-7} keV \\ C &= 9.999 \times 10^{-2} \pm 2.074 \times 10^{-3} keV \end{aligned} \tag{4.1}$$

where E is the energy in keV of X, which is the channel number of the ADC and A,B and C are coefficients determined by fitting the calibration data.

It is essential to take calibration data when whole system is ready for experiment and no parameters is going to change. In our case we take calibration data before and after the experiment by using ^{241}Am, ^{152}Eu, ^{137}Cs, ^{133}Ba and ^{60}Co calibration standards. Only peaks from the ^{152}Eu isotopic radiation source with the highest known precision was considered to enhance the precision of the calibration. The result of the final BEGe calibration as comparison of tabulated and calibrated energies is shown in the Tab. 4.1, which can be found also in [110].

Isotope	Energy [keV]	Tabulated Energy [keV]	Energy difference [eV]
^{241}Am	59.5410(26)	59.5409(1)	-0.1
^{133}Ba	81.0010(27)	80.9979(11)	-3.1
^{152}Eu	121.7797(30)	121.7817(3)	2
^{152}Eu	244.6924(56)	244.6974(8)	5
^{133}Ba	276.3944(65)	276.3989(12)	4.5
^{133}Ba	302.8553(62)	302.8508(5)	-4.5
^{152}Eu	344.2782(68)	344.2785(12)	0.3
^{133}Ba	356.0155(70)	356.0129(7)	-2.6
^{137}Cs	661.655(15)	661.657(3)	2
^{152}Eu	778.9066(198)	778.9045(24)	-2.1
^{152}Eu	867.387(26)	867.380(3)	-7

TABLE 4.1: Comparison of γ-ray energies of ^{241}Am, ^{152}Eu, ^{137}Cs and ^{133}Ba calibration standards deduced from present data using polynomial calibration with tabulated values from the Evaluated Nuclear Structure Data File (ENSDF) [111–114]. This table in extended form can be found also in [110].

The calibration of the Si(Li) detector is not an easy task, since proper open calibration sources with the electron emission were not available at ISOLDE. In addition, low energy γ rays and X-rays are a little bit shifted in energy because of the electron-environment interaction and the dead layer of the detector and due to $-500\,\mathrm{V}$ bias of the Si(Li) detector. However, γ-electron coincidences can be used when the internal conversion is present and electrons are shifted from corresponding γ rays roughly by well known electron binding energy of studied element.

4.2 Singles spectra analyses

When all detectors were calibrated, the next step was the singles spectrum creation. The singles spectrum is produced from all events within one detector regardless of the time window. Within this spectrum, data from the whole decay chain and the room background were present. In order to separate the decay of interest from the daughters decay and the room background a special procedure [110] was employed. This procedure is based on the time-stamped data and longer measurements than the half-life of the studied isotope. Two singles γ-ray spectra were created using two different time windows. The first window was significantly shorter than time of one sample measurement, the time when the decay of interest dominates (e.g. 0-$5\,\mathrm{s}$ in case of ^{183}Hg decay while its half-life is $9.4(7)\,\mathrm{s}$ [115]), and the second window was wide as the time of the sample measurement. The Compton continuum in both spectra was subtracted using the TSpectrum class [116] of the ROOT package and were normalised using known γ rays from the decay of interest, subsequently subtracted from each other. The result of this procedure are two spectra, which one

contains almost only γ rays due to the decay of interest and the second one, where dominates contamination γ rays. Examples of the original, the clean mother decay and the contamination spectrum from the ^{181}Hg data are shown in Fig. 4.2.

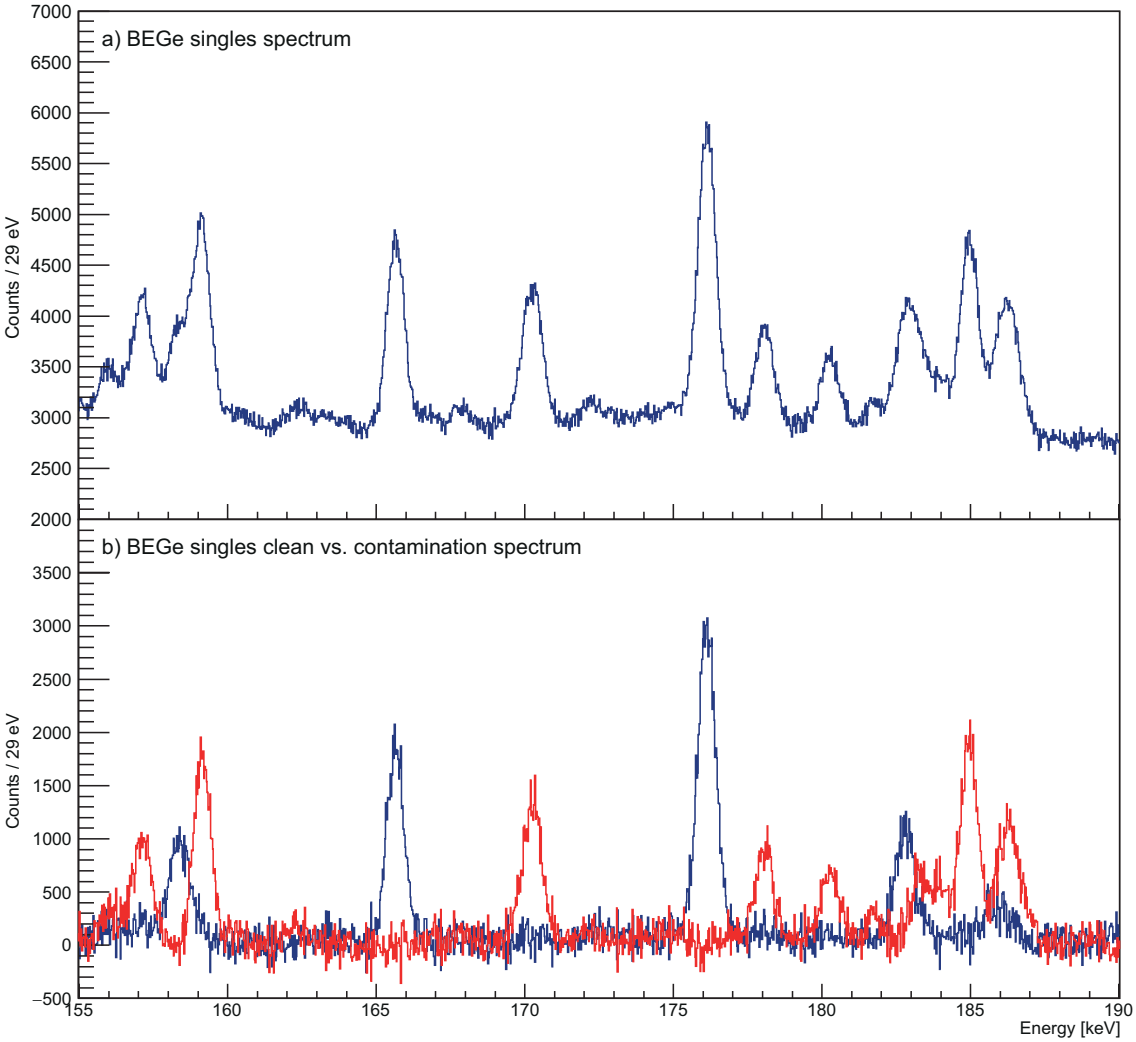

FIGURE 4.2: a) Part of the γ-ray singles spectrum detected with the BEGe detector. b) The part of the singles spectra assigned to ^{181}Hg decay (blue line) and to its daughter decay (red line). The spectra were distinguished by the method described in text.

Once the clean mother decay spectrum is obtained, peaks assigned to it can be recognised and fitted in the original singles spectrum. As the fitting function, the Gaussian distribution with a linear background can be used in the most cases. The HDTV - Nuclear Spectrum Analysis Tool was used for the peak fitting and peak parameters with errors were obtained.

The significant role in the precise determination of γ-ray energies played the BEGe detector, which has excellent resolution, smooth background and nearly ideal Gaussian shaped peaks for energies up to $900\,\mathrm{keV}$. This make the fitting process very

precise, see Fig. 4.3 and Fig. 4.4. The precision of the fit depends on statistics, peak shapes and the background and can be evaluated by the χ^2 test. The ideal fit should have reduced χ^2 equals to 1. Results of the analyses are given in Chapter 5.

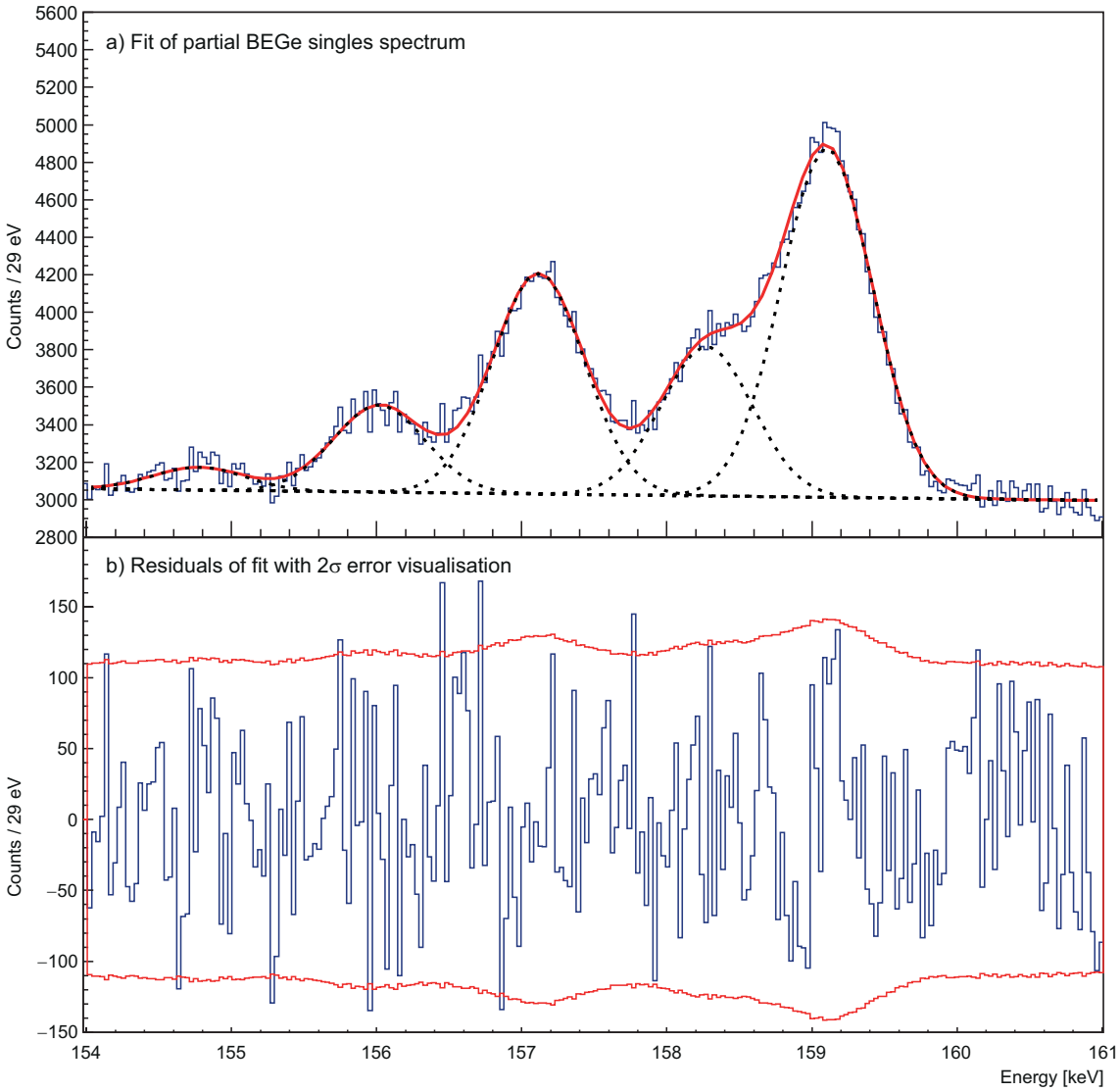

FIGURE 4.3: a) Part of the γ-ray singles spectrum detected with the BEGe detector (blue line), a fit of it (red line) with multiple Gaussian peaks (black dashed line) and with linear background. The reduced χ^2 of the fit is 1.15. b) The fit residuals (blue line) with an indicated 2σ confidence interval (red lines).

4.3 Coincidence analyses

In order to investigate properties and patterns of the emitted radiation of the certain decay the coincidence analysis take its place. It can reveal the relationship

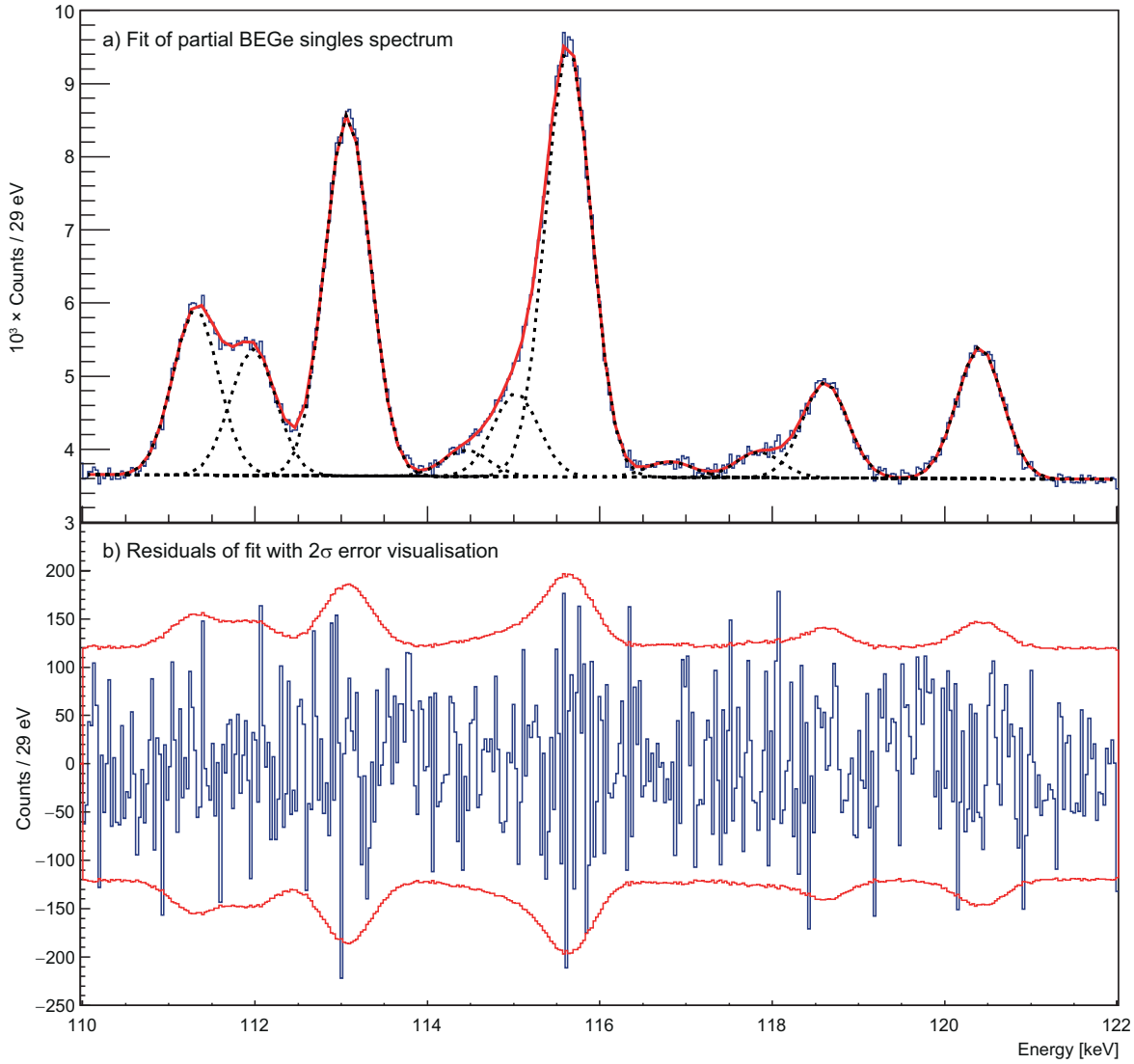

FIGURE 4.4: a) Part of the γ-ray singles spectrum detected with the BEGe detector (blue line), a fit of it (red line) with multiple Gaussian peaks (black dashed line) and with linear background. The reduced χ^2 of the fit is 1.03. b) The fit residuals (blue line) with an indicated 2σ confidence interval (red lines).

between various γ rays in γ cascade or γ rays and conversion electrons. The coincidence analysis is based on time and energy gates (intervals) applied on time sorted events from various detectors.

The first step was the determination of the time gate during which the prompt coincidence is present, for each couple of used detectors. The time difference between subsequent events versus number of events was plotted for every couple of detectors twice, due to the time shift of incoming signals caused by the different cable length of detectors and electronics. During the time outside the prompt coincidence gate the random coincidences are present and due to its random character, they can be used

for background subtraction from prompt coincidences when intervals of prompt and random coincidences are the same. The example of prompt and random coincidence gates from the ^{181}Hg decay analysis are in Fig. 4.5.

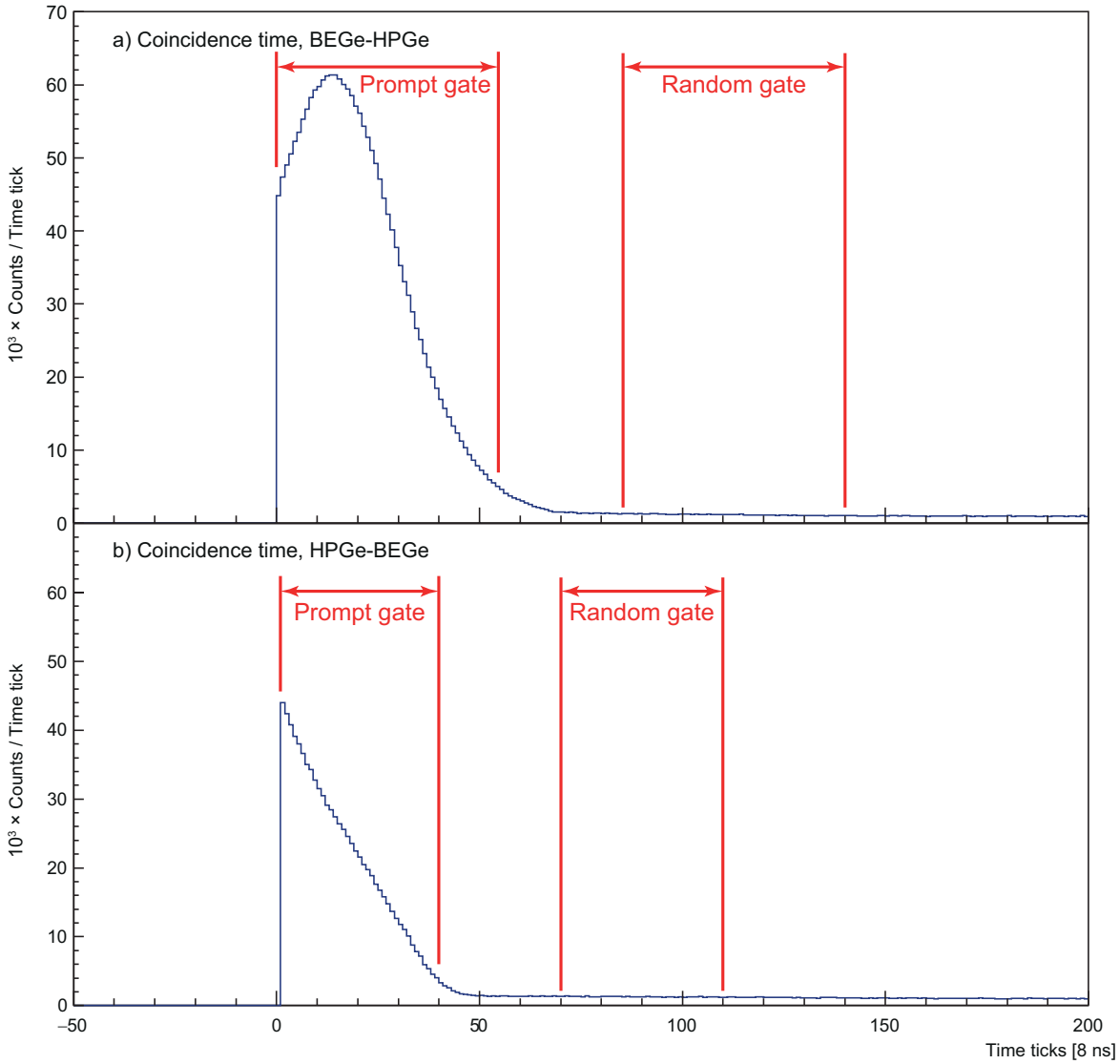

FIGURE 4.5: Histograms of time differences between two subsequent events detected by two detectors (HPGe coaxial and BEGe detectors). Prompt and random coincidence gates (time intervals) are illustrated by red arrows. a) The situation when event from BEGe came first. b) The situation when event from HPGe came first.

The next step was the creation of matrices, 2D spectra, which have an energy measured by one detector on X-axis and an energy measured by another detector on Y-axis. This means that one point in a matrix consists of two events from two detectors and the time difference between them have to be within the prompt coincidence gate. The most useful matrices in our analysis were the symmetric γ-γ matrix made of events from all HPGe detectors regardless of which come first, the asymmetric γ-γ matrix made of events from BEGe and HPGe detectors and the γ-electron matrix,

when the Si(Li) detector was employed. In the process of sorting data to create coincidence matrices, both prompt and random coincidence gates were considered and the random coincidence background was subtracted.

To obtain coincident γ rays from these matrices, 1D spectra were projected within the region of certain peak area on X-axis or Y-axis used as an energy gate. However, this 1D spectrum contains a lot of background mainly consists of Compton scattered events from higher energy γ rays. Assuming that this Compton scattered background is more or less homogeneous within a small region, we putted another gate right next to our peak of interest where it seems no other peak was present and we subtracted this spectrum from the first one. Clear coincident spectra gated on peaks identified as belonging to the decay of interest were obtained.

Chapter 5

Experimental results and discussion

5.1 ^{183}Hg decay

The results in this section are published in [7, 110]. The half-life of ^{183}Hg is $9.4(7)\,\mathrm{s}$ [115] and the β-decay energy is $6385(12)\,\mathrm{keV}$ [117]. Total absorption experiment shown that a large concentration of β-decay strength to states in ^{183}Au in the excitation energy range from $1600\,\mathrm{keV}$ to $1900\,\mathrm{keV}$ [118]. Analysis of the IS521 data, presented here, revealed that, a single state at $1682.30\,\mathrm{keV}$ excitation energy appears to be very strongly fed by β^+/EC decay of the ^{183}Hg. This suggests its spin and parity of $1/2^-$ or $3/2^-$, since the ground state of the ^{183}Hg is $1/2^-$ [119] and for

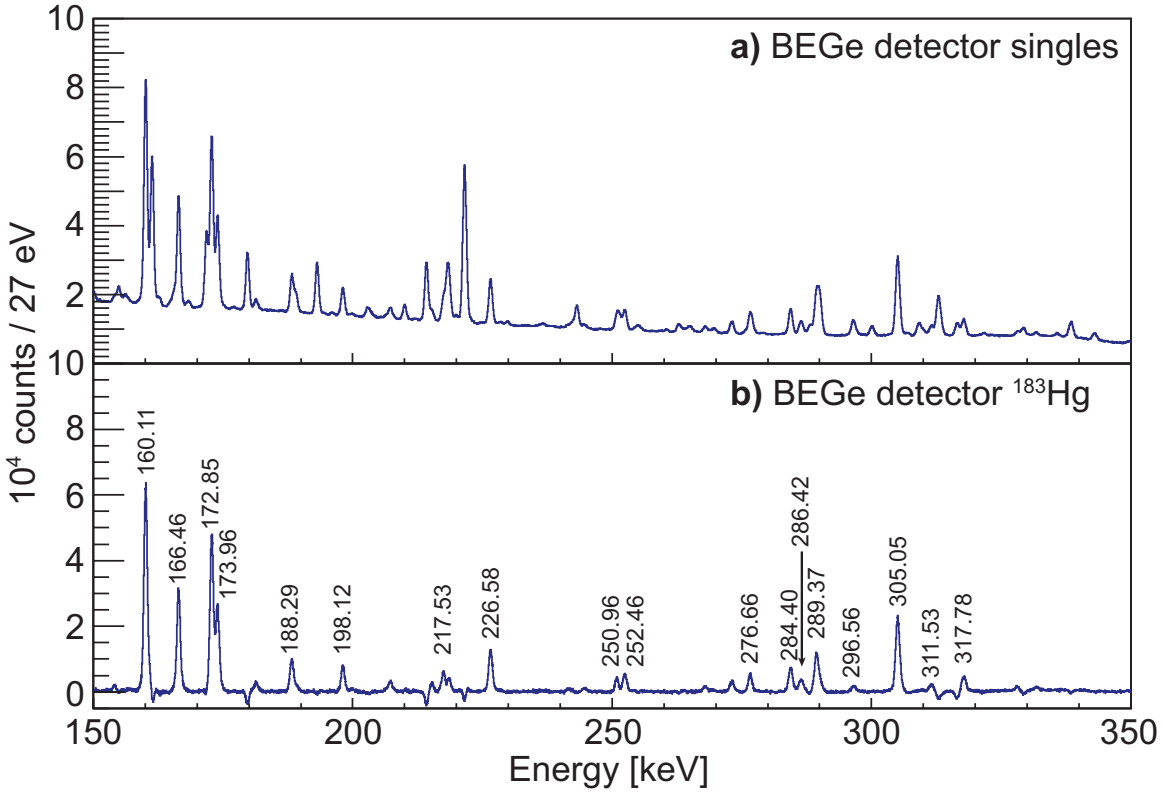

FIGURE 5.1: Singles γ-ray spectra measured with BEGe detector. (a) is total singles spectrum and (b) is singles spectrum assigned to the ^{183}Hg decay. Figure is published in [7].

^{183}Au ground state it is $5/2^-$ [120]. This state appeared to be critical to elucidate the structure of ^{183}Au isotope, see discussion later.

The focus of this study is to extend systematics of the energies of the lowest-lying $1h_{9/2}$ and $2f_{7/2}$ intruder states in ^{183}Au relative to the non-intruder $2d_{3/2} \oplus 3s_{1/2}$ states. This was carried out in systematic studies in the heavier odd-mass Au isotopes, see Section 5.3. Excited states at very low excitation energy ($< 50\,\mathrm{keV}$) are common in odd-mass Au isotopes in this mass region, which make a level scheme construction more difficult. For identification of these states in ^{183}Au, many deexcitation paths of the $1682.30\,\mathrm{keV}$ state were used with combination of high precision γ-ray spectroscopy by employing BEGe detector at high gain.

The method described in Chapter 4 was used to both conversion-electron and γ-ray data and all transitions assigned to the decay of ^{183}Hg, with their energies, intensities, and some multipolarities are given in Tab. 5.1. A comparison of total singles (a) and deconvoluted ^{183}Hg decay singles spectra (b) measured with BEGe detector is in Fig. 5.1, and measured with Si(Li) detector is in Fig. 5.2. A comparison of Si(Li) singles (a) and BEGe singles (b) spectra is given in Fig. 5.3, note that spectrum of conversion electrons is shifted by binding energy of K electron in Au (80.725 keV) to show γ-ray positions according to their K-electron peaks.

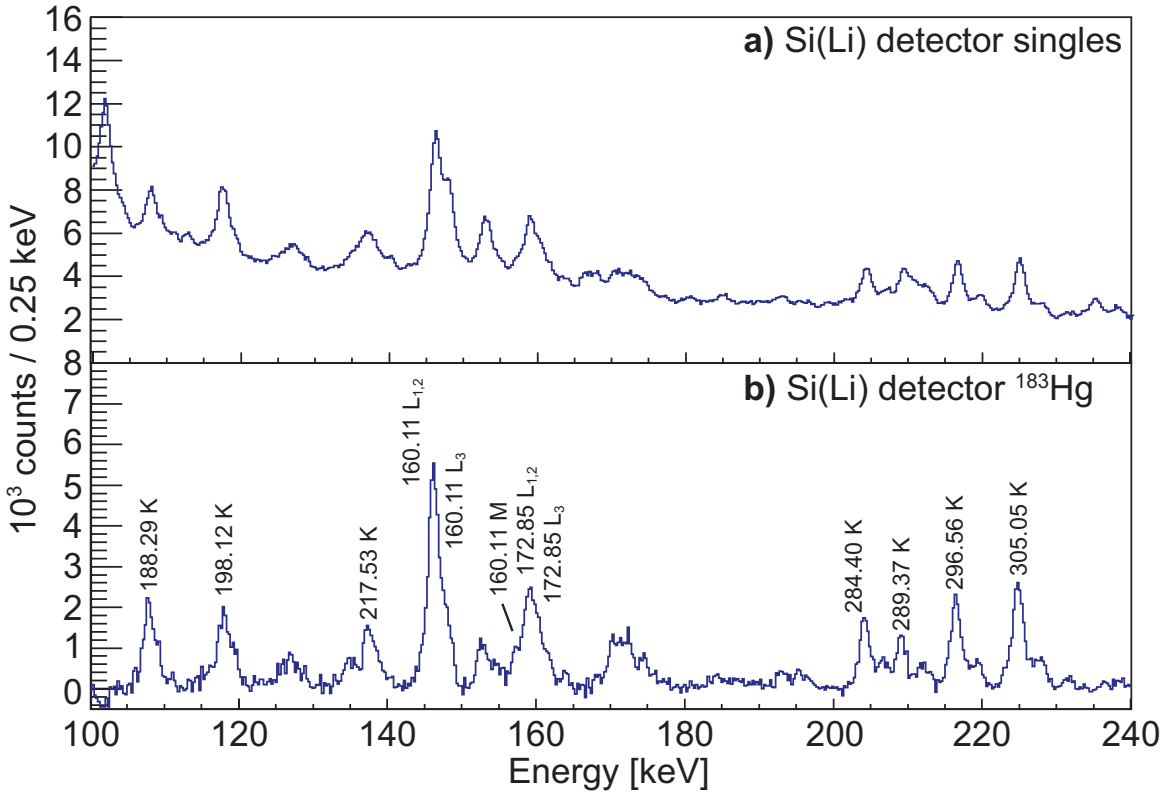

FIGURE 5.2: Electron singles spectra detected with the Si(Li) detector. (a) is total singles spectrum and (b) is single spectrum assigned to the ^{183}Hg decay. Figure is published in [7].

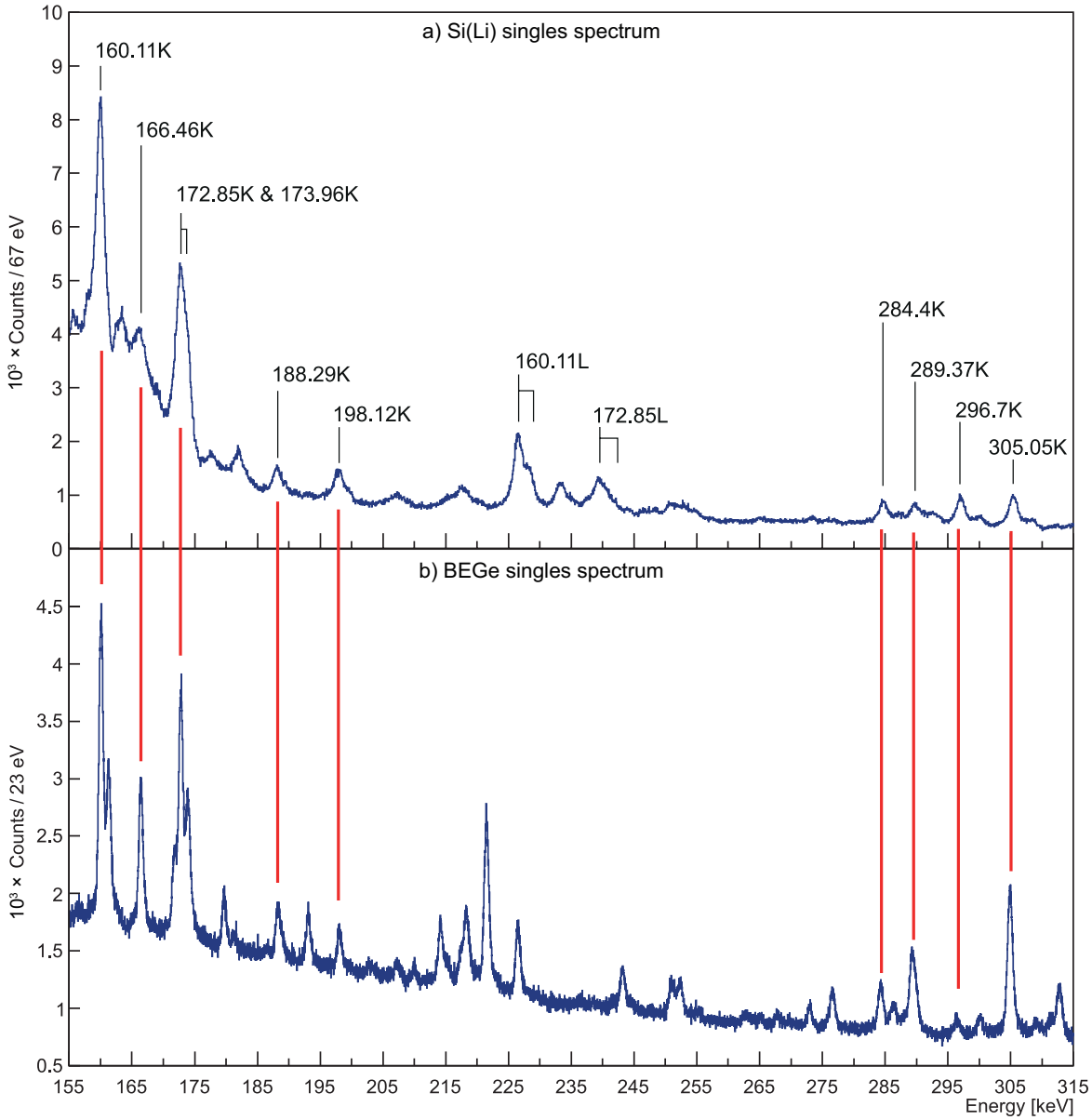

FIGURE 5.3: (a)Electron spectrum from the ^{183}Hg decay measured by Si(Li) detector and (b) γ-ray spectrum measured with BEGe detector. Spectrum of conversion electrons is shifted by binding energy of K electron in Au (80.725 keV) to show γ-ray positions according to their K-electron peaks (red lines).

Multipolarities of transitions assigned to the decay of ^{183}Au were determined by comparison of experimental values with BrIcc [32] calculated values of internal conversion coefficients. Internal conversion coefficients, K/L shell ratios, multipolarities and BrIcc calculated values are given in Tab. 5.2. Due to limited statistics collected for conversion electrons only few internal conversion coefficients were determined.

The level schemes of ^{183}Au were constructed on the basis of γ-γ-ray coincidences in conjunction with the Rydberg–Ritz combination principle. Coincidences of γ rays with conversion electrons were investigated separately. However, only a few

E_γ [keV]	I_γ	Multipolarity	E_γ [keV]	I_γ	Multipolarity
60.37(1)	440(80)	$E1$	490.45(2)	5(1)	
90.84(3)	14(4)		516.11(1)	32(3)	
91.25(6)	3(1)		583.10(2)	12(2)	
160.11(1)[1]	100(10)	$M1$ (+$E2$)	607(1)	11(3)	
161(1)	13(3)		638.33(7)	4(2)	
166.46(1)	50(5)	$M1$ + 40(10)% $E2$	645.21(2)	19(2)	
172.85(1)	82(8)	$M1$	663.29(3)	5(1)	
173.96(1)	46(5)	$M1$	688.52(7)	4(2)	
181.44(2)	6(1)		704.33(2)	13(3)	
188.29(1)	19(2)	$M1$ (+$E2$)	730.93(2)	7(1)	
198.12(1)	19(2)	$M1$	767.09(5)	20(2)	
217.53(1)	14(2)	$M1$ (+$E2$)	779.81(3)	12(2)	
218.30(1)	11(2)		798.52(2)	20(2)	
226.58(1)	29(6)		805.34(3)	16(2)	
250.96(2)	11(2)		811.31(7)	6(2)	
252.46(1)	16(2)		864.21(3)	13(1)	
276.66(2)	20(2)		871.05(3)	18(2)	
284.40(2)	11(2)	$E0$ + $M1$ + ...	902.42(8)	17(2)	
286.42(1)	13(2)		1242(1)	7(2)	
289.37(2)	37(4)	$M1$ + $E2$	1297(1)	12(1)	
296.54(2)	6(1)	$E0$ + $M1$ + ...	1364(1)	10(1)	
305.05(1)	81(8)	$M1$	1393(1)	20(2)	
311.53(2)	10(2)		1428(1)	83(8)	
317.78(2)	17(2)		1437(1)	16(2)	
462.04(2)	17(2)		1509(1)	32(3)	

[1] Intensities are relative to this line.

TABLE 5.1: Energies, intensities and multipolarities of γ rays assigned to the ^{183}Au [7]. The γ-ray intensities are given relative to the $160.11\,\mathrm{keV}$ line. Note that γ rays above $1\,\mathrm{MeV}$ were detected with coaxial detectors only and their energies could not be determined precisely due to high density of lines and lower energy gain, therefore they are given only as integer values. Also note that the 161 and $607\,\mathrm{keV}$ transitions were either dominated by strong lines arising from daughter activities or are part of unresolved doublets in the BEGe singles spectrum and therefore could not be determined precisely. However, their placement in the level scheme is evident from the γ-γ coincidence analysis.

coincidence gates of conversion electrons with sufficient statistical quality could be produced due to limited running time. Examples of γ-ray spectra, relevant for the level scheme construction, detected in a coincidence with other γ rays are given in Figures 5.7 - 5.13. The partial level scheme of low-lying negative-parity states associated with $1h_{9/2}$ and $2f_{7/2}$ intruder configurations that are fed by deexcitation of the $1682.30\,\mathrm{keV}$ level is given in Fig. 5.4. The partial level scheme of low-lying positive-parity states associated with the $2d_{3/2} \oplus 3s_{1/2}$ proton–hole configurations, which is also fed by deexcitation of the $1682.30\,\mathrm{keV}$ level is given in Fig. 5.5.

The $1682.30\,\mathrm{keV}$ state can be used to determine the energy difference between

E_γ [keV]	Experimental value	BrIcc (M1)	BrIcc (E2)	Multipolarity
60.37	α_L =0.22(4)	4.355	37.68	$E1$
	α_M =0.04(2)	1.011	9.782	
160.11	α_K/α_L =4.7(18)	5.99	0.72	$M1$ (+ $E2$)
166.46	α_K/α_L =3.4(5)	5.994	0.782	$M1$ + 40(10)% $E2$
	α_L =0.24(5)	0.233	0.338	
172.85	α_K =1.25(28)	1.257	0.242	$M1$
173.96	α_K =1.25(28)	1.234	0.238	$M1$
188.29	α_K =0.87(20)	0.989	0.197	$M1$ (+ $E2$)
198.12	α_K =0.88(20)	0.858	0.174	$M1$
217.53	α_K =0.54(13)	0.661	0.138	$M1$ (+ $E2$)
284.40	α_K =1.21(33)	0.316	0.071	$E0$ + $M1$ + ...
289.37	α_K =0.25(6)	0.302	0.068	$M1$ + $E2$
296.54	α_K =2.84(74)	0.282	0.064	$E0$ + $M1$ + ...
305.05	α_K =0.26(6)	0.261	0.060	$M1$
	α_L =0.04(1)	0.043	0.029	

TABLE 5.2: Experimental values and BrIcc calculation [32] values of internal conversion coefficients and multipolarities of transitions determined from present data [7].

intruder and "normal" configurations. Its excitation energy is determined using 871.05 - $798.52\,\mathrm{keV}$ and 864.21 - $805.34\,\mathrm{keV}$ cascades, which are highlighted in green and red in Fig. 5.4.

The excitation energy of the first excited state was determined using energy differences between transitions feeding the ground state and the first excited state, arising from deexcitation of the 172.85, 289.37, 317.78, and $779.80\,\mathrm{keV}$ states. The cascade of 60.37 - 173.96 - 730.93 - $704.33\,\mathrm{keV}$ feeding the first-excited state gives its initial excitation state $1682.30\,\mathrm{keV}$ (within experimental uncertainties). This cascade is highlighted by red lines in Fig. 5.5 and all these transitions except $60.37\,\mathrm{keV}$ are found in coincidence with each other, while $60.37\,\mathrm{keV}$ is clearly assigned to the ^{183}Hg decay. The singles spectrum detected with the Si(Li) detector was used to determine the multipolarity of the $60.37\,\mathrm{keV}$ transition. The M-shell internal conversion coefficient, α_M = 0.04 was deduced, which is in agreement with the BrIcc calculated value of 0.05 for $E1$ multipolarity, since see Ta. 5.2. Values for other multipolarities are greater than 1. The previous study [8] assigned the $60.37\,\mathrm{keV}$ transition as an "abnormal" $E1$ transition. Abnormality of the transition was concluded from anomalously high α_{L2} value of 0.79, while the BrIcc code gives 0.0629. The Si(Li) detector cannot resolve subshell components of the L conversion electrons multiplet. However, if one of the subshell components was anomalously large, the α_L would not agree with the BrIcc calculation, which is not the case for the present data. Therefore, we assign the $60.37\,\mathrm{keV}$ as an $E1$ transition with no abnormality and it was assigned as parity-changing $1/2^+ \rightarrow 3/2^-$ transition. The absence of a transition to the $5/2^-$ ground state supports the spin assignment of $1/2^+$. An analogous $E1$ transition is known in

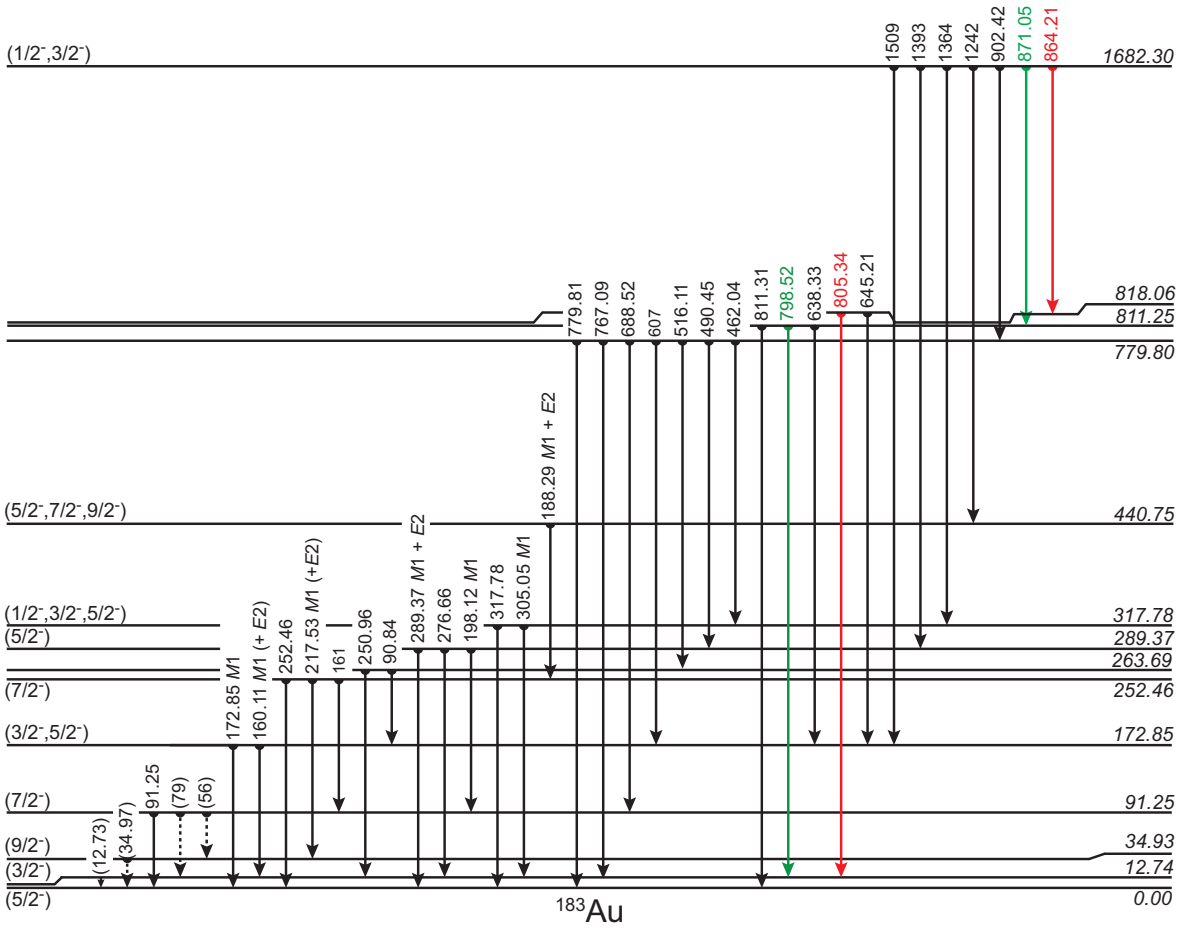

FIGURE 5.4: Partial level scheme of low-lying, negative-parity states associated with the $1h_{9/2}$ and $2f_{7/2}$ intruder configurations in the ^{183}Au isotope deduced from the present work [7]. Transition energies were determined using the γ-ray singles spectrum detected with the BEGe detector. Transitions with energies given as integer numbers are either weak, dominated by other γ lines, or their energy exceeds $980\,\mathrm{keV}$, which was the upper limit for the BEGe detector in this experiment, see the text for details. Their location in the scheme is proved by the γ–γ coincidences. All states are populated via the decay of the $1682.30\,\mathrm{keV}$ state. Decay path used for the localisation of the critical $60.73\,\mathrm{keV}$ transition connecting intruder and proton–hole states are highlighted with red colour.

^{179}Au [93].

Two transitions with mixed $E0+M1+E2$ multipolarity reported in previous study [8] were observed in present data set with energies of 296.54 and $284.40\,\mathrm{keV}$, see Fig. 5.1 and Fig. 5.2. Both transitions are highly converted due to their $E0$ components, and therefore rather conversion electrons were used for coincidence analysis than γ rays due to the limited counting statistics of the present data set. The $311.53\,\mathrm{keV}$ γ rays and K electrons from $296.54\,\mathrm{keV}$ transition are in prompt coincidence with the same γ lines (1297 and $1437\,\mathrm{keV}$), see Fig. 5.7. The energy difference between $311.53\,\mathrm{keV}$ and $296.54\,\mathrm{keV}$ transitions is $14.99\,\mathrm{keV}$, which is in

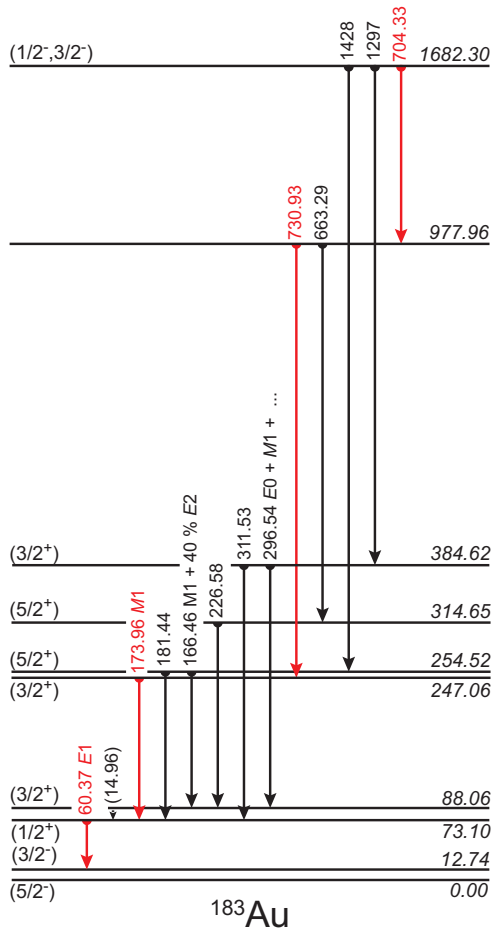

FIGURE 5.5: Partial level scheme of low-lying, positive-parity states associated with the $3s_{1/2}$ and $2d_{3/2}$ proton-hole configurations in the ^{183}Au isotope deduced from the present work [7]. Transition energies were determined using the γ-ray singles spectrum detected with the BEGe detector. Transitions with energies given as integer numbers are either weak, dominated by other γ lines, or their energy exceeds $980\,\mathrm{keV}$, which was the upper limit for the BEGe detector in this experiment, see the text for details. Their location in the scheme is proved by the γ–γ coincidences. All states are populated via the decay of the $1682.30\,\mathrm{keV}$ state. Decay paths used for the localisation of the critical $60.73\,\mathrm{keV}$ transition connecting intruder and proton–hole states are highlighted in red colour.

agreement (within experimental uncertainties) with $14.98\,\mathrm{keV}$ separation between the $1/2^+$ and $3/2^+$ states (difference between 181.44 and $166.46\,\mathrm{keV}$ transitions). This defines a new excited state at $384.62\,\mathrm{keV}$, see Fig. 5.4. No coincidences were observed for $284.40\,\mathrm{keV}$ transition due to the limited counting statistics of the present data set, and therefore it was not placed into the level scheme.

A set of 218.30, 286.42 and $583.10\,\mathrm{keV}$ transitions were observed in present data set in prompt coincidence, see Fig. 5.8. This set of transitions associated with the $1h_{11/2}$ proton–hole cascade was reported in a previous study [8]. The $11/2^-$ band

head associated with the $1h_{11/2}$ configuration is known to decay to the $9/2^-$ proton-intruder state via a retarded $M1$ transition [61]. The deduced partial level scheme associated with the $1h_{11/2}$ proton–hole configuration together with the $9/2^-$ proton-intruder state is given in Fig. 5.6.

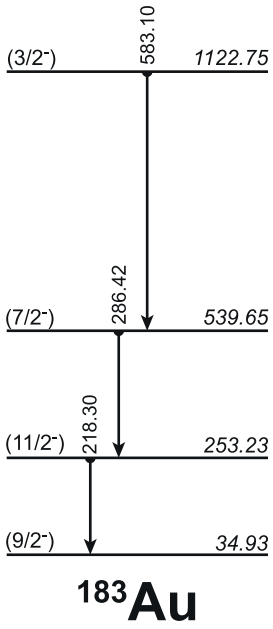

FIGURE 5.6: Partial level scheme of negative-parity states associated with the $1h_{11/2}$ proton–hole configuration and $9/2^-$ state of the $1h_{9/2}$ intruder configuration in the ^{183}Au isotope deduced from the present work and it is published in [7].

Previous in-beam high-spin γ-ray studies [121, 122] of ^{183}Au placed the $9/2^-$ and the $7/2^-$ states at a separation of $56.2\,\mathrm{keV}$, which is in agreement with the energy separation of $56.32\,\mathrm{keV}$ (between the $34.93\,\mathrm{keV}$ and the $91.25\,\mathrm{keV}$ states) determined from present work.

A number of incorrect features in the previous study of the $^{183}\mathrm{Hg} \rightarrow {}^{183}\mathrm{Au}$ decay scheme [8] has been discovered. A major disagreement is in the assignment of the $12.3\,\mathrm{keV}$ level with a spin-parity of $9/2^-$ [8]. This assignment was based on cascade of γ-rays with energies of 250.9, 516.3, and $902.2\,\mathrm{keV}$ from a $1682.1\,\mathrm{keV}$ level and it was argued to come from a pair of γ-rays with energies of 284.4, $296.7\,\mathrm{keV}$. Note that the difference between the energy sum of the cascade and the $1682.1\,\mathrm{keV}$ level is $12.7\,\mathrm{keV}$, not $12.3\,\mathrm{keV}$. In the present work, the energies for cascade from the $1682.30\,\mathrm{keV}$ level are 250.96, 516.11 and $902.42\,\mathrm{keV}$, which is terminating in a level at $12.81\,\mathrm{keV}$, which is in agreement (within experimental uncertainties) with the level at $12.74\,\mathrm{keV}$ in Fig. 5.4. We observe γ-ray lines at 284.40 and $296.54\,\mathrm{keV}$ with the energy difference of $12.14\,\mathrm{keV}$. However, the γ-ray gated electron data do not support that these two

γ-rays originating from the same level and the $296.54\,\mathrm{keV}$ transition was assigned in the present level scheme in a different location to that presented in [8], see Fig. 5.5.

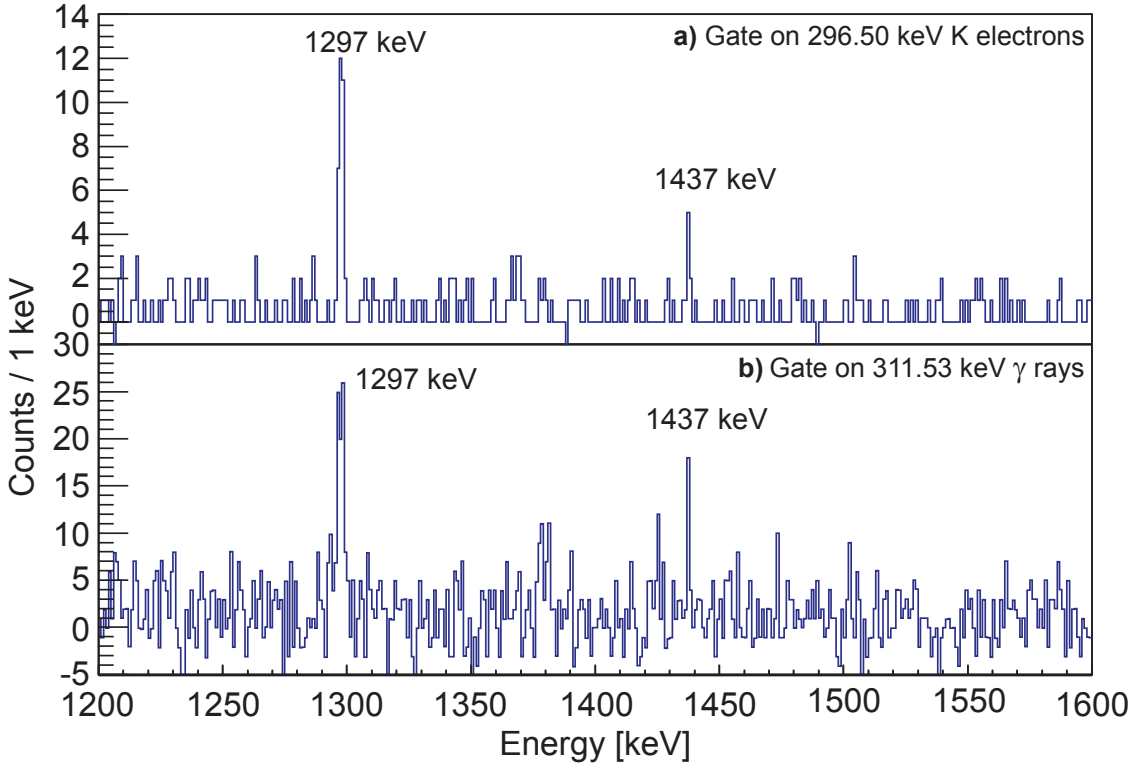

FIGURE 5.7: Spectra of γ rays detected in prompt coincidence with (a) K electrons from $296.54\,\mathrm{kev}$ transition and (b) $311.53\,\mathrm{kev}$ γ rays. Figure is published in [7].

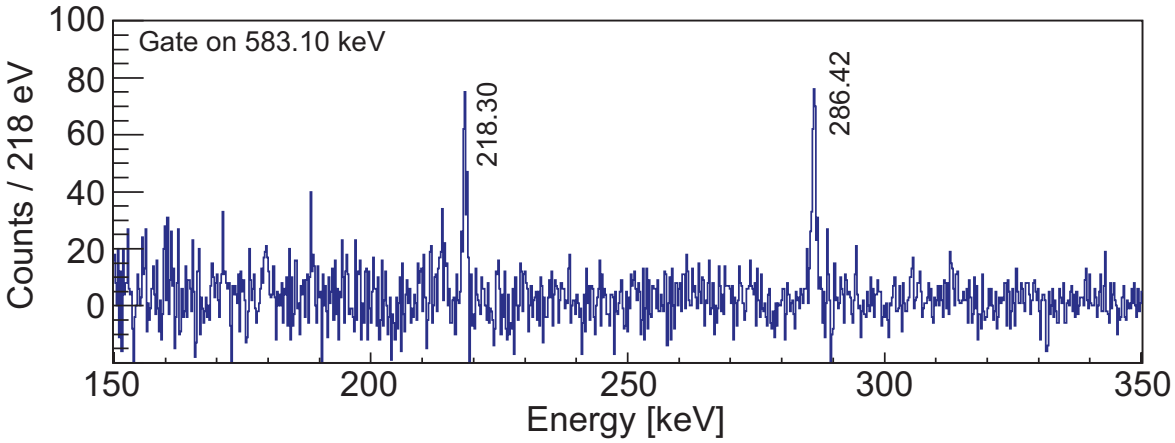

FIGURE 5.8: Spectrum of γ rays detected in prompt coincidence with $583.10\,\mathrm{kev}$ γ rays. Figure is published in [7].

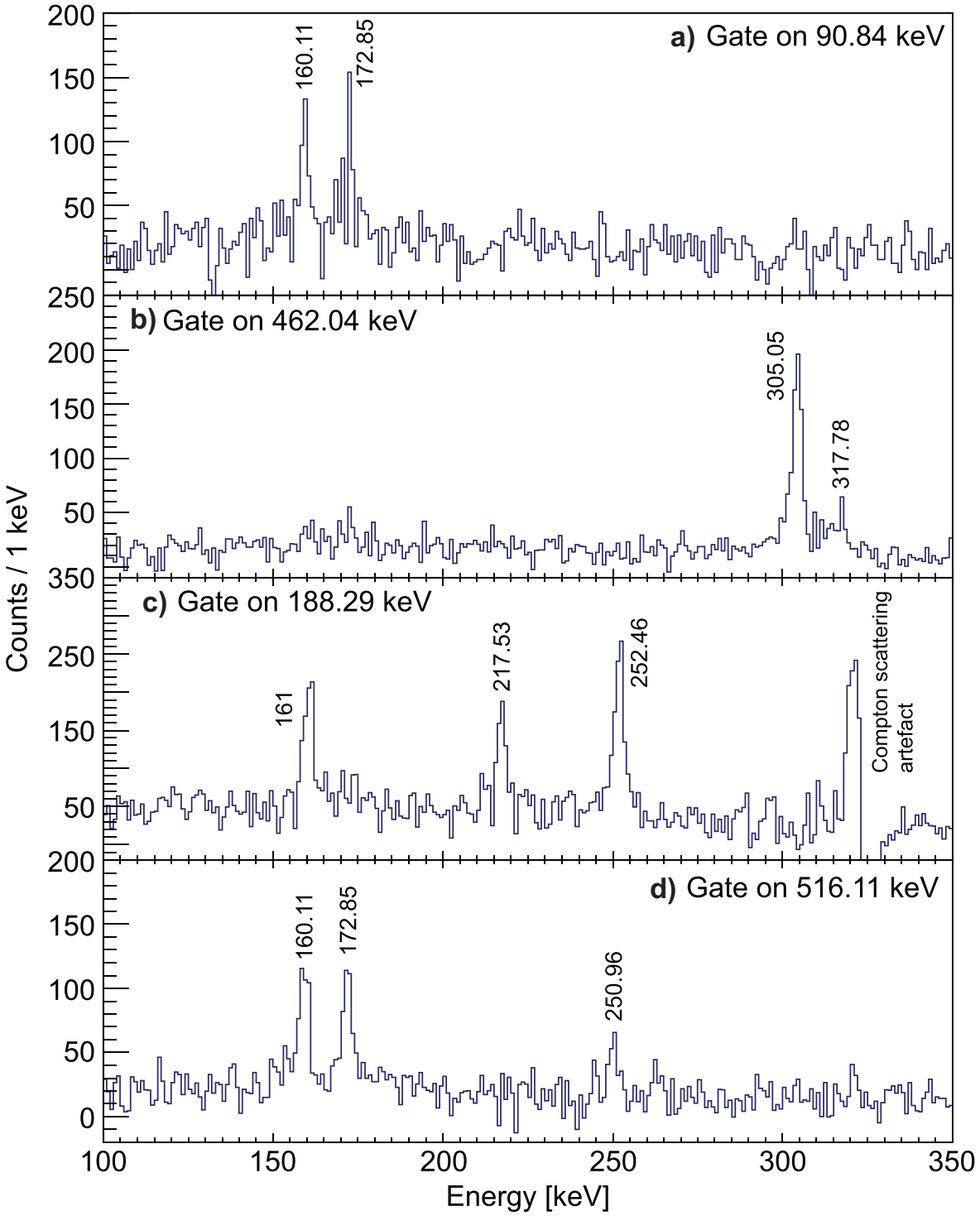

FIGURE 5.9: Spectra of γ rays detected in prompt coincidence with (a) $90.84\,\mathrm{kev}$ γ rays, (b) $462.04\,\mathrm{kev}$ γ rays, (c) $188.29\,\mathrm{kev}$ γ rays and (d) $516.11\,\mathrm{kev}$ γ rays. Figure is published in [110].

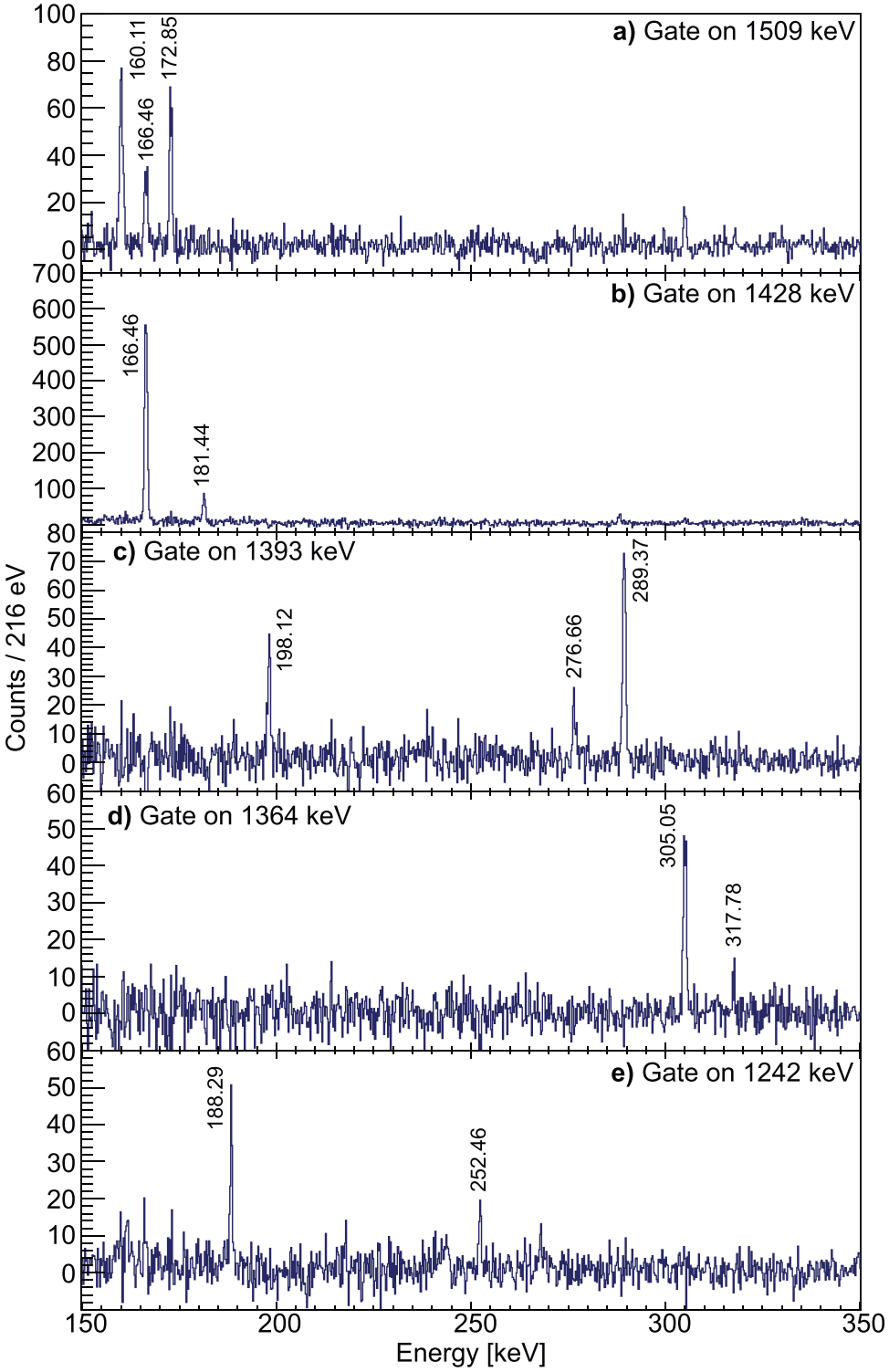

FIGURE 5.10: Spectra of γ rays detected in prompt coincidence with (a) 1509 kev γ rays, (b) 1428 kev γ rays, (c) 1393 kev γ rays, (d) 1364 kev γ rays and (e) 1242 kev γ rays. Figure is published in [110].

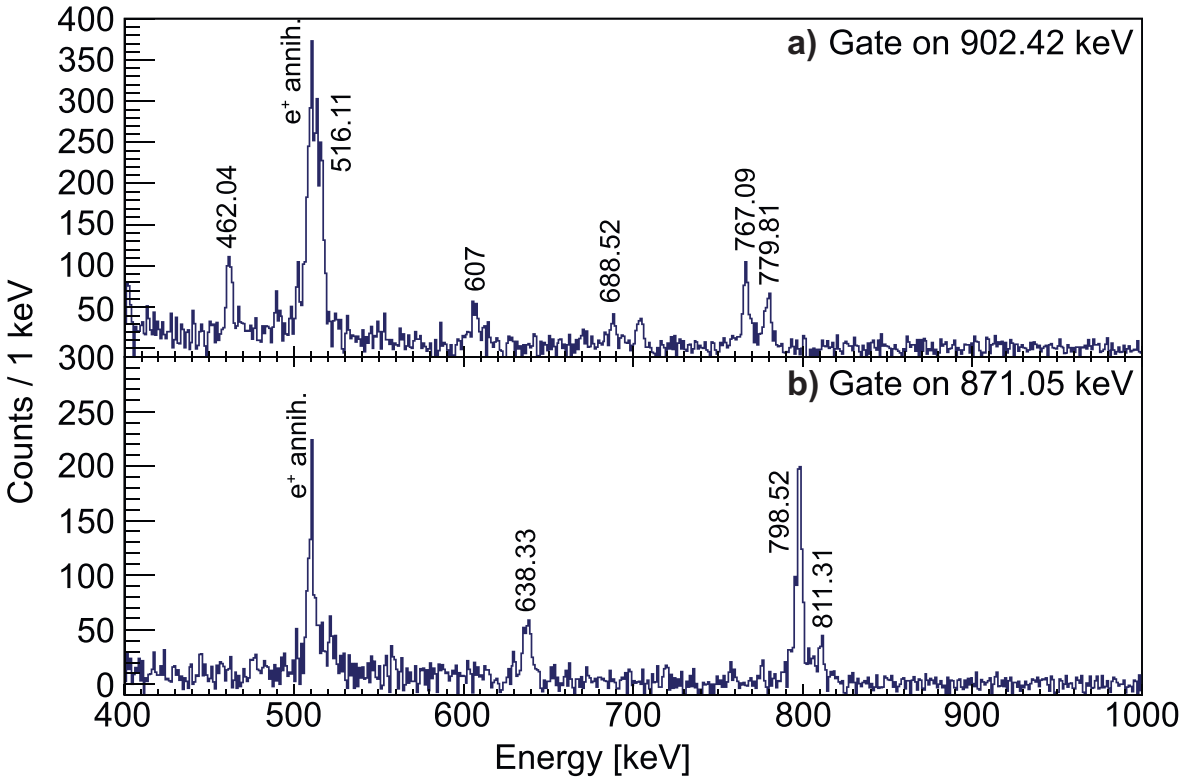

FIGURE 5.11: Spectra of γ rays detected in prompt coincidence with (a) $902.42\,\mathrm{kev}$ γ rays and (b) $871.05\,\mathrm{kev}$ γ rays. Figure is published in [110].

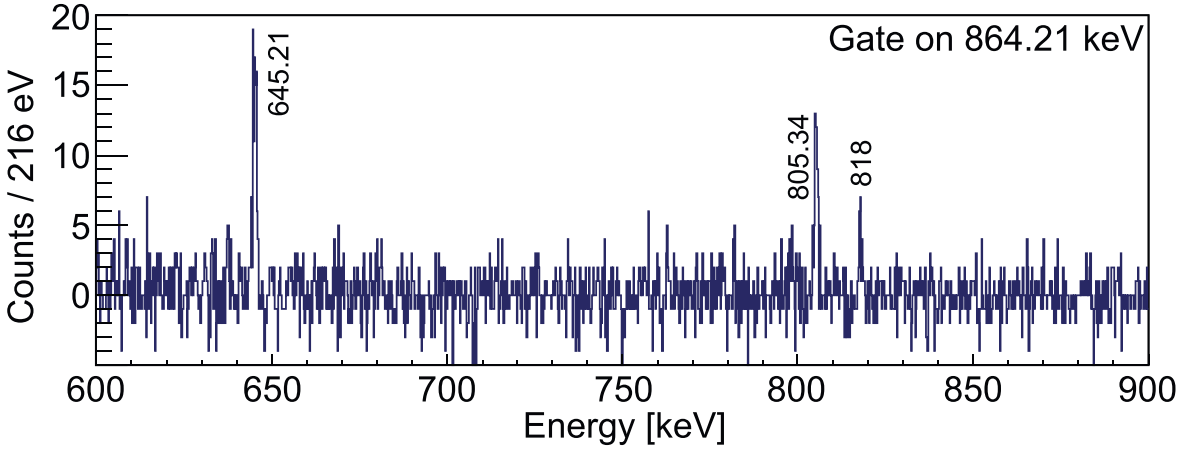

FIGURE 5.12: Spectrum of γ rays detected in prompt coincidence with $864.21\,\mathrm{kev}$ γ rays. Figure is published in [110].

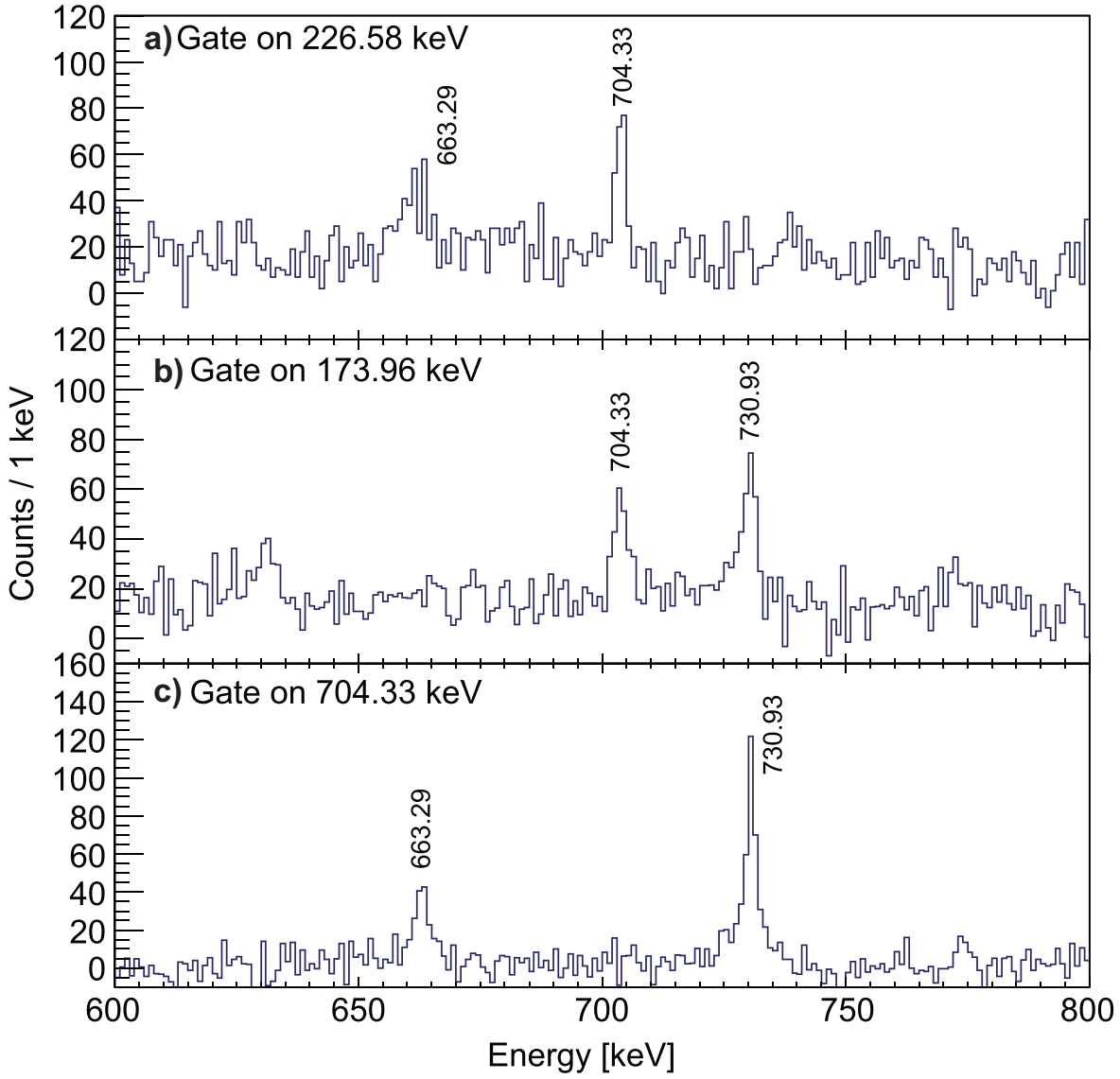

FIGURE 5.13: Spectra of γ rays detected in prompt coincidence with (a) 226.58 kev γ rays, (b) 173.96 kev γ rays, (c) 704.33 kev γ rays. Figure is published in [110].

5.2 ^{181}Hg decay

The half-life of ^{181}Hg is $3.6(1)\,\mathrm{s}$ [115] and the β-decay energy is $7210(25)\,\mathrm{keV}$ [117]. A decay chain of the ^{181}Hg isotope with half-lifes, decay modes and its probabilities of isotopes is given in Fig. 5.14.

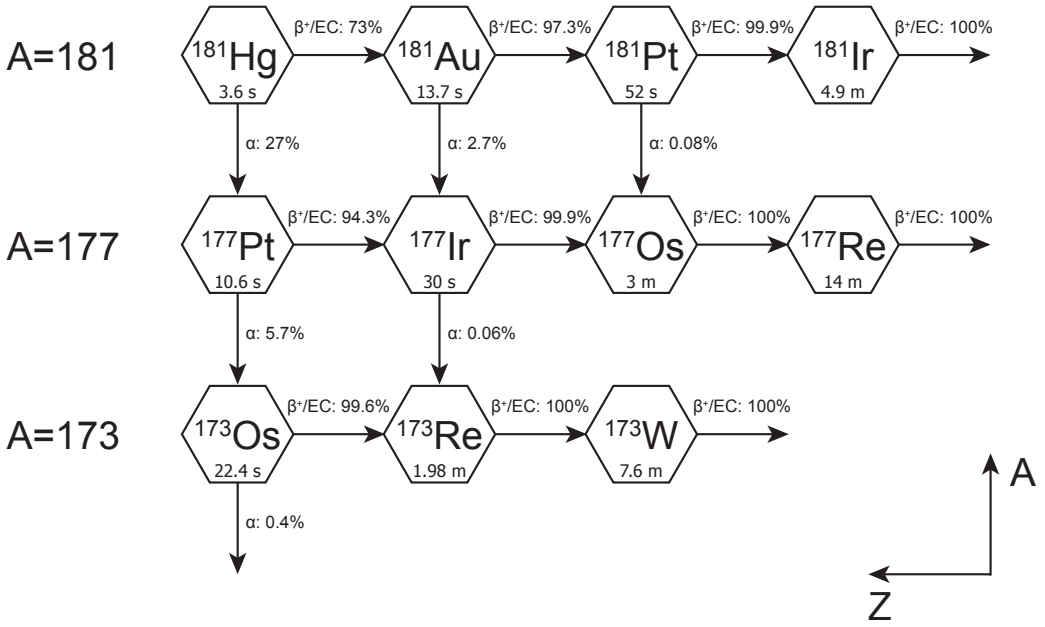

FIGURE 5.14: Decay chain of the ^{181}Hg isotope with half-lifes, decay modes and its probabilities of isotopes. Only isotopes with half-life less than $15\,\mathrm{min}$ are depicted. The data were taken from [115].

Previously, the $^{181}\mathrm{Hg} \rightarrow {}^{181}\mathrm{Au}$ isotope was studied only at the ISOCELE facility [86] at Orsay. This experiment used a Pt-B alloy target placed inside of the ion source of ISOCELE mass separator. This target was irradiated either by $200\,\mathrm{MeV}$ proton or $270\,\mathrm{MeV}$ ^{3}He beam delivered by Orsay synchrocyclotron with typical intensity of $2\,\mu\mathrm{A}$. Proton-beam irradiation produced ^{181}Au activity, while ^{3}He-beam irradiation a

E_γ [keV]	I_γ	E_γ [keV]	I_γ	E_γ [keV]	I_γ
30.8	13	194.7[1]	10	330.9	21
42.5	76	210.9	19	385.6[1]	18
147.8	300	214.1	13	1202.2[1]	5
157.4[1]	16	217.9	7.3	1394.4[1]	18
165.8	16	223.2[1]	32	1776.9[1]	27
180.1[1]	16	265.4[1]	29	1986.7[1]	50
185.0[1]	35	281.0	11		

[1] Assigned to daughter decays of ^{181}Hg according to present work.

TABLE 5.3: Energies and intensities of γ rays assigned to the ^{181}Hg decay in previous work [86]. Wrongly assigned γ rays according to present study are marked with footnote mark.

mixture of ^{181}Hg and ^{181}Au activities. Both datasets were strongly contaminated with ^{181}Pt. Pure spectrum of ^{181}Au was obtained by subtraction of proton- and ^{3}He-beam data. Resulting spectrum was still strongly contaminated with ^{181}Pt transitions as it

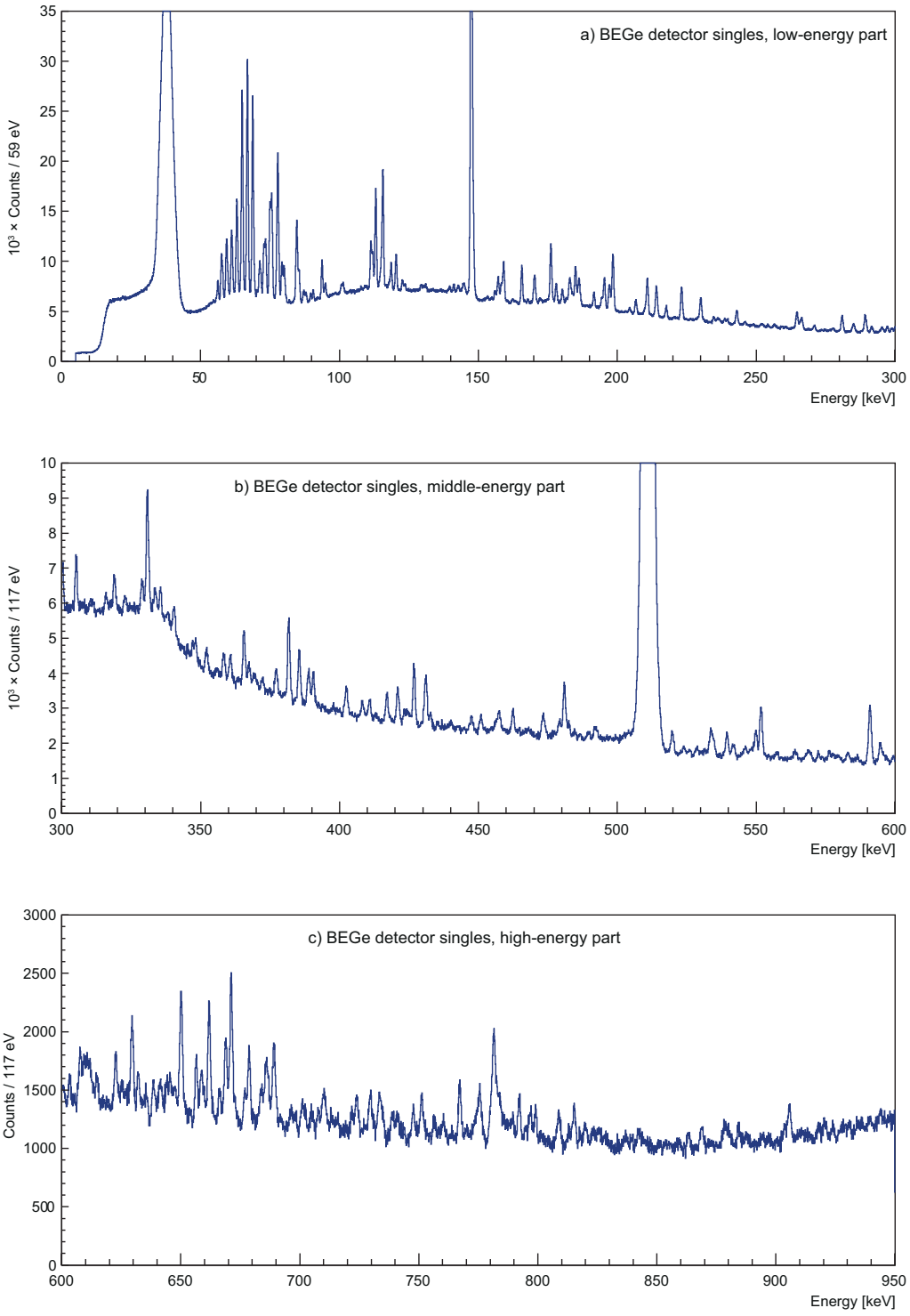

FIGURE 5.15: Singles γ-ray spectrum measured with the BEGe detector divided into three energy regions. (a) is lower-energy part, (b) is middle-energy part and (c) is higher-energy part.

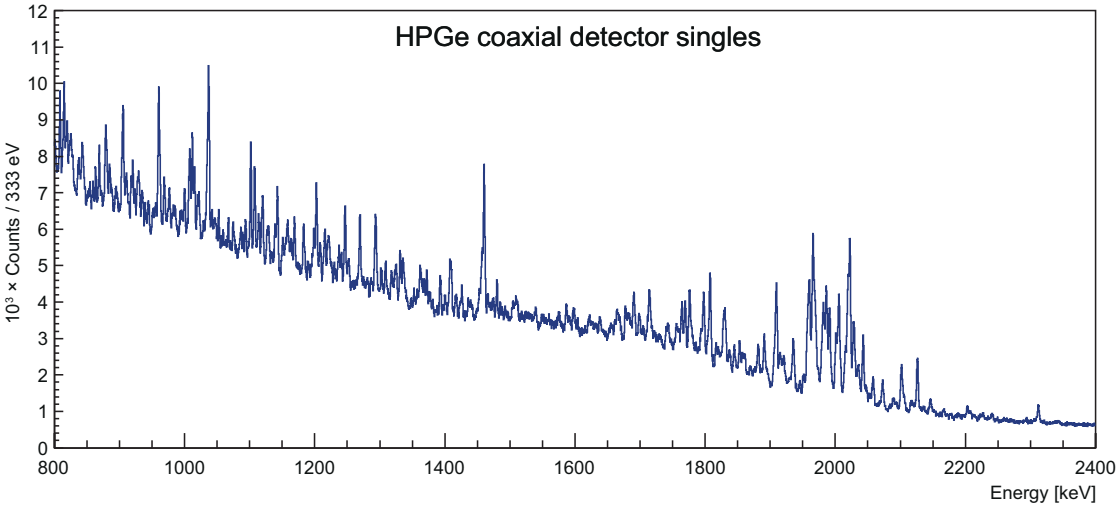

FIGURE 5.16: Higher-energy part of total singles γ-ray spectrum measured with a coaxial HPGe detector.

is explicitly stated by authors of the study [86]. No level scheme was constructed for ^{181}Hg, only the table with γ rays is given in [86], see Tab. 5.3. The only other literature relevant to the structure of the ^{181}Au isotope are in-beam studies [121, 122].

Data for analysis of ^{181}Hg were obtained during IS521 experiment in 2014 only. One BEGe and two coaxial HPGe detectors were employed and singles γ-ray spectra measured with them are given in Fig. 5.15 and Fig. 5.16. The method described in Chapter 4 was used and all transitions assigned to the decay of ^{181}Hg, with their energies and intensities are given in Tab. 5.4. The comparison of total singles (a) and deconvoluted ^{181}Hg decay singles spectra (b) measured with the BEGe detector is in Fig. 5.17 and measured with one of the coaxial HPGe detectors is in Fig. 5.18.

The level scheme of ^{181}Au deduced from present work is given in Fig. 5.20. The level scheme construction is based on γ-γ-ray coincidences in conjunction with Rydberg–Ritz combination principle. The spin and parity assignments are based on γ-γ-ray coincidences and similarities in systematics of adjacent odd-Au isotopes, see Section 5.3.2. Only part of the transitions from Tab. 5.4 was placed into the level scheme due to insufficient counting statistics for γ-γ-ray coincidence analysis and missing of conversion-electron data.

The excitation energy of the first excited state was determined as weighted average of energy differences between couples of transitions feeding the ground state and the first excited state: 111.34, 113.11, 264.66, 266.44, 878.41 and 880.22 keV states. The 111.34 keV line is part of the doublet with peak assigned to daughter decays, see Fig. 5.19. The 111.34 keV together with the 113.11 keV transitions carry out most of the γ-ray intensity, which means that deexcitation path of many γ-ray cascades goes through the 113.11 keV level. This is shown in the level scheme, Fig. 5.20, and it is

supported by coincidence analysis, see Fig. 5.23. In previous study [86], these lines were not recognized due to the strong contamination of the beam with ^{181}Pt, which emits intensive γ rays in this region together with the ^{181}Hg daughter decays and with worse energy resolution of used detectors, these lines can be missed.

Some of peaks appeared in both deconvolved singles spectra, assigned to ^{181}Hg decay and to its daughter decays. This is due to the presence of long lived activity of isotopes in the decay chain during the whole measurement, e.g., the $115.65\,\mathrm{keV}$ peak assigned to ^{177}W decay [124], see Fig. 5.19. The ^{181}Hg isotope has significant α-decay branch of $27\,\%$ [115]. When α particle is emitted in a direction to the tape, recoiling effect (approximately $60\,\mathrm{keV}$) of daughter nucleus can be ejected from the tape. This contaminates the measurement chamber with daughter activities. Note that many

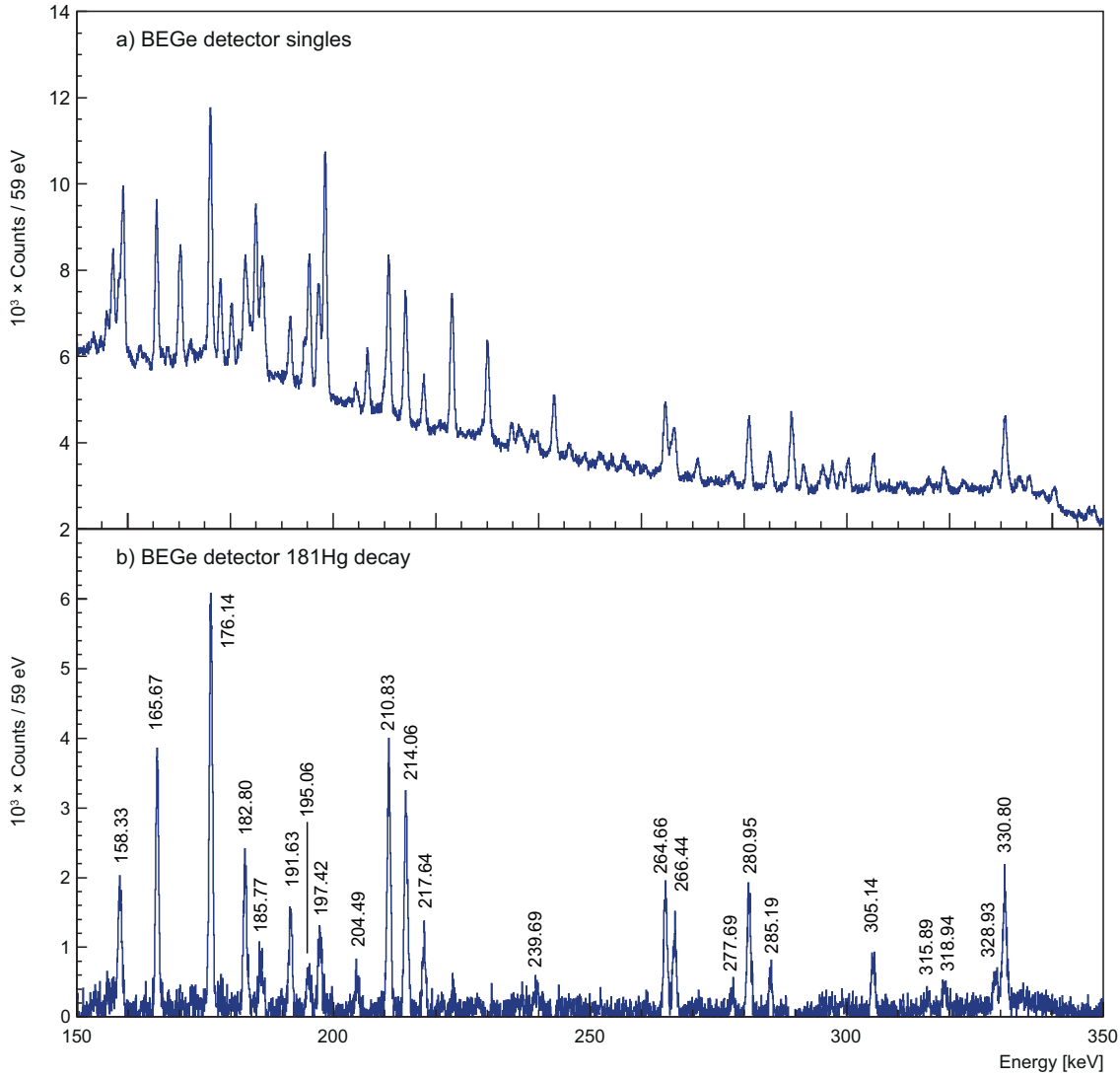

FIGURE 5.17: Part of singles γ-ray spectra measured with the BEGe detector. (a) is total singles spectrum and (b) is single spectrum assigned to the ^{181}Hg decay.

characteristic X-rays are present in singles spectra (see see Fig. 5.15), even from Ta, which would be not the case in the situation when all daughter activity is carried away by the tape.

The strong cascade of 607.76, 305.14 and $158.33\,\mathrm{keV}$ γ rays was assigned to $1h_{11/2}$ configuration based on its systematics in adjacent odd-Au isotopes, see Fig 5.29, and therefore spin and parity of according states were determined as $3/2^-$, $7/2^-$, $11/2^-$ and cascade is ending on $9/2^-$ state of $1h_{9/2}$ configuration, see Fig. 5.21. The state $9/2^-$ is of unknown excitation energy, labelled as x in the level scheme. No γ rays with lower energy were observed in prompt coincidence for $158.33\,\mathrm{keV}$ transition.

The most significant γ-γ-ray coincidences, used for the level scheme construction, are given in Figures 5.22 - 5.28.

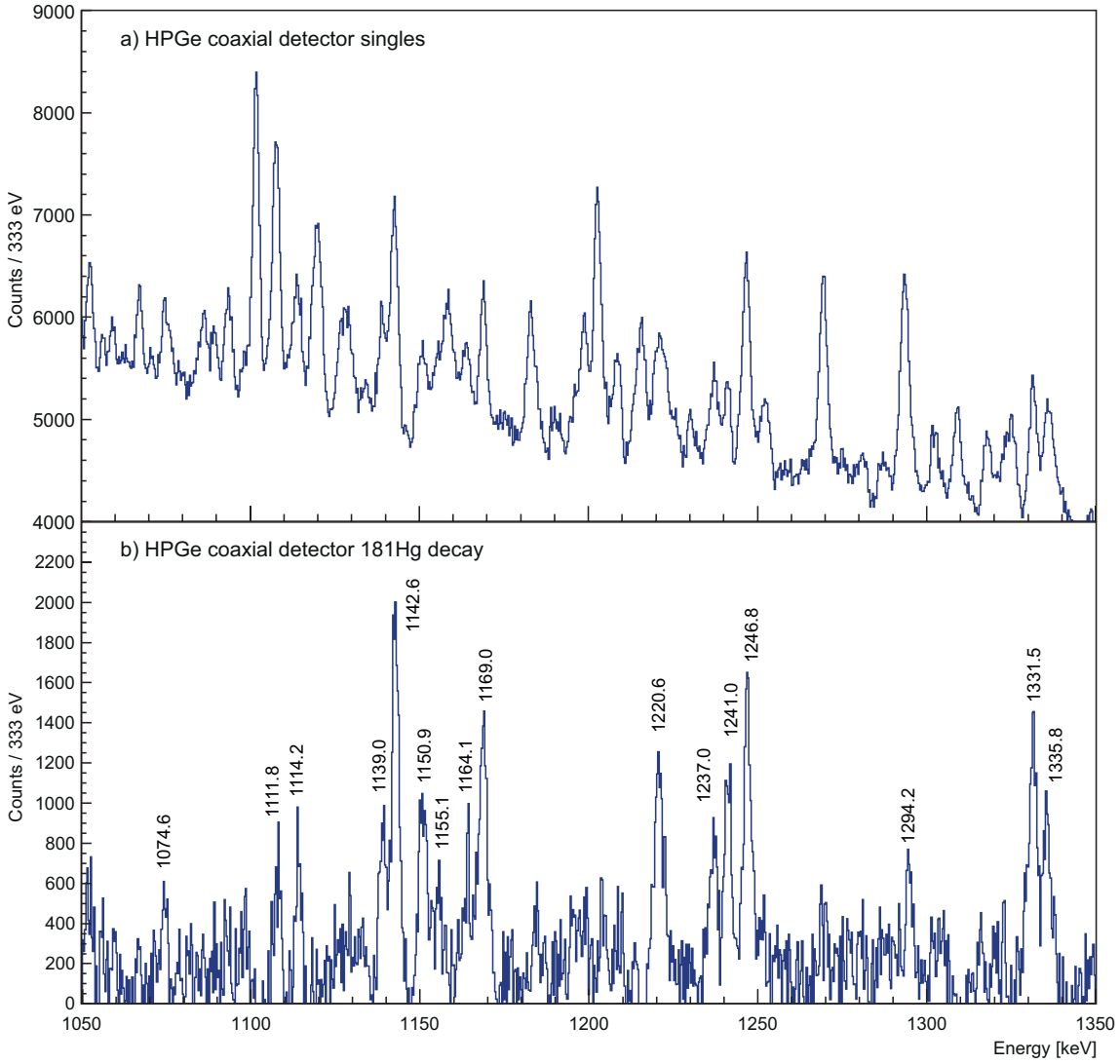

FIGURE 5.18: Part of singles γ-ray spectra measured with coaxial HPGe detector. (a) is total singles spectrum and (b) is single spectrum assigned to the ^{181}Hg decay.

E_γ [keV]	I_γ	E_γ [keV]	I_γ	E_γ [keV]	I_γ
111.34(4)	205	572.43(10)	11	1139.0(1)	43
113.11(4)	428	590.90(6)	96	1142.6(1)	87
139.68(6)	9	607.76(7)	32	1150.9(2)	43
142.84(6)	16	629.48(6)	55	1155.0(2)	16
147.48(4)[12]	3138	632.07(8)	28	1164.1(1)	20
158.33(5)	79	641.30(8)	31	1169.0(1)	51
165.67(4)[2]	191	658.57(9)	27	1220.6(2)	54
176.14(4)	354	668.77(6)	54	1237.0(1)	39
182.80(6)	130	676.88(8)	21	1241.0(1)	33
185.77(15)	22	685.67(10)	38	1246.8(1)	72
191.63(5)	36	689.69(32)	14	1294.2(4)	19
195.06(18)	16	697.88(17)	8	1331.5(1)	62
197.42(9)	34	702.07(23)	8	1335.8(2)	53
204.49(6)	11	705.04(13)	11	1409.9(1)	50
210.83(5)[2]	100	740.88(10)	16	1416.1(3)	12
214.06(7)[12]	82	743.30(20)	4	1590.9(3)	18
214.41(15)	18	760.18(12)	12	1599.3(3)	24
217.64(5)[2]	30	767.11(7)	44	1664.9(2)	46
239.69(7)[1]	16	780.01(11)	26	1677.8(1)	50
264.66(5)	67	782.90(20)	26	1691.3(3)	47
266.44(5)	41	798.95(8)	30	1756.1(1)	16
277.69(8)	13	813.07(15)	11	1769.1(1)	67
280.95(5)[2]	69	815.13(8)	38	1828.4(1)	70
285.19(10)	25	823.09(14)	16	1845.0(1)	33
305.14(5)	35	863.20(11)	15	1853.0(1)	41
315.89(8)	12	878.41(13)	28	1857.2(1)	26
318.94(6)	22	923.2(2)	24	1881.6(1)	59
328.93(6)	25	930.1(2)	37	1905.8(2)	36
330.80(5)[23]	100	934.6(1)	39	1909.5(1)	182
360.62(6)	21	960.4(1)	153	1957.3(1)	99
388.85(10)	31	973.1(2)	17	1965.8(1)	233
390.47(6)	33	976.6(1)	50	1979.4(1)	52
462.38(6)	28	1037.4(5)	38	1992.4(5)	29
482.45(8)	14	1042.1(1)	33	2008.0(3)	25
519.77(6)	26	1074.6(2)	11	2019.2(1)	140
549.79(6)	39	1111.8(2)	9	2028.8(1)	149
551.67(5)	79	1114.2(1)	22	2047.6(2)	14
563.95(9)	14				

[1] Assigned to α-decay of ^{181}Hg [123].
[2] Present also in previous work [86].
[3] Intensities are relative to this line.

TABLE 5.4: Energies and intensities of γ rays assigned to the ^{181}Au. The γ-ray intensities are given relative to the 330.80 keV line.

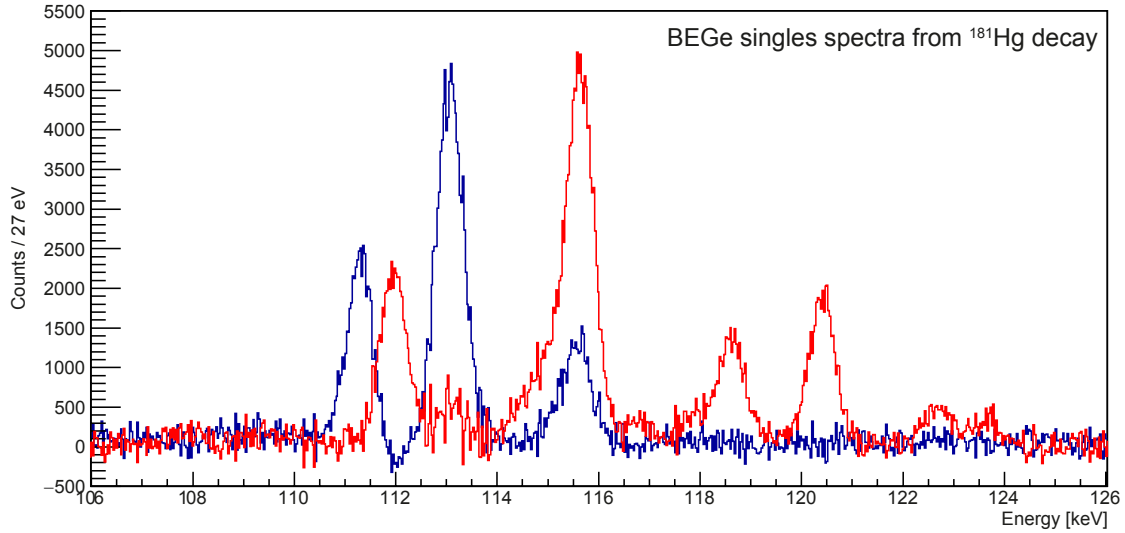

FIGURE 5.19: Part of the deconvoluted singles spectra measured with BEGe detector. Spectrum assigned to ^{181}Hg decay is depicted by blue colour while spectrum assigned to daughter decays is drawn by red line. Note that $115.65\,\mathrm{keV}$ peak, assigned to ^{177}W decay [124], is present in both. This is due to long lived contamination of the vacuum chamber caused by α-decay recoils, which are getting out of the tape.

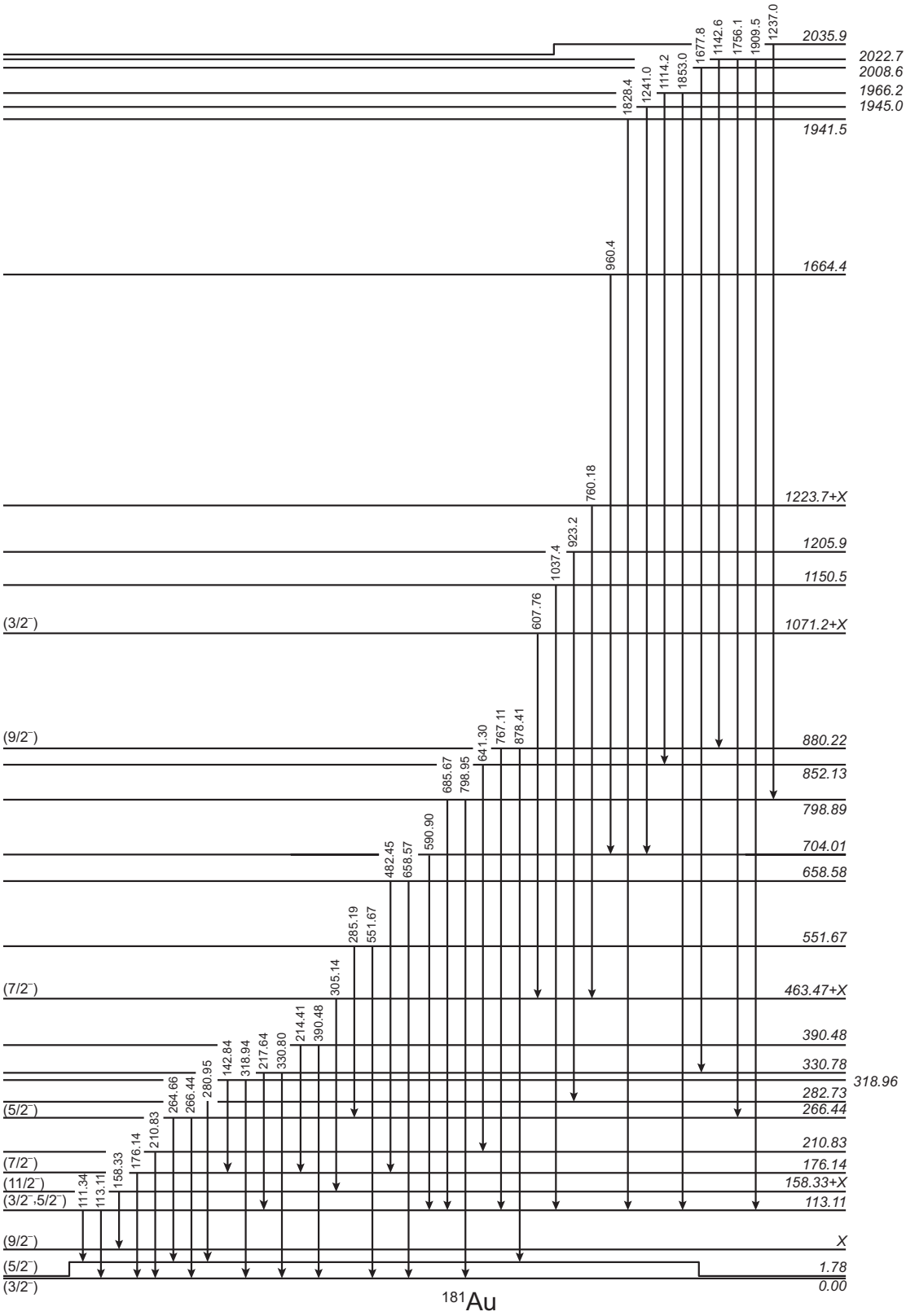

FIGURE 5.20: Level scheme of the ^{181}Au deduced from the present work.

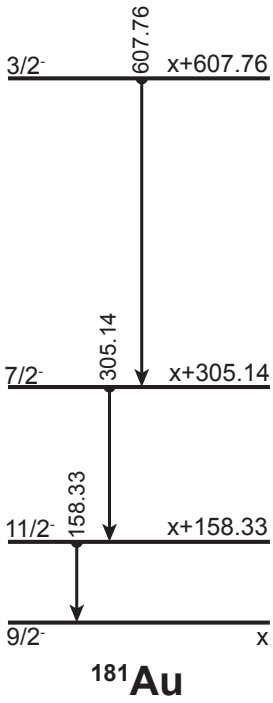

FIGURE 5.21: Partial level scheme of ^{181}Au assigned to $1h_{11/2}$ configuration and $9/2^-$ intruder state.

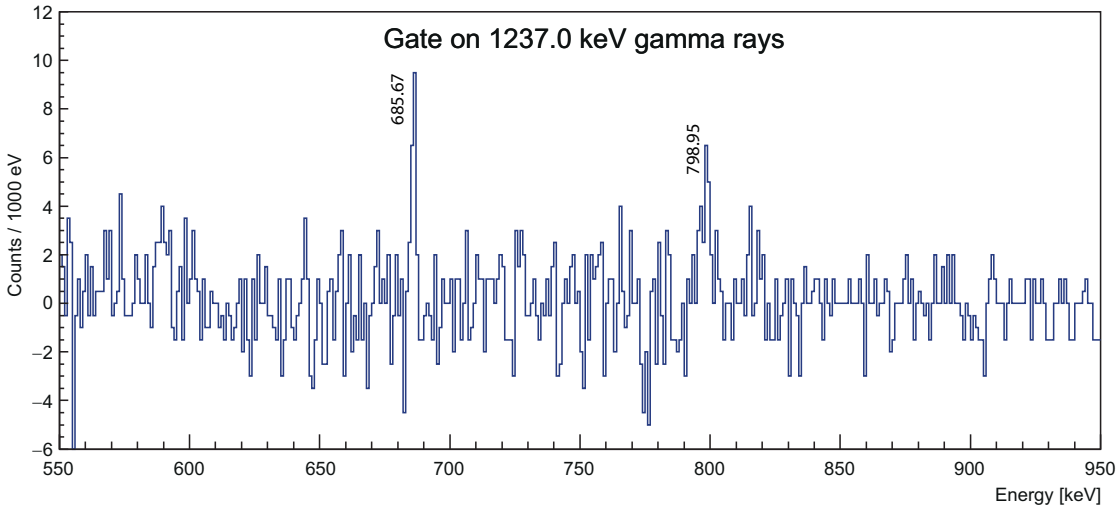

FIGURE 5.22: Spectrum of γ rays detected in prompt coincidence with $1237.0\,\mathrm{kev}$ γ rays.

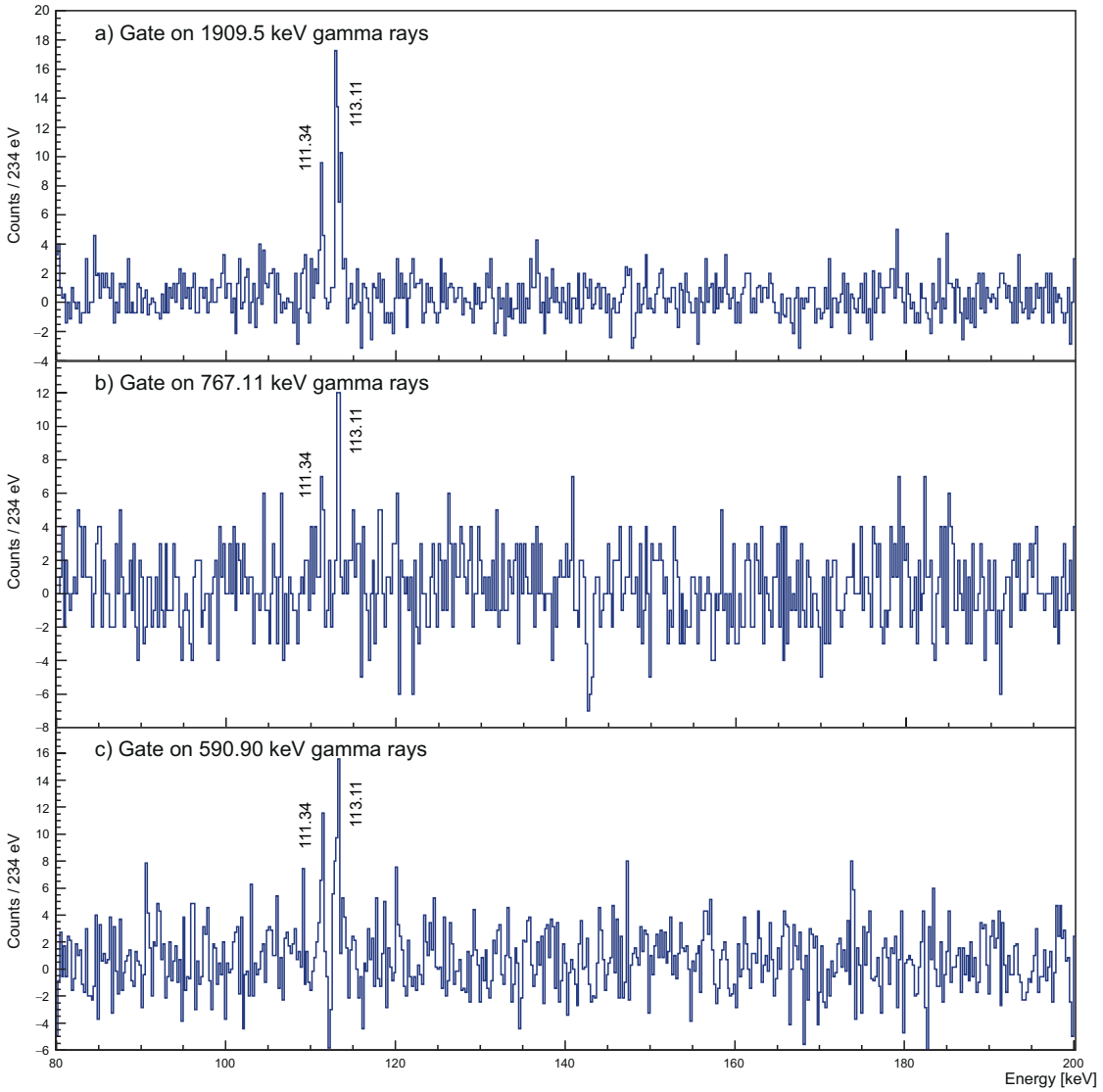

FIGURE 5.23: Spectra of γ rays detected in prompt coincidence with (a) $1909.5\,\mathrm{kev}$ γ rays, (b) $767.11\,\mathrm{kev}$ γ rays and (c) $590.90\,\mathrm{kev}$ γ rays.

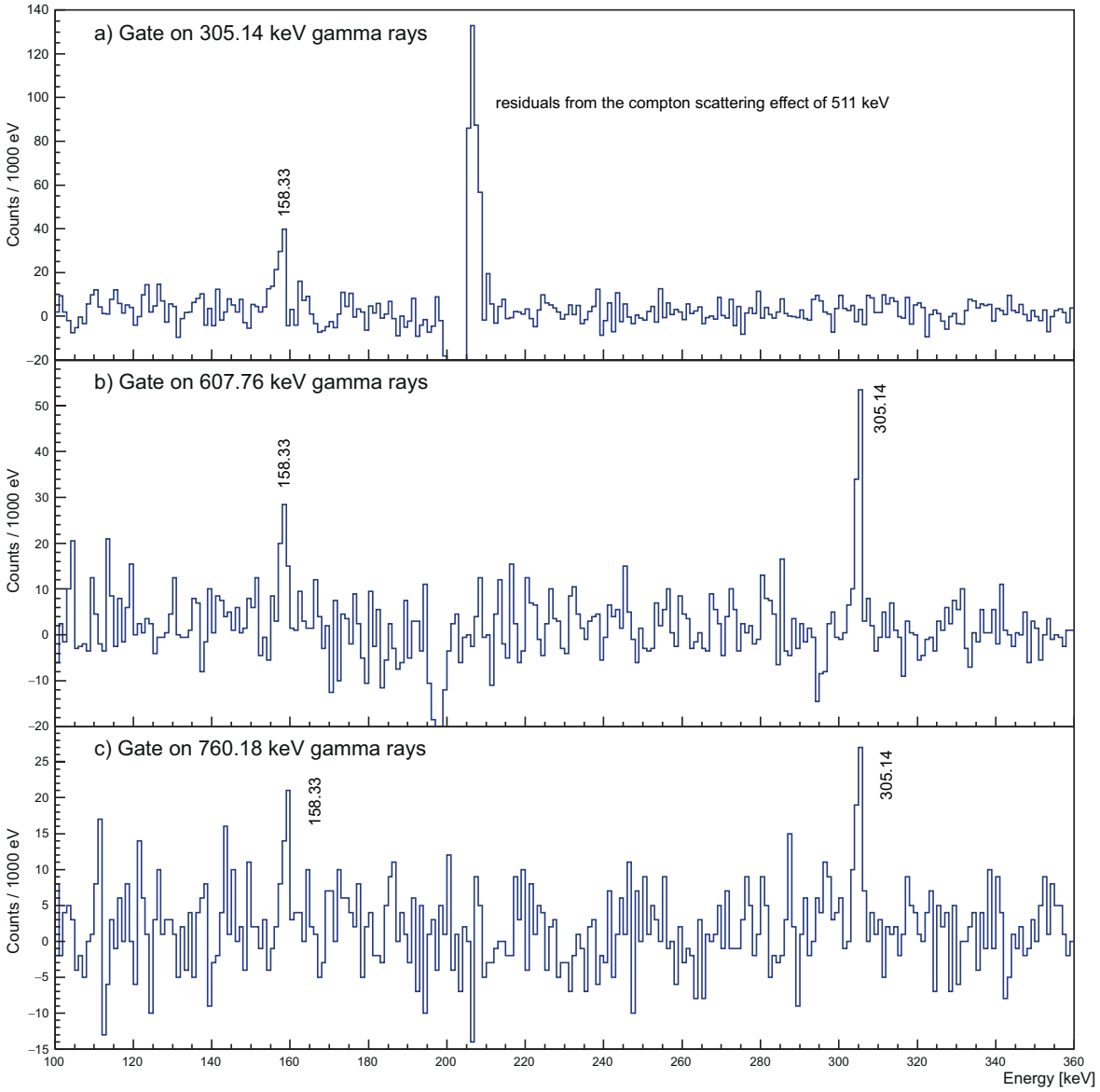

FIGURE 5.24: Spectra of γ rays detected in prompt coincidence with (a) $305.14\,\mathrm{kev}$ γ rays, (b) $607.76\,\mathrm{kev}$ γ rays and (c) $760.18\,\mathrm{kev}$ γ rays.

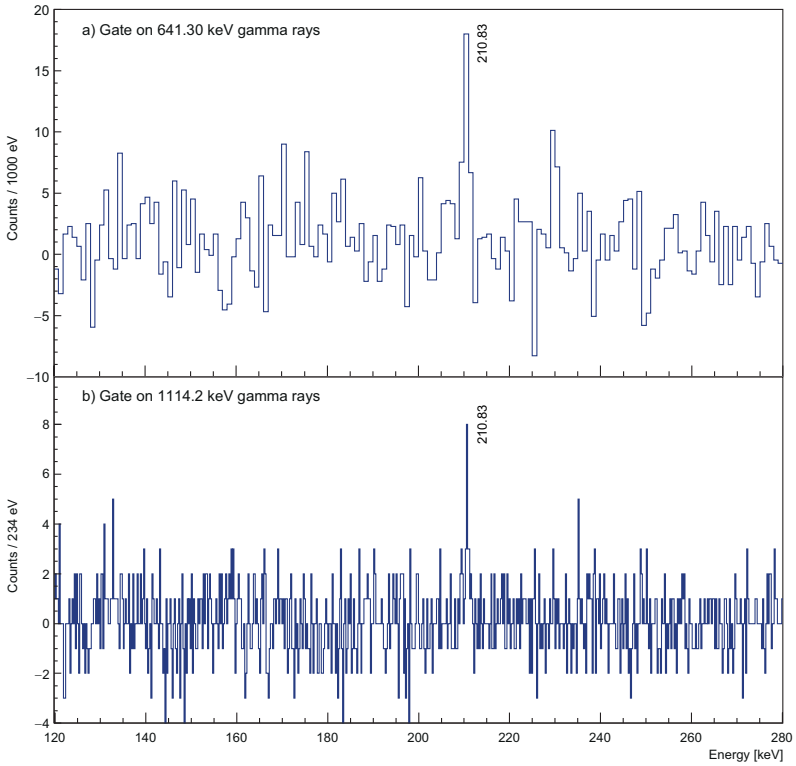

FIGURE 5.25: Spectra of γ rays detected in prompt coincidence with (a) $641.30\,\mathrm{kev}$ γ rays and (b) $1114.2\,\mathrm{kev}$ γ rays.

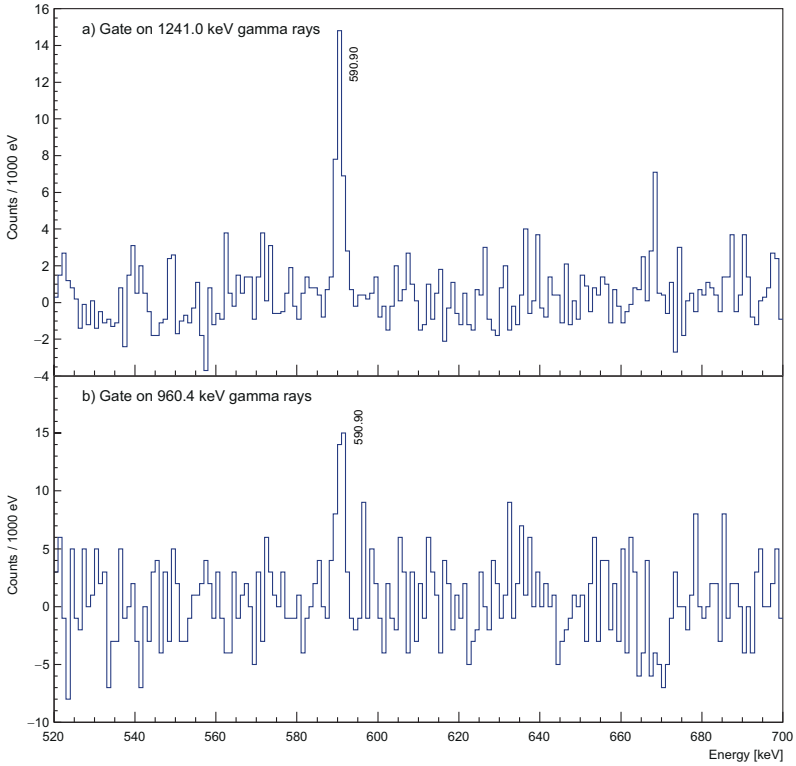

FIGURE 5.26: Spectra of γ rays detected in prompt coincidence with (a) $1241.0\,\mathrm{kev}$ γ rays and (b) $960.4\,\mathrm{kev}$ γ rays.

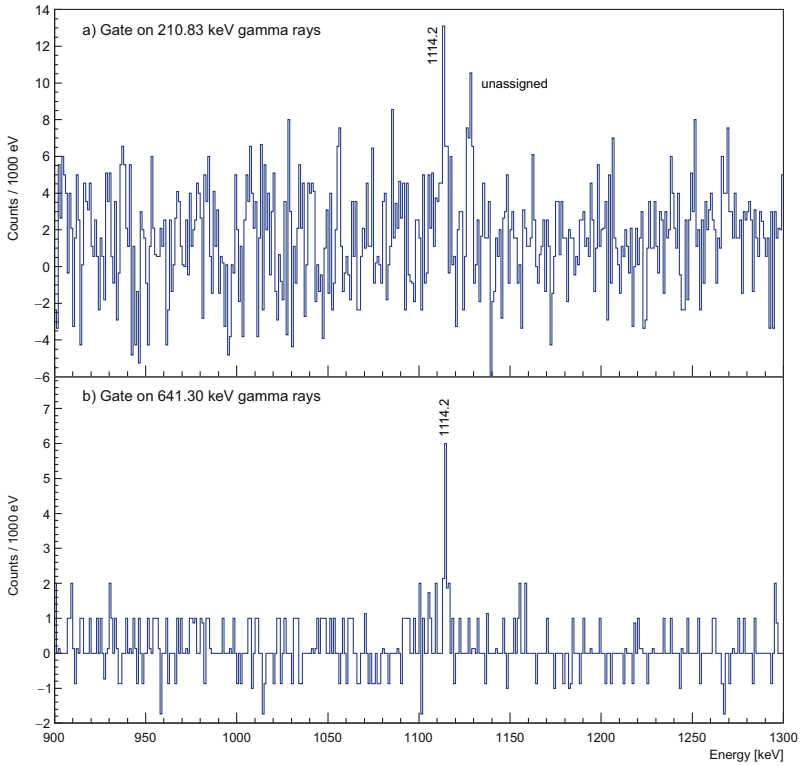

FIGURE 5.27: Spectra of γ rays detected in prompt coincidence with (a) $210.83\,\mathrm{kev}$ γ rays and (b) $641.30\,\mathrm{kev}$ γ rays.

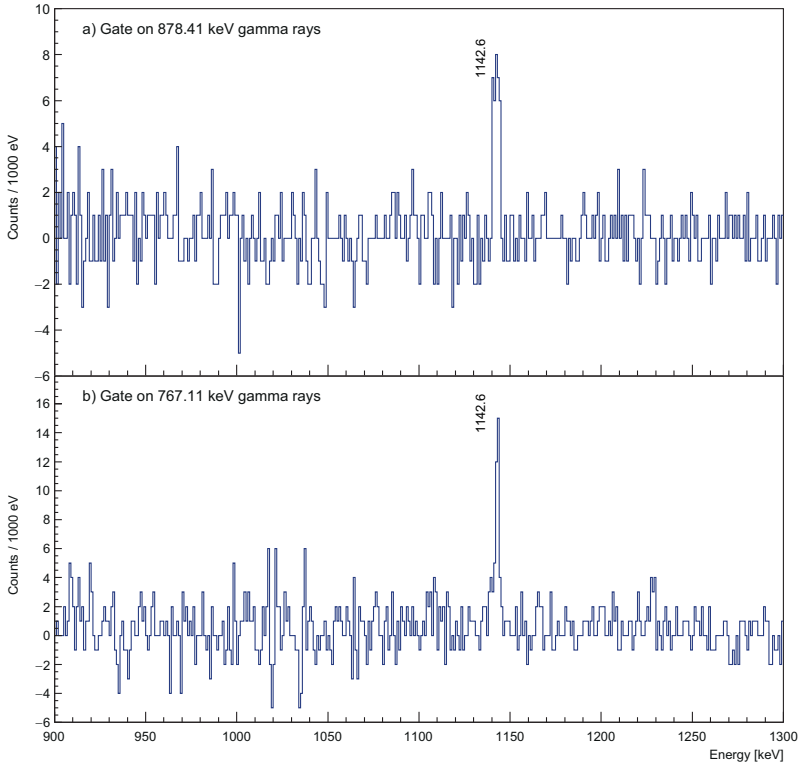

FIGURE 5.28: Spectra of γ rays detected in prompt coincidence with (a) $878.41\,\mathrm{kev}$ γ rays and (b) $767.11\,\mathrm{kev}$ γ rays.

5.3 Systematics of odd-mass Au isotopes nuclear states

5.3.1 Systematics of $1h_{11/2}$ proton-hole structure

In a comprehensive study of ^{187}Au isotope [77], a rich spectrum (up to spin $19/2^-$) of excited states associated with the $1h_{11/2}$ proton-hole structure was observed. Two families of states were identified: either due to coupling of the $1h_{11/2}$ proton hole with weakly deformed ground state, or with strongly deformed 0^+ intruder state in ^{188}Hg core. To characterize these states, calculations with the particle + triaxial rotor model (PTRM) [125] using a Woods-Saxon potential for deformed mean field were performed in study [77]. Weakly deformed triaxial shape with $\beta_2 = 0.15$ and $\gamma = 32^o$ was used for description of states corresponding to coupling of the proton hole with ground state of ^{188}Hg. The triaxiality parameter has been fitted to energy difference of $15/2^-$ and $13/2^-$ states. In general, there is a good agreement between theory and experiment, and every state predicted by the calculation has its experimental counterpart, see Fig. 19 in [77]. Intensities of gamma rays connecting excited states of the $1h_{11/2}$ structure were also calculated, see Tab. IV. in [77]. Overall the agreement is reasonably good, although some discrepancies clearly exist. The systematics has been extended to ^{185}Au isotope [61, 126].

In present study, only $3/2^-$, $7/2^-$, and $11/2^-$ members of the $1h_{11/2}$ proton-hole

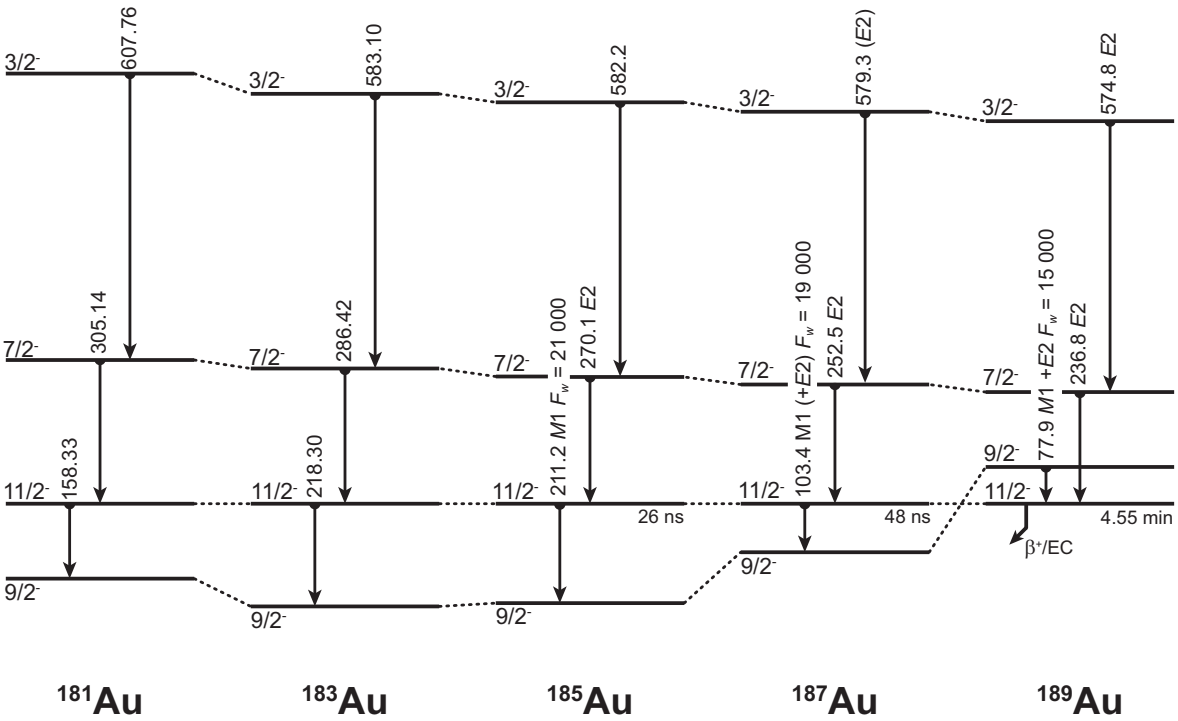

FIGURE 5.29: Systematics of the $3/2^-$, $7/2^-$, and $11/2^-$ states of the $1h_{11/2}$ configuration together with $9/2^-$ intruder state in odd-Au isotopes. The data are taken from present work and from [61, 77, 126].

configuration could be identified in ^{181,183}Hg isotopes. Only the low-spin isomer is present in ^{181,183}Hg. This is not the case of heavier isotopes that have also $13/2^+$ isomer, which decays via β^+/EC decay. Fig. 5.29 gives the systematics of the $3/2^-$, $7/2^-$, and $11/2^-$ states of the $1h_{11/2}$ configuration together with $9/2^-$ intruder state, which is the final state of the deexcitation of $11/2^-$ band head (fed by retarded $M1$ transition).

The excitation energy of $3/2^-$ and $7/2^-$, relative to the $11/2^-$ band head appears to be notably stable, suggesting very similar structure as was established in ^{187}Au by authors of study [77]. However, there is slight increase in split of $3/2^-$ and $7/2^-$ states. The same trend is observed also in the systematics of these states in heavier Au isotopes, see Fig. 2.4 and [76]. According to calculations using PTRM model, see Fig. 5.30, this indicates a slight change in the triaxiality from "oblatish" to "prolatish" shape with decreasing neutron number.

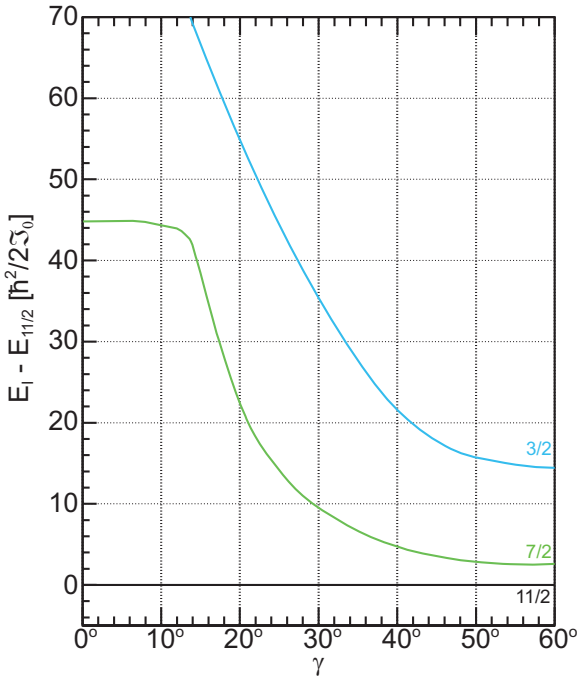

FIGURE 5.30: Spectrum based on PTRM calculations as a function of the γ parameter for $\beta A^{2/3} = 5$, $\lambda_F = \epsilon_1$, and $j = 11/2$. Only $3/2^-$ and $7/2^-$ states are given.

5.3.2 Systematics of $2d_{3/2} \oplus 3s_{1/2}$ proton-hole configuration

Fig. 5.31 gives the systematics of positive-states associated with mixed $2d_{3/2} \oplus 3s_{1/2}$ proton-hole configuration in ^{183,185,187,189}Au isotopes. The data are from present work (^{183}Au) and from [61, 77, 127]. Sequence of states is markedly similar through given isotopes. However, the states are more compressed with decreasing neutron number. This can be explained by presence of low-spin intruder states, which appear due to

coupling of proton hole with coexisting 0^+ states in even-Hg cores. Mixing repulsion between the states with the same spin-parity may cause the compression in isotopes close to N = 104 midshell point.

Electric monopole transition was identified between $3/2^+$ states in ^{183}Au, see systematics in Fig. 5.31 and level scheme in Fig. 5.5. This is probably deexcitation of one of above mentioned positive-parity intruder configurations. Such transition does not have any precedents in heavier isotopes. Note that some $E0$ transitions were reported in unpublished thesis [126] for the ^{185}Au isotope. In ^{187}Au, two $3/2^+$ states, decaying with $E0$ transitions, were observed [77] at excitation energies of 591 and $595\,\mathrm{keV}$, respectively. However, their $E0$ deexcitations are feeding second $3/2^+$ of the $2d_{3/2} \oplus 3s_{1/2}$ configuration, and not the first as it is in ^{183}Au. Therefore they may a different configurations than that observed in ^{183}Au. If these "extra" $3/2^+$ states were strongly-deformed structures, rotational bands would be expected on top of them. Investigation of these associated bands would help to elucidate the structure of these states.

Calculations on the basis of the PTRM model, performed for ^{187}Au in [77], suggest slightly deformed triaxial configuration with $\beta_2 = 0.15$ and $\gamma = 45^o$. A discrepancy between gamma deformation obtained for $1h_{11/2}$, see previous subsection, may be caused by mixing that affects the states associated with $2d_{3/2} \oplus 3s_{1/2}$ configuration more than those associated with $1h_{11/2}$ configuration. That is an unique-parity orbital

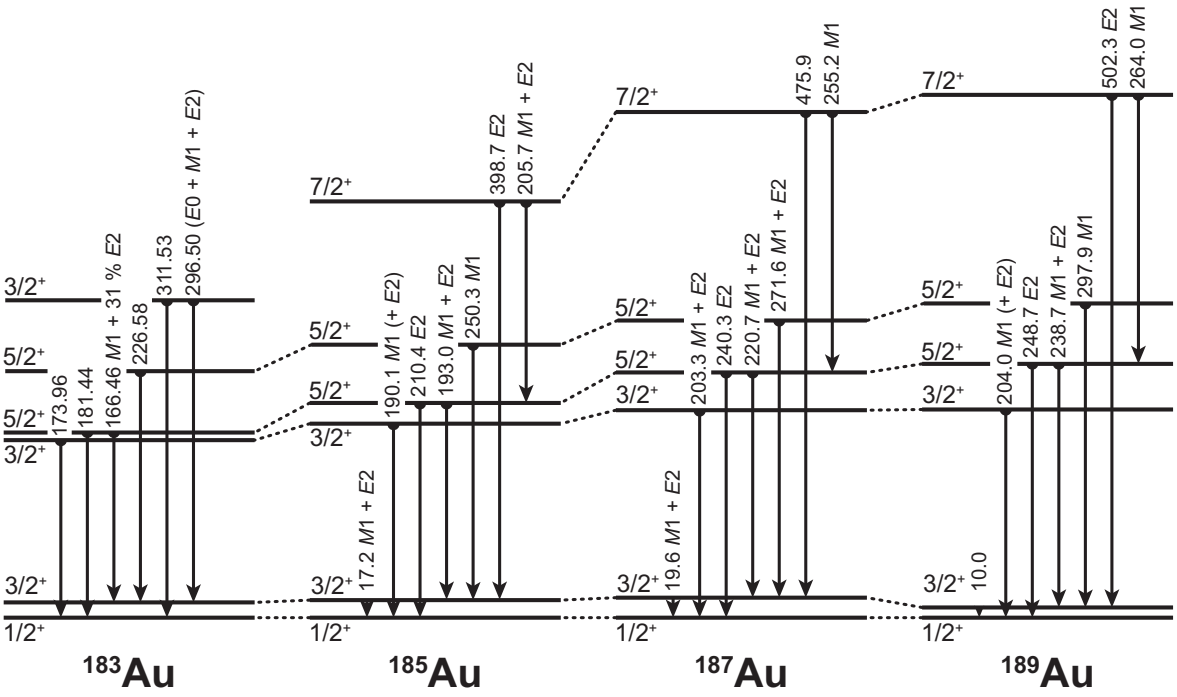

FIGURE 5.31: Systematics of positive-parity states of $2d_{3/2} \oplus 3s_{1/2}$ proton-hole configurations in odd-Au isotopes. The data are taken from present work (^{183}Au) and from [61, 77, 127].

and thus is very pure configuration.

In ^{181}Au isotope, no candidates for positive states were identified. However, the Tab. 5.4 contains several unassigned transitions with energies similar to those observed in ^{183}Au, e.g. $165.67\,\mathrm{keV}$, $182.80\,\mathrm{keV}$. These are probably transitions between positive parity states. Due to lack of the statistics, no coincidences were observed for them and therefore they cannot be assigned into the level scheme. Thus, new spectroscopy investigation of ^{181}Au isotope is highly demanding. This must involve detection of conversion electrons, including low energies.

5.3.3 Systematics of intruder configurations

The key result of the IS521 experiment is shown in Fig. 5.32. It gives a systematics of $3/2^-$, $5/2^-$, $7/2^-$, and $9/2^-$ states associated with intruder configurations,

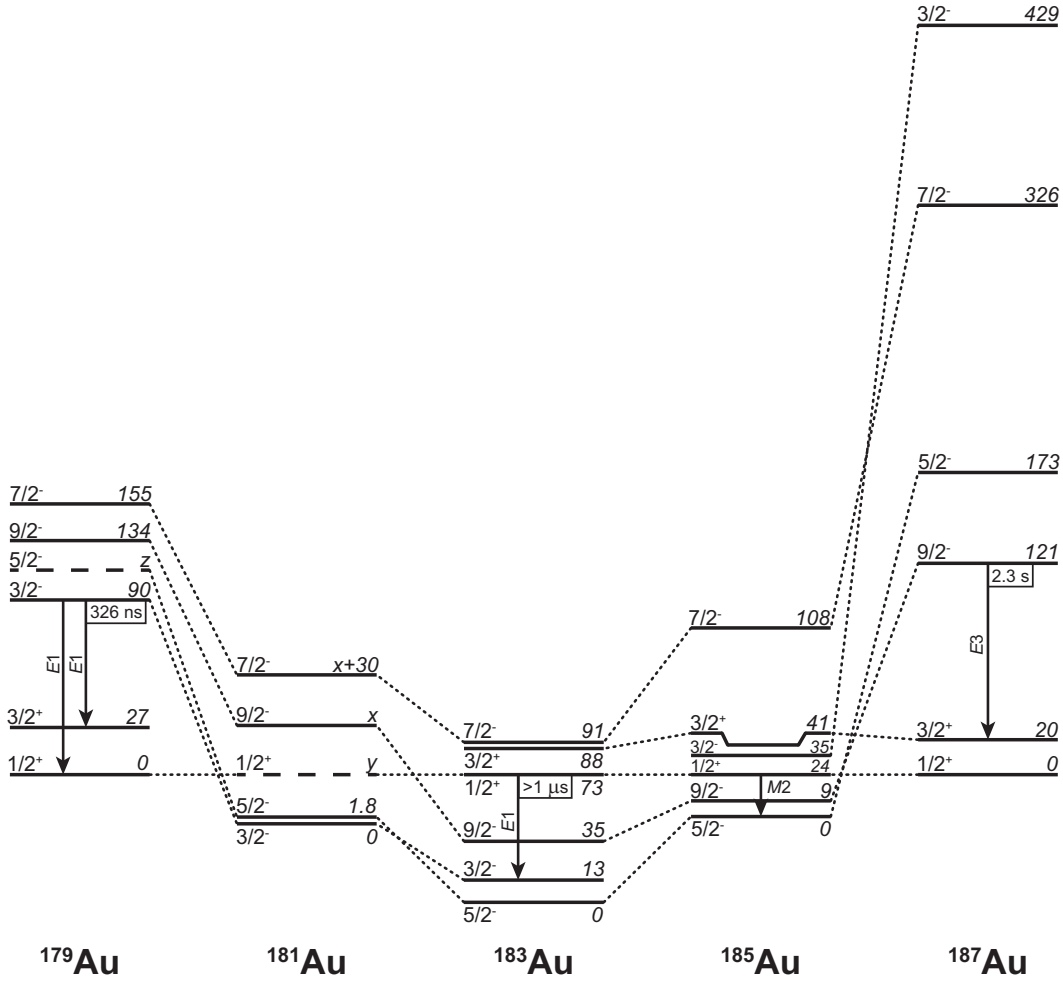

FIGURE 5.32: Systematics of $3/2^-$, $5/2^-$, $7/2^-$, and $9/2^-$ states associated with intruder configurations, depicted relatively to $1/2^+$, and $3/2^+$ states associated with $2d_{3/2}\oplus 3s_{1/2}$ proton–hole configurations in odd-Au isotopes. The data are taken from this work and from [61, 77, 93, 127]

depicted relatively to $1/2^+$, and $3/2^+$ states of "normal" configuration. It reveals parabolic trend, which emerges to be a general characteristic of intruder configurations [2]. Minimum is located at N = 104, i.e., exactly in the midshell point.

Conclusion

This thesis is aimed on γ-ray and conversion-electron spectroscopy of neutron-deficient ^{181,183}Au isotopes. Data were taken during two runs of IS521 experiment at ISOLDE. Excited states of ^{181,183}Au were populated by β^+/EC decay of ^{181,183}Hg isotopes. For the purpose of the γ-ray and conversion-electron spectroscopy, the TATRA spectrometer was employed. After first run of IS521 experiment, the TATRA spectrometer was modified for better transmission of low-energy γ rays and its vacuum condition was enhanced. TATRA has the tape transportation system, which can cooperate with the device under ultra high vacuum (UHV) conditions without differential pumping system. Coaxial HPGe and BEGe detectors were used for γ-ray measurements and windowless liquid-nitrogen-cooled Si(Li) detector was used for measurement of conversion electrons with the resolution (FWHM) of $1.5\,\mathrm{keV}$. Fully digital acquisition system was used together with GO-Box amplifiers and custom signal converter for Si(Li) detector, which was developed.

Using of the BEGe detectors at high gain was essential for this study due to their excellent resolution, smooth background and nearly ideal Gaussian shaped peaks for energies up to $900\,\mathrm{keV}$. This allowed peak recognitions in many multiplets and the determination of peak energies with $30\,\mathrm{eV}$ precision.

A method for separation parent decay from daughter decays in singles spectra was developed. This procedure is based on the time-stamped data acquired with a digital acquisition system operated in triggerless list mode. This method was used to distinguish peaks due to the decay of interest from total singles spectra and energies were obtained by peak fitting. The construction of the level scheme is based on coincidence relationships in conjunction with the Rydberg-Ritz combination principle, when γ-ray energies were determined precisely enough. The decays of ^{181,183}Hg isotopes were analysed and γ-ray energies, intensities and multipolarities of some were determined and level schemes of ^{181,183}Au were constructed.

For the ^{183}Au, two partial level schemes were constructed. One for positive-parity states associated with the $2d_{3/2} \oplus 3s_{1/2}$ proton-hole configurations and one for negative-parity states associated with the $1h_{9/2}$ and $2f_{7/2}$ intruder configurations. Two transitions with $E0$ component were confirmed and one of them was placed into the level scheme. The parity-changing transition with the energy of $60.37\,\mathrm{keV}$ was

identified and placed into the level scheme. Contrary to the previous study, its multipolarity of $E1$ with no abnormality was observed. The excitation energy of $12.74\,\mathrm{keV}$ of the first excited state was determined and the number of incorrect features in the previous study of the ^{183}Hg $\rightarrow$ ^{183}Au decay scheme has been discovered.

For the ^{181}Au, the level scheme based on β^+/EC decay of the ^{181}Hg isotope was constructed for the first time. Previously, only table with γ rays was given and even in this table the incorrect assignment to some γ rays were observed. New γ rays were determined and some multipolarities were tentative assigned, based on the systematics in adjacent odd-Au isotopes.

Systematics of $1h_{11/2}$, $2d_{3/2} \oplus 3s_{1/2}$ proton-hole and $1h_{9/2}$ and $2f_{7/2}$ proton-intruder configurations were expanded. Tiny increase in split of $3/2^-$ and $7/2^-$ states was observed in $1h_{11/2}$ proton-hole configuration, which indicates a slight change in the triaxiality from "oblatish" to "prolatish" shape with decreasing neutron number. Only in ^{183}Au, positive-parity states associated to the $2d_{3/2} \oplus 3s_{1/2}$ proton-hole configurations were identified, due to lack of the statistics in ^{181}Au data. The key result is observation of a parabolic trend in the systematics of intruder states with its minimum in neutron midshell point N = 104 (^{183}Au).

However, the statistical quality of the present data sets are insufficient to place all observed transitions to the level schemes. In the case of the ^{181}Au, low-energy γ rays together with coincidence analysis and conversion electrons can provide valuable missing informations about, e.g., multipolarities of the states, $E0$ transition identification, positive-parity states identification or energy determination of the X level in the level scheme. In the case of the ^{183}Au, is critical to place the $284.40\,\mathrm{keV}$ transition with confirmed $E0$ character into the level scheme. Therefore, another experiments dedicated to study excited states of the ^{181,183}Au isotopes are demanding. For this purpose, a new version of TATRA system is already under development at Department of Nuclear Physics. Experimental program will continue at ISOLDE after long shutdown of CERN. New data will be collected also for ^{179,185,189}Au isotopes.

Zhrnutie

Táto práca je zameraná na γ spektroskopiu a spektroskopiu konverzných elektrónov neutrónovo deficitných izotopov zlata, ^{181,183}Au. Dáta pre túto štúdiu boli odmerané počas dvoch fáz experimentu IS521. Excitované stavy izotopov ^{181,183}Au boli populované β^+/EC premenou ^{181,183}Hg prekurzorov. Spektrometer TATRA bol použitý pre účel merania γ kvánt a konverzných elektrónov. Pred druhou fázou experimentu IS521 bol spektrometer TATRA prebudovaný za účelom lepšej transmisie nízkoenergetických γ kvánt a bola zlepšená jeho schopnosť dosiahnuť ešte lepšie vákuum. TATRA spektrometer obsahuje páskový transportný systém, ktorý je určený na prácu v ultra vysokom vákuu bez potreby diferenciálneho čerpania. Koaxiálne HPGe a BEGe detektory boli použité na meranie γ kvánt a bezoknový Si(Li) detektor, ktorý je chladený tekutým dusíkom, bol použitý na meranie konverzných elektrónov s rozlíšením (FWHM) $1.5\,\mathrm{keV}$. Na zber dát bol použitý digitálny zberový systém a signály z detektorov boli upravené pomocou na mieru robenej elektroniky ako je GO-Box, alebo konvertor signálov pre Si(Li) detektor, ktorý bol vyvinutý ako súčasť tejto práce.

Kľúčové pre túto štúdiu bolo použitie BEGe detektora (spolu so zosilňovačom), ktorý má výborné rozlíšenie, spojité pozadie a takmer ideálne tvarované píky podobné Gaussovému rozdeleniu pre energie až do $900\,\mathrm{keV}$. Tieto vlastnosti umožňujú rozoznanie píkov v multipletoch a určenie energie píkov s presnosťou na $30\,\mathrm{eV}$.

Bola využitá inovatívna metóda na separáciu spektier z premeny východzieho izotopu od spektier z premeny dcérskych izotopov. Táto metóda je založená na spracovaní dát s časovou značkou zozbieraných digitálnym zberovým systémom, ktorý pracuje v móde zapisovania všetkých dát do súboru. Pomocou tejto metódy je možné rozlíšiť píky prislúchajúce študovanej premene v celkovom spektre a ich energie sú následne určené fitom. Konštrukcie rozpadových schém boli založené na koincidenčnej analýze a na kombinačnom princípe, ktorý navrhli Rydberg a Ritz, ak sú energie určene s dostatočnou presnosťou. Premeny vzoriek izotopov ^{181,183}Hg boli analyzované, pričom boli identifikované γ kvantá, ich energie, intenzity a niektoré multipolarity a boli skonštruované rozpadové schémy izotopov ^{181,183}Au.

Dve čiastočné rozpadové schémy boli skonštruované pre izotop ^{183}Au. Jedna pre hladiny s pozitívnou paritou spojené s $2d_{3/2} \oplus 3s_{1/2}$ konfiguráciou protón-diera a jedna pre hladiny s negatívnou paritou spojené s $1h_{9/2}$ a $2f_{7/2}$ vnorenými (intruder)

konfiguráciami. Dva prechody s $E0$ charakterom boli potvrdené. Prechod s energiou $60.37\,\mathrm{keV}$, ktorý je medzi dvomi stavmi s rozdielnou paritou bol identifikovaný a umiestnený do rozpadovej schémy. Multipolarita tohto prechodu bola určená ako $E1$ bez známok abnormality, na rozdiel od predošlej štúdie, ktorá tento prechod určila ako abnormálny $E1$ prechod. Energia prvého vzbudeného stavu bola určená ako $12.74\,\mathrm{keV}$ a bolo identifikovaných množstvo nezrovnalostí v rozpadovej schéme, ktorú navrhovali autori predchádzajúcej štúdie.

rozpadová schéma izotopu ^{181}Au založená na β^+/EC premene izotopu ^{181}Hg bola skonštruovaná po prvýkrát. V predošlej štúdii bola udaná iba tabuľka s energiami a intenzitami niektorých γ kvánt a aj z tých sa ukázalo, že niektoré boli zle priradené. Nové prechody boli identifikované a niekoľko multipolarít bolo pridelených na základe systematík okolitých nepárnych izotopov zlata.

Boli doplnené systematiky $1h_{11/2}$, $2d_{3/2} \oplus 3s_{1/2}$, $1h_{9/2}$ a $2f_{7/2}$ konfigurácií. Mierne zväčšenie energetického rozdielu medzi hladinami $3/2^-$ a $7/2^-$ konfigurácie $1h_{11/2}$ bolo pozorované, čo naznačuje miernu zmenu v tvare jadra zo sploštěného na viac pretiahnuté so zmenšujúcim sa neutrónovým číslom. Stavy s pozitívnou paritou prislúchajúce konfigurácii $2d_{3/2} \oplus 3s_{1/2}$ boli identifikované iba pre izotop ^{183}Au, pretože štatistický súbor pre izotop ^{181}Au nebol dostatočný. Hlavným výsledkom práce je pozorovanie parabolického trendu v systematike vnorených (intruder) stavov s minimom presne medzi dvoma neutrónovými uzavretými vrstvami, N = 104, čo zodpovedá izotopu ^{183}Au.

Avšak štatistický súbor nebol dostatočný na umiestnenie všetkých pozorovaných prechodov do rozpadových schém. V prípade izotopu ^{181}Au by mohli dodatočné merania konverzných elektrónov a γ kvánt a koincidenčná analýza priniesť lepšie poznanie napríklad: multipolarít stavov, rozpoznanie $E0$ prechodov, identifikáciu stavov s pozitívnou paritou alebo doplnenie rozpadovej schémy o energiu hladiny X. V prípade izotopu ^{183}Au je dôležité umiestnenie prechodu s energiou $284.40\,\mathrm{keV}$, ktorý ma potvrdený $E0$ charakter. Preto je žiadúce pripraviť ďalšie experimenty zamerané na štúdium izotopov ^{181,183}Au. Pre tento účel je na Oddelení jadrovej fyziky nová verzia systému TATRA. Experimentálny program bude na na zariadení ISOLDE pokračovať potom, ako skončí veľká odstávka CERNu. Nové dáta pre izotopy ^{179,185,189}Au budú odmerané.

Bibliography

[1] E. Rutherford. "The scattering of α and β particles by matter and the structure of the atom". In: *The London, Edinburgh, and Dublin Philosophical Magazine and Journal of Science* 21 (1911), pp. 669–688. DOI: 10.1080/14786440508637080.

[2] K. Heyde and J. L. Wood. "Shape coexistence in atomic nuclei". In: *Reviews of Modern Physics* 83 (2011), pp. 1467–1521. DOI: 10.1103/RevModPhys.83.1467.

[3] J. L. Wood et al. "Coexistence in even-mass nuclei". In: *Physics Reports* 215 (1992), pp. 101–201. DOI: 10.1016/0370-1573(92)90095-H.

[4] K. Heyde et al. "Coexistence in odd-mass nuclei". In: *Physics Reports* 102 (1983), pp. 291–393. DOI: 10.1016/0370-1573(83)90085-6.

[5] M. Venhart et al. "Simultaneous spectroscopy of γ rays and conversion electrons: Systematic study of E0 transitions and intruder states in close vicinity of mid-shell point in odd-Au isotopes". In: *CERN-INTC* 302 (Jan. 2011), pp. 1–10.

[6] W. Ritz. "On a New Law of Series Spectra". In: *Astronomical Journal* 28 (1908), pp. 237 –243. DOI: 10.1086/141591.

[7] M. Venhart et al. "New systematic features in the neutron-deficient Au isotopes". In: *Journal of Physics G: Nuclear and Particle Physics* 44 (2017), p. 074003. DOI: 10.1088/1361-6471/aa7297.

[8] M. I. Macias-Marques et al. "Decays of 183Hg and 183Au". In: *Nuclear Physics A* 427 (1984), pp. 205 –223. DOI: 10.1016/0375-9474(84)90082-4.

[9] D. J. Rowe and J. L. Wood. *Fundamentals of Nuclear Models: Foundational Models*. Vol. 1. 5 Toh Tuck Link, Singapore 596224: World Scientific Publishing Co. Pte. Ltd., Mar. 2010. ISBN: 978-981-256-955-4.

[10] J. L. Wood. *The Shell Model and the Pairing Model of the Nucleus: unpublished lecture notes*. 2005.

[11] G. F. Knoll. *Radiation Detectibn and Measurement*. 3rd ed. John Wiley & Sons, Inc., 2000. ISBN: 0-471-07338-5.

[12] C. Grupen. *Particle Detectors*. Cambridge University Press, Dec. 1996. ISBN: 0521552168.

[13] K. Debertin and R.G. Helmer. *Gamma- and X-Ray Spectrometry with Semiconductor Detectors*. North Holland, Dec. 1988. ISBN: 978-0444871077.

[14] K. S. Krane. *Introductory Nuclear Physics*. 3rd ed. John Wiley & Sons, Inc., 1988. ISBN: 978-0471805533.

[15] P. Ring and P. Schuck. *The Nuclear Many-Body Problem*. 1st ed. Springer-Verlag Berlin Heidelberg, 1980. ISBN: 978-3-540-21206-5.

[16] R. F. Casten. *Nuclear Structure from a Simple Perspective*. 2nd ed. Oxford University Press Inc., 2001. ISBN: 0-19-850724-0.

[17] M. Venhart. *Personal notes and private communication*. unpublished. 2019.

[18] M. G. Mayer. "On Closed Shells in Nuclei. II". In: *Physical Review* 75 (12 1949), pp. 1969–1970. DOI: 10.1103/PhysRev.75.1969.

[19] O. Haxel, J. H. D. Jensen, and H. E. Suess. "On the "Magic Numbers" in Nuclear Structure". In: *Physical Review* 75 (1949), pp. 1766–1766. DOI: 10.1103/PhysRev.75.1766.2.

[20] S. G. Nilsson et al. "On the nuclear structure and stability of heavy and superheavy elements". In: *Nuclear Physics A* 131.1 (1969), pp. 1 –66. ISSN: 0375-9474. DOI: 10.1016/0375-9474(69)90809-4.

[21] I.-L. Lamm. "Shell-model calculations on deformed nuclei". In: *Nuclear Physics A* 125.3 (1969), pp. 504–530. DOI: 10.1016/0375-9474(69)90745-3.

[22] A. N. Bohr. "The coupling of nuclear surface oscillations to the motion of individual nucleons". In: *Matematisk-fysiske Meddelelser Danske Videnskabernes Selskab* 26.14 (1952), pp. 1–40.

[23] J. Meyer-Ter-Vehn, F. S. Stephens, and R. M. Diamond. "Evidence for Asymmetric Shapes from High-Spin Odd-A Spectra". In: *Phys. Rev. Lett.* 32 (24 1974), pp. 1383–1386. DOI: 10.1103/PhysRevLett.32.1383.

[24] J. Meyer-Ter-Vehn. "Collective model description of transitional odd-A nuclei: (I). The triaxial-rotor-plus-particle model". In: *Nuclear Physics A* 249.1 (1975), pp. 111 –140. DOI: 10.1016/0375-9474(75)90095-0.

[25] J. Meyer-Ter-Vehn. "Collective model description of transitional odd-A nuclei: (II). Comparison with unique parity states of nuclei in the A = 135 and A = 190 mass regions". In: *Nuclear Physics A* 249.1 (1975), pp. 141 –165. DOI: 10.1016/0375-9474(75)90096-2.

[26] A. de Shalit. "Core Excitations in Nondeformed, Odd-A, Nuclei". In: *Physical Review* 122 (1961), pp. 1530–1536. DOI: 10.1103/PhysRev.122.1530.

[27] F. S. Stephens. "Coriolis effects and rotation alignment in nuclei". In: *Rev. Mod. Phys.* 47 (1 1975), pp. 43–65. DOI: 10.1103/RevModPhys.47.43.

[28] J. Meyer-ter-Vehn. "Transitional nuclei and triaxial shapes". In: *Journal de Physique Colloques* 39 (1978), pp. C3–154–C3–163. DOI: 10.1051/jphyscol:1978322.

[29] J. Meyer-ter-Vehn, F. S. Stephens, and R. M. Diamond. "Evidence for Asymmetric Shapes from High-Spin Odd-A Spectra". In: *Physical Review Letters* 32 (1974), pp. 1383–1386. DOI: 10.1103/PhysRevLett.32.1383.

[30] J. M. Blatt and V. F. Weisskopf. *Theoretical nuclear physics*. New York, Wiley, 1952.

[31] S. V. Rigby et al. "Decay of a $\pi h_{11/2} \bigotimes \nu h_{11/2}$ microsecond isomer in $^{136}_{61}\mathrm{Pm}_{75}$". In: *Physical Review C* 78 (3 2008), p. 034304. DOI: 10.1103/PhysRevC.78.034304.

[32] T. Kibédi et al. "Evaluation of theoretical conversion coefficients using BrIcc". In: *Nuclear Instruments and Methods in Physics Research Section A: Accelerators, Spectrometers, Detectors and Associated Equipment* 589 (2008), pp. 202 –229. DOI: 10.1016/j.nima.2008.02.051.

[33] J. A. Bearden and A. F. Burr. "Reevaluation of X-Ray Atomic Energy Levels". In: *Reviews of Modern Physics* 39 (1 1967), pp. 125–142. DOI: 10.1103/RevModPhys.39.125.

[34] H. Morinaga. "Interpretation of Some of the Excited States of $4n$ Self-Conjugate Nuclei". In: *Physical Review* 101 (1956), pp. 254–258. DOI: 10.1103/PhysRev.101.254.

[35] D. J. Rowe, G. Thiamova, and J. L. Wood. "Implications of Deformation and Shape Coexistence for the Nuclear Shell Model". In: *Physical Review Letters* 97 (2006), p. 202501. DOI: 10.1103/PhysRevLett.97.202501.

[36] J. Bonn et al. "Sudden change in the nuclear charge distribution of very light mercury isotopes". In: *Physics Letters B* 38 (1972), pp. 308–311. DOI: 10.1016/0370-2693(72)90253-5.

[37] B. A. Marsh et al. "Characterization of the shape-staggering effect in mercury nuclei". In: *Nature Physics* 14 (2018), pp. 1163–1167. DOI: 10.1038/s41567-018-0292-8.

[38] J. Elseviers et al. "Shape coexistence in ^{180}Hg studied through the β decay of ^{180}Tl". eng. In: *Physical Review C* 84 (2011), p. 034307. DOI: 10.1103/PhysRevC.84.034307.

[39] N. Rud et al. "Lifetimes in the Ground-State Band of ^{184}Hg". In: *Physical Review Letters* 31 (1973), pp. 1421–1423. DOI: 10.1103/PhysRevLett.31.1421.

[40] D. Proetel, R.M. Diamond, and F.S. Stephens. "Nuclear deformations in ^{186}Hg from lifetime measurements". In: *Physics Letters B* 48.2 (1974), pp. 102–104. DOI: https://doi.org/10.1016/0370-2693(74)90653-4.

[41] J. H. Hamilton et al. "Crossing of Near-Spherical and Deformed Bands in ^{186,188}Hg and New Isotopes ^{186,188}Tl". In: *Physical Review Letters* 35 (1975), pp. 562–565. DOI: 10.1103/PhysRevLett.35.562.

[42] J. D. Cole et al. "Behavior of the Excited Deformed Band and Search for Shape Isomerism in ^{184}Hg". In: *Physical Review Letters* 37 (1976), pp. 1185–1188. DOI: 10.1103/PhysRevLett.37.1185.

[43] M. Sandzelius et al. "First observation of excited states in ^{172}Hg". In: *Physical Review C* 79 (2009), p. 064315. DOI: 10.1103/PhysRevC.79.064315.

[44] M. Muikku et al. "Study of shape coexistence in the very neutron-deficient nucleus ^{176}Hg". In: *AIP Conference Proceedings* 495 (1999), pp. 249–250. DOI: 10.1063/1.1302307.

[45] L. P. Gaffney et al. "Shape coexistence in neutron-deficient Hg isotopes studied via lifetime measurements in ^{184,186}Hg and two-state mixing calculations". In: *Physical Review C* 89 (2014), p. 024307. DOI: 10.1103/PhysRevC.89.024307.

[46] E. Rapisarda et al. "Shape coexistence studied in ^{182,184}Hg via the β decay of ^{182,184}Tl". In: *Journal of Physics G: Nuclear and Particle Physics* 44 (2017), p. 074001. DOI: 10.1088/1361-6471/aa6bb6.

[47] N. Bree et al. "Shape Coexistence in the Neutron-Deficient Even-Even $^{182-188}$Hg Isotopes Studied via Coulomb Excitation". In: *Physical Review Letters* 112 (2014), p. 162701. DOI: 10.1103/PhysRevLett.112.162701.

[48] H. De Witte et al. "Nuclear Charge Radii of Neutron-Deficient Lead Isotopes Beyond N=104 Midshell Investigated by In-Source Laser Spectroscopy". In: *Physical Review Letters* 98 (2007), p. 112502. DOI: 10.1103/PhysRevLett.98.112502.

[49] A. N. Andreyev et al. "A triplet of differently shaped spin-zero states in the atomic nucleus 186Pb". In: *Nature* 405 (2000), p. 430.

[50] J. Pakarinen et al. "Evidence for oblate structure in ^{186}Pb". In: *Physical Review C* 72 (2005), p. 011304. DOI: 10.1103/PhysRevC.72.011304.

[51] G. D. Dracoulis et al. "Spherical and deformed isomers in ^{188}Pb". In: *Physical Review C* 60 (1999), p. 014303. DOI: 10.1103/PhysRevC.60.014303.

[52] G. D. Dracoulis et al. "Spectroscopy of $^{188}_{82}Pb_{106}$: Evidence for shape coexistence". In: *Physical Review C* 69 (2004), p. 054318. DOI: 10.1103/PhysRevC.69.054318.

[53] P. M. Walker and G. D. Dracoulis. "Energy traps in atomic nuclei". In: *Nature* 399 (1999), p. 35. DOI: doi.org/10.1038/19911.

[54] M. Ionescu-Bujor et al. "g factors of coexisting isomeric states in ^{188}Pb". In: *Physical Review C* 81 (2010), p. 024323. DOI: 10.1103/PhysRevC.81.024323.

[55] J. L. Wood et al. "Electric monopole transitions from low energy excitations in nuclei". In: *Nuclear Physics A* 651 (1999), pp. 323–368. DOI: 10.1016/S0375-9474(99)00143-8.

[56] T. Kibédi and R.H. Spear. "Electric monopole transitions between 0+ states for nuclei throughout the periodic table". In: *Atomic Data and Nuclear Data Tables* 89 (2005), pp. 77 –100. DOI: 10.1016/j.adt.2004.11.002.

[57] W. P. Alford et al. "$J^\pi = 0^+$ states in the (fp) shell excited in the (^{3}He, n) reaction". In: *Nuclear Physics A* 243 (1975), pp. 269 –297. DOI: 10.1016/0375-9474(75)90248-1.

[58] E. F. Zganjar et al. "Rotation-aligned coupling and axial asymmetry in $^{189-195}$Au". In: *Physics Letters B* 58 (1975), pp. 159–162. DOI: 10.1016/0370-2693(75)90627-9.

[59] V. Berg, R. Foucher, and Å. Höglund. "Quasi-prolate and quasi-oblate bands in soft 189Au". In: *Nuclear Physics A* 244.3 (1975), pp. 462 –486. DOI: 10.1016/0375-9474(75)90552-7.

[60] C. Bourgeois et al. "Étude par spectroscopie "en ligne" des états d'énergie de ^{187}Au: Interprétation en termes de déformations nucléaires triaxiales". In: *Nuclear Physics A* 295 (1978), pp. 424 –444. DOI: 10.1016/0375-9474(78)90184-7.

[61] M. O. Kortelahti et al. "Nuclear systematics far from the line of beta stability: the low-lying excited states of 185,187,189 Au". In: *Journal of Physics G: Nuclear Physics* 14.11 (1988), p. 1361.

[62] D. Rupnik et al. "Coexistence effects in ^{187}Au: Evidence for nearly identical diabatic intruder structures". In: *Physical Review C* 51 (1995), R2867–R2870. DOI: 10.1103/PhysRevC.51.R2867.

[63] D. Rupnik et al. "Levels of ^{187}Au: A detailed study of shape coexistence in an odd-mass nucleus". In: *Physical Review C* 58 (2 1998), pp. 771–795. DOI: 10.1103/PhysRevC.58.771.

[64] C. D. Papanicolopulos et al. "Very converted transitions and particle-core coupling in neutron-deficient odd-mass au isotopes". In: *Zeitschrift für Physik A Atomic Nuclei* 330 (1988), pp. 371–376. DOI: 10.1007/BF01290122.

[65] M. Venhart et al. "Shape coexistence in odd-mass Au isotopes: Determination of the excitation energy of the lowest intruder state in 179Au". In: *Physics Letters B* 695.1-4 (2011), pp. 82 –87. DOI: 10.1016/j.physletb.2010.10.055.

[66] W. B. Ewbank et al. "Nuclear Spins of Six Neutron-Deficient Gold Isotopes". In: *Physical Review* 120 (1960), pp. 1406–1410. DOI: 10.1103/PhysRev.120.1406.

[67] C. Ekström, S. Ingelman, and G. Wannberg. "An atomic-beam magnetic resonance (ABMR) system for on-line hyperfine structure measurements in short-lived nuclides". In: *Nuclear Instruments and Methods* 148 (1978), pp. 17 –28. DOI: 10.1016/0029-554X(78)90329-4.

[68] C. Ekström et al. "Nuclear spins of ^{186,187,188,189,189m}Au". In: *Physics Letters B* 60 (1976), pp. 146 –148. DOI: 10.1016/0370-2693(76)90409-3.

[69] C. Ekström et al. "Nuclear ground-state spin of ^{185}Au and magnetic moments of ^{187,188}Au: Further evidence for coexisting nuclear shapes in this mass region". In: *Nuclear Physics A* 348 (1980), pp. 25 –44. DOI: 10.1016/0375-9474(80)90543-6.

[70] J. G. Cubiss et al. "Change in structure between the I=1/2 states in ^{181}Tl and ^{177,179}Au". In: *Physics Letters B* 786 (2018), pp. 355–363. DOI: 10.1016/j.physletb.2018.10.005.

[71] B. A. Marsh et al. "Development of a RILIS ionisation scheme for gold at ISOLDE, CERN". In: *Hyperfine Interactions* 171 (2006), pp. 109–116. DOI: 10.1007/s10751-006-9498-8.

[72] M. D. Seliverstov et al. "Electromagnetic moments of odd-A $^{193--203,211}$Po isotopes". In: *Physical Review C* 89 (3 2014), p. 034323. DOI: 10.1103/PhysRevC.89.034323.

[73] E. H. Spejewski, R. L. Mlekodaj, and H. K. Carter. "Present status of the unisor facility". In: *Nuclear Instruments and Methods in Physics Research* 186 (1981), pp. 71 –78. DOI: 10.1016/0029-554X(81)90889-2.

[74] R. L. Mlekodaj et al. "The UNISOR integrated target-ion source". In: *Nuclear Instruments and Methods* 139 (1976), pp. 299–303. DOI: 10.1016/0029-554X(76)90689-3.

[75] R. L. Mlekodaj, E. F. Zganjar, and J. D. Cole. "A new concept for a compact tape transport system". In: *Nuclear Instruments and Methods in Physics Research* 186 (1981), pp. 239–241. DOI: 10.1016/0029-554X(81)90911-3.

[76] E. F. Zganjar et al. "Rotation-aligned coupling and axial asymmetry in $^{189-195}$Au". In: *Physics Letters B* 58 (1975), pp. 159 –162. DOI: 10.1016/0370-2693(75)90627-9.

[77] D. Rupnik et al. "Levels of ^{187}Au: A detailed study of shape coexistence in an odd-mass nucleus". In: *Physical Review C* 58 (1998), pp. 771–795. DOI: 10.1103/PhysRevC.58.771.

[78] D. Rupnik et al. "Coexistence effects in ^{187}Au: Evidence for nearly identical diabatic intruder structures". In: *Physical Review C* 51 (1995), R2867–R2870. DOI: 10.1103/PhysRevC.51.R2867.

[79] J. L. Wood et al. "Symmetry between particle and hole level systems in ^{189}Au". In: *Physical Review C* 14 (1976), pp. 682–684. DOI: 10.1103/PhysRevC.14.682.

[80] Y. Xu et al. "Shape coexistence and electric monopole transitions in ^{184}Pt". In: *Physical Review Letters* 68 (1992), pp. 3853–3856. DOI: 10.1103/PhysRevLett.68.3853.

[81] M. Cailliau et al. "Étude de la désintégration ^{184}Au$\rightarrow$^{184}Pt ($T_{1/2} = 53{,}0 \pm 1{,}4$ s)". In: *Journal de Physique (Paris)* 35 (1974), pp. 469–482. DOI: 10.1051/jphys:01974003506046900.

[82] C. Bourgeois et al. "Decays of $^{185m+g}$Hg: Low-spin levels of ^{185}Au as a test of nuclear models". In: *Nuclear Physics A* 386 (1982), pp. 308 –332. DOI: 10.1016/0375-9474(82)90115-4.

[83] J. D. Cole et al. "Decay of ^{188}TI and observed shape coexistence in the bands of ^{188}Hg". In: *Physical Review C* 30 (1984), pp. 1267–1275. DOI: 10.1103/PhysRevC.30.1267.

[84] J. D. Cole et al. "Shape coexistence in ^{186}Hg and the decay of ^{186}Tl". In: *Physical Review C* 16 (1977), pp. 2010–2018. DOI: 10.1103/PhysRevC.16.2010.

[85] C. R. Bingham et al. "α-decay rates for ^{181,186}Au and ^{181,185}Pt isotopes". In: *Physical Review C* 51 (1995), pp. 125–135. DOI: 10.1103/PhysRevC.51.125.

[86] J. Sauvage et al. "Decays of ^{181}Hg ($T_{1/2} = 3.6$ s) and ^{181}Au ($T_{1/2} = 11.4$ s), and low-spin states of ^{181}Pt and ^{177,181}Ir". In: *Nuclear Physics A* 540 (1992), pp. 83–116. DOI: 10.1016/0375-9474(92)90196-Q.

[87] A. N. Andreyev et al. "Decay of the $9/2^-$ isomer in ^{181}Tl and mass determination of low-lying states in ^{181}Tl, ^{177}Au, and ^{173}Ir". In: *Physical Review C* 80 (2009), p. 024302. DOI: 10.1103/PhysRevC.80.024302.

[88] K. T. Hecht and G.R. Satchler. "Asymmetric rotator model of odd-mass nuclei". In: *Nuclear Physics* 32 (1962), pp. 286 –318. DOI: 10.1016/0029-5582(62)90340-1.

[89] Ch. Vieu et al. "The particle-asymmetric rotor descriptions of 193-199 Au (positive parity states)". In: *Journal of Physics G: Nuclear Physics* 4 (1978), p. 531.

[90] J. O. Rasmussen. "Alpha-Decay Barrier Penetrabilities with an Exponential Nuclear Potential: Odd-Mass Nuclei". In: *Physical Review* 115 (1959), pp. 1675–1679. DOI: 10.1103/PhysRev.115.1675.

[91] G. L. Poli et al. "Proton and α radioactivity below the $Z = 82$ shell closure". In: *Physical Review C* 59 (1999), R2979–R2983. DOI: 10.1103/PhysRevC.59.R2979.

[92] A. N. Andreyev et al. "α-decay spectroscopy of the chain ^{179}Tl$^g \rightarrow ^{175}$Au$^g \rightarrow ^{171}$Ir$^g \rightarrow ^{167}$Re^m". In: *Physical Review C* 87 (2013), p. 054311. DOI: 10.1103/PhysRevC.87.054311.

[93] M. Venhart et al. "Shape coexistence in odd-mass Au isotopes: Determination of the excitation energy of the lowest intruder state in 179Au". In: *Physics Letters B* 695 (2011), pp. 82 –87. DOI: 10.1016/j.physletb.2010.10.055.

[94] M. Leino et al. "Gas-filled recoil separator for studies of heavy elements". In: *Nuclear Instruments and Methods in Physics Research Section B: Beam Interactions with Materials and Atoms* 99 (1995), pp. 653 –656. DOI: 10.1016/0168-583X(94)00573-7.

[95] R. D. Page et al. "The GREAT spectrometer". In: *Nuclear Instruments and Methods in Physics Research Section B: Beam Interactions with Materials and Atoms* 204 (2003), pp. 634 –637. DOI: 10.1016/S0168-583X(02)02143-2.

[96] J. G. Cubiss et al. "Charge radii and electromagnetic moments of $^{195--211}$At". In: *Physical Review C* 97 (2018), p. 054327. DOI: 10.1103/PhysRevC.97.054327.

[97] M. Venhart et al. "De-excitation of the strongly coupled band in ^{177}Au and implications for core intruder configurations in the light Hg isotopes". In: *Physical Review C(R)* 95 (2017), p. 061302. DOI: 10.1103/PhysRevC.95.061302.

[98] K.-H. Schmidt et al. "Gamma-Spectroscopic investigations in the radiative fusion reaction 90Zr + 90Zr". In: *Physics Letters B* 168 (1986), pp. 39–42. DOI: https://doi.org/10.1016/0370-2693(86)91456-5.

[99] E. S. Paul et al. "In-beam γ-ray spectroscopy above ^{100}Sn using the new technique of recoil decay tagging". In: *Physical Review C* 51 (1995), pp. 78–87. DOI: 10.1103/PhysRevC.51.78.

[100] A. Herlert. "Laboratory Portrait: The ISOLDE Facility". In: *Nuclear Physics News International* 20 (Dec. 2010), pp. 5–12.

[101] V. Matoušek et al. "TATRA: a versatile high-vacuum tape transportation system for decay studies at radioactive-ion beam facilities". In: *Nuclear Instruments and Methods in Physics Research Section A: Accelerators, Spectrometers, Detectors and Associated Equipment* 812 (2016), pp. 118 –121. DOI: 10.1016/j.nima.2015.12.039.

[102] T. E. Cocolios et al. "The Collinear Resonance Ionization Spectroscopy (CRIS) experimental setup at CERN-ISOLDE". In: *Nuclear Instruments and Methods in Physics Research Section B: Beam Interactions with Materials and Atoms* 317 (2013), pp. 565–569. DOI: 10.1016/j.nimb.2013.05.088.

[103] R. L. Mlekodaj, E. F. Zganjar, and J. D. Cole. "A new concept for a compact tape transport system". In: *Nuclear Instruments and Methods in Physics Research* 186 (1981), pp. 239–241.

[104] P. Duhaj, V. Sládek, and P. Mrafko. "PRODUCTION OF THIN AMORPHOUS SAMPLES USING A RAPIDLY ROTATING MILL DEVICE". In: *Československý časopis pro fysiku sekce A* A 23.6 (1973), 617–619.

[105] Atlas Technologies. *Atlas Al/SS CF^{TM} Flange*. [Online; accessed December-2018]. 2018.

[106] L. J. Harkness-Brennan et al. "An experimental characterisation of a Broad Energy Germanium detector". In: *Nuclear Instruments and Methods in Physics Research A* 760 (Oct. 2014), pp. 28–39. DOI: 10.1016/j.nima.2014.05.080.

[107] G. Meierhofer et al. "GERDA - a new neutrinoless double beta experiment using76Ge". In: *Journal of Physics: Conference Series* 312 (2011), p. 072011. DOI: 10.1088/1742-6596/312/7/072011.

[108] H. Tan et al. "Evaluation of Multi-Channel ADCs for Gamma-Ray Spectroscopy". In: *IEEE Transactions on Nuclear Science* 60 (2013), pp. 599–605. DOI: 10.1109/TNS.2013.2243468.

[109] R. Brun R. and F. Rademakers. "ROOT - An Object Oriented Data Analysis Framework". In: *Nuclear Instruments and Methods in Physics Research A* 389 (1996), pp. 81–86. DOI: 10.1016/S0168-9002(97)00048-X.

[110] M. Venhart et al. "Application of the Broad Energy Germanium detector: A technique for elucidating β-decay schemes which involve daughter nuclei with very low energy excited states". In: *Nuclear Instruments and Methods in Physics Research Section A: Accelerators, Spectrometers, Detectors and Associated Equipment* 849 (2017), pp. 112–118. DOI: 10.1016/j.nima.2016.12.048.

[111] Yu. Khazov, A. Rodionov, and F.G. Kondev. "Nuclear Data Sheets for A = 133". In: *Nuclear Data Sheets* 112 (2011), pp. 855 –1113. DOI: 10.1016/j.nds.2011.03.001.

[112] E. Browne and J.K. Tuli. "Nuclear Data Sheets for A = 137". In: *Nuclear Data Sheets* 108.10 (2007), pp. 2173 –2318. DOI: 10.1016/j.nds.2007.09.002.

[113] M. J. Martin. "Nuclear Data Sheets for A = 152". In: *Nuclear Data Sheets* 114.11 (2013), pp. 1497 –1847. DOI: 10.1016/j.nds.2013.11.001.

[114] M. S. Basunia. "Nuclear Data Sheets for A = 237". In: *Nuclear Data Sheets* 107 (2006), pp. 2323 –2422. DOI: 10.1016/j.nds.2006.07.001.

[115] J.K. Tuli. *Current Version of Nuclear Wallet Cards*. 2017. (Visited on 02/20/2019).

[116] M. Morháč et al. "Background elimination methods for multidimensional coincidence gamma-ray spectra". In: *Nuclear Instruments and Methods in Physics Research Section A: Accelerators, Spectrometers, Detectors and Associated Equipment* 401 (1997), pp. 113–132. DOI: 10.1016/S0168-9002(97)01023-1.

[117] M. Wang et al. "The Ame2012 atomic mass evaluation". In: *Chinese Physics C* 36 (2012), pp. 1603–2014. DOI: 10.1088/1674-1137/36/12/003.

[118] P. Hornshøj et al. "Beta-strength functions of neutron-deficient isotopes in the xenon and mercury regions". In: *Nuclear Physics A* 239 (1975), pp. 15–28. DOI: 10.1016/0375-9474(75)91130-6.

[119] J. Bonn et al. "Spins, moments and charge radii in the isotopic series ^{181}Hg–^{191}Hg". In: *Zeitschrift für Physik A Atoms and Nuclei* 276 (1976), pp. 203–217. DOI: 10.1007/BF01412098.

[120] U. Krönert et al. "Observation of strongly deformed ground-state configurations in ^{184}Au and ^{183}Au by laser spectroscopy". In: *Zeitschrift für Physik A: Atomic Nuclei* 331 (1988), pp. 521–522. DOI: 10.1007/BF01291911.

[121] L. T. Song et al. "High-spin level scheme of ^{183}Au". In: *Physical Review C* 71 (2005), p. 017302. DOI: 10.1103/PhysRevC.71.017302.

[122] W. F. Mueller et al. "High-spin structure in ^{181,183}Au". In: *Physical Review C* 59 (1999), pp. 2009–2032. DOI: 10.1103/PhysRevC.59.2009.

[123] E. Hagberg et al. "Alpha decay of neutron-deficient mercury isotopes and their daughters". In: *Nuclear Physics A* 318 (1979), pp. 29 –44. DOI: 10.1016/0375-9474(79)90467-6.

[124] B. L. Ader and N. N. Perrin. "Niveaux d'énergie du $^{177}_{73}$Ta". In: *Nuclear Physics A* 197 (1972), pp. 593–619. DOI: 10.1016/0375-9474(72)91032-9.

[125] S. E. Larsson, G. Leander, and I. Ragnarsson. "Nuclear core-quasiparticle coupling". In: *Nuclear Physics A* 307 (1978), pp. 189–223. DOI: 10.1016/0375-9474(78)90613-9.

[126] C. D. Papanicolopoulos. "Shape Coexistence in Odd-Mass Nuclei Near Z = 82 Closed Shell: A Study of the Excited States of ^{185}Au in the β^+/EC Decay of ^{185}Au." PhD thesis. Georgia Institute of Technology, 1987.

[127] J. L. Wood et al. "Decay of mass-separated ^{189m}Hg (8.7 min) and ^{189g}Hg (7.7 min) to ^{189}Au". In: *Nuclear Physics A* 600 (1996), pp. 283–334. DOI: 10.1016/0375-9474(95)00478-5.

Appendix A

Publications

V. Matoušek, M. Sedlák, M. Venhart, D. Janičkovič, J. Kliman, K. Petrík, P. Švec, P. Švec, Sr., M. Veselský.
"*TATRA: a versatile high-vacuum tape transportation system for decay studies at radioactive-ion beam facilities*".
Nuclear Instruments and Methods in Physics Research Section A **812**, 118–121 (2016).

M. Venhart, J. L. Wood, A. J. Boston, T. E. Cocolios, L. J. Harkness-Brennan, R. D. Herzberg, D. T. Joss, D. S. Judson, J. Kliman, V. Matoušek, Š. Motyčák, R. D. Page, A. Patel, K. Petrík, M. Sedlák, M. Veselský.
"*Application of the Broad Energy Germanium detector: A technique for elucidating decay schemes which involve daughter nuclei with very low energy excited states*".
Nuclear Instruments and Methods in Physics Research Section A **849**, 112–118 (2017).

M. Venhart, J. L. Wood, M. Sedlák, M. Balogh, M. Bírová, A. J. Boston, T. E. Cocolios, L. J. Harkness-Brennan, R.-D. Herzberg, L. Holub, D. T. Joss, D. S. Judson, J. Kliman, J. Klimo, L. Krupa, J. Lušsnák, L. Makhathini, V. Matoušek, Š. Motyčák, R. D. Page, A. Patel, K. Petrík, A. V. Podshibyakin, P. M. Prajapati, A. M. Rodin, A. Špaček, R. Urban, C. Unsworth, M. Veselský.
"*New systematic features in the neutron-deficient Au isotopes*".
Journal of Physics G: Nuclear and Particle Physics **44**, 074003 (2017).

M. Venhart, F. A. Ali, W. Ryssens, J. L. Wood, D. T. Joss, A. N. Andreyev, K. Auranen, B. Bally, M. Balogh, M. Bender, R. J. Carroll, J. L. Easton, P. T. Greenlees, T. Grahn, P.-H. Heenen, A. Herzáň, U. Jakobsson, R. Julin, S. Juutinen, D. Kĺč, J. Konki, E. Lawrie, M. Leino, V. Matoušek, C. G. McPeake, D. O'Donnell, R. D. Page, J. Pakarinen, J. Partanen, P. Peura, P. Rahkila, P. Ruotsalainen, M. Sandzelius, J. Sarén, B. Sayği, M. Sedlák, C. Scholey, J. Sorri, S. Stolze, A. Thornthwaite, J. Uusitalo, M. Veselský.
"*De-excitation of the strongly coupled band in ^{177}Au and implications for core intruder configurations in the light Hg isotopes*".
Physical Review C **95**, 061302(R) (2017).